REFLEX 2012
Regional Experiments
For Land-atmosphere Exchanges

PREFACE TO THE SPECIAL SECTION

Bob SU

Faculty of Geo-Information Science and Earth Observation (ITC),
University of Twente, Enschede, The Netherlands;
e-mail: z.su@utwente.nl

This special issue reports some of the scientific findings of the "Regional Experiments For Land-atmosphere Exchanges" (REFLEX 2012), a training workshop supported by the EUropean Facility for Airborne Research (EUFAR) under the European Commission seventh Framework Programme (FP7) and the "Spectral Sampling Tools for Vegetation Biophysical Parameters and Flux Measurements in Europe" (EUROSPEC) action under the intergovernmental framework for European Cooperation in Science and Technology (COST). REFLEX 2012 took place in Albacete and Barrax, Spain from 18 to 28 July 2012. The theme of the training workshop was the organizing and conducting of a hyper-spectral multi-angular airborne campaign for multi-scale ("leaf-to-ecosystem") land-atmosphere exchange research.

Timmermans *et al.* (a) provides an overview of the REFLEX 2012 campaign, describing the objectives and the technical details of the campaign. The measurements and observations included multi-temporal, multi-

directional, multi-spectral, and multi-spatial space-borne and airborne obser-
vations, measurements of the local meteorological variables, energy fluxes,
soil temperature and soil moisture profiles, surface temperature, as well as
canopy structure and leaf-level biophysical properties. Multispectral and
thermo-dynamical monitoring were conducted at selected sites.

The details of collected data by the Airborne Hyperspectral Scanner
(AHS) and Compact Airborne Spectrographic Imager (CASI) sensors as well
their processing methods and results are described by de Miguel *et al.*
Calleja *et al.* reported relating the hyperspectral airborne data to ground
measurements, and van der Tol *et al.* provided an analysis of turbulent heat
fluxes and the energy balance during the REFLEX 2012 campaign.

Andreu *et al.* studied the influence of thermal components for dual
source energy flux estimates over a drip-irrigated vineyard in the Barrax area
and Timmermans *et al.* (b) illustrated the use of land surface temperature
with a simple approach for monitoring evapotranspiration, which are com-
plemented by a study by Corbari *et al.* in intercomparison of surface energy
fluxes estimates by two different models over the heterogeneous
REFLEX 2012 site.

The European Space Agency and the University of Twente provided ad-
ditional financial supports in addition to that by EUFAR and EUROSPEC
that enabled the successful conduction of the REFLEX 2012 campaign.

An Overview of the Regional Experiments for Land-atmosphere Exchanges 2012 (REFLEX 2012) Campaign

Wim J. TIMMERMANS[1], Christiaan van der TOL[1], Joris TIMMERMANS[1],
Murat UCER[1], Xuelong CHEN[1], Luis ALONSO[2], Jose MORENO[2],
Arnaud CARRARA[3], Ramon LOPEZ[3], Fernando de la CRUZ TERCERO[4],
Horacio L. CORCOLES[4], Eduardo de MIGUEL[5], Jose A.G. SANCHEZ[5],
Irene PÉREZ[5], Belen FRANCH[6], Juan-Carlos J. MUNOZ[6],
Drazen SKOKOVIC[6], Jose SOBRINO[6], Guillem SORIA[6],
Alasdair MacARTHUR[7], Loris VESCOVO[8], Ils REUSEN[9],
Ana ANDREU[10], Andreas BURKART[11], Chiara CILIA[12],
Sergio CONTRERAS[13], Chiara CORBARI[14], Javier F. CALLEJA[15],
Radoslaw GUZINSKI[16], Christine HELLMANN[17], Ittai HERRMANN[18],
Gregoire KERR[19], Adina-Laura LAZAR[20], Benjamin LEUTNER[21],
Gorka MENDIGUREN[13], Sylwia NASILOWSKA[22], Hector NIETO[16],
Javier PACHEGO-LABRADOR[13], Survana PULANEKAR[23], Rahul RAJ[1],
Anke SCHIKLING[11], Bastian SIEGMANN[24], Stefanie von BUEREN[25],
and Zhongbo (Bob) SU[1]

[1]University of Twente, Faculty of Geo-information Science and Earth Observation,
Department of Water Resources, Enschede, The Netherlands
e-mail: w.j.timmermans@utwente.nl (corresponding author)

[2]Laboratory for Earth Observation, Department of Earth Physics,
University of Valencia, Valencia, Spain

[3]Fundacion CEAM, Parque Tecnologico, Valencia, Spain

[4]Instituto Técnico Agronómico Provincial de Albacete (ITAP),
Albacete, Spain

[5]Instituto Nacional de Tecnica Aerospacial (INTA), Depto.
De Observacion de la Tierra, Teledeteccion y Atmosfera, Madrid, Spain

[6]Global Change Unit (GCU), Department of Earth Physics,
University of Valencia, Valencia, Spain

[7]NERC Field Spectroscopy Facility, University of Edinburgh,
Edinburgh, United Kingdom

[8]Fondazione Edmund Mach-Research and Innovation Centre,
San Michele all'Adige, Trento, Italy

[9]Flemish Institute for Technological Research (VITO), Mol, Belgium

[10]Instituto de Investigación y Formación Agraria y Pesquera (IFAPA),
Sevilla, Spain

[11]Institute of Bio- and Geosciences, IBG-2: Plant Sciences,
Forschungszentrum Jülich, Jülich, Germany

[12]University Milano Bicocca, Milano, Italy

[13]Consejo Superior de Investigaciones Científicas (CSIC), Madrid, Spain

[14]Politecnico di Milano, Milano, Italy

[15]University of Oviedo, Oviedo, Spain

[16]University of Copenhagen, Copenhagen, Denmark

[17]Experimental and Systems Ecology, University of Bielefeld, Bielefeld, Germany

[18]The Remote Sensing Laboratory, Jacob Blaustein Institutes for Desert Research,
Ben-Gurion University of the Negev, Beer-Sheva, Israel

[19]German Aerospace Center (DLR), Oberpfaffenhofen, Wessling, Germany

[20]Babes-Bolyai University, Cluj-Napoca, Romania

[21]University of Würzburg, Würzburg, Germany

[22]University of Warsaw, Warsaw, Poland

[23]University of Reading, Reading, United Kingdom

[24]University of Osnabruck, Osnabruck, Germany

[25]Massey University, Palmerston North, New Zealand

Abstract

The REFLEX 2012 campaign was initiated as part of a training course on the organization of an airborne campaign to support advancement of the understanding of land-atmosphere interaction processes. This article describes the campaign, its objectives and observations, remote as well as *in situ*. The observations took place at the experimental Las Tiesas farm in an agricultural area in the south of Spain. During the period of ten days, measurements were made to capture the main processes controlling the local and regional land-atmosphere exchanges. Apart from multi-temporal, multi-directional and multi-spatial space-borne and airborne observations, measurements of the local meteorology, energy fluxes, soil temperature profiles, soil moisture profiles, surface temperature, canopy structure as well as leaf-level measurements were carried out. Additional thermo-dynamical monitoring took place at selected sites.

After presenting the different types of measurements, some examples are given to illustrate the potential of the observations made.

1. INTRODUCTION

Quantification of bio-geophysical variables of different surfaces is essential for understanding the earth system and for the development of earth system models for prediction of climate and environmental change (Kornelsen and Coulibalya 2013, Mishra and Singh 2011, Rast *et al.* 2014, Seneviratne *et al.* 2010, Wang and Dickinson 2012). Remote sensing monitoring is essential for the development and validation of these observational and process models as well as retrieval algorithms (Gamon *et al.* 2010, Rodell *et al.* 2004, Salama *et al.* 2012, van Dijk and Renzullo 2011, Yebra *et al.* 2013).

Understanding the retrieval of bio-geophysical variables from optical-thermal and microwave data and the modeling of the underlying processes over inhomogeneous terrain remains problematic due to a lack of observational data at appropriate scales (McCabe and Wood 2006, Timmermans *et al.* 2008, 2013, Wu and Li 2009). Thereto a campaign was designed to use airborne sensors for multi-angular hyper-spectral optical-thermal data acquisition and to collect field measurements over several land-cover units. In addition, optical-thermal satellite data for the same period were acquired. The obtained data-set was then used for model validation and inversion algorithms that are used to extract quantitative surface variables and for land-atmosphere interaction studies.

To advance the understanding of land-atmosphere exchanges of water and heat at spatial and temporal scales, measurements of these exchanges and of thermo-dynamic states of the atmosphere and surface were carried out over several land-cover units. Since turbulent fluxes occur from molecular to regional scales and are influenced by internal biophysical characteristics and external forcing (*e.g.*, solar radiation and wind), the measurements of these fluxes are very challenging over a heterogeneous terrain (Novick *et al.* 2014, Prueger *et al.* 2012). Because the terrain heterogeneity (in terms of surface roughness and soil and vegetation properties) in combination with the turbulent fluxes causes thermo-dynamic changes of the surface state, a number of ground based instruments is employed. These were distributed over several different land-cover units to ensure a complete observation and understanding of these fluxes at spatial and temporal scales.

The campaign was carried out under the umbrella of the REFLEX 2012 training course supported by the FP7-funded European Facility For Airborne Research (EUFAR) and Cost Action-funded ES0903 EUROSPEC projects

and took place in Albacete and Barrax, Spain, during 18 to 28 July 2012. The theme of the course was the organizing and conducting of a hyper-spectral multi-angular airborne campaign in the framework of multi-scale ("leaf-to-ecosystem") land-atmosphere exchange research.

2.   MAIN OBJECTIVES AND TASKS OF THE CAMPAIGN

The general objectives of the campaign were:

❑   advancement of the process understanding that describes radiative and turbulent transfer in land-atmosphere interactions,

❑   acquisition of simultaneous multi-temporal, multi-angular, and multi-sensor hyper-spectral data over a heterogeneous area,

❑   validation of bio-geophysical variables extraction from satellite data using airborne and *in situ* data,

❑   improvement of soil moisture retrieval by using both multi-angular and hyper-spectral optical-thermal observations.

To reach these objectives, a specific tailor-made flight plan was designed concurrent to field measurements supporting the airborne data processing and analysis. To ensure the availability of multi-angular and multi-scale optical-thermal observations, satellite data, comprising Compact High Resolution Imaging Spectrometer – Project for On-Board Autonomy (CHRIS–PROBA) and Meteosat Second Generation (MSG), were collected during the campaign as well. The CASA 212-INTA airplane was used for mounting the Airborne Hyperspectral Scanner (AHS) and Compact Airborne Spectrographic Imager (CASI) sensors in order to collect multi-sensor hyper-spectral data and a flight plan was developed so as to ensure multi-angular and multi-temporal observations at high spatial resolution.

Information of the atmospheric state, which mainly concerns the Aerosol Optical Thickness (AOT), the ozone and water vapour content, is needed to carry out atmospheric corrections of spaceborne and airborne measurements. Several types of atmospheric and field-based observations supporting this were obtained simultaneously, comprising atmospheric soundings as well as *in situ* measurements using sun photometers. Different groups were simultaneously operating Analytical Spectral Devices (ASD) FieldSpec Pro FR, CIMEL, and Everest radiometers for measuring reflectance and emittance from calibration targets in the solar and thermal range of the electromagnetic spectrum.

Knowledge of the heat transfer, needed for understanding the exchanges of water vapour and energy between a canopy and the surrounding atmosphere, was obtained in several ways, depending on the scale. Locally this involved the monitoring of individual leaf and soil sunlit and shadowed temperatures, whereas more towards a regional scale, micro-meteorological

and turbulent flux measurements were carried out from masts at specific se-lected sites. These comprised Eddy-Covariance (EC) and Large Aperture Scintillometer (LAS) measurements, covering multiple land-cover units, in combination with profile observations of specific humidity, air temperature and windspeed, and profiles of soil temperature, soil heat flux, and soil mois-ture.

Finally, a limited number of field-based biophysical (soil, vegetation, and water) measurements were carried out over different land-cover units. Among other things, they comprised the estimates of Fractional Vegetation Cover (FVC), Leaf Area Index (LAI), Photosynthetically Active Radiation (PAR), leaf reflectance, leaf transmittance, surface emissivity, and soil mois-ture.

3. EXPERIMENT AND DATASETS

3.1 Experimental site and background climatology

The campaign area was the well-known Barrax test site, situated at a plateau 700 m a.s.l. within the La Mancha region, in the south-east of Spain (Fig. 1). The agricultural area is located in the west of the Albacete province, 20 km from the capital town Albacete.

The area is characterized by a flat morphology and large, uniform land use units and consists of approximately 65% of dry land, and 35% of irri-
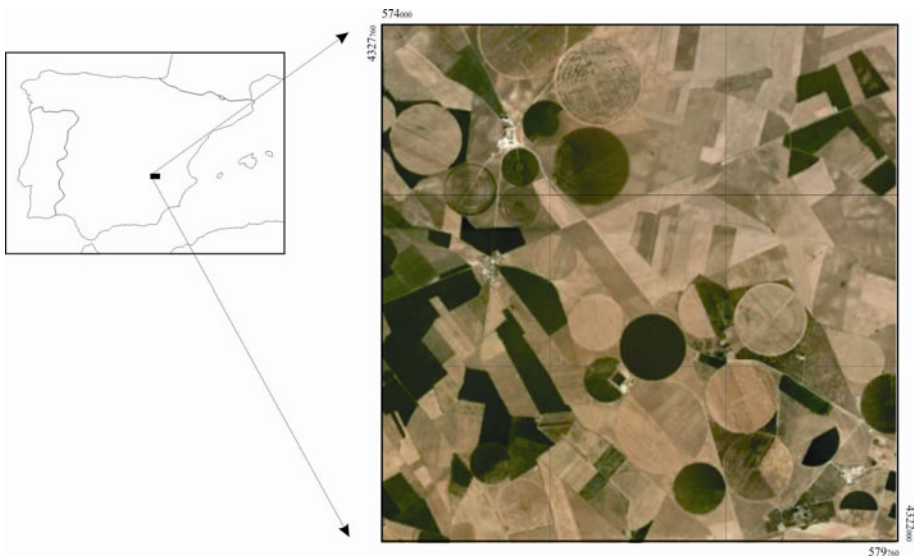
Fig. 1. Site location (zoom from Google Earth).

gated land with different agricultural crops and orchards. Field sizes range from a few tens of meters up to almost 1 km in diameter, where the larger fields are circular shaped and irrigated by a rotating pivot system.

The majority of the campaign activities were concentrated in the fields of the Las Tiesas experimental farm, operated by the Instituto Tecnico Agronomico Provincial (ITAP) of Albacete, Spain, which has been used extensively in previous campaigns for calibration and validation of remote sensing observations (Sobrino *et al.* 2009, Su *et al.* 2008). A landcover map for the Las Tiesas fields is digitally available. The main land use types during the current campaign included: bare soil, vineyard, maize, forest nursery, barley (stubble), wheat (stubble), poppy, (young) sunflower, walnut and pistachio orchards, and camelina (from the mustard family). At the time of the campaign, most of the crops were already harvested. The only canopies with a significant green vegetation fraction during the campaign were maize, vineyard, and sunflower (early growth stage) as well as orchards and forest nursery.

The La Mancha region has a mid-latitude semi-arid climate with most of the rainfall concentrated during the spring and autumn seasons, and lower levels during the summer. With an annual rainfall which averages around 350 mm, La Mancha is one of the driest regions of Europe and potential evaporation rates reach up to 900 mm per year. Due to these dry conditions combined with intensive irrigation practices the regional water table is about 20-30 m below the land surface.

The area is characterized by cold winters and hot dry summers. Monthly averages of minimum temperature range from 2 °C in January to 19 °C during July, whereas monthly maximum temperatures range from 11 °C to 34 °C in these months. During the summer months, temperatures above 40 °C are not uncommon and rainfall is rare.

3.2 Remote sensing data acquisitions

Satellite data acquisitions

To comply with the multi-directional, multi-temporal, and multi-spatial character of the land-atmosphere exchange experiment undertaken, space-borne observations from two specific platforms were acquired during the campaign. The multi-temporal aspect was covered by the acquisition of MSG observations every 15 min during the entire campaign at a low spatial resolution of 3 km, whereas the multi-directional aspect was covered by acquiring Compact High Resolution Imaging Spectrometer (CHRIS) data at a relatively high spatial resolution of 36 m.

CHRIS is a small and relatively light (weight less than 15 kg) spectrometer and it operates in push-broom mode. Its main application areas are in for-

estry, environmental monitoring and precision farming. Its orbit is at 600 km, which results in a 14 km swath with a spatial resolution of 18 m. This is slightly variable because the altitude varies along the orbit. CHRIS is mounted on the PROBA (PRoject for On-Board Autonomy) platform, which has steering capabilities in the along- and across-track directions. This enables observation of selectable targets far outside the nominal field of view of 1.3°. Images are generally acquired in sets of 5, taken at along track angles of ±55 degrees, ±36 degrees, and at nadir (see Fig. 2).

CHRIS operates in the visible to near infrared wavelength region (400 to 1050 nm) and can either operate in 63 spectral bands at a reduced spatial resolution of 36 m, or with 18 bands at full spatial resolution. Its spectral resolution is variable from 2-3 nm at the blue end of the spectrum, to some 12 nm at the 1050 nm edge. As such, the instrument is very flexible and different sets of bands and configurations can be used for different applications.

The Meteosat Second Generation 1 (MSG1) satellite, renamed Meteosat-8, carries the Spinning Enhanced Visible and Infrared Imager (SEVIRI) which is its main payload. This optical imaging radiometer consists of three visible and near infrared channels, eight infrared channels, and one visible broadband channel called the High Resolution Visible channel (HRV). The spatial resolution of SEVIRI channels is 3 km at sub-satellite point, except for the HRV channel which has a 1 km resolution. The temporal resolution is 15 min. The data acquisition for the period of the campaign was standard and the imagery is freely available. For downloading the data the following link from the Unified Meteorological Archive and Retrieval Facility (UMARF) is recommended: http://www.eumetsat.int/Home/Main/Data Access/EUMETSATDataCentre/index.htm?l=en where one should select: "High Rate SEVIRI Level 1.5 Image data" and select "HRIT data sets in tar
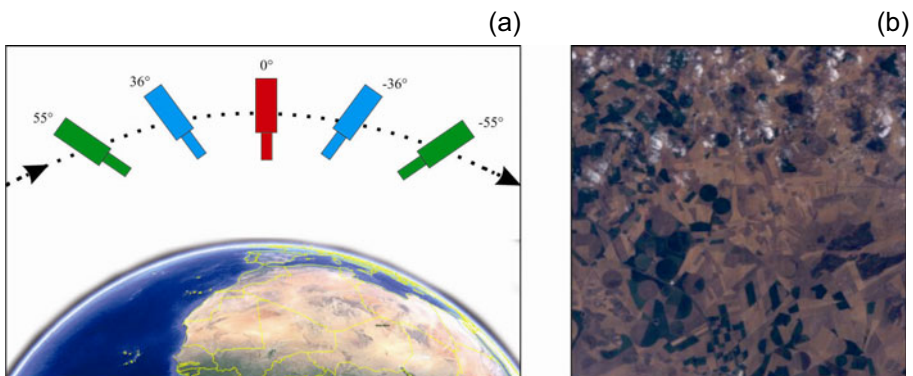
Fig. 2. Illustration of how CHRIS can hold a target in view by using PROBA's pitch control (a) and nadir view of CHRIS-PROBA acquisition over the Barrax site on 22 July 2012, 07:56 UTC (b), channels 23-9-5 for RGB.

Overview of the space- and air-borne observations

Sensor	Number of channels	Spectral range [μm]	Resolution [m]	Acquisition date	Acquisition DOY
MSG	12	0.60-14.40	1000/3000	18-28 July 2012	200-210
CHRIS	63	0.40-1.05	36	22 July 2012	204
AHS	80	0.43-12.70	2.1/3.9	25/26 July 2012	207-208
CASI	144/288	0.38-1.05	0.48/0.98	25/26 July 2012	207-208

file" to receive HRIT files. Background information and the freeware to process the data is available at: http://52north.org/communities/earth-observation/ about-geonetcast. An overview of the sensor characteristics of the satellite and airborne observations is provided in Table 1.

Airborne data acquisitions

Two airborne sensors have been operated during the REFLEX 2012 campaign to acquire important data for bio-geo-physical variable estimation over the Barrax site. The Airborne Hyperspectral Scanner (AHS) and Compact Airborne Imaging Spectrometer (CASI) sensors were mounted on the CASA 212-200 N/S 270 "Paternina" airplane of INTA. Because the campaign was primarily aiming at land-atmosphere interactions, the thermal observation capacities of the AHS sensor were prioritized. Therefore, the flight configuration was designed such that if conflicting criteria between AHS and CASI occurred, preference was given to AHS.

With respect to the timing of the airborne data acquisitions, there were no constraints with respect to linking the acquisitions to simultaneous satellite overpasses; the CHRIS–PROBA overpass fell outside the possible window for airborne acquisitions due to the unavailability of the airplane, whereas the MSG acquisitions have a frequency much higher than an airborne acquisition window (typically one hour or more).

From a scientific viewpoint it was desirable to obtain at least one night-time acquisition in order to determine thermal inertia. Thermal inertia is highly correlated with soil/canopy moisture content and as such of major importance for land-atmosphere flux exchanges. Other aspects in the flight line design were the need for multiple viewing angles and the need to cover a full daily cycle. The first objective resulted in flight lines that had a considerable overlap (see Fig. 3). The second objective resulted in planning for a daytime flight, followed by a night-time flight, immediately followed by another daytime flight the next afternoon.

Weather conditions were such that the window of 25 and 26 July was chosen for acquiring the airborne data. The flight lines were then designed to

(a)   (b)
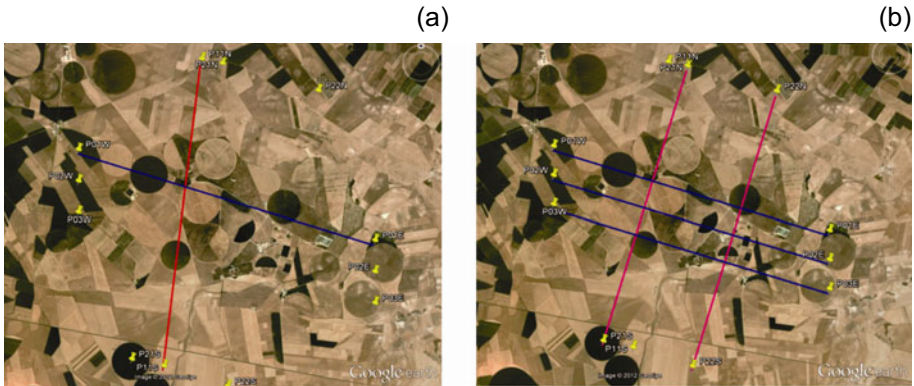
Fig. 3: (a) the flight pattern for the low (1000 m a.g.l.) flights; (b) the flight pattern for the high (2000 m a.g.l.) flights (presented on Google Earth).

match the selected calibration/validation sites as well as the flux observation sites.

The first flight was on Wednesday, 25 July 2012. Weather conditions: some high clouds, and southern wind with a variable intensity. Data acquisition started at 08:41 UTC (10:41 local time). Two lines are performed over the test site at 1000 m a.g.l., resulting in a high spatial resolution, and five more lines are covered at an altitude of 2000 m a.g.l., resulting in a reduced resolution (Table 1). Data acquisition was completed at 09:47 UTC (11:47 local time). The second flight was a night flight and took place on the same day. Weather conditions: clear skies. Data acquisition started at 21:30 UTC (23:30 local time) and was completed at 22:41 UTC (00:41 local time).

The third flight took place on Thursday, 26 July 2012, when weather conditions were: clear skies with a south-eastern wind. Data acquisition started at 08:42 UTC (10:42 local time) and was completed at 09:38 UTC (11:38 local time). The flight lines for the second and the third flights were similar to the first flight with the exception of lines P02 and P03 (see Fig. 3), which were skipped since the multi-directional aspect was covered during the first flight. Additional details of the flight lines (timing, exact location) are provided in the flight report, which is present in the REFLEX 2012 database.

The Airborne Hyper-spectral Scanner (AHS) is a linescanner with a concept shared with classical airborne linescanners, similar to the well-known HyMap instrument. The INTA AHS sensor has 63 bands in the reflective part of the electromagnetic spectrum, 7 bands in the 3 to 5 microns range and 10 bands in the 8 to 13 microns region. The Instantaneous Field Of View (IFOV) equals 2.5 mrad, and the Field Of View (FOV) is 90°. This resulted in a resolution of 2.1 and 3.9 m at the low and high altitude flights, respectively.

The CASI sensor is a pushbroom imager based on a bidimensional Charge Coupled Device (CCD); the instrument measures the incoming radiance along up to 1500 spatial pixels "across-track" in up to 288 separate spectral bands. The spectral bands can be placed anywhere within a ~680 nm spectral range, which itself can be placed anywhere between 380 and 1050 nm. The CASI is thus sensitive to wavelengths in the visible part of the electromagnetic spectrum, as well as in the near infrared. In the current campaign the settings were such that 144 spectral bands were used, covering the full range from 0.38 to 1.05 µm during the high altitude flights, whereas for the low flights the full spectral resolution was used, resulting in 288 spectral bands. The FOV is 40° and IFOV is 0.5 mrad, thus potentially providing a spatial resolution 5 times better than AHS at the same flight altitude. In the current setting this resulted in a spatial resolution of 0.48 and 0.98 m at the low and high altitude flights, respectively.

3.3 *In situ* measurements

Atmospheric data acquisitions

Knowledge of the atmospheric conditions, especially the ozone and water vapor content, as well as their vertical profiles is required to perform accurate atmospheric corrections of the space and airborne observations. Two types of measurements are available during this campaign: routinely collected atmospheric soundings and *in situ* ground-based atmospheric measurements.

Though remote (some 150 from the area), atmospheric soundings from Murcia and Madrid are typical for atmospheric conditions on site, depending on wind directions. When eastern winds are prevailing, typical on-site conditions usually resemble atmospheric characteristics as recorded over Murcia. Under western winds the Madrid conditions prevail in the study area. These soundings are carried out twice daily and for the days of airborne overpasses these soundings are available in the database. They contain profiles of pressure, air temperature, dewpoint, relative humidity, mixing ratio, wind direction, windspeed, potential air temperature, and virtual potential air temperature (Fig. 4).

In addition, *in situ* atmospheric measurements were carried out at several selected sites using microtops sunphotometers. The instruments were configured to measure the total water vapor column and aerosol optical thickness at 500 nm. These measurements, carried out by several teams on a continuous basis throughout the airborne overpasses, were made in conjunction with radiometric characterization observations at these selected sites. They are described in more detail in the next section.
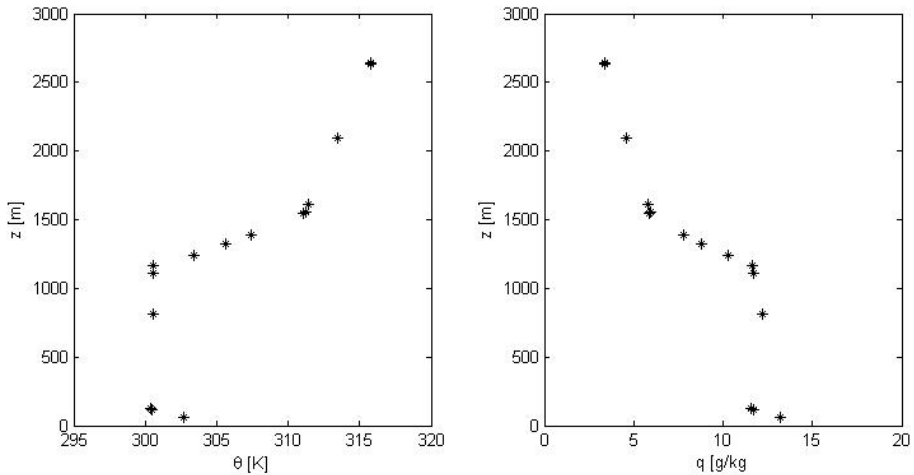
Fig. 4. Madrid mid-day sounding for 26 July 2012, showing profiles of potential temperature, θ [K], and specific humidity, q [g/kg].

Radiometric measurements

Several ground radiometric measurements were carried out at different selected sites. They mainly comprised near-ground spectroscopy, so-called solar range radiometric measurements and thermal infrared radiometric measurements. The sites were selected based on homogeneity at a sufficiently large scale and representativeness of the main land-cover units. In addition, they should show a sufficiently large spread in reflective and emissive behavior and ideally also cover the flux observation sites. An overview of the different locations of these measurements is shown in Fig. 5, where also the flux tower sites and the reference meteorological stations are shown.

Near-ground spectroscopy was carried out for calibration and validation purposes at 5 selected sites comprising grass, wheat stubble, maize, camelina, and vineyard. At these sites, detailed Bidirectional Reflectance Distribution Functions (BRDFs), calibration reflectance and irradiance measurements were carried out as well as observations of atmospheric optical thickness and water vapor content and hemispherical sky photos. At a number of additional sites, comprising bare soil, poppy, wheat stubble, black fabric, grass, and open water calibration reflectance measurements were carried out as well.

Radiometric measurements in the thermal infrared region were also carried out with various instruments that included fixed Field Of View (FOV) and single band as well as multi-band radiometers. In addition, black bodies (calibration sources) for calibrating the instruments were used. These measurements, which aimed at calibrating and validating the thermal air-borne
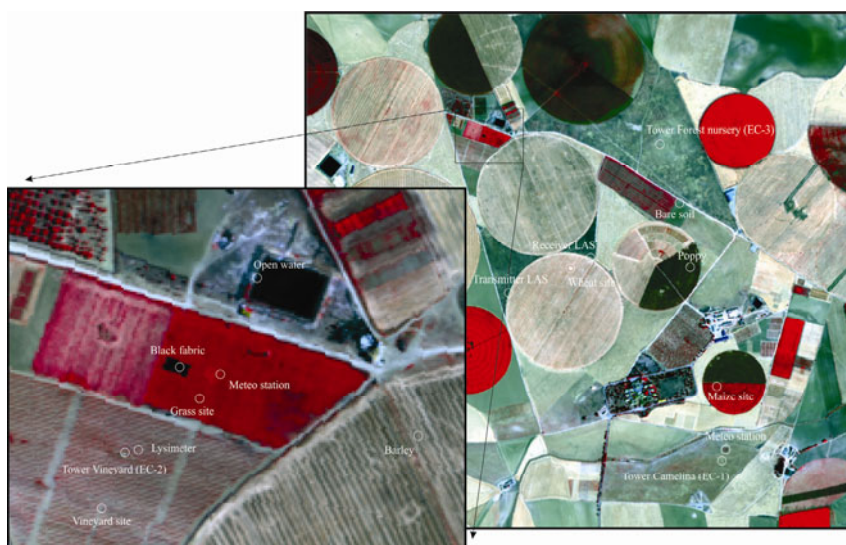
Fig. 5. Overview of the main ground observation location; background image is a false color composite of AHS channels 15-8-4 (RGB) of the 25 July morning overpass. The zoom is on the grassland super site central in the area, where a high concentration of ground observations took place.

observations, consisted of transects which were carried out concurrently to the overpasses of AHS/CASI. They consisted of temperature measurements with different field radiometers (CIMEL, RAYTEK, OPTRIS, and EVEREST), at regular steps of 3 m over different land covers. These comprised grass, barley stubble, alfalfa, forest nursery, bare soil, wheat stubble, vineyard, poppy, maize, and open water. The data was acquired in a period of time centered around the flight overpasses. The data was then processed following the so-called Temperature and Emissivity Separation (TES) algorithm (Gillespie *et al.* 1998) to obtain Land Surface Temperature (LST) and surface emissivity.

Biophysical measurements

Biophysical measurements consisted of the collection of Leaf Area Indices (LAI), Leaf Angle distribution, fraction of Absorbed Photosynthetically Active Radiation (fAPAR) and soil moisture, as well as leaf-level measurements of fluorescence, water, and nitrogen content. For the fluorescence measurements, use has been made of the Pulse-Amplitude Modulated (PAM) method as well as by the so-called leaf-clip, developed by the Laboratory for Earth Observation of the University of Valencia, whereas leaf water- and nitrogen-content analyses were carried out at the David J. Bonfil Laboratory at the Gilat agricultural research center, Israel. The measure-

ments, which were basically limited to the maize and, partly, sunflower fields, were carried out at several selected plots within the fields. The plots were selected in order to cover the slightly wider range of canopy heights, fAPAR and LAI of the maize field, due to non-homogeneous irrigation, terrain morphology, and soil texture. Data acquisition took place at days 25, 26, and 27 July 2012.

Top-of canopy fAPAR measurements were performed at the plots, by means of a SSI Sunscan Delta-T system. In addition to these top-of-canopy fAPAR observations, incident PAR measurements were carried out at 0.25 m intervals throughout the canopy to characterize the fAPAR profile in the canopy.

Thermo-dynamic measurements

The architecture of most of the vegetation canopies leads to a complex three-dimensional exchange of heat requiring temperature measurements of the different canopy and soil components at a very local scale. Therefore, a MIDAC thermal range hyper-spectral Fourier Transform Infrared Spectrometer (FTIR) spectrometer was employed along with sensors such as a ThermoTracer thermal camera and thermal radiometers. The ThermoTracer was mounted on a tripoid to acquire daytime-cycle, very high spatial and temporal resolution observations, which were calibrated *versus* a gold plate with well-known emissivity and temperature. As such, these sensors monitored the temperatures of different land surface components (shadowed *versus* sunlit, leafs *versus* soil) on a continuous basis. These component temperatures might then be implemented into a canopy model for the simulation of directional temperatures.

Surface energy budget and micrometeorological measurements

Measurements of boundary layer heat and moisture fluxes, carbon fluxes, high resolution (in a spectral, spatial, and temporal sense) thermal radiation and other relevant meteorological variables were continuously logged from 16 to 28 July 2012. The objective of the collection of this type of data was to facilitate the modeling of heat, water, and carbon transfer inside and above the canopy, as well as above bare soil. Several characteristic areas were carefully selected, which resulted in the installation of three Eddy Covariance (EC) flux-towers: one over a camelina field, one over the vineyard, and another over the main reforestation area (see Fig. 5 for their respective locations). In addition, a Large Aperture Scintillometer (LAS) was installed over a wheat-stubble field, whereas two reference meteorological stations were continuously storing relevant meteorological variables over the grassland super site and the camelina as well. An overview of the instrumentation used at the flux sites is provided in Table 2.

Table 2

Instrumentation overview of the flux sites

System	EC-1	EC-2	EC-3	LAS
Landcover	Camelina	Vineyard	Forest nursery	Wheat
Canopy height	0.50	2.00	1.00	0.15
Scintillometer				2.18
3-D Sonic	1.30, 2.38, 5.20	5.70	5.00	
H_2O	2.38	5.70	5.00	
CO_2	2.38		5.00	
Rel. Hum.	1.30, 2.20, 4.10	2.50, 3.50, 5.00	1.45, 2.50, 4.00	2.18
Air temperature	1.30, 2.20, 4.10	2.50, 3.50, 5.00	1.45, 2.50, 4.00	2.18
Net radiometer	1.00	4.00		
Surface temperature			4.00	
Soil heat flux	−0.08, −0.13	−0.02	−0.10	−0.13
Soil moisture	−0.05, −0.10, −0.20		−0.10	
Soil temperature	−0.01, −0.02, −0.04, −0.08, −0.16, −0.32	−0.025		
Wind speed		2.50, 3.50, 5.00	1.45, 2.50, 4.00	1.85
Air pressure	1.80			

At these so-called flux sites, continuous monitoring took place of the main components that determine the surface energy budget:

$$R_N = G_0 + H + \lambda E \ , \tag{1}$$

where R_N represents the net radiation, G_0 the surface soil heat flux, H the sensible heat flux, and λE the latent heat flux (all in $W \cdot m^{-2}$). At the scintillometer site, however, no net radiation and latent heat flux was measured, whereas at the forest nursery site, for net radiation, only the outgoing long-wave component was monitored. An example is shown in the top panel of Fig. 6, where the four fluxes are plotted for a larger part of the campaign at the camelina site.

Profile measurements of meteorological variables (relative humidity, air temperature, windspeed, and at selected places wind direction) were carried out at all sites, for which the humidity and temperature sensors were inter-calibrated to ensure a sufficiently high accuracy. Windspeed at higher levels was clearly showing higher values than at lower levels, as may be expected. During daytime, when typically strongly unstable atmospheric conditions prevailed, the lower temperature sensors showed higher responses, whereas the opposite was noted for the humidity sensors. During the night, character-ized by stable atmospheric conditions, the lower temperature sensors at most
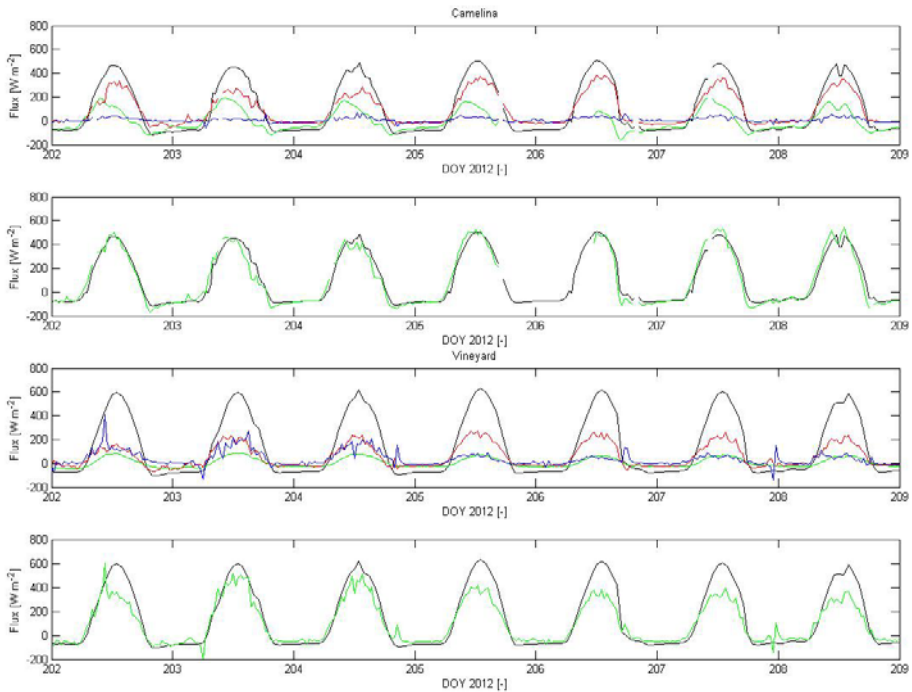
Fig. 6. Surface energy budget components (R_N in black, G_0 in green, H in red, and *LE* in blue) measured during the campaign period. In the second and fourth panel the sum of the components is represented in green.

times recorded lower temperatures, but differences were significantly smaller than during daytime.

Soil moisture and soil temperature observations, needed for post-processing the soil heat fluxes (van der Tol 2012), were obtained at several depths as well. Typically, the largest daily fluctuations were noticed close to the surface, whereas a damping and delay effect is noticed further away from the surface.

In the second panel of Fig. 6 the net radiation is plotted *versus* the sum of soil and turbulent fluxes, *i.e.*, sensible and latent heat flux, to examine the well-known energy closure issue (Foken 2008) over the camelina site. In this site, the closure is quite good throughout the campaign, which might be at-tributed to the very low values of one of the turbulent fluxes (the latent heat flux). However, at certain moments the sum of the soil and turbulent fluxes is slightly larger than the net radiation. This is attributed to the correction procedure necessary to convert soil heat flux from the measured depth to the surface value. Details on this procedure and a discussion of the obtained re-sults are provided in van der Tol *et al.* (2015).

The closure over the vineyard site is considerably poorer. This is shown in the lower two panels of Fig. 6, where in the third panel from the top the four individual fluxes are shown, and in the lowest panel the net radiation and the sum of the soil, sensible and latent heat flux.

It is noted that the measured net radiation, especially during daytime conditions, is consistently higher than the sum of the components. This is attributed to the fact that the field of view of the net radiometer was dominated by canopy, resulting in a relatively low albedo and thus high net radiation. Another striking feature is that starting on Day Of Year (DOY) 205 the latent heat fluxes drop from a daily maximum around 200 $W·m^{-2}$ to a value as low as 50 $W·m^{-2}$. Wind conditions play a major role here. The first period of the campaign was characterized by winds between 1.5 and 3.0 $m·s^{-1}$ for 90% of the time, whereas the second period daytime windspeed was higher than 5 $m·s^{-1}$ during 90% of the time. Moreover, prevailing wind direction in the first period was from the north-west, whereas in the second period this was from the south-east. To the north of the vineyard a well-irrigated grassland was located, whereas to the east a large wheat stubble field existed. The observed fluxes in the first period may be partly influenced by the (wet) grassland, whereas during the second period the fluxes may be partly influenced by the (dry) wheat-stubble field. Detailed footprint analyses have to be carried out when a useful comparison between remote sensing-based and ground-based estimates of these fluxes has to be made (Timmermans *et al.* 2009).

3.4 Data quality

Remote sensing data

With respect to the space-borne data acquisitions, both the CHRIS as well as the MSG data are available at level 1, meaning they consist of radiometrically calibrated and geo-located at-aperture radiances. However, no additional ground validation has been carried out yet for the space-borne observations.

The airborne data acquisitions are available at level 2, meaning they are radiometrically calibrated and geo-located hemispherical-directional reflectance factor and kinematic temperature. As for the AHS system, the radiometric calibration of the Visible and Near InfraRed (VNIR) and Shortwave InfraRed (SWIR) detectors is achieved illuminating the system with a uniform and known radiance source. The thermal infrared detectors, Middle InfraRed (MIR) and Thermal InfraRed (TIR), are calibrated by means of an extended black body source set at known temperature. Radiometric calibration of the detectors also provides Signal-Noise-Ratio (SNR) values, used to check if the system performance keeps within specified values. Channels 44

and 46 had a very low Signal-to-Noise Ratio (SNR) due to detector malfunctioning; they should be used with reservations. Flight line AHS P11BD on 26 July shows a recording anomaly, which resulted in a small data gap.

For the CASI system, the radiometric calibration is achieved by illuminating the system with an integrating sphere. As with the AHS sensor, the radiometric calibration also provides SNR values which are used to check if the system performance keeps within specified values. For the high altitude flights column number 1441 is not valid. All CASI images suffer a slight spectral shift under flight conditions. A resampling of the input radiance from the estimated band centers to the reported band centers is performed before calibration. This procedure has a limited accuracy and might affect the radiometric accuracy in the absorption regions. The SNR for each band is reported in a statistics file, which should be checked before data analysis.

In situ data

The majority of the REFLEX 2012 *in situ* data has undergone standard post-processing up to level 2, meaning they are available in geo-physical units that are calibrated and geo-located. The atmospheric *in situ* data and the radiometric and biophysical measurements are quality checked and the corresponding data are accompanied by metadata describing this.

With respect to the surface energy budget and micro-meteorological measurements, additional analysis was carried out on top of the standard post-processing and quality checking (van der Tol *et al.* 2015). Air temperature and humidity sensors from several sites were cross-calibrated *versus* each other which removed the bias and reduced relative errors induced by differences in sensor sensitivities by up to 90%. Energy closure at the different sites was variable, ranging from 94% at the homogeneous camelina site to 67% for the vineyard site. A detailed analysis of the turbulent fluxes and the energy balance is provided in van der Tol *et al.* (2015).

4. PRELIMINARY RESULTS AND RECOMMENDATIONS

A complete overview of the airborne and *in situ* measurements of the REFLEX 2012 Campaign, designed to advance our understanding of land-atmosphere exchanges of water and heat in space and time, is presented in this paper. Some preliminary analysis of the observational data is presented in some of the sections. The analysis included a near-surface atmospheric characterization and retrieval of a limited amount of biophysical variables. Envisaged advanced products include the following:

❑ land surface temperature and emissivity from AHS data,

❑ emissivity from hyperspectral thermal *in situ* observations,

❑ intercomparison/cross-calibration of spectroscopy sensors,

❑ monitoring of turbulence observations over multiple sites,

❑ intercomparison of energy/water balance modeling schemes,

❑ thermal component derivation for multiple source energy flux estimates,

❑ estimation of evapotranspiration from airborne hyperspectral scanner data,

❑ photochemical reflectance index (PRI) as a water-stress index,

❑ soil moisture and surface emissivity over the heterogenous Barrax site.

Full details of several of the products above, and additional analyses, are reported elsewhere in this issue. As such, they represent current state-of-the-art in the process understanding of land-atmosphere interactions and at the same time provide a base for expanding our understanding of these interactions.

Therefore, all data and all described advanced products that are obtained during and after the campaign are available via the REFLEX 2012 Campaign ftp site (ftp.uv.es/reflex/reflex database). The database is freely available to the scientific community and access can be acquired through a username and password which can be obtained by sending an email to w.j.timmermans@utwente.nl, or by contacting the individual authors directly.

References

Foken, T. (2008), The energy balance closure problem: An overview, *Ecol. Appl.* **18**, 6, 1351-1367, DOI: 10.1890/06-0922.1.

Gamon, J.A., C. Coburn, L.B. Flanagan, K.F. Huemmrich, C. Kiddle, G.A. Sanchez-Azofeifa, D.R. Thayer, L. Vescovo, D. Gianelle, D.A. Sims, A.F. Rahman, and G.Z. Pastorello (2010), SpecNet revisited: bridging flux and remote sensing communities, *Can. J. Remote Sens.* **36**, Suppl. 2, 376-390, DOI: 10.5589/m10-067.

Gillespie, A., S. Rokugawa, T. Matsunaga, J.S. Cothern, S. Hook, and A.B. Kahle (1998), A temperature and emissivity separation algorithm for Advanced Spaceborne Thermal Emission and Reflection Radiometer (ASTER) images, *IEEE T. Geosci. Remote Sens.* **36**, 4, 1113-1126, DOI: 10.1109/36.700995.

Kornelsen, K.C., and P. Coulibaly (2013), Advances in soil moisture retrieval from synthetic aperture radar and hydrological applications, *J. Hydrol.* **476**, 460-489, DOI: 10.1016/j.jhydrol.2012.10.044.

McCabe, M.F., and E.F. Wood (2006), Scale influences on the remote estimation of evapotranspiration using multiple satellite sensors, *Remote Sens. Environ.* **105**, 4, 271-285, DOI: 10.1016/j.rse.2006.07.006.

Mishra, A.K., and V.P. Singh (2011), Drought modeling – A review, *J. Hydrol.* **403**, 1-2, 157-175, DOI: 10.1016/j.hydrol.2011.03.049.

Novick, K., S. Brantley, C.F. Miniat, J. Walker, and J.M. Vosee (2014), Inferring the contribution of advection to total ecosystem scalar fluxes over a tall forest in complex terrain, *Agr. Forest Meteorol.* **185**, 1-13, DOI: 10.1016/j.agrformet.2013.10.010.

Prueger, J.H., J.G. Alfieri, L.E. Hipps, W.P. Kustas, J.L. Chavez, S.R. Evett, M.C. Anderson, A.N. French, C.M.U. Neale, L.G. McKee, J.L. Hatfield, T.A. Howell, and N. Agam (2012), Patch scale turbulence over dryland and irrigated surfaces in a semi-arid landscape under advective conditions during BEAREX08, *Adv. Water Resour.* **50**, 106-119, DOI: 10.1016/j.advwatres.2012.07.014.

Rast, M., J. Johannessen, and W. Mauser (2014), Review of understanding of Earth's hydrological cycle: Observations, theory and modelling, *Surv. Geophys.* **35**, 3, 491-513, DOI: 10.1007/s10712-014-9279-x.

Rodell, M., P.R. Houser, U. Jambor, J. Gottschalck, K. Mitchell, C.-J. Meng, K. Arsenault, B. Cosgrove, J. Radakovich, M. Bosilovich, J.K. Entin, J.P. Walker, D. Lohmann, and D. Toll (2004), The global land and data assimilation system, *Bull. Am. Meteorol. Soc.* **85**, 3, 381-394, DOI: 10.1175/BAMS-85-3-381.

Salama, M.S., R. van der Velde, H.J. van der Woerd, J.C. Kromkamp, C.J.M. Philippart, A.T. Joseph, P.E. O'Neill, R.H. Lang, T. Gish, P.J. Werdell, and Z. Su (2012), Technical note: Calibration and validation of geophysical observa-tion models, *Biogeosciences* **9**, 2195-2201, DOI: 10.5194/bg-9-2195-2012.

Seneviratne, S.I., T. Corti, E.L. Davin, M. Hirschi, E.B. Jaeger, I. Lehner, B. Orlowsky, and A.J. Teuling (2010), Investigating soil moisture-climate interactions in a changing climate: A review, *Earth Sci. Rev.* **99**, 3-4, 125-161, DOI: 10.1016/j.earscirev.2010.02.004.

Sobrino, J.A., J.C. Jiménez-Muñoz, P.J. Zarco-Tejada, G. Sepulcre-Cantó, E. de Miguel, G. Sòria, M. Romaguera, Y. Julien, J. Cuenca, V. Hidalgo, B. Franch, C. Mattar, L. Morales, A. Gillespie, D. Sabol, L. Balick, Z. Su, L. Jia, A. Gieske, W. Timmermans, A. Olioso, F. Nerry, L. Guanter, J. Moreno, and Q. Shen (2009), Thermal remote sensing from Airborne Hyperspectral Scanner data in the framework of the SPARC and SEN2FLEX projects: an overview, *Hydrol. Earth Syst. Sci.* **13**, 2031-2037, DOI: 10.5194/hess-13-2031-2009.

Su, Z., W.J. Timmermans, A. Gieske, L. Jia, J.A. Elbers, A. Olioso, J. Timmermans, R. van der Velde, X. Jin, H. van der Kwast, F. Nerry, D. Sabol, J.A. Sobrino, J. Moreno, and R. Bianchi (2008), Quantification of land-atmosphere exchanges of water, energy and carbon dioxide in space and time over the heterogeneous Barrax site, *Int. J. Remote Sens.* **29**, 17-18, 5215-5235, DOI: 10.1080/01431160802326099.

Timmermans, J., Z. Su, C. van der Tol, A. Verhoef, and W. Verhoef (2013), Quantifying the uncertainty in estimates of surface-atmosphere fluxes through joint evaluation of the SEBS and SCOPE models, *Hydrol. Earth Syst. Sci.* **17**, 1561-1573, DOI: 10.5194/hess-17-1561-2013.

Timmermans, W.J., G. Bertoldi, J.D. Albertson, A. Olioso, Z. Su, and A.S.M. Gieske (2008), Accounting for atmospheric boundary layer variability on flux estimation from RS observations, *Int. J. Remote Sens.* **29**, 17-18, 5275-5290, DOI: 10.1080/01431160802036383.

Timmermans, W.J., Z. Su, and A. Olioso (2009), Footprint issues in scintillometry over heterogeneous landscapes, *Hydrol. Earth Syst. Sci.* **13**, 2179-2190, DOI: 10.5194/hess-13-2179-2009.

van der Tol, C. (2012), Validation of remote sensing of bare soil ground heat flux, *Remote Sens. Environ.* **121**, 275-286, DOI: 10.1016/j.rse.2012.02.009.

van der Tol, C., W. Timmermans, C. Corbari, A. Carrara, J. Timmermans, and Z. Su (2015), An analysis of turbulent heat fluxes and the energy balance during the REFLEX campaign, *Acta Geophys.* **63**, 6, 1516-1539, DOI: 10.1515/acgeo-2015-0061 (this issue).

van Dijk, A.I.J.M., and L.J. Renzullo (2011), Water resource monitoring systems and the role of satellite observations, *Hydrol. Earth Syst. Sci.* **15**, 39-55, DOI: 10.5194/hess-15-39-2011.

Wang, K., and R.E. Dickinson (2012), A review of global terrestrial evapotranspiration: Observation, modeling, climatology, and climatic variability, *Rev. Geophys.* **50**, 2, RG2005, DOI: 10.1029/2011RG000373.

Wu, H., and Z.-L. Li (2009), Scale issues in remote sensing: A review on analysis, processing and modeling, *Sensors* **9**, 3, 1768-1793, DOI: 10.3390/s90301768.

Yebra, M., A. van Dijk, R. Leuning, A. Huete, and J.P. Guerschman (2013), Evaluation of optical remote sensing to estimate actual evapotranspiration and canopy conductance, *Remote Sens. Environ.* **129**, 250-261, DOI: 10.1016/j.rse.2012.11.004.

DE GRUYTER OPEN

AHS and CASI Processing for the REFLEX Remote Sensing Campaign: Methods and Results

Eduardo de MIGUEL, Marcos JIMÉNEZ, Irene PÉREZ,
Óscar G. de la CÁMARA, Félix MUÑOZ,
and José A. GÓMEZ-SÁNCHEZ

Instituto Nacional Técnica Aeroespacial (INTA),
Torrejón de Ardoz, Spain; e-mail: demiguel@inta.es

A b s t r a c t

The airborne spectroradiometers AHS and CASI were used as a source of hyperspectral and thermal remote sensing data during the REFLEX campaign. Data geolocation and a first simple atmospheric correction was performed by INTA in near-real time with a specific on-site setup and distributed to all campaign participants. In this paper we present briefly the AHS and CASI REFLEX flight campaign followed by a detailed description of the methodology used for image processing and finally the results obtained in terms of image quality. As a conclusion, near-real time processing for AHS and CASI level 1 geolocated products was successful as most of CASI level 2 results but further work is needed for achieving accurate AHS level 2 products.

Key words: AHS, CASI, image processing, remote sensing.

1. INTRODUCTION

The reflectance spectrum of a surface contains information on its composition and status; further information can be retrieved from its temperature.

The capability to retrieve the reflectance spectrum, the surface temperature or both is the basis of remote sensing techniques.

Hyperspectral remote sensing (Ben-Dor *et al.* 2013) is a powerful technology that produces a continuous record of the ground leaving radiance over a specific area in enough spectral bands as to recover the reflectance spectrum with a spectral resolution suitable for many bio-geophysical studies. On the other hand, thermal remote sensing (Prakash 2000) is aimed to measure extensively emitted radiance which in turn provides surface temperature and, eventually, the surface spectral emissivity.

Airborne sensors are currently the only way to obtain simultaneously the high spectral resolution required by hyperspectral remote sensing with a spatial resolution of few meters. The same applies for thermal remote sensing. In addition, airborne instrumentation provides a unique flexibility which is critical in research activities when coupling with extensive ground measurements or specific acquisition details (time of flight, sensor configuration or others) are needed.

AHS and CASI are two airborne spectroradiometers owned and operated by INTA (Spanish National Institute for Aerospace Technology). Together with calibration and navigation equipment, ground truth instrumentation, and a specific Processing and Archiving Facility (PAF) they form the INTA airborne remote sensing system. INTA offers this system as a technological service to public institutions or commercial companies. This is the system that was used as main source of remote sensing data during the REFLEX course.

The main objective of the REFLEX training course held in July 2012 in Las Tiesas experimental farm (Barrax, Spain) was to teach early-stage researchers how to organize and conduct an airborne field campaign with hyperspectral imaging sensors supporting their research in the framework of multi-scale ("leaf to ecosystem") land-atmosphere exchanges. An airborne campaign funded by EUFAR with the INTA C-212-200 RS aircraft in a well recognized ground reference agricultural site was part of the training course. More details on REFLEX are given in Timmermans *et al*. (2014).

The magnitude measured by airborne radiometers like AHS and CASI is just the incoming radiance at the sensor aperture. The magnitudes of interest in bio-geophysical studies, like surface reflectance, temperature and emissivity and their accurate and precise geolocation must be estimated from the original measurement through a set of data analysis procedures which is often labelled image processing (or, sometimes, pre-processing).

In this paper we present briefly the AHS and CASI REFLEX flight campaign followed by a detailed description of the methodology used for image processing and finally the results obtained in terms of image quality.

2. AHS AND CASI CHARACTERISTICS

2.1 AHS

The INTA Airborne Hyperspectral Scanner (AHS) is an 80-bands airborne imaging radiometer developed by ArgonST (USA) and operated by INTA since 2003. Together with calibration and navigation equipment, auxiliary ground instrumentation. and a specific processing and archiving facility it forms the INTA AHS system.

The AHS has 63 bands in the reflective part of the electromagnetic spectrum, 7 bands in the 3 to 5 microns range and 10 bands in the 8 to 13 microns region. The first element of the optical subsystem is a rotating mirror which directs the surface radiation to a cassegrain-type telescope. The telescope design includes a so-called pfund assembly defining a 2.5 mrad instantaneous field of view (IFOV) acting as a field stop for all bands and redirects the radiation to a spectrometer placed above the telescope. In the spectrometer dichroic filters split the incoming radiation in five optical ports: Port 1 (corresponding to VNIR wavelengths), Port 2a (for a single band at 1.6 micrometers), Port 2 (SWIR), Port 3 (MIR), and Port 4 (TIR). For each of these ports, a grating disperses the radiation and a secondary optical assembly focuses it onto an array of detectors which defines the spectral bands. Bands 22 to 24 and 60 to 63 are located at wavelengths with strong atmospheric absorption and have very low signal to noise ratio (SNR).

The AHS has two blackbodies (with size > IFOV) that are observed, respectively, at the start and end of each scanline. These blackbodies (BB1 and BB2) are thermally controlled and monitored; they have an emissivity above 0.95 in the MIR and TIR regions and a reflectivity < 1% in the VNIR-SWIR range. Therefore for each AHS band and image line, two "dark" or thermal reference pixels are available.

2.2 CASI

The CASI-1500i (abbreviated to CASI through this article) is a pushbroom imaging spectrometer based on a bidimensional CCD; the instrument measures the incoming radiance along up to 1500 spatial pixels "across-track" in up to 288 separate spectral bands covering a spectral range between 380 and 1050 nm. The band-to-band distance between spectral rows is 2.4 nm while the bandwidth of each spectral row is around 3 nm. Each (#spatial × #spectral) array of pixels is called a frame. FOV is 40° and IFOV is 0.5 mrad, thus providing an across-track spatial resolution 5 times better than the INTA AHS at the same flight altitude.

Two different configurations of the CCD were used in REFLEX. In the spectral row sum 2 configuration (filename identification E2) 1440 out of the 1500 pixels across-track are recorded and a binning factor 2 is used to read the spectral information, resulting in 144 spectral bands with ≈ 5 nm band to

Table 1

Flights performed and images acquired

Flight	Survey	Line ID	Time (UTC)	Sensor	Image ID
25 July (120725) diurnal D01	D01-1 $Z \approx 1000$ m (above terrain)	AHS + CASI P11	8:43	AHS	P11BD
				CASI	P11SF
		AHS + CASI P01	8:51	AHS	P01BD
				CASI	P01SF
	D01-2 $Z \approx 2000$ m	AHS + CASI P01	9:02	AHS	P01ID
				CASI	P01E2
		AHS + CASI P02	9:11	AHS	P02ID
				CASI	P02E2
		AHS + CASI P03	9:19	AHS	P03I1
				CASI	P03E2
		AHS + CASI P03 (repet. of above)	9:28	AHS	P03I2
				CASI	PR3E2
		AHS + CASI P21	9:46	AHS	P21ID
				CASI	P21E2
		AHS + CASI P22	9:38	AHS	P22ID
				CASI	P22E2
25 July (120725) night N01	N01-1 $Z \approx 1000$ m	AHS P11	21:32	AHS	P11B2
		AHS P11	22:01	AHS	P11B3
		AHS P01	22:10	AHS	P01B2
	N01-2 $Z \approx 2000$ m	AHS P01	22:20	AHS	P01I2
		AHS P21	22:32	AHS	P21I2
		AHS P22	22:40	AHS	P22I2
26 July (120726) diurnal D02	D02-1 $Z \approx 2000$ m	P11	8:42	AHS	P11BD
				CASI	P11SF
		P01	8:51	AHS	P01BD
				CASI	P01SF
	D02-2 $Z \approx 2000$ m	P01	9:07	AHS	P01ID
				CASI	P01E2
		P21	9:17	AHS	P21ID
				CASI	P21E2
		P22	9:25	AHS	P22ID
				CASI	P22E2
	D02-1 $Z \approx 2000$ m	P01	9:38	AHS	P01BD
				CASI	P01E2

band separation. In the alternative spatial mode (filename identification SF) all 1500 spatial pixels and 288 spectral bands are acquired with the cost of an increase in integration time and, therefore, along-track pixel size.

Raw images have a data depth of 14 bits. The so-called dark frames and uniformity frames are recorded before and after each imaged scene by the use of specific elements of a wheel mounted in front of the aperture. Dark frames are obtained by placing a shutter instead of the nominal slit while uniformity frames (intended to detect an eventual contamination of the aperture slit) use an optical diffuser. Masked columns in the edges of the CCD are used to estimate electronic offset while columns which are neither masked nor illuminated by the slit are used to estimate focal plane straylight.

2.3 Flight campaign

The flight campaign was designed after detailed discussions with the campaign participants. It considered, as main drivers, the need to have day and night time measurements and multiangle observations of key field areas and the repetition of some flight lines at two different altitudes in order to optimize, respectively, AHS and CASI configurations and pixel size. Note that as terrain is flat through the study area the observation zenith angle for each target is directly determined by its location within the sensor field of view.

The resulting design consisted of 12 flight lines that were performed on 25 July morning and early night; 6 of the flight lines were repeated on 26 July. Table 1 lists the flights performed and the images acquired.

Simultaneously to the flights the INTA team acquired reflectance spectra over several large, homogeneous targets suitable for ground reference after atmospheric correction. A CIMEL sunphotometer (CIMEL electronique, France) was operated on 25 and 26 July mornings to retrieve atmospheric water vapor and aerosol optical thickness at 550 nm for image atmospheric correction. Table 2 summarizes the values obtained for 25 July.

Table 2

CIMEL measurements of atmospheric water vapour,
Aerosol Optical Thickness (AOT) at 550 nm during the D01 flight session

Time (UTC)	Sun zenith angle	WV [cm]	AOT 550 nm
08:40:00	49.753	2.080	0.248
08:50:00	47.842	2.111	0.254
09:00:00	45.940	2.147	0.262
09:15:00	43.111	2.194	0.280
09:30:00	40.318	2.177	0.284
09:45:00	37.576	2.158	0.372
10:00:00	34.899	2.147	0.323
10:15:00	32.304	2.114	0.328
10:30:00	29.827	2.059	0.327

3.   IMAGE PROCESSING

Image processing was performed on near-real time with a specific hardware and software setup deployed at the REFLEX course headquarters. Image processing consisted mainly of:

- ❑ radiometric calibration and noise estimation,
- ❑ fine tuning of CASI spectral calibration,
- ❑ atmospheric correction and estimation of surface reflectance,
- ❑ estimation of surface temperature and emissivity from AHS images,
- ❑ geolocation and image orthorectification.

The description of the methods used is given below.

3.1 AHS

Radiometric calibration transforms the image values from digital number to at-sensor radiance (*Ls*). For VNIR/SWIR region:

$$Ls_{i,j,k} = cc_k / g_k \left(DN_{i,j,k} - DNbb_{i,k} \right) .$$

The subscripts $\{i, j, k\}$ correspond to image {row, column, band}, respectively; *cc* is the calibration coefficient, *g* an adjustable electronic gain, *DN* the raw Digital Number, and *DNbb* the average of BB1 and BB2 data over a 15-rows moving window centered in row "i". Note that in this linear model the slope depends on laboratory measurements but the offset is estimated from the actual image. An empirical correction factor to *cc* (fe_k) was introduced to account for system degradation since laboratory calibration. Actual values of cc_k, g_k, and fe_k are reported in the REFLEX campaign metadata.

For MIR and TIR bands calibration is performed building *DN*-radiance model from the cold and hot blackbodies information (temperature, emissivity, and digital number). In this linear model both the slope and the offset are estimated from the actual image.

During image calibration the short-term standard deviation of BB1 and BB2 is computed and used as an estimation of the AHS instrumental noise.

Spectral calibration was performed in April 2012 at INTA facilities. A monochromator was used to illuminate the AHS with steps of 0.1 nm and a bandwidth around 5 nm. The relative instrument response at the different wavelengths was used to build a responsivity curve for each band. These curves are nearly Gaussian and bandcenter and full width half maximum (FWHM) are annotated as metadata while the detailed spectral responsivity curves are available upon request to REFLEX users. AHS spectral performance is very stable under flight conditions and no specific in-flight calibration was performed for REFLEX images.

The geolocation of each AHS pixel was performed using the direct georeferencing code PARGE (Schläpfer and Richter 2002). The inputs required are the exterior orientation information provided by the Inertial Navigation System Applanix POSAV and processed with Applanix POSPAC, a digital elevation model (DEM) and a detailed sensor model (including misalignment angles from the AHS geometric calibration). The basic output of the process is an Input Geometry file (IGM) for each image. IGM image files report the UTM Easting and Northing values derived by the geolocation process for each original image pixel.

The ENVI routine Georeference from IGM was used to generate sample orthorectified images on a cartographic UTM grid from a subset of the AHS bands. The output grid pixel size was 3 m for low altitude flights and 5 m for the high altitude flights. These georectified images were delivered to the REFLEX course participants mainly as a quicklook to display the expected output of the orthorectification process. The users of the REFLEX AHS data are then expected to choose a resampling algorithm or UTM grid size to produce the complete orthorectified data cube from the delivered IGM with the geolocated quicklook as reference.

Atmospheric and illumination correction was performed with ATCOR4 (Richter and Schläpfer 2002) which is a LUT-based implementation of MODTRAN5 targeted for airborne remote sensing data. The values used for ATCOR4 configuration are reported in Table 4. The visibility and aerosol type were initially selected according to the values estimated with the CIMEL sunphotometer deployed by INTA during the flight. Next, the SPECTRA module in ATCOR4 was used to refine scene visibility parameter using field spectra acquired simultaneously on reference surfaces with an ASD-FS3 spectroradiometer (Analytical Spectral Devices, Boulder, CO, USA). The ATCOR4 maritime aerosol type was the best fit for the specific scattering properties of the rather hazy atmosphere during the flights. Note that following the definitions in Schaepman-Strub *et al.* (2006) the magnitude estimated by ATCOR4 for solar bands is the Hemispherical-Directional Reflectance Factor (HDRF) of the observed surface. To compute surface temperature from ATCOR4, band AHS75 was selected because it has the highest SNR. A constant emissivity of 0.9825 (suitable for water and vegetation but not for bare soils) was assumed and with this value the Planck law was inverted from the ATCOR4-estimated atmospherically corrected radiance. The retrieved surface temperature was in turn used to estimate emissivity in the other thermal bands. This approach to temperature and emissivity estimation is very simplistic and was only performed to obtain a first approximation to thermal analysis. It was expected that REFLEX users would work in this issue with more rigorous procedures and specific ancillary data.

3.2 CASI

CASI radiometric calibration was performed using ITRES software "rad-corr". "Radcorr" first removes some non-signal additive terms from the measured digital count and next calibrates the corrected digital counts to at-sensor radiance using laboratory coefficients.

The additive terms are estimated from the raw data analysis, as:

$$DN_{i,j,k} = DN0_{i,j,k} - DC_k - ISL_{i,k} - FSS_{i,k} \quad ,$$

where the subscripts $\{i, j, k\}$ correspond again to image {row, column, band}, respectively. *DN* is the corrected but uncalibrated signal, *DN0* is the raw signal, *DC* is the average dark data for band k (including dark current and electronic offset) as measured just before image acquisition, *ISL* is the internally scattered light for band k, and *FSS* is frame shift smear. This is a non-target signal originated during the transfer of data from the scene image area of the CCD to its read-out register. It occurs mainly in the spectral dimension and is maximum at longer wavelengths. "Radcorr" includes an algorithm to estimate and remove frame shift smear.

Once the corrected *DN* is available, the calibration is performed by

$$Ls(i, j, k) = 1/sc_{j,k} \, DN_{i,j,k} \quad ,$$

where $sc_{j,k}$ is the absolute calibration coefficient for band k and detector j. It is computed in the laboratory, illuminating the system with a half meter integrating sphere from Sphere Optics (NH, USA). Dark frames are used to obtain the system output at zero input radiance. Considering also CCD smear and straylight, a linear model relating digital values to input radiance is built for each detector element. For this purpose we use the Itres software Sparcal. The radiometric calibration coefficients for REFLEX was performed at INTA in March 2012.

For noise estimation, the uniformity frames acquired right before each image file are used. These frames are collected with a semi-transparent diffusing cover between sensor and scene, and only retain the scene low frequency structure; they are, thus, a good candidate for instrumental noise assessment. After removal of the low frequency structure the standard deviation of the radiometrically calibrated uniformity data was taken as estimation of CASI instrumental noise and reported in the image metadata.

Pushbroom sensors are generally affected by spectral shift, *i.e.*, a change in the effective band center of the detector during image acquisition when compared to the nominal (laboratory) band center. The Remote Sensing Area at INTA has developed a tool to create an image specific CCD spectral map that works on CASI modes SF, E2, similar to the one described in Guanter *et al.* (2006). The image specific CCD spectral map can then be input to

"speccorr" which is an Itres tool to estimate the radiance levels in the nominal band centers (those reported to the user) given the actual band centers defined by our tool. Every REFLEX CASI image was analysed to assess its shift and was afterwards shifted to match the nominal bandwidths.

The geolocation was performed with the same basis than in AHS. However, for CASI the direct geolocation algorithm used is "geocor", a tool provided by Itres. The image geometry map is in this case identified with the acronym GLU (Geographic Look-up Table).

A relevant point in CASI is the choice of output pixel size on a cartographic UTM grid. To maximize the spectral information the selected integration time defines an along-track pixel size which is significantly above the across-track pixel size defined by the instrument IFOV (see Table 3). In such cases, resampling to a square grid must consider a compromise between redundancy (original samples that are used more than once when generating the resampled product) and data loss (raw original samples that are not mapped to the resampled product). The values used in the geolocated quicklook are reported in column 4 in Table 3.

Atmospheric correction to transform the L1 product (at sensor radiance) to L2 (HDRF) was performed with ATCOR4, configured as in Table 4.

Table 3

Actual ground IFOV (GIFOV) in across-track (X) and along-track (Y) directions *versus* the pixel size used in the georectified imagery

Configuration	GIFOV-X (nadir)	GIFOV-Y (nadir)	Output grid
Row sum 2 (E2)	1.4 m	1.7 m	1.25 m
Spatial (SF)	0.9 m	3.2 m	1.50 m

Note: The GIFOV figures given are average values for nadir view for the two CASI configurations.

Table 4

Parameters used in the configuration of ATCOR4

Flight	D01		N01	D02	
Sensor	AHS	CASI	AHS	AHS	CASI
Aerosol model	maritime	maritime	not used	maritime	maritime
Visibility [km]	40	40	not used	30	30
Water vapor	variable	variable	constant 2.9 gr/cm^2	variable	variable

Note: Visibility and aerosol type where selected using the field spectra as reference data for adjusting ATCOR4, but shall not be considered an estimation of the actual atmospheric conditions.

4.   RESULTS

All acquired images were successfully processed. A number of points relevant to image quality are reported below.

AHS bands 22, 23, and 64 are at the edge of atmospheric windows; they have very low signal to noise ratio and are unlikely to be useful. Bands 44 and 46 have a very low SNR due to detector malfunctions. They should be used with reservations. File AHS P11BD on 26 July shows a recording anomaly, namely a set of corrupted image rows (rows 4587 to 4600) followed by 20 rows with duplicated info and finally a small data gap.

In CASI images some samples from very low reflectance targets display a radiance <0 in the water absorption region around 935 nm and beyond 1020 nm. This is due to the combination of low signal, noise, and an excess straylight correction which unfortunately could not be optimized.

A visual check of the geolocation performance is obtained overlaying two different images acquired over the same area but with different tracks or with different sensors as shown in Fig. 1. The smooth transition between images means a good relative registration.

The absolute geographical accuracy of the images is initially estimated considering the expected uncertainty of input data, as determined by the POSPAC quality tools and the misalignment information calculated by INTA during the geometric calibration. It is expected to be about half a pixel.

(a)   (b)
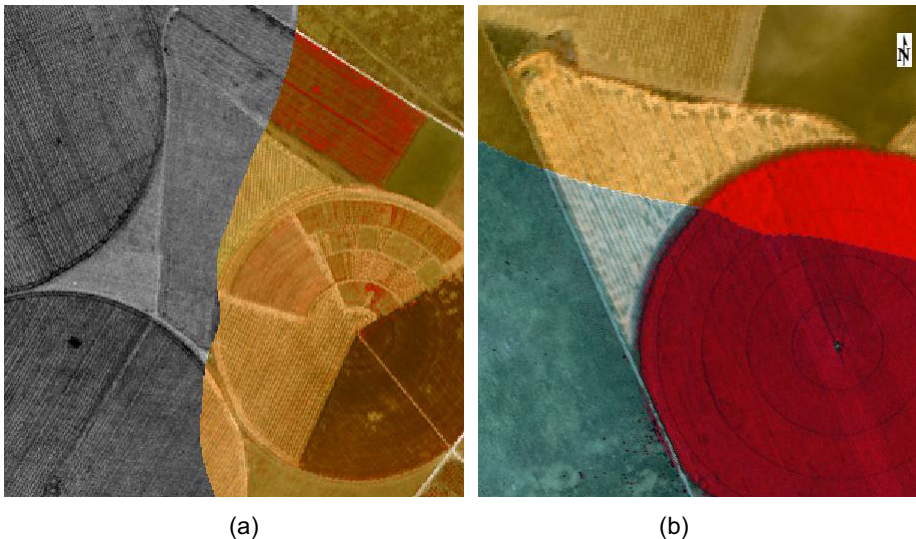
Fig. 1: (a) Part of a thermal AHS band from P11B3 (night flight, NE to SW track) overlaid on top of a color infrared composition of AHS P01BD (morning flight, NW to SE); (b) Detail of CASI color infrared from P01E2 overlaid on AHS P01BD; the apparent color difference is a result of specific enhancement for displaying purposes.

This was confirmed by visual check against available orthoimagery and AHS to CASI comparison. For the REFLEX images no estimation of geolocation error from ground control points was considered necessary. Note that measurements of absolute accuracy on resampled, georectified images must account for the effects of the resampling which, as explained above, is a critical factor in CASI and could introduce more uncertainty than using the expected error budget.

The radiometric quality can be reported in terms of noise which determines the radiometric resolution and of absolute radiometric accuracy.

From the user's side it is more relevant to estimate the noise equivalent in terms of surface reflectance, temperature or emissivity, or in terms of SNR. Figure 2 shows AHS and CASI SNR for P01BD on 25 July and the AHS noise equivalent in temperature (NEdT) for the same image. For SNR signal is estimated as the average scene value while noise is computed from dark data as described in previous sections.

The AHS VNIR performance is excellent with SNR well beyond 500. Most of the CASI bands show also a good SNR, above 100; but in the blue end and above 980 nm noise is significant. On the SWIR, AHS performance is not so good (apart from the problems in bands 44 and 46), and beyond 2.4 microns data analysis is difficult. Finally, AHS TIR data show a very low noise with amplitude below 0.25°C, except in the longer wavelengths.

Another look to radiometric quality is given by the comparison of AHS and CASI measurements over the same area. An example is shown in Fig. 3.

For evaluating the absolute radiometric accuracy, the field spectra acquired with ASD-FS3 were used. Figure 4 shows a field spectrum obtained
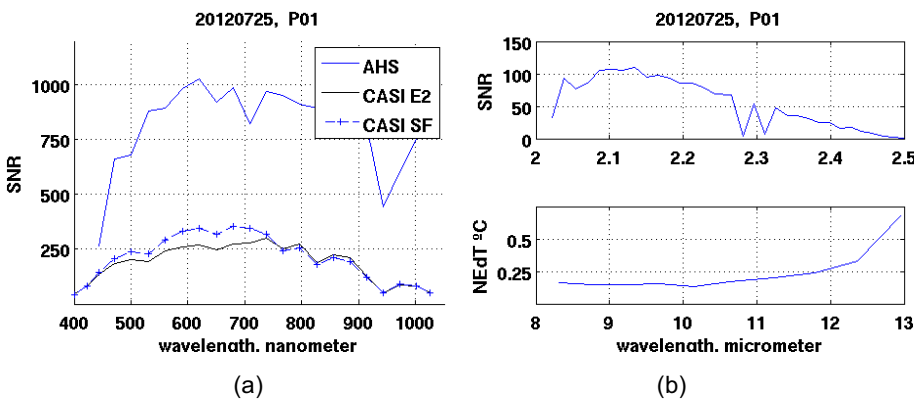
Fig. 2. Noise estimation for P01 scene: (a) SNR for AHS and CASI VNIR bands; note that CASI noise is reported for both E2 and SF images but only for a subset of bands corresponding to AHS bandcenters; (b) SNR for AHS SWIR bands and NEdT for TIR bands.
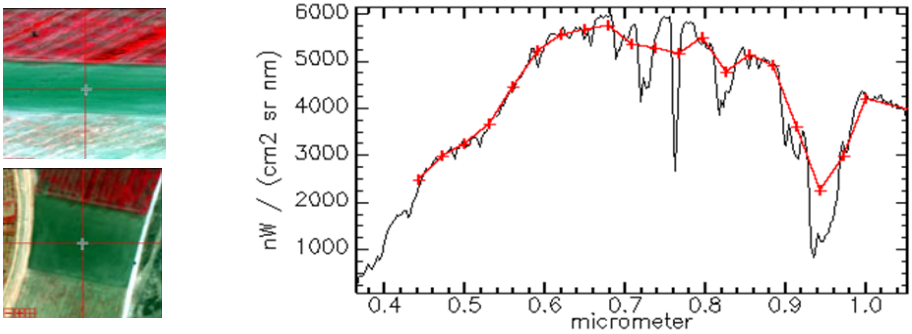
Fig. 3. Spectral radiance measured by AHS (red line, plus symbols) and CASI (black line) on the same bare soil location. The images used, displayed left to the plot, are AHS P01BD and CASI P01SF.
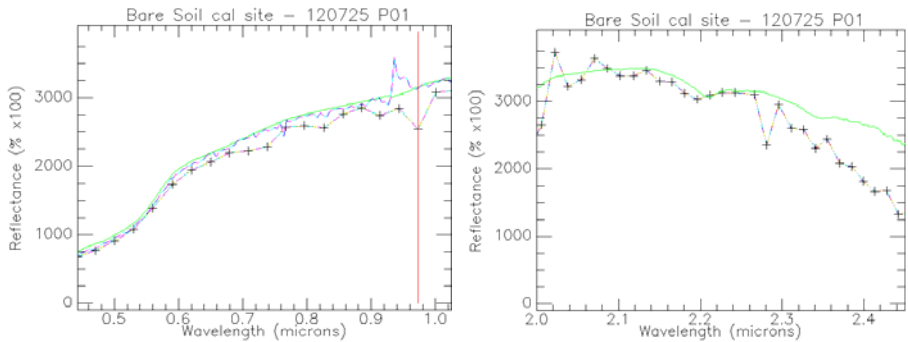
Fig. 4. Reflectance spectrum of the bare soil calibration site as estimated for CASI (blue dashed line), AHS (black plus line), and ASD-FS3 (green line).

from ASD-FS3 data on a bare soil surface. The spectra obtained from AHS and CASI are overlaid. The CASI data match accurately the ground truth, except for bands in the 935 nm water vapor absorption. For AHS the match depends on the band considered. Again, bands affected by water vapor absorption show the worst match. The signal underestimation around 1000 nm could be due to adjacency effects. These problems points out to the need of an improved atmospheric correction if such bands are relevant for the intended analysis. On the thermal side, the retrieved surface temperature was validated with simultaneous ground measurements from a water pond, showing a difference below 1°C. It is assumed that this uncertainty is applicable to most images on water and vegetation where the 0.9825 emissivity is valid; but the simple temperature-emissivity separation applied does not support the rigorous use of the thermal information for other surfaces.

5.   CONCLUSIONS

The REFLEX flight campaign was performed successfully with all planned images acquired and processed. Radiometric correction and calibration of the data was successful and, in the case of CASI, also spectral recalibration. The geolocation of the images was achieved on-site with results that are similar to those obtained offline at the INTA facilities. Overall, the methods applied to obtain level 1 orthorectified images performed flawlessly in near real time, showing that it is possible to process AHS and CASI images in operational conditions outside the INTA facilities.

The quick and operational atmospheric correction performed on the data led to a first estimation of surface magnitudes. For CASI the obtained reflectance products are accurate enough for most users. But improved methods considering advanced algorithms and all available ancillary data and ground truth should be applied for detailed analysis of the AHS thermal data and water absorption bands. This shows that near real time estimation of level 2 AHS and (to a lesser extent) CASI products for operational bio-geophysical studies is still an open task.

R e f e r e n c e s

Ben-Dor, E., D. Schläpfer, A.J. Plaza, and T. Malthus (2013), Hyperspectral remote sensing. **In:** M. Wendisch, and J.-L. Brenguier (eds.), *Airborne Measurements for Environmental Research: Methods and Instruments*, Wiley-VCH Verlag & Co. KGaA, Weinheim, 413-456, DOI: 10.1002/9783527653218.ch8.

Guanter, L., R. Richter, and J. Moreno (2006), Spectral calibration of hyperspectral imagery using atmospheric absorption features, *Appl. Optics* **45**, 10, 2360-2370, DOI: 10.1364/AO.45.002360.

Prakash, A. (2000), Thermal remote sensing: concepts, issues and applications, *Int. Arch. Photogram. Remote Sens.* **32**, B1, 239-243.

Richter, R., and D. Schläpfer (2002), Geo-atmospheric processing of airborne imaging spectrometry data. Part 2: Atmospheric/topographic correction, *Int. J. Remote Sens.* **23**, 13, 2631-2649, DOI: 10.1080/01431160110115834.

Schaepman-Strub, G., M.E. Schaepman, T.H. Painter, S. Dangel, and J.V. Marton-chik (2006), Reflectance quantities in optical remote sensing – definitions and case studies, *Remote Sens. Environ*. **103**, 1, 27-42, DOI: 10.1016/j.rse.2006.03.002.

Schläpfer, D., and R. Richter (2002), Geo-atmospheric processing of airborne imaging spectrometry data. Part 1: Parametric orthorectification, *Int. J. Remote Sens*. **23**, 13, 2609-2630, DOI: 10.1080/01431160110115825.

Timmermans, W., C. van der Tol, J. Timmermans, M. Ucer, X. Chen, L. Alonso, J. Moreno, A. Carrara, R. Lopez, F. de la Cruz Tercero, H.L. Corcoles, E. de Miguel, J.A.G. Sanchez, I. Pérez, B. Franch, J.-C.J. Munoz, D. Skokovic, J. Sobrino, G. Soria, A. MacArthur, L. Vescovo, I. Reusen, A. Andreu, A. Burkart, C. Cilia, S. Contreras, C. Corbari, J.F. Calleja, R. Guzinski, C. Hellmann, I. Herrmann, G. Kerr, A.-L. Lazar, B. Leutner, G. Mendiguren, S. Nasilowska, H. Nieto, J. Pachego-Labrador, S. Pulanekar, R. Raj, A. Schikling, B. Siegmann, S. von Bueren, and Z.B. Su (2015), An overview of the Regional Experiments For Land-atmosphere Exchanges 2012 (REFLEX 2012) campaign, *Acta Geophys.* **63**, 6, 1465-1484, DOI: 10.2478/s11600-014-0254-1 (this issue).

Relating Hyperspectral Airborne Data
to Ground Measurements
in a Complex and Discontinuous Canopy

Javier F. CALLEJA[1], Christine HELLMANN[2,3], Gorka MENDIGUREN[4],
Suvarna PUNALEKAR[5], Juanjo PEÓN[6], Alasdair MacARTHUR[7],
and Luis ALONSO[8]

[1]Department of Physics, University of Oviedo, Polytechnic School in Mieres,
Mieres, Spain; e-mail: jfcalleja@uniovi.es

[2]University of Bielefeld, Experimental and Systems Ecology, Bielefeld, Germany;
e-mail: christine.hellmann@uni-bielefeld.de

[3]University of Bayreuth, Agroecosystem Research, BAYCEER, Bayreuth, Germany

[4]Institute of Economy, Geography and Demography, CCHS-CSIC, Madrid, Spain;
e-mail: gorka.mendiguren@cchs.csic.es

[5]University of Reading, Department of Geography and Environmental Science,
Reading, United Kingdom; e-mail: s.m.punalekar@pgr.reading.ac.uk

[6]Area of Cartographic, Geodesic and Photogrammetric Engineering, University of
Oviedo, Polytechnic School in Mieres, Mieres, Spain; e-mail: peonjuan@uniovi.es

[7]NERC Field Spectroscopy Facility, School of Geosciences,
University of Edinburgh, Scotland; e-mail: alasdair.macarthur@ed.ac.uk

[8]Image Processing Laboratory, University of Valencia, Paterna, Valencia, Spain;
e-mail: luis.alonso@uv.es

A b s t r a c t

The work described in this paper is aimed at validating hyperspec-
tral airborne reflectance data collected during the Regional Experiments
For Land-atmosphere EXchanges (REFLEX) campaign. Ground reflec-
tance data measured in a vineyard were compared with airborne reflec-

tance data. A sampling strategy and subsequent ground data processing had to be devised so as to capture a representative spectral sample of this complex crop. A linear model between airborne and ground data was tried and statistically tested. Results reveal a sound correspondence between ground and airborne reflectance data ($R2 > 0.97$), validating the atmospheric correction of the latter.

1. INTRODUCTION

Hyperspectral Remote Sensing has been proven to be a very powerful technique in land surface studies (Govender *et al.* 2009). It has evolved as an important tool for deriving high spectral and spatial resolution information about soil and vegetation (Blackburn 2007, Yao *et al.* 2010). The applications of hyperspectral data can be cited in various fields like agriculture, forestry and biodiversity, mineral and oil explorations as well as soil characterization. Specifically, narrow band spectral indices derived using this data are particularly efficient in deriving information about land surface, as they rely on the specific spectral response of the targeted object (Cho *et al.* 2008, Delalieux *et al.* 2009, haboudane *et al.* 2004) . These indices have been used mostly in empirical models for retrieval of biophysical parameters like Leaf Area Index (LAI) (Haboudane *et al.* 2004, Johnson 2003), leaf chlorophyll and dry matter content (Zarco-Tejada *et al.* 2005 and references therein). They have also been utilized in net photosynthesis models to take into account the plant's physiological status (Dobrowski *et al.* 2005, Osório *et al.* 2012). Beyond spectral indices, hyperspectral remote sensing data have also been found useful for complex physically based radiative transfer models (Darvishzadeh *et al.* 2010, Zarco-Tejada *et al.* 2004) that are a proxy to the real field spectra. However, irrespective of the approach adapted for exploitation of hyperspectral research it is important to validate this data with appropriately designed scientific field spectroscopic measurements (Anderson *et al.* 2011). In the case of hyperspectral remote sensing, the trade-off between the spatial and spectral resolution becomes quite critical and so does the field validation plan. Airborne hyperspectral remote sensing applications require high spatial and spectral resolutions. Hyperspectral airborne sensors like the Airborne Hyperspectral Scanner (AHS) offer a full coverage of the visible and near infrared range of the spectrum (400-2500 nm) but a spatial resolution limited to a few metres. This spatial resolution may not be high enough for some applications and it determines the validation procedure. Especially for heterogeneous landscapes, capturing the variability through field spectroscopic measurements for the validation of remotely acquired data demands a carefully designed field spectroscopic

plan. During the Regional Experiments For Land-atmosphere EXchanges (REFLEX) campaign, airborne hyperspectral images were captured by the AHS sensor from Instituto Nacional de Técnicas Aeroespaciales, Spain (INTA) over the Las Tiesas Experimental Farm. This site is a good example of combination of different vegetative covers. It consists of maize field, grassland, bare ground, plantations of various crops and a vineyard (Timmermans *et al.* 2014). All these land covers are different with respect to their spectral response and hence would need different field spectroscopic plans for proper characterization.

The focus of this paper is on the validation of aerial images over a vineyard. A detailed description of the sampling strategy devised is presented and a thorough statistical analysis is performed, which are the most remarkable contributions of this work. A vineyard field is very heterogeneous due to its row structure, consisting of an irregular canopy mixed with bright and dark soil areas. In this case, scaling-up methods are needed to account for canopy structure and soil reflectance. For these methods to be applied, a characterization of the structure of the vineyard is needed, since structural parameters like separation of rows, relative orientation to the sun and the sensor and height for vines are needed for the models. At the same time, a careful spectroscopic characterization of the vineyard is mandatory. Surface reflectivity spectra measured at ground level are used for validation and model parameterization (Guanter *et al.* 2007) and in the recalibration of the reflectivity spectra obtained from remote sensing data. Validation of airborne and satellite data over Las Tiesas Experimental Farm has been carried out in previous campaigns. Extensive data can be found concerning validation of satellite-derived products like LAI (Martínez *et al.* 2009) and thermal airborne data (Sobrino *et al.* 2006). Regarding reflectance data, comparison of field and airborne reflectance data has also been undertaken in the past. Measurements of reflectance over homogeneous fields of bare soil, barley, and alfalfa were compared with HyMap airborne imaging spectrometer data (Beisl *et al.* 2000). Reflectance airborne data obtained using the Compact Airborne Spectrographic Imager (CASI) spectrometer and field reflectance data were compared in Guanter *et al.* (2007) over alfalfa, corn, bare soil, and reforestry fields.

For the spectroscopic characterization, spectroscopic measurements over the vineyard were performed using a GER 1500 spectroradiometer. Taking into consideration the pixel size of airborne images in this work (3 m), it can be stated that the pixels in the image would always be mixture of spectral signatures of soil and vegetation. Hence, a sampling strategy had to be devised so that the area sampled was representative of the heterogeneity of the field.

2.   EXPERIMENTAL PROCEDURE

2.1 Description of the test sites

Field measurements were conducted in a vineyard at Las Tiesas Experimental Farm (39°3.544′ N, 2°6.082′ W, elevation *ca.* 700 m a.s.l., Fig. 1), located in the La Mancha region in Southern Spain, *ca.* 20 km west of Albacete. Flat morphology and large, uniform land use units render Las Tiesas a suitable test site for remote sensing applications. Approximately 65% of the area is dry land and 35% is irrigated and cultivated with different crops. The climate is Mediterranean, with low average annual rainfall (400 mm), which is mainly concentrated in spring and autumn. La Mancha is among the driest regions of Europe, with water tables between 20 and 30 m below the land surface.

The vineyard covers an area of *ca.* 6.8 ha and it is irrigated. Field measurements were restricted to an area of 2.4 ha in the northern part of the vineyard (Fig. 1b), which was planted with the same variety of vine (*Vitis vini-*
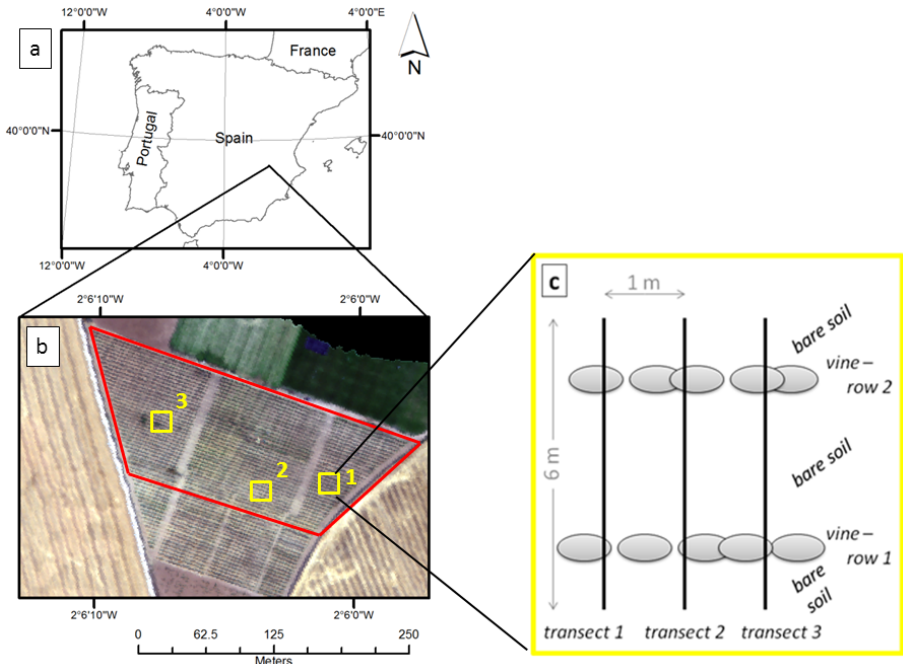
Fig. 1: (a) Location of the study site within Spain; (b) Aerial image of the vineyard. Real colour composite with AHS channel centred at 650 nm as red, AHS channel centred at 530 nm as green and AHS channel centred at 471 nm as blue. The study site is framed in a red box. Approximate locations of plots 1-3, where field measurements were conducted, are demarcated by yellow boxes; (c) Schematic depicting of the sampling strategy within each plot (please see text for details).

fera). Vines were *ca.* 1.3 m in height and were planted in roughly NW-SE oriented rows approximately 3 m apart, with a cross-row canopy extension of approximately 0.2-0.3 m at the time of the study. Areas in between the rows were dominated by bare soil with some sparse cover of small forbs.

2.2 Field measurements and airborne data

Within the vineyard, three plots (3×6 m²) were randomly chosen (Fig. 1b), each consisting of 3 transects. Transects were 1 m apart and 6 m long, such that the starting and end points of each transect would be in the middle in between two rows of vines, and the transects would cross two rows of vines (Fig. 1c). One 6 m transect can thus be considered the smallest "homogenous" measurement unit, such that although the transects were moved within the vineyard, it would always cover two rows of vines and two inter-row areas (from now on referred to as bare soil), *i.e.*, fractions of canopy and bare soil would be representative for any given 6 m transect within the study site. Plot 1 and the first transect of plot 2 were sampled on 25 July 2012, from 8:00 to 10:10 UTC; transect 2 and 3 of plot 2 and complete plot 3 were sampled on 26 July 2012, 8:20 to 11:59 UTC. Airborne data were acquired on the same dates as the field measurements, and nearly simultaneously. On 25 July 2012 airborne data acquisition started at 8:41 UTC and was completed at 9:47 UTC. On 26 July 2012 airborne data acquisition started at 8:42 UTC and was completed at 9:38 UTC (de Miguel *et al.* 2015, Timmermans *et al.* 2014).

Two GER 1500 spectroradiometers (Spectra Vista Corporation, Poughkeepsie, NY, USA) were operated in Dual-Beam Bi-Conical mode, using a notebook equipped with the DFOV 1500 software. In the Dual-Beam Bi-Conical mode, one spectroradiometer (from now on target sensor) can be used to measure the target, while the second device (from now on reference sensor) simultaneously measures the Spectralon reference panel. This mode of operation provides simultaneous measurements of reference and target, minimizing uncertainties due to changes in irradiance between target and reference scans. To complete the measurement procedure, a reference panel must be measured using the target sensor to allow for intercalibration of both spectrometers. These measurements were performed at the beginning and at the end of each plot. Two different Spectralon reference panels were used, one for each spectrometer. The spectral response of both Spectralon reference panels (25×25 cm² reflective area, Labsphere Inc., North Sutton, NH, USA) was known. For target measurements, the reference sensor remained at a fixed point over the reference panel, with both, sensor and reference panel, being fixed to tripods. The target sensor was mounted to the top of a 2.8 m pole, using a tripod and duct tape. The angle between pole and spec-

trometer was set to *ca.* 25°, so that when the pole was tilted by *ca.* 25°, measurements could be taken from 2.5 m height from nadir, with the operator interfering as little as possible with the field of view of the sensor. GER 1500 spectroradiometers recorded the spectral range from 350 to 1050 nm, with a spectral resolution of 3.2 nm and a sampling interval of 1.5 nm. 8° foreoptics were used, resulting in a field of view of 35 cm on the ground with a measuring height of 2.5 m. With this field of view, and given the cross-row canopy extension and the separation of the rows of vines, the field spectrum of soil contains most probably pure soil information, whilst the field spectrum of the vegetation contains for sure not only vegetation but soil information too. Integration speed was set to automatic. Each sample represents the average of 16 scans. GER 1500 devices were switched on and warmed up at least 20 min before the start of measurements. Intercalibration was conducted between reference and target sensor and finally Hemispherical Conical Reflectance Factor (HCRF) (Schaepman-Strub *et al.* 2006) was calculated following the methodology proposed by NERC Field Spectroscopy Facility (Anderson *et al.* 2011). Once this step was done, all spectra were resampled to match the spectral resolution of the AHS sensor using the spectral response function of each band provided by INTA. In order to capture a representative sample, *i.e.*, an unbiased representation of fractional covers of vegetation and bare soil within one transect, spectra were recorded every 25 cm on each transect. Transects and the measuring points were marked on the ground, so the operator just needed to place the pole at each point ensuring consistency in the measurements along time. Taking into account the field of view of 35 cm, transects were thus completely recorded by this method. In total, 236 spectra were collected. Differences in illumination conditions during field measurement acquisition were considered. Due to the orientation of the vines (NW-SE) and the time at which the field measurements were taken (7:30 to 10:00 UTC) the shadow effect in soil measurements was minimum as sun azimuth at 7:30 UTC is 85° whilst at 10:00 UTC is 114° (0° taken pointing north). Furthermore, as nadir looking geometry was maintained for the measurements, we assume that the target measurements on top of the canopy were captured with least fraction of shadow possible. As we will see below, the role of shadows is also minimized by discarding the four adjacent measurements on both sides of the vines, avoiding thus the areas most affected by shadows.

Airborne hyperspectral data were acquired using AHS sensor mounted on a CASA 212-200 aircraft, property of INTA. Several flights were undertaken simultaneously to ground measurements. The data presented in this paper correspond to the flight at 8:43 a.m. on 25 July 2012 at an altitude of 1700 m a.s.l. Figure 2 is a false colour composite of the area covered by the flight. The INTA AHS sensor has 63 channels in the reflective part of the
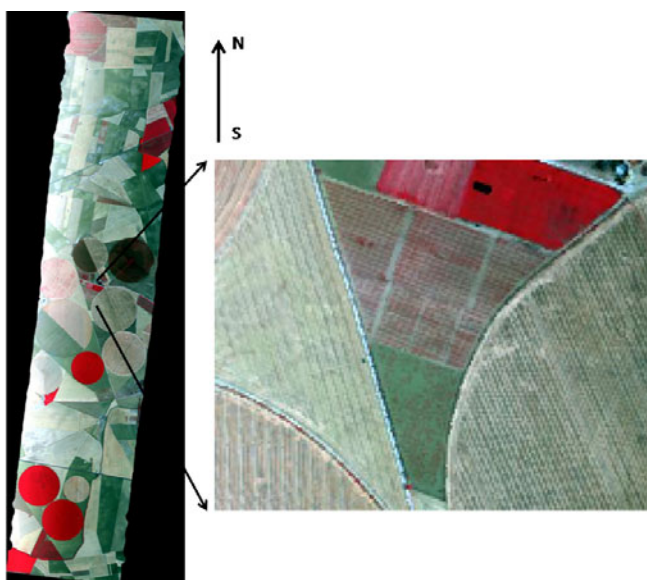
Fig. 2. False color RGB composite of the flight line (left) and of an enlarged image of the vineyard (right),taking the AHS channel centred at 856 nm as red, the channel centred at 650 nm as green, and the channel centred at 530 nm as blue.

electromagnetic spectrum (20 bands from 442 to 1019 nm, 1 band from 1491 to 1650 nm, and 20 bands from 2028 to 2498 nm), 7 bands in the 3 to 5 microns range, and 10 bands in the 8 to 13 microns range. The Instantaneous Field Of View (IFOV) is 2.5 mrad with a Field Of View (FOV) of 90°. The Full Width Half Maximum (FWHM) of the bands from 442 to 1019 nm (the bands that coincide with the GER spectral range) is 27-30 nm. At sensor radiance data were corrected by INTA using ATmospheric CORrection (ATCOR4) (Richter and Schläpfer 2011) to produce Hemispherical Directional Reflectance Factor (HDRF) since ATCOR4 does not correct for the hemispherical irradiance (Schaepman-Strub *et al.* 2006). In this way we assure that ground and airborne reflectance products are comparable. Data were subsequently georeferenced to a 3-m-on-a-side pixel.

After resampling of the ground measurements, each spectral HDRF and HCRF consists of 19 values of reflectance, each one for each of the 19 AHS channels from 442 up to 973 nm.

2.3 Modeling

Once the data from both sources was comparable, a statistical approach was applied to understand some of the issues on the upscaling process in a heterogeneous crop such as a vineyard. It is well known that the agreement be-

tween airborne and ground spectra depends on the nature of the target, spatial resolution, viewing geometry, and regarding remote sensing of vegetation; it becomes less when the proportion of soil increases (Guanter *et al.* 2007). In the case of the vineyard field, given the pixel size and the distribution of soil and vines, airborne spectra were modelled as a linear combination of two ground reflectances, representing domination of soil and vegetation, respectively:

$$(AHS) = S \times \rho_s + V \times \rho_v \ , \qquad S, V \geq 0 \ . \tag{1}$$

where $\rho(AHS)$ is the HDRF obtained from airborne data (the reflectance spectrum of a pixel), and ρ_s and ρ_v are soil and vegetation ground HCRF spectra obtained using the GER spectroradiometer. Spectral signatures ρ_s and ρ_v do not have to be understood as pure-soil and pure-vegetation ground spectral signatures, but as two spectral signatures obtained from ground measurements that represent the two ends of all the measured mixed soil-vegetation spectra. This is clearly understood in the case of ρ_v, since even in the case of measuring just above the canopy, some signal from the soil will enter the radiometer, due to the FOV of the instrument, the sparse canopy and the reflected soil energy transmitted from the canopy. Coefficients S and V are the contributions of each of these ground endspectra to the spectrum of each pixel. Since we are comparing ground against airborne data the restriction $S + V \leq 1$ was not imposed. This analysis is not intended to be a spectral unmixing to obtain abundances of soil and vegetation. Further analysis should be carried out in order to obtain the spectral unmixing endmembers from ρ_s and ρ_v like matching field spectra with the image endmembers spectra (Schmid *et al.* 2004) or other techniques (Quintano *et al.* 2012). The restriction $S + V = 1$ must have been imposed in the case of having obtained ρ_s and ρ_v as image endmembers or after having related them to the image endmembers. Nevertheless, S and V provide an estimation of the weight of soil and vegetation in the pixel spectrum. As we will see later, for some pure soil pixels we obtained $V = 0$ and $S > 1$, an unsurprising result since ρ_s is not the soil endmember of the image.

3. RESULTS AND DISCUSSION

For each plot, we obtained ρ_s and ρ_v as the mean values of the reflectance spectra of soil targets and vegetation targets, respectively, as explained below. To identify a target as soil target or vegetation target we used the ground NDVI obtained from the GER field spectra, named NDVI_GER. Figure 3 shows the NDVI_GER for all the targets measured in the three plots. In order to calculate ρ_v for each plot, we firstly identified the six targets with maximum NDVI_GER. We then calculated the reflectance spec-
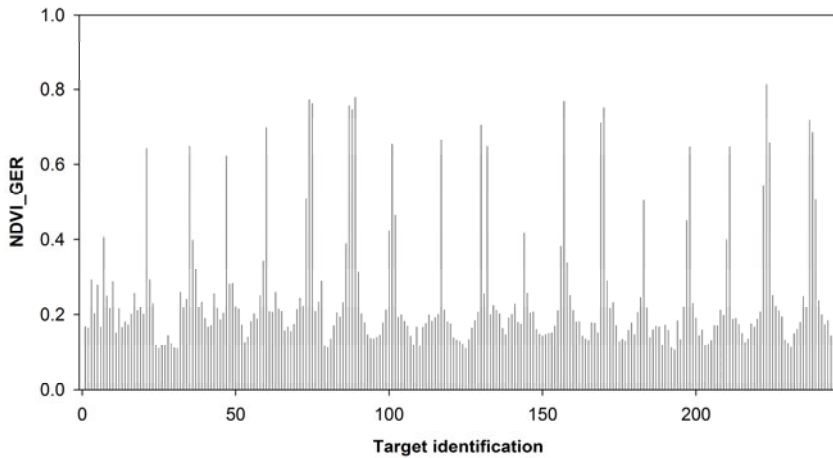
Fig. 3. NDVI obtained from field reflectance spectra taken on transects across the vine rows (NDVI_GER). Target measurements were given consecutive numbers. The periodicity in NDVI_GER reflects the transitions between soil- and vegetation-dominated targets as moving across the rows of vine.

trum of vegetation for each plot as the mean value of the six targets with maximum NDVI_GER. We took 6 targets since, according to the sampling strategy described above, the spectroradiometer was placed just above the vine canopy 6 times exactly on each plot. So those targets with the maximum NDVI_GER correspond to measurements taken just above the vine canopy. Ground soil reflectance spectrum ρ_s was then calculated as the mean of the rest of the targets, ignoring the four nearest targets to those with the maximum NDVI_GER (corresponding to two targets at each side of the vine) in order to avoid contamination from the canopy.

Figures 4 and 5 show the correlation between ρ_v and ρ_s for the three plots (named P_1, P_2, and P_3) measured in the vineyard for the 19 bands between 442 and 973 nm. It is noteworthy that ρ_v and ρ_s for the three plots exhibit a linear relationship between each other with very high correlation, a slope close to 1 and a very small offset (see the fitting equations inserted in Figs. 4 and 5).

Thus, ρ_v and ρ_s from one single plot are representative for all three plots, suggesting that ρ_v and ρ_s from one single plot can be used to describe the part of the vineyard framed in the red box in Fig. 1; let us remind that the southern part of the vineyard is not taken into account since it has a slightly different structure.

The spectral properties of the soil and the vegetation change from sample to sample. But since the variety of vine is the same over the whole area under study and the soil is homogeneous, it has to be possible to find a repre-
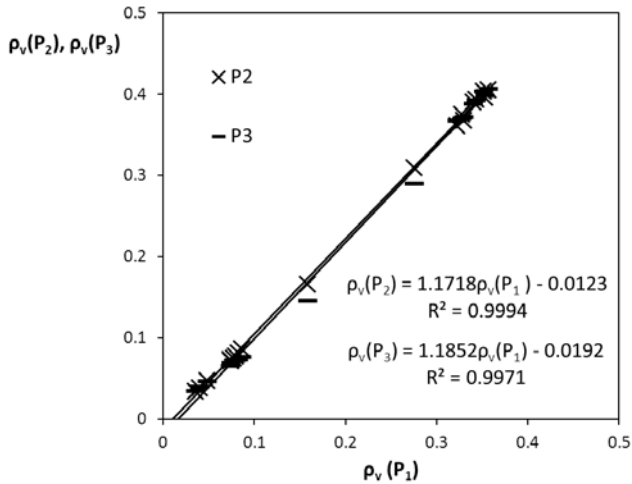
Fig. 4. Correlation between ground ρ_v measured in the three plots, P_1, P_2, and P_3. Least-square fits of $\rho_v(P_2)$ *versus* $\rho_v(P_1)$ and $\rho_v(P_3)$ *versus* $\rho_v(P_1)$ are presented.

$$\rho_v(P_2) = 1.1718\rho_v(P_1) - 0.0123$$
$$R^2 = 0.9994$$

$$\rho_v(P_3) = 1.1852\rho_v(P_1) - 0.0192$$
$$R^2 = 0.9971$$
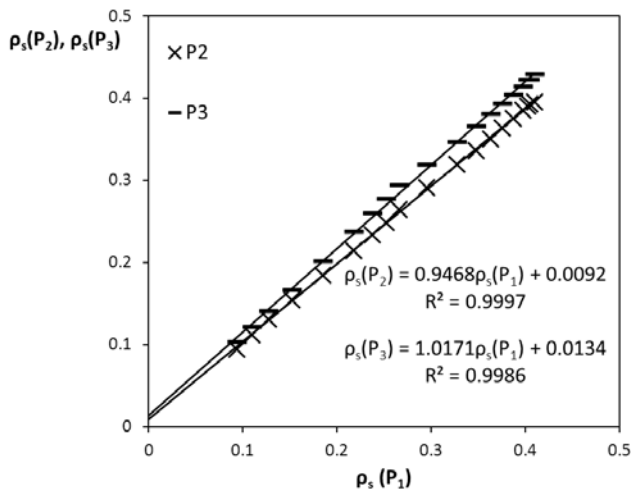
Fig. 5. Correlation between ground ρ_s measured in the three plots, P_1, P_2, and P_3. Least-square fits of $\rho_s(P_2)$ *versus* $\rho_s(P_1)$ and $\rho_s(P_3)$ *versus* $\rho_s(P_1)$ are presented.

$$\rho_s(P_2) = 0.9468\rho_s(P_1) + 0.0092$$
$$R^2 = 0.9997$$

$$\rho_s(P_3) = 1.0171\rho_s(P_1) + 0.0134$$
$$R^2 = 0.9986$$

sentative spectrum of the soil and of the vegetation of the study area. A good sampling strategy has to be able to provide these representative spectra. The results shown in Figs. 4 and 5 prove that the sampling strategy was correct; otherwise, different ρ_v and ρ_s would have been obtained for each plot.

To investigate the validity of the linear relationship between airborne and ground data (Eq. 1), ρ_v and ρ_s from plot 1 are going to be used from now on. Each pixel in the image is supposed to have ρ_v and ρ_s of plot 1, and then the
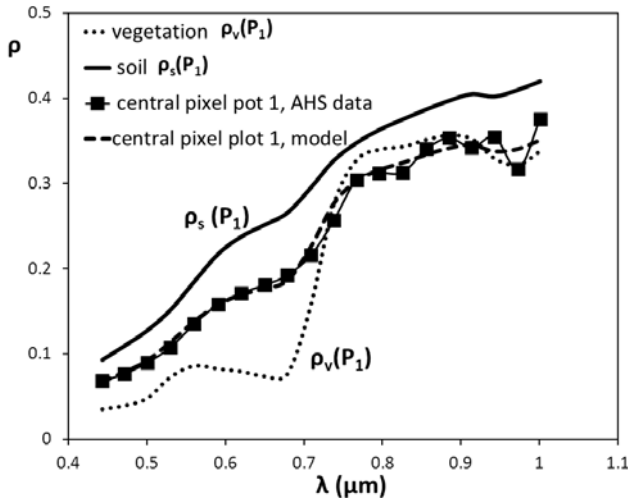
Fig. 6. AHS reflectance spectral signature for a pixel located at plot 1 and the fit to the ground spectra using the model in Eq. 1.

actual reflectance spectrum of that pixel is used to calculate S and V using Eq. 1. The hypothesis of a linear relationship between ρ(AHS) and ρ_v and ρ_s will be tested using the determination coefficient R^2 of the fit and the p-values of the t-test on coefficients S and V for each pixel. As an example, ground ρ_v and ρ_s as a function of wavelength from plot 1 are plotted in Fig. 6, along with the reflectance for a pixel located at plot 1, ρ(AHS), and the reflectance fitted using Eq. 1.

The model was applied for the whole vineyard. For each pixel, we calculated the values of S, V, and the corresponding p-values along with the determination coefficient R^2 of the fit. Results are shown in Figs. 7-10. The model can be considered of statistical significance (with a significance level of 5%) for those pixels for which p-value $(S) < 0.05$ and p-value $(V) < 0.05$. Results are shown in Table 1. According to these results, 230 pixels (8.3%) can be regarded as pure soil ($V = 0$), corresponding to the two parallel wide

Table 1

Distribution of pixels according to the values of V, S, and their p-values

S, V, p-value (S), p-value (V)	Number of pixels	Percentage
$V > 0$ and p-value $(V) < 0.05$	2351	84.8
$V > 0$ and p-value $(V) > 0.05$	190	6.9
$V = 0$	230	8.3
$S > 0$ and p-value $(S) < 0.05$	2771	100
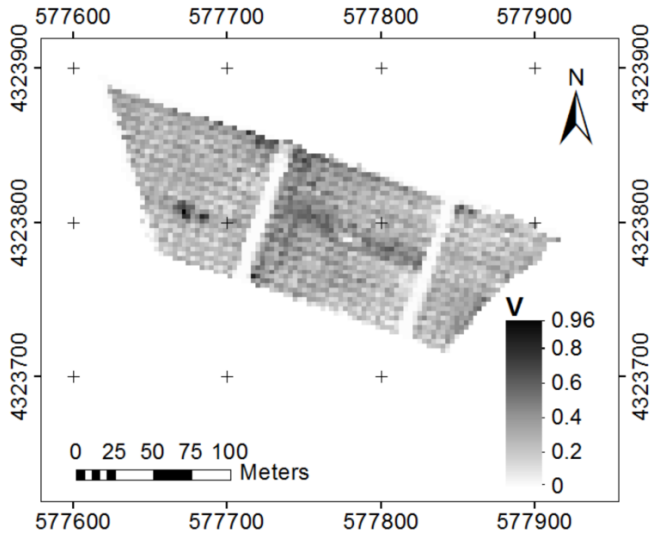
Fig. 7. Distribution of the values of V across the vineyard. Pixels with $V = 0$ represent pure soil pixels. Map is provided in UTM WGS-84 30N.
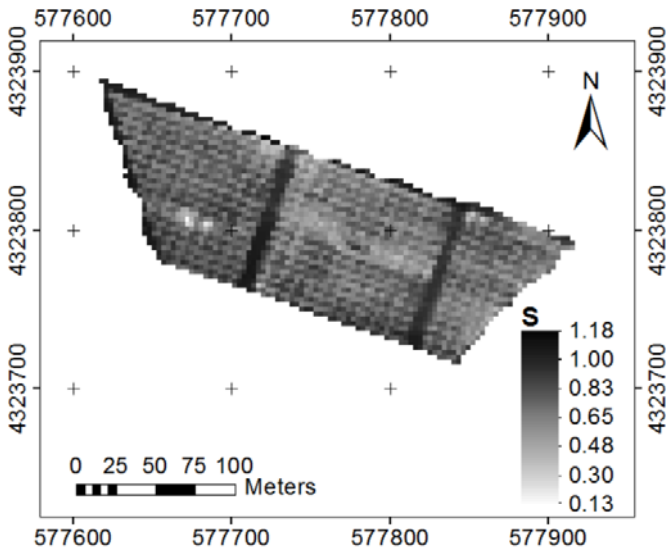
Fig. 8. Distribution of the values of S across the vineyard. Map is provided in UTM WGS-84 30N.

soil paths crossing the vineyard from NE to SW. Moreover, the model provides values of V with p-value $(V) > 0.05$ for only 6.9% of the pixels. $S > 0$ with a p-value below 0.05 were obtained in 100% of the pixels.
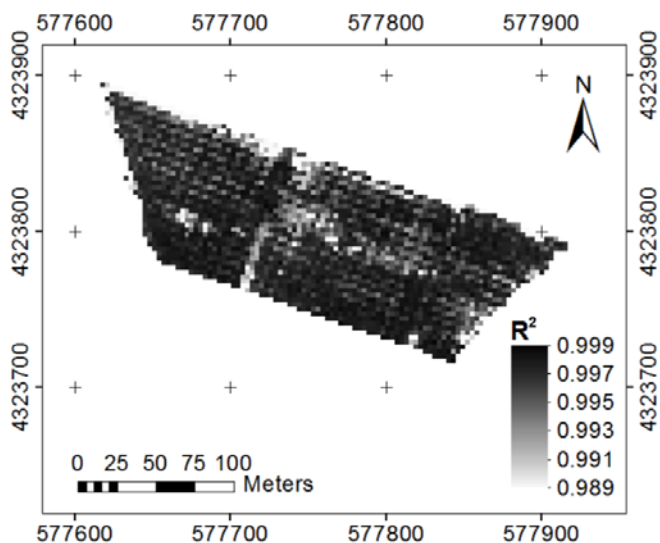
Fig. 9. Distribution of the values of R^2 across the vineyard. Map is provided in UTM WGS-84 30N.
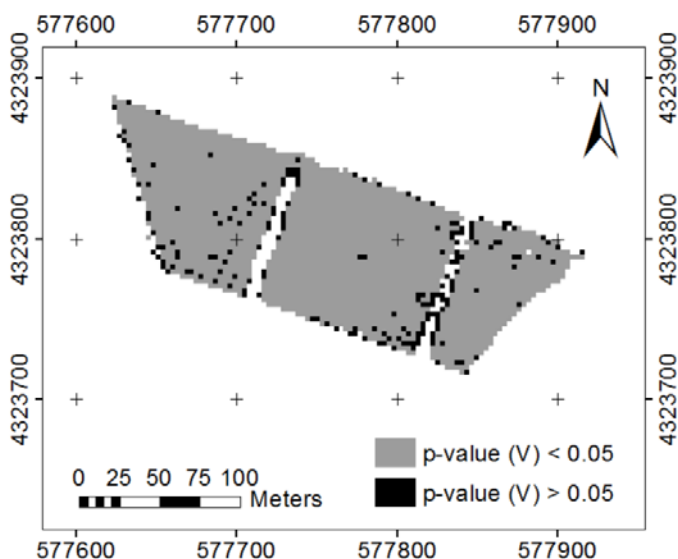
Fig. 10. Distribution of the values of p-value (V) across the vineyard. White pixels have $V = 0$ (pure soil pixels). Map is provided in UTM WGS-84 30N.

The obtained values of V and S clearly reproduce the rowed structure of the vineyard, as can be seen in Figs. 7 and 8. Rows of alternatively high (low) and low (high) $S(V)$ values running parallel to the vines were obtained.

The high values of R^2 obtained across the vineyard confirm the validity of the model. It is noteworthy that pixels with p-value $(V) > 0.05$ are mainly located in the vicinity of soil paths (see Fig. 10) where no reliable, extremely low V values are expected. On the other hand, shadows might affect the vegetation field spectra more, and this is shown in the larger number of pixels with p-value $(V) > 0.05$ (6.9% of the pixels) than pixels with p-value $(S) > 0.05$ (0% of the pixels).

The results from the statistical analysis confirm that the sampling strategy is suited to capture the variability of the site. They can also be used as a validation of airborne data and of the atmospheric correction performed. Previous studies of reflectance performed over the same site do not provide a description of the sampling strategy and lack a sound statistical analysis of the data. In the case of the HyMap airborne imaging spectrometer data (Beisl *et al.* 2000) over bare soil, barley and alfalfa, the disagreement between field and airborne data was attributed to either the varying angular behaviour of the reflectance or to the fact that non-representative samples were collected in the field. In the case of the CASI spectrometer over bare soil, alfalfa, corn and reforestry (Guanter *et al.* 2007), the agreement between airborne and field reflectance data became worse when the proportion of soil increased, explained by those authors as probably due to the high heterogeneity of bare soils. A thorough statistical analysis of the results was not given in any of the two studies.

In order to reinforce the results, we tried to correlate coefficient V with vegetation properties. Coefficient V is expected to provide information about the condition of the canopy. To confirm this, we plotted the value of the NDVI measured from AHS data (NDVI_AHS) *versus* the value of V for
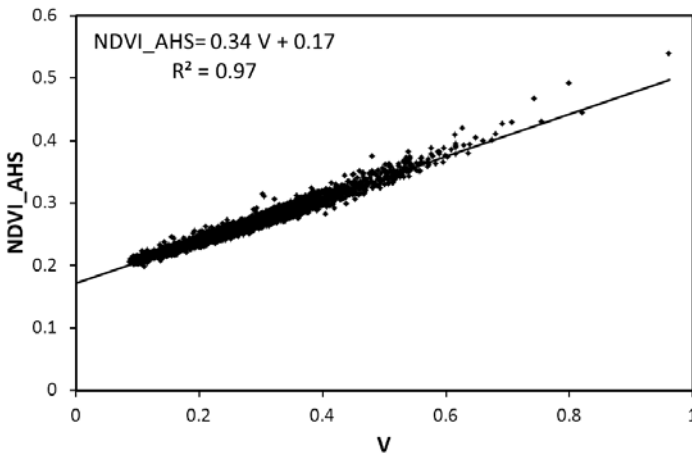
Fig. 11. NDVI_AHS *versus* V for 2351 pixels with $V > 0$ and p-value $(V) < 0.05$.

the 2351 vineyard pixels for which $V > 0$ and p-value $(V) < 0.05$ (Fig. 11). A strong correlation was confirmed. The offset (0.17) would provide an estimation of the mean value of the NDVI of the soil.

4.   CONCLUSIONS

Validation of airborne hyperspectral HDRF product has been carried out comparing airborne data with ground measurements over a vineyard. A sampling strategy was devised and a subsequent ground data processing was undertaken in order to obtain ground reflectance products comparable to airborne ones. Ground spectral reflectance of a pixel area was simulated as a linear combination of soil and vegetation contributions and then compared to airborne spectral reflectance on a pixel by pixel basis. Statistical analyses show that there is a strong correlation between airborne and ground data. These results indicate that a sound atmospheric correction has been performed for the AHS bands under consideration.

References

Anderson, K., J.L. Dungan, and A. MacArthur (2011), On the reproducibility of field-measured reflectance factors in the context of vegetation studies, *Remote Sens. Environ.* **115**, 8, 1893-1905, DOI: 10.1016/j.rse.2011.03.012.

Beisl, U., G. Strub, and C. Dickerhof (2000), Validation of hyperspectral imaging data from the Barrax test site with BRDF ground measurements in the reflective wavelength range. **In:** *2nd EARSeL Workshop on Imaging Spectroscopy, 11-13 July 2000, Enschede, The Netherlands.*

Blackburn, G.A. (2007), Hyperspectral remote sensing of plant pigments, *J. Exp. Bot.* **58**, 4, 855-867, DOI: 10.1093/jxb/erl123.

Cho, M.A., I. Sobhan, A.K. Skidmore, and J. de Leeuw (2008), Discriminating species using hyperspectral indices at leaf and canopy scales, *Int. Arch. Photogram. Remote Sens. Spat. Inf. Sci.* **37**, B7, 369-376.

Darvishzadeh, R., C. Atzberger, A. Skidmore, and M. Schlerf (2010), Retrieval of vegetation biochemicals using a radiative transfer model and hyperspectral data. **In:** W. Wagner, and B. Székely (eds.), *TC VII Symposium – 100 Years ISPRS – Advancing Remote Sensing Science*, 5-7 July 2010, Vienna, Austria, 171-175.

de Miguel, E., M. Jiménez, I. Pérez, O.G. de la Cámara, F. Muñoz, and J.A. Gómez-Sánchez (2015), AHS and CASI processing for the REFLEX remote sensing campaign: methods and results, *Acta Geophys.* **63**, 6, 1485-1498, DOI: 10.1515/acgeo-2015-0031 (this issue).

Delalieux, S., B. Somers, W.W. Verstraeten, J.A.N. van Aardt, W. Keulemans, and P. Coppin (2009), Hyperspectral indices to diagnose leaf biotic stress of apple plants, considering leaf phenology, *Int. J. Remote Sens.* **30**, 8, 1887-1912, DOI: 10.1080/01431160802541556.

Dobrowski, S.Z., J.C. Pushnik, P.J. Zarco-Tejada, and S.L. Ustin (2005), Simple reflectance indices track heat and water stress-induced changes in steady-state chlorophyll fluorescence at the canopy scale, *Remote Sens. Environ.* **97**, 3, 403-414, DOI: 10.1016/j.rse.2005.05.006.

Govender, M., P.J. Dye, I.M. Weiersbye, E.T.F. Witkowski, and F. Ahmed (2009), Review of commonly used remote sensing and ground-based technologies to measure plant water stress, *Water SA* **35**, 5, 741-752, DOI: 10.4314/wsa.v35i5.49201.

Guanter, L., V. Estellés, and J. Moreno (2007), Spectral calibration and atmospheric correction of ultra-fine spectral and spatial resolution remote sensing data. Application to CASI-1500 data, *Remote Sens. Environ.* **109**, 1, 54-65, DOI: 10.1016/j.rse.2006.12.005.

Haboudane, D., J.R. Miller, E. Pattey, P.J. Zarco-Tejada, and I.B. Strachan (2004), Hyperspectral vegetation indices and novel algorithms for predicting green LAI of crop canopies: Modeling and validation in the context of precision agriculture, *Remote Sens. Environ.* **90**, 3, 337-352, DOI: 10.1016/j.rse.2003.12.013.

Johnson, L.F. (2003), Temporal stability of an NDVI-LAI relationship in a Napa Valley vineyard, *Aust. J. Grape Wine Res.* **9**, 2, 96-101, DOI: 10.1111/j.1755-0238.2003.tb00258.x.

Martínez, B., F.J. García-Haro, and F. Camacho-de Coca (2009), Derivation of high-resolution leaf area index maps in support of validation activities: Application to the cropland Barrax site, *Agr. Forest Meteorol.* **149**, 1, 130-145, DOI: 10.1016/j.agrformet.2008.07.014.

Osório, J., M.L. Osório, and A. Romano (2012), Reflectance indices as nondestructive indicators of the physiological status of Ceratonia siliqua seedlings under varying moisture and temperature regimes, *Funct. Plant Biol.* **39**, 7, 588-597, DOI: 10.1071/FP11284.

Quintano, C., A. Fernández-Manso, Y.E. Shimabukuro, and G. Pereira (2012), Spectral unmixing, *Int. J. Remote Sens.* **33**, 17, 5307-5340, DOI: 10.1080/01431161.2012.661095.

Richter, R., and D. Schläpfer (2011). Atmospheric/topographic correction for airborne imagery. DLR Report, DLR-IB 565-02/11, Wessling, Germany.

Schaepman-Strub, G., M.E. Schaepman, T.H. Painter, S. Dangel, and J.V. Martonchik (2006), Reflectance quantities in optical remote sensing—definitions

and case studies, *Remote Sens. Environ.* **103**, 1, 27-42, DOI: 10.1016/ j.rse.2006.03.002.

Schmid, T., M. Koch, J. Gumuzzio, and P.M. Mather (2004), A spectral library for a semi-arid wetland and its application to studies of wetland degradation using hyperspectral and multispectral data, *Int. J. Remote Sens.* **25**, 13, 2485-2496, DOI: 10.1080/0143116031000117001.

Sobrino, J.A., J.C. Jiménez-Muñoz, P.J. Zarco-Tejada, G. Sepulcre-Cantó, and E. de Miguel (2006), Land surface temperature derived from airborne hyperspectral scanner thermal infrared data, *Remote Sens. Environ.* **102**, 1-2, 99-115, DOI: 10.1016/j.rse.2006.02.001.

Timmermans, W., C. van der Tol, J. Timmermans, M. Ucer, X. Chen, L. Alonso, J. Moreno, A. Carrara, R. Lopez, F. de la Cruz Tercero, H.L. Corcoles, E. de Miguel, J.A.G. Sanchez, I. Pérez, B. Franch, J.-C.J. Munoz, D. Skokovic, J. Sobrino, G. Soria, A. MacArthur, L. Vescovo, I. Reusen, A. Andreu, A. Burkart, C. Cilia, S. Contreras, C. Corbari, J.F. Calleja, R. Guzinski, C. Hellmann, I. Herrmann, G. Kerr, A.-L. Lazar, B. Leutner, G. Mendiguren, S. Nasilowska, H. Nieto, J. Pachego-Labrador, S. Pulanekar, R. Raj, A. Schikling, B. Siegmann, S. von Bueren, and Z. Su (2015), An overview of the Regional Experiments for Land-atmosphere Exchanges 2012 (REFLEX 2012) Campaign, *Acta Geophys.* **63**, 6, 1465-1484, DOI: 10.2478/s11600-014-0254-1 (this issue).

Yao, Y., N. Wei, Y. Chen, Y. He, and P. Tang (2010), Soil moisture monitoring using hyper-spectral remote sensing technology. **In:** Q. Luo (ed.), *2010 2nd IITA Int. Conf. on Geoscience and Remote Sensing (IITA-GRS), 28-31 August 2010, Qingdao, China*, IEEE, 373-376, DOI: 10.1109/IITA-GRS.2010. 5604219.

Zarco-Tejada, P.J., J.R. Miller, J. Harron, B. Hu, T.L. Noland, N. Goel, G.H. Mohammed, and P. Sampson (2004), Needle chlorophyll content estimation through model inversion using hyperspectral data from boreal conifer forest canopies, *Remote Sens. Environ.* **89**, 2, 189-199, DOI: 10.1016/j.rse.2002. 06.002.

Zarco-Tejada, P.J., A. Berjón, R. López-Lozano, J.R. Miller, P. Martín, V. Cachorro, M.R. González, and A. de Frutos (2005), Assessing vineyard condition with hyperspectral indices: Leaf and canopy reflectance simulation in a row-structured discontinuous canopy, *Remote Sens. Environ.* **99**, 3, 271-287, DOI: 10.1016/j.rse.2005.09.002.

An Analysis of Turbulent Heat Fluxes and the Energy Balance During the REFLEX Campaign

Christiaan van der TOL[1], Wim TIMMERMANS[1], Chiara CORBARI[2],
Arnaud CARRARA[3], Joris TIMMERMANS[1], and Zhongbo SU[1]

[1]Department of Water Resources, Faculty ITC, University of Twente,
Enschede, The Netherlands; e-mail: c.vandertol@utwente.nl

[2]Department of Hydraulic, Environmental and Surveying Engineering,
Politecnico di Milano, Milano, Italy

[3]CEAM, Fundación de la Comunidad Valenciana
Centro de Estudios Ambientales del Mediterraneo, Paterna, Spain

A b s t r a c t

Three eddy covariance stations were installed at the Barrax experimental farm during the Land-Atmosphere Exchanges (REFLEX) airborne training and measurement campaign to provide ground truth data of energy balance fluxes and vertical temperature and wind profiles. The energy balance closure ratio (EBR) was 105% for a homogeneous camelina site, 86% at a sparse reforestation site, and 73% for a vineyard. We hypothesize that the lower closure in the last site was related to the limited fetch. Incorporating a vertical gradient of soil thermal properties decreased the RMSE of the energy balance at the camelina site by $16 \, \mathrm{W\,m^{-2}}$. At the camelina site, eddy covariance estimates of sensible and latent heat fluxes could be reproduced well using mean vertical profiles of wind and temperature, provided that the Monin–Obukhov length is known. Measured surface temperature and sensible heat fluxes suggested high excess resistance for heat ($\mathrm{kB}^{-1} = 17$).

Key words: eddy covariance, SEB modelling, soil heat flux, surface roughness.

1. INTRODUCTION

Quantifying surface energy fluxes is relevant for boundary layer meteorology, climatology, ecology, hydrology, and agronomy. In those fields, the spatial variability of evapotranspiration and sensible heat is of great importance. Remote sensing techniques may assist in obtaining spatial estimates of these fluxes through radiometric observations. However, as fluxes cannot be observed directly, the remote sensing observations always have to be combined with models. One class of these models (among others, see Cleugh *et al.* 2007) are surface energy balance (SEB) models. SEB models that calculate land-atmosphere exchanges of energy and matter rely on observations of the temperature gradient between the land surface and the air to estimate the turbulent exchange of sensible and latent heat from surface to atmosphere (for a review, see Kalma *et al.* 2008).

These SEB models, however, are relatively "simple" models, and consequently their applicability needs to be carefully assessed. In particular, two parameters are of key importance: the difference between the surface and air temperature, and the aerodynamic resistance.

One of the problems of SEB models is that the difference between surface and air temperature can be relatively small, and thus prone to errors (Cleugh *et al.* 2007). Air temperature data are not available at the same spatial resolution as surface temperature, and often not even at the same time (Kustas and Norman 1996). Horizontal interactions within and between pixels are usually ignored, while this is not always justified (Gash 1987). Dual source models, used for pixels with partial vegetation cover (*e.g.*, Kustas *et al.* 1996), only partly solve this problem as, even in these schemes, horizontal fluxes are poorly represented and between-pixel interactions ignored. Timmermans *et al.* (2008) studied the effect of feedback mechanisms between fluxes on the one hand, and the surface to air temperature gradient on the other hand, by means of large eddy simulation (LES). They found a negative feedback between fluxes and the temperature gradient, which causes the extreme fluxes (lowest and highest values) to dampen. Models that do not include such interaction and that, for example, use a constant value or interpolated map for air temperature as input, may thus overestimate the extremes of sensible heat flux, which directly propagates into the estimate of latent heat flux and leads to errors in the estimates of vegetation water use.

Another problem with remote sensing driven land surface models is that the aerodynamic resistance for heat is difficult to estimate. The resistance for matter can be calculated from a wind profile, but estimating the resistance for heat requires extrapolation of the logarithmic vertical air temperature profile to the radiometrically measured temperature. The virtual height at which the extrapolated temperature equals surface temperature, z_{0h}, is usually

smaller than the roughness height for momentum, z_{0m} (Su *et al.* 2001). The ratio z_{0h}/z_{0m} can be expressed as an excess resistance (Owen and Thomson 1963), but several studies have shown that this excess resistance varies widely (Stewart *et al.* 1994, Verhoef *et al.* 1997, Massman 1999), in particular in areas with partial vegetation cover (Gökmen *et al.* 2012).

Both problems can be addressed if accurate measurements of temperature gradients and fluxes are available. The data collected during the Land-Atmosphere Exchanges (REFLEX) airborne training and measurement campaign at the Las Tiesas experimental farm in Spain serve this purpose. The area where the campaign took place is heterogeneous, due to the presence of irrigated agriculture in an otherwise naturally dry environment (Su *et al.* 2008). Although REFLEX was not the first airborne campaign at the farm, it had the unique aspect that the flights were optimized to provide information needed to study the heterogeneity of land-atmosphere fluxes of energy and water (Timmermans *et al.* 2014). The combination of high resolution airborne and ground data makes it possible to evaluate land surface models and model concepts at fine spatial resolution.

The objectives of the present paper are: (i) to evaluate the quality of eddy covariance collected during the REFLEX campaign, and (ii) to provide local estimates of surface fluxes, resistances, and vertical profile weather data. The paper describes results from three eddy covariance (EC) flux towers established for ground truth data collection at the experimental site between 17 and 29 July 2012. The focus of the present study is on one of the sites, where instrumentation was most elaborate. Of particular importance for later use in LES simulations were accurate local estimates of the surface energy balance fluxes, and vertical profiles of wind speed, temperature, and humidity in the vegetation and surface layer. Because the instruments were placed close to the surface, we were able to measure the energy balance of individual fields with a fairly homogeneous fetch at the stations, except for a station in a vineyard. We analyse the energy balance at the stations, address potential problems of energy balance closure, and verify the quality of measurements of vertical gradients of wind u, relative humidity RH, and air temperature T_a (Section 3.4), and radiometric surface temperature (Section 3.5) by estimating sensible and latent heat flux from profile data.

2. SITE DESCRIPTION AND INSTRUMENTATION

The study site is located in the La Mancha region in Spain, 20 km west of the city of Albacete. The experimental farm of Las Tiesas (also known as Barrax site) is located in a dryland area of which about 35% is used for irrigated agriculture, the remainder is either bare land or used for extensive, rain fed agriculture. The experimental farm is located on a (flat) plateau of about 700 m above mean sea level. The ground water level is about 20-30 m below
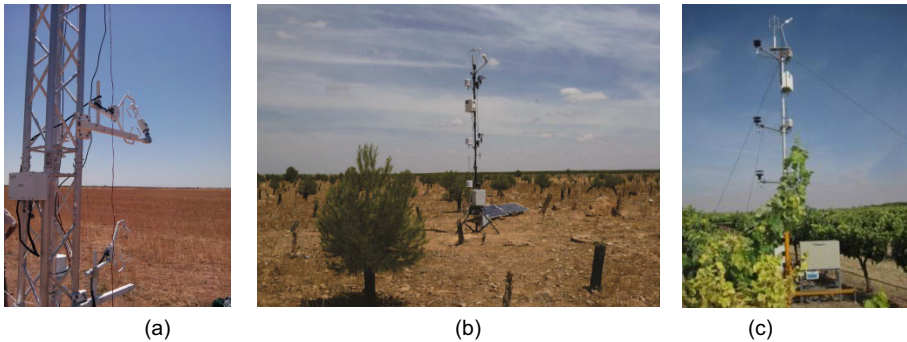
Fig. 1. Photographs of the three stations: (a) camelina field, (b) reforestation, and (c) vineyard.

Table 1

Instrumentation used at the three flux tower sites

Site name coordinates (WGS84)	Camelina 39.04109°N 2.08246°W	Reforestation 39.05975°N 2.08708°W	Vineyard 39.0598°N 02.2.1009°W
Dataloggers	CR5000, CR800 (Campbell Sci. Inc., USA) HOBO temperature dataloggers (Onset, USA) Degacon datalogger	CR23X, CR3000 (Campbell Sci. Inc., USA)	Fit-PC (EC), CR3000 with AM16/32 and AM25T multiplexers (Campbell Sci. Inc., USA)
Radiometers	CNR1 four component (Kipp and Zonen, Delft, Netherlands)	IRTS Apogee infrared temperature sensor	ThermoHygrometer (Thies Clima) at 2.50, 3.50, and 5.00 m height
Air temperature and relative humidity	CS215 (Campbell Sci. Inc., USA) at 1.20, 2.20, and 4.10 m height	CS215 (Campbell Sci. Inc., USA) at 1.45, 2.50, and 4.00 m height	2D Wind Sonic (Gill) at 2.50, 3.50, and 5.00 m height
Wind speed	Gill 2D at 5.20 m height	Cup anemometers Gill at 1.45, 2.50, and 4.00 m height	R3-50 (Gill) at 5.7 m height
Sonic anemometers	CSAT3 (Campbell Sci. Inc., USA) at 2.38 and 1.30 m height. Azimuth: 165° from N	Young 81000 at 5.00 m height (top of mast)	Sonic anemometer Young 81000 (top of mast)
Gas analysers	LI7500 at 2.38 m height	LI7500 at 5.00 m height	LI7500 at 5.70 m height
Soil temperature	Onset soil temperature sensors at 1, 2, 4, 8, 16, and 32 cm depth		3x PT100 between 0 and 5 cm depth
Soil heat flux	Hukseflux (HFP01) at 8 and 13 cm depth	Hukseflux (HFP01) at 10 cm depth	Hukseflux (HFP01) at 2 cm depth
Soil moisture content	Degacon soil moisture sensors	CS616 at 10 cm depth	

the surface (Su *et al.* 2008). The three eddy covariance sites (Fig. 1) were located less than 2 km apart (see Timmermans *et al.* 2014), but in rather different land cover types (Table 1): a senescent camelina (*Camelina sativa*) field (0.5 m height), a reforestation plantation (bare soil and sparse trees of 1 to 3 m height), and a drip irrigated vineyard (about 1.8 m heigh).

2.1 Climate

The climate is Mediterranean (Köppen classification: Csa); the monthly average temperatures range from 11 °C (January) to 25 °C (July), and the mean annual rainfall is 400 mm. April, May, October, and November are the wettest months (~40-50 mm rainfall per month), and July and August the driest (~15 mm rainfall per month). The wind direction during the field campaign was predominantly southeast (Fig. 2). Mid-day air temperatures ranged from 31 to 38 °C, and night temperatures from 14 and 19 °C. The wind speed at 2.38 m height varied from 0.2 to 6.7 m s^{-1}, and the mean and standard deviations of wind speed were 3.0 and 1.6 m s^{-1}, respectively. The relative humidity ranged from 6% (midday) to 96% (night).
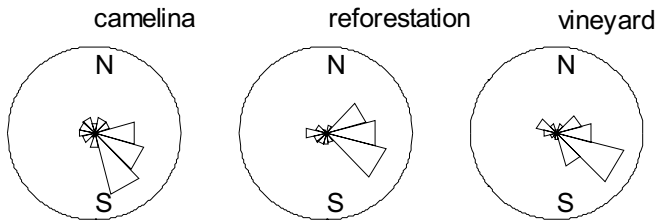
Fig. 2. Rose diagrams of wind direction at the three eddy covariance sites during the REFLEX campaign.

2.2 Instrumentation

At the three flux tower sites, the turbulent heat exchange, net radiation, and ground heat flux were estimated from measurements with the equipment listed in Table 1. Comparable equipment was used at each site. At each station, an eddy covariance system with 3-D sonic anemometer and gas analyser was installed. The dataloggers at the flux stations were programmed to collect the eddy covariance data at 20 Hz. The raw data were stored at the vineyard and camelina sites, while processed data were stored at the reforestation site. All other measurements were carried out at 0.2 Hz, and 1-minute averages were stored.

Wind speed, temperature, and relative humidity were measured at three or four heights above the surface at the flux tower sites. The sonic anemometers were installed at the top of the tower in the reforestation and vineyard

site, and at the south side of the tower at the camelina site (due to a different tower construction and mounting system). The gas analyser was located 20 cm northwest of the sonic anemometer at the camelina site, about 15 cm south at the reforestation site, and about 15 cm north at the vineyard site (see Fig. 1). The instrumentation at the camelina site was most complete. For this reason, the camelina site has been used for detailed analysis of the individual energy balance components.

3.   METHODOLOGY

3.1 Turbulent heat fluxes and surface roughness

The turbulent heat fluxes (H and λE) were calculated with the software Alt-Eddy (Alterra, WUR, Netherlands), ver. 3.71 (http://www.climatexchange.nl/projects/alteddy/) for the camelina and vineyard sites. The wind vector was double rotated for each averaging interval separately: horizontally rotated into the main wind direction (first rotation) and vertically (second rotation) so that average lateral and vertical wind speeds were zero. Furthermore, the following corrections were performed: de-spiking, 2-D axis rotation, WPL (Webb *et al.* 1980) correction, SND (Schotanus *et al.* 1983) correction, and a frequency response correction. The exact formulation for the frequency response correction as applied in AltEddy was not known, but for comparison Eqs. 11-13 in Horst (1997) were applied manually using the sampling frequency of 20 Hz, measurement height, wind speed, and Monin–Obukhov length as input. Due to the high measurement frequency and the low wind speed, the frequency response losses were small (around 2%). Tests for steady state within each averaging interval and integral turbulence characteristics have been carried out (Foken *et al.* 2005), and an overall quality flag was assigned according to Table 9.5 therein. Fluxes with an overall quality flag higher than 3 were rejected. In this way it was ensured that only data of high quality were included in the analysis, but this was still the majority of the half-hourly measurements in the time series.

At the reforestation site, flux calculations were carried out on the datalogger and the results stored immediately following the measurements due to limited data storage capacity for raw data. These flux calculations were carried out with the PEC software (Corbari *et al.* 2012) which has been developed for real time average data management. The same corrections as for the camelina site were carried out. A comparison between corrected fluxes from high frequency and from 30 min average data at a different site, notably a maize field in Italy, showed that low errors could be obtained with mean absolute daily difference of 6.1 W m^{-2} for H and 13.2 W m^{-2} for λE (Corbari, unpublished data).

The surface roughness was calculated from the sonic anemometer data for 30°-azimuthal classes by means of the following equation:

$$u = \frac{u_*}{k}\left[\ln\left(\frac{z-d}{z_{0m}}\right) - \Psi_m\left(\frac{z-d}{L}\right)\right] + \Psi_m\left(\frac{z_{0m}}{L}\right), \tag{1}$$

where u is the horizontal wind speed [m s^{-1}], u_* the friction velocity [m s^{-1}], $k = 0.41$ the von Kármán constant, z the measurement height [m], d the zero-displacement height [m], and Ψ_m is a stability correction function according to Paulson (1970). For unstable conditions:

$$\Psi_m = 2\ln\big((1+x)/2\big) + \ln\big((1+x^2)/2\big) - 2\arctan(x) + \pi/2 , \tag{2}$$

where (Dyer 1974):

$$x = 1 - 16\left(\frac{z}{L}\right)^{-0.25} . \tag{3}$$

For stable conditions:

$$\Psi_m = 1 + 5\frac{z}{L} . \tag{4}$$

The friction velocity was calculated as the square root of the covariance of measured vertical and horizontal wind speed, and d was assumed 2/3 of the canopy height for the camelina (a closed crop), and a rough estimate of d of 0.4 m was made based on Fig. 1 in Raupach (1994) for the other two stations (with sparse vegetation). The value of z_{0m} was calculated by minimizing the squared difference between measured (sonic anemometer) and calculated (Eq. 1) horizontal wind speed u. This minimization was carried out on data in 12 classes of wind direction of 30° each, in order to evaluate the roughness in different directions from the towers. This procedure was repeated for different values of d since d was estimated only roughly, but varying d resulted in only very small variations in the calculated z_{0m}.

The source areas of the fluxes were estimated following Hsieh *et al.* (2000) for main wind and Detto *et al.* (2006) for the lateral wind direction. These models require the surface roughness, main wind speed, u, and lateral wind speed, v, vector as input. The flux tower data and the estimated z_{0m} values have been used.

3.2 Soil heat flux

At the camelina site, six ground heat flux plates were installed, while only two were installed on the two other sites. Therefore, the analysis of the soil heat flux was carried out at the camelina site, where below-ground measurements were most elaborate. The soil thermal properties found at this site were thereafter used for the other sites as well, assuming equal thermal soil

properties for all sites, to convert soil heat flux from the measurement depth to the surface (soil types were visibly similar, and soil moisture in the topsoil was very low – around 10% at 10 cm depth, and less near the surface).

For the camelina site, the soil heat flux at the surface was calculated from temperature profile measurements at 6 depths below the surface radiometric surface temperature and the measured heat flux at 8 cm depth. The soil heat flux measured at 13 cm depth was used for validation. All soil temperature sensors were calibrated prior to the campaign.

The 10-day half hourly averaged soil temperature time series at 8 cm depth was fitted to a Fourier series with a number of harmonics of 1/7th of the number of data points. The soil temperatures measured at the other depths together with the radiometric soil temperature were used to tune the diffusivity D [m^2 s^{-1}], used in the thermal diffusion equation of de Vries (1963):

$$\frac{\partial T}{\partial t} = -D \frac{\partial^2 T}{\partial z^2} \tag{5}$$

by minimizing the quadratic difference between measured and modelled soil temperatures. The derivatives of the Fourier series were calculated analytically according to van der Tol (2012). The heat conductivity of the soil, κ [Wm^{-1} K^{-1}], was solved from

$$G = -\kappa \frac{\partial T}{\partial z} \tag{6}$$

by means of a linear regression of the vertical temperature gradient and the measured heat flux at 8 cm depth. Because it appeared that D and κ were not constant with depth (see results section), separate values for these two soil thermal properties were derived for the depth intervals between consecutive pairs of soil temperature measurements (e.g., 8-4, 4-2 cm depth, etc.), working upward and downward away from the 8 cm depth, in order to obtain a better estimate of the soil heat flux with depth, in particular at the surface.

The 10-day average soil temperatures consistently decreased with depth, revealing a downward, seasonal component of the soil heat flux. This seasonal heat flow could not be modelled with the harmonics for this relatively short time series of 10 days. For this reason, the observed 10-day mean values of soil temperature at each depth were subtracted from the observed soil temperatures, such that the soil temperatures corrected for seasonal heat flow had a zero mean at all depths. A similar normalization procedure was carried out to the measured heat fluxes: the 10-day mean soil heat flux was subtracted from the measurements at 8 cm depth prior to fitting the heat conductivity. The fitting procedure described above was applied to these normalized soil temperatures and heat fluxes. The measured 10-day means were added to the modelled temperature time series afterwards.

The heat flux at the surface obtained with the normalized temperatures lacks the seasonal component. The seasonal component was calculated separately from the 10-day average temperatures and heat conductivity using Eq. 3. As a further verification of this procedure, the calculated value of the seasonal heat flux component was compared to the 10-day average value of the measured heat flux at 8 cm depth.

3.3 Energy balance closure

The energy balance was evaluated by regression of $H + \lambda E$ *versus* $R_n - G$. The regression is only meaningful if there is no random error in the independent variable (Wilson *et al.* 2002). Although the random error in $R_n - G$ is probably lower than that in the turbulent heat fluxes, it is not zero. For this reason we also evaluated the EBR: the ratio of the cumulative $H + \lambda E$ over cumulative $R_n - G$.

Because the reforestation lacked a four component radiometer, incoming radiation from the camelina site was used, and airborne data were used to estimate albedo. Flights took place during the campaign, as described in Timmermans *et al.* (2014). The albedo of the reforestation was estimated from spectrally integrated (0.43-2.2 μm), atmospherically corrected reflectance measurements of the airborne hyperspectral scanner (AHS), a hyperspectral mapper in the optical and thermal domain on board of the aircraft. Upwelling longwave radiation was measured with the IRTS Apogee sensor.

3.4 Sensible and latent heat flux from vertical profiles

The temperature and relative humidity sensors used at the camelina site were calibrated against each other across the range of observed temperature and relative humidity values with linear regression. In two cases, second order polynomial fits were required to obtain a satisfactory inter-calibration. The calibration removed the bias and reduced the relative errors induced by differences in sensor sensitivities by 90% to less than 0.06 °C for T and 0.12% for RH for the CS215 sensors used at the camelina site. With this accuracy, S:N ratio of the vertical differences in temperature and humidity increases from approximately 0.5-2.5 to 5-25.

The sensible heat flux was estimated from pairs of temperature and wind speed data as:

$$H_{\text{profile}} = -\rho_a c_p k^2 \frac{\left(T(z_i) - T(z_j)\right) \cdot \left(u(z_k) - u(z_l)\right)}{\left[\ln\left(\frac{z_i}{z_j}\right) - \Psi_h\left(\frac{z_i}{L}\right) + \Psi_h\left(\frac{z_j}{L}\right)\right]\left[\ln\left(\frac{z_k}{z_l}\right) - \Psi_m\left(\frac{z_k}{L}\right) + \Psi_m\left(\frac{z_l}{L}\right)\right]}, \quad (7)$$

where ρ_a is the air density [kg m^{-3}], and c_p the heat capacity of the air [J kg^{-1} K^{-1}], both considered as constants; z_i and z_j are measurement heights of temperature less the zero plane displacement height d; and z_k and z_l measurement heights of wind speed minus d. The Obukhov length L was obtained from the processed eddy covariance data.

Latent heat flux was calculated from $H_{profile}$ with the Bowen ratio, Bo, (Bowen 1926):

$$E_{BR} = \frac{H_{profile}}{Bo} \quad , \qquad (8)$$

where Bo is calculated from the temperature and humidity measurements at two heights:

$$Bo = \frac{c_p}{\lambda} \frac{T(z_i) - T(z_j)}{q(z_i) - q(z_j)} \quad , \qquad (9)$$

where λ is the latent heat for evaporation [J kg^{-1}], and q the specific humidity [kg vapour kg^{-1} air], calculated from air temperature and relative humidity.

3.5 Sensible heat flux from radiometric temperature

Sensible heat flux from radiometric, T_r, and air temperature, H_{rad}, was also calculated with Eq. 4 after replacing $T(z_i)$ by the radiometric temperature T_r, z_i by the roughness height for heat, z_{0h}, and z_k by the roughness height for momentum, z_{0m}. The unknown value of z_{0h} was calibrated by tuning the value of $\ln(z_{0m}/z_{0h})$ to match calculated sensible heat flux with the eddy covariance estimate of sensible heat flux (Stewart et al. 1994).

4. RESULTS

4.1 Surface roughness

The roughness length at the flux stations appeared to peak in some specific upwind directions compared to other directions. This was the case at all three flux stations, but the directions in which the peaks occur differed among the sites (Fig. 3). In all cases, the peaks coincided with the position of the gas analyser relative to the sonic anemometer, suggesting that the instrument influenced the roughness estimates by increasing its values. This suggestion is supported by a comparison of the roughness calculated from the measurements of the two sonic anemometers at the camelina site, one without and one with an gas analyser in the vicinity. The roughness length calculated from the anemometer data with gas analyser showed a peak in the direction of the gas analyser (northwest of the anemometer), while the roughness length from the anemometer data without gas analyser did not show this
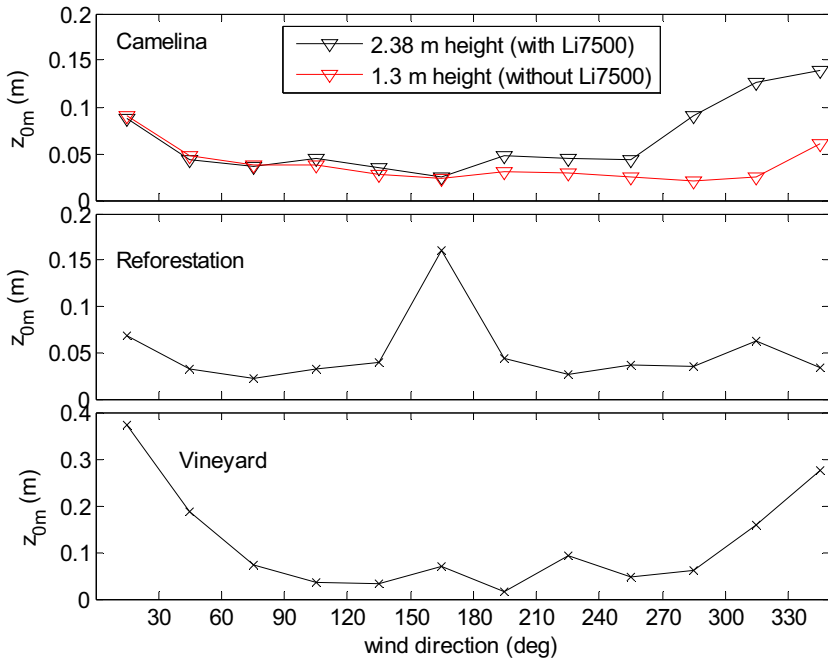
Fig. 3. Variation of roughness length for momentum z_{0m} around the measurement towers with wind direction. LiCor gas analyser positions were: 300° (camelina), 170° (reforestation), and 0° (vineyard).
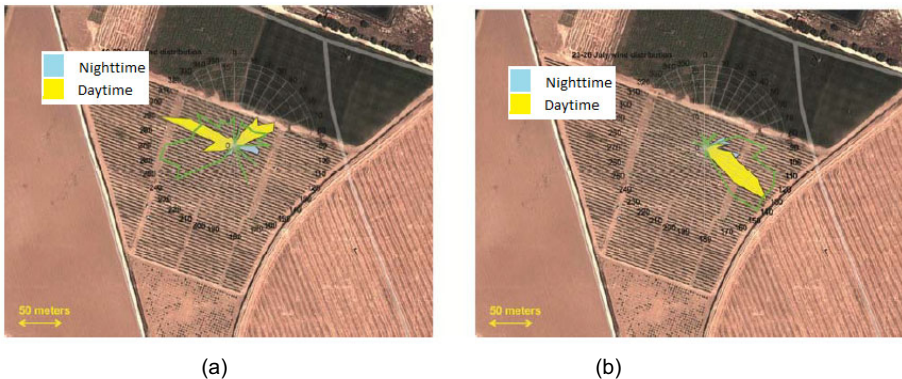
Fig. 4. Wind conditions at the vineyard site during the campaign. In the period from 19 to 22 July (panel a) daytime wind speed was between 1.5 and 3.0 m/s during 90% of the time, whereas in the second period from 23 to 26 July (panel b) daytime wind speed was higher than 5 m/s during 90% of the time. Prevailing wind directions in the first period were from the north, in the second period from the southeast.

peak. At the camelina site, there is also evidence for a wind shadow caused by the tower: the roughness length appeared higher for wind from the north. Hence, data contaminated by the disturbance of the measured turbulence by the gas analyser and tower were excluded from further analysis.

The situation at the vineyard site is more complicated than at the camelina site, because of the smaller fetch and the orientation of the grape vines in rows (Fig. 4). The airborne color composite in Fig. 4 shows the orientation of the rows from WNW to ESE, and a relatively small fetch in the north direction of 50 m compared to >100 m in other directions. The higher roughness in the north direction (300-60°) suggests that the contrast between the grass field and the vineyard is responsible for the higher roughness in this direction.

4.2 Energy balance closure

Time series of measurements of the three flux stations are shown in Fig. 5. At the reforestation and camelina sites, sensible heat flux was relatively high and latent heat flux low, except for the last 24 hours (DOY 209 to 210), when a rainstorm occurred. At that time, only the camelina station was still operational. Evaporation peaked in the night following the rainstorm, at the expense of negative sensible and soil heat fluxes.
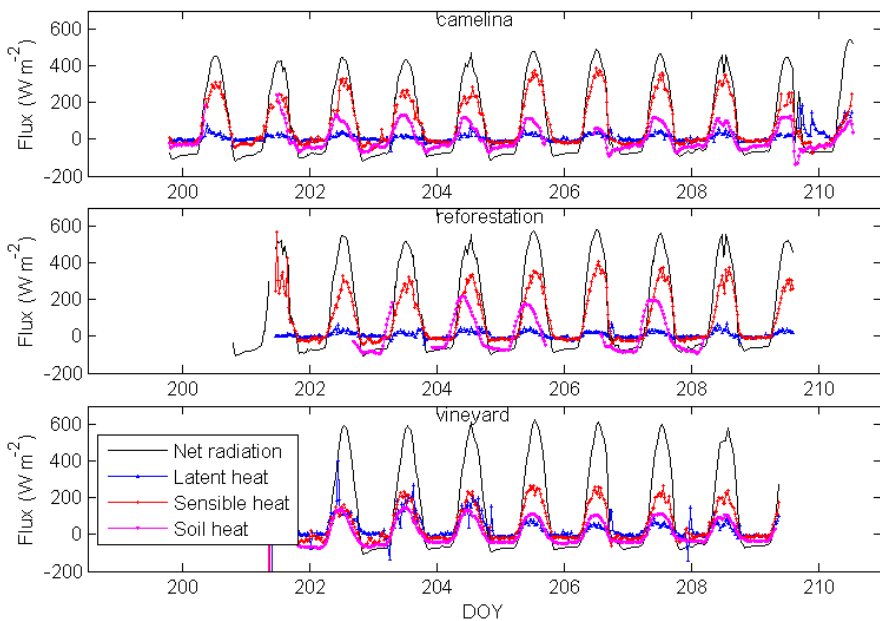
Fig. 5. Thirty-min interval net radiation R_n, ground heat flux G, and turbulent heat fluxes (H and λE) *versus* day of year (DOY) for the three flux stations.
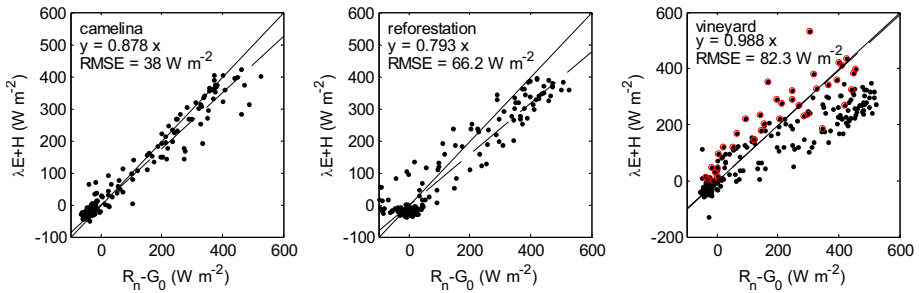
Fig. 6. Thirty-min interval turbulent heat fluxes (*H* and *λE*) *versus* available energy $(R_n - G)$ for the three flux station sites, with 1:1 lines (solid), and linear regressions forced through the origin (dashed). For the vineyard site, all data are shown (black dots) as well data with an 80% upwind footprint area completely within the vineyard (red circles; ~10% of the data): less than 200 m upwind distance and wind direction from 30 to 330°. RMSE and slope were calculated for the footprint areas completely in the vineyard.
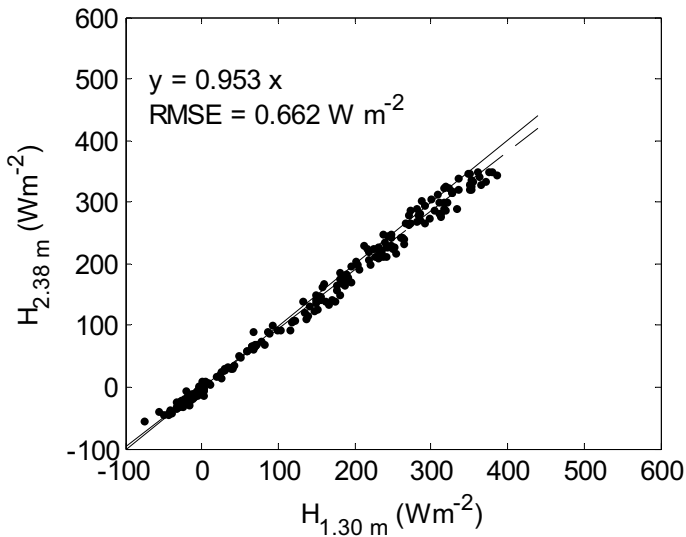
Fig. 7. Comparison of the sensible heat flux measured at the camelina site at two heights, with 1:1 line (solid) and linear regression (dashed).

The overall energy balance closure was 88, 79, and 99% at the camelina, reforestation and vineyard sites, respectively, based on regression of $H - \lambda E$ *versus* $R_n - G_0$, while the EBRs were 1.05, 0.91, and 0.73. The RMSE was 38, 66, and 83 Wm^{-2} for the half-hourly values of $R_n - H - \lambda E - G_0$ (Fig. 6). The contrasting result for the regression (99% closure) and EBR (73% closure) for the vineyard site is due to the low number of data points (41) in-

cluded. Data with wind directions between 330 and 30° were rejected, as well as data with an 80% upwind footprint area exceeding 200 m. This resulted in 90% of the data being excluded from the calculation. For the camelina and reforestation sites, only the data that were affected by the position of the gas analyser were rejected. At these sites, the 80% footprint area did not extend beyond the field except for a few occasions during stable night-time conditions. At the camelina site, two sonic anemometers were present, at 1.30 and at 2.38 m height, which provided similar results (Fig. 7).

4.3 Soil heat flux

Calibration of the soil heat flux model to the temperature profile and heat flux measurements at the camelina site resulted in a soil heat diffusivity D of $0.273 \times 10^6 \, \mathrm{m^2 \, s^{-1}}$, heat conductivity κ of $0.359 \, \mathrm{W m^{-1} \, K^{-1}}$, and volumetric heat capacity c_p of $1.32 \times 10^6 \, \mathrm{J m^{-3} K^{-1}}$; the latter value corresponds to a volumetric soil moisture content of 6 at 40% porosity, following de Vries (1963).

An evaluation of the modelled temperature profile indicated that these thermal properties could not have been constant with depth. With a single value for D and another for κ fitted for the entire soil profile (0-32) cm, the temperature curves for the top 4 cm could not be reproduced: the model overestimates the phase shift and underestimates the amplitude shift. Fitting the thermal properties separately for each pair of sensors at consecutive depth improved the correspondence of measured and modeled temperature (Fig. 8), and, more importantly, led to a more realistic phase of the ground heat flux diurnal cycle while the amplitude was hardly affected by vertically changing thermal properties. The resulting thermal conductivity in the upper 1 cm was an order of magnitude higher and the heat capacity an order of magnitude lower than that deeper in the soil. The RMSE of the closure term was reduced by $16 \, \mathrm{W m^{-2}}$ when the soil thermal properties were varied with depth.

It should be noted that the radiometric surface temperatures had a diurnal amplitude equal to that at 1 cm depth, and midday values that were sometimes lower than those at 1 cm depth. One would expect the opposite: a higher amplitude and consistently higher daytime temperatures at the surface. An error in the emissivity value of 0.945, tuned to match the 10-day mean radiometric temperature and the 10-day mean of the temperature at 1 cm depth, could not explain the difference in amplitude. The most obvious explanation for the relatively low amplitude is the fact that radiometric temperature includes contributions from the vegetation, which was exposed to turbulence in the vegetation layer and which is affected by cooling due to transpiration (although the latent heat flux was low the crop was senescent).
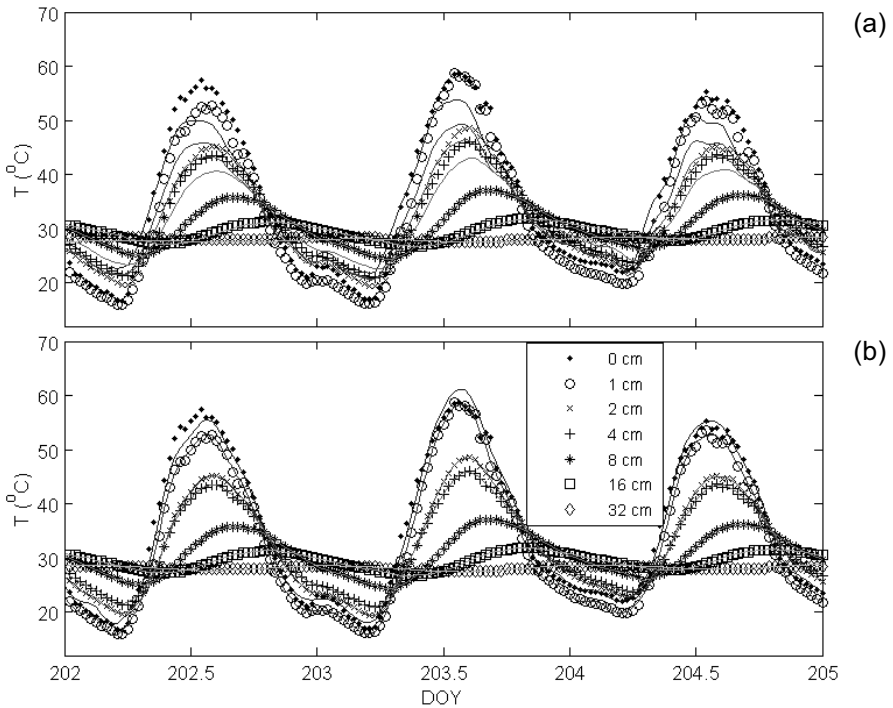
Fig. 8. Measured (symbols) and modelled (lines) time series of soil temperature at the camelina site for part of the measurement campaign, with constant thermal properties with depth (a), and with thermal properties that varied with depth (b).

4.4 Turbulent heat fluxes from temperature, humidity, and wind profiles

Although vertical differences in air temperature were low at the camelina site (Fig. 9), they were large enough to estimate sensible heat flux (Eq. 7) and latent heat flux (Eq. 8). For temperature and humidity, the heights of 2.20 and 1.20 m were used, closest to the wind speed, and friction velocity measurements at 1.35 and 2.58 m height. Modelled H and λE match well with observations (RMSE of 60 and 38 $W\,m^{-2}$, respectively), even during the last 24 hours of the measurement period in which rainfall occurred (Figs. 10 and 11).

Of particular importance are the terms Ψ_h and Ψ_m in Eq. 7 for stability. Omitting these terms (*i.e.*, assuming neutral conditions) would result in a RMSE of 90 $W\,m^{-2}$ for the sensible heat flux, and a slope of the linear regression between measured and modelled H of 1.8 (*i.e.*, underestimate of sensible heat flux) due to very unstable conditions at the camelina site. Here the functions Ψ_h and Ψ_m had been obtained from the eddy covariance data of

(a)

(b)

(c)

(d)
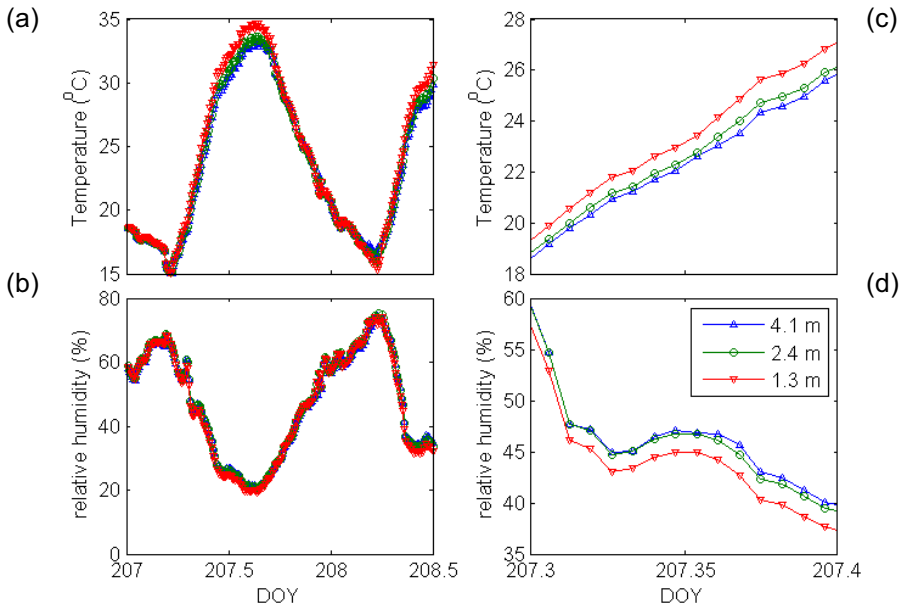
Fig. 9. Air temperature (a, c) and relative humidity (b, d) profiles at the camelina site during the day of overpass (a, b), and zoomed in for the hours of the overpass.

(a)

(b)
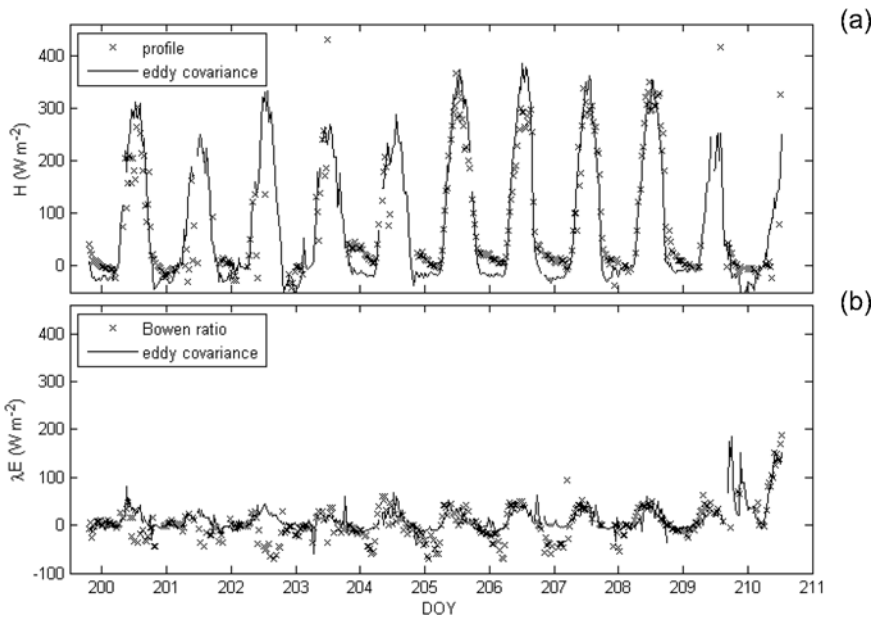
Fig. 10. Profile (Eq. 7) modelled sensible heat flux (a) and Bowen ratio derived latent heat flux (b) at the camelina site *versus* day of the year 2012, both with their equivalents derived from eddy covariance and gas exchange measurements directly.
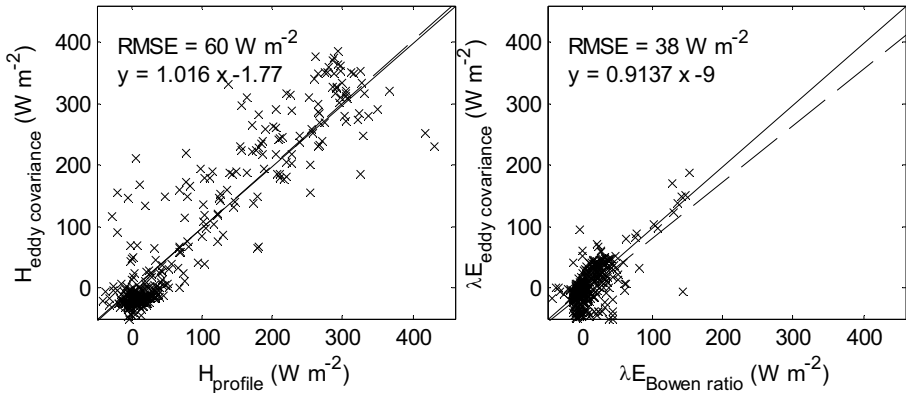
Fig. 11. The data of Fig. 10 presented as scatter plots, with 1:1 line (solid) and linear regression (dashed).

friction velocity and stability. These two variables can also be obtained iteratively from modelled H and the temperature and wind profiles. Doing so results in a RMSE of H of 64 W m^{-2}, somewhat higher than using the eddy covariance data, but much better than when omitting the stability corrections.

During most of the nights, the profile data show negative H, which is in agreement with the eddy covariance estimates. In four warmest nights (DOY 204 to 207), the temperature profile was reversed: the highest temperatures at the lowest level (1.3 m) and the lowest temperature at the highest level (4.3 m), which would mean that unstable conditions and positive H continued during the night. The eddy covariance estimates of H were nevertheless negative during these nights. It should be noted that during these relatively warm nights, the temperature differences between the sensors were as low as 0.1 °C, while the measurement error was up to 0.06 °C.

Applying the same procedure to the reforestation and vineyard sites (not shown) resulted in RMSE of sensible heat flux of 277 and 242 W m^{-2}, respectively. These much higher errors are related to both the lower signal to noise ratio of the data (the sensors were not inter-calibrated), and the fact that the temperature profiles may be affected by advection.

4.5 Sensible heat flux from radiometric surface temperature

The sensible heat flux calculated from radiometric temperature varied widely with the value of the parameter $kB^{-1} = \ln(z_{0m}/z_{0h})$, where B is the Stanton number at the camelina site. At the value $kB^{-1} = 17$, the RMSE of modelled H had a minimum, and eddy covariance sensible heat flux was well reproduced (Fig. 12), but at values of kB^{-1} below 10, the RMSE quickly rose to
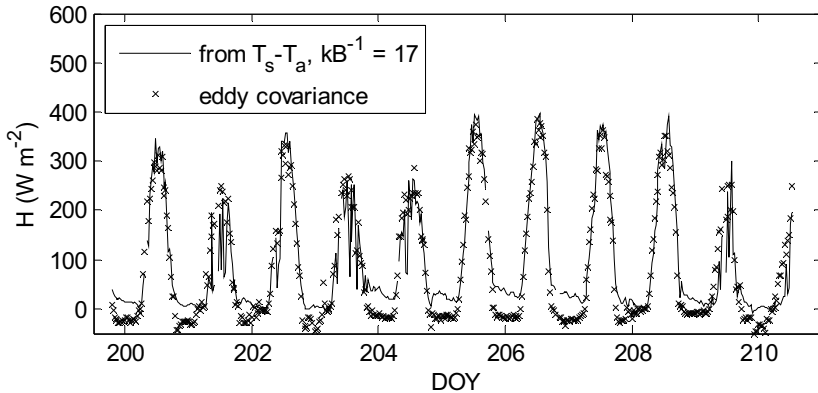
Fig. 12. Time series of sensible heat flux calculated from the difference between radiometric surface temperature and air temperature (symbols) and eddy covariance derived sensible heat flux at the camelina site.
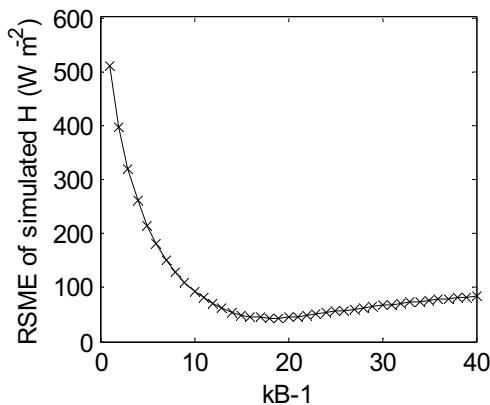
Fig. 13. Effect of the parameter kB^{-1} on the RMSE of simulated heat fluxes at the camelina site, for the whole time series of the experiment.

unrealistic values (Fig. 13). The parameter kB^{-1}, first introduced by Owen and Thomsom (1963), is known to vary, especially in areas with partial vegetation cover: Stewart *et al.* (1994) found values between 3.5 and 12.5 for grass, forest, rocks, and savannah sites, all in arid regions. Verhoef *et al.* (1997) found a similar range for savannahs in Africa. They argued that kB^{-1} is not only difficult to estimate, but that even the approach of extrapolating the temperature profile to the radiometric surface temperature is questionable. Physically based models are able to capture the full range of kB^{-1} values (Massman 1999, Su *et al.* 2001). These models require knowledge of the drag and heat transfer coefficients of leaves. Reproducing the high value of

kB^{-1} of 17 with the model of Massman (1999) requires an exceptionally low heat transfer coefficient of the leaf. The parameter kB^{-1} may also vary with time (Yang *et al.* 2003), but in the present study with fairly constant weather conditions and soil moisture, the sensible heat fluxes could be reproduced well with a single value for kB^{-1}.

4.6 Effects of a rainfall event

A rainfall event (including hail) of 14.1 mm on the last day of the measurement campaign (evening of DOY 209) caused some interesting features in the time series. For example, the radiometric surface temperature at the camelina site dropped by 30 °C within half an hour to a value below air temperature. The rain event was followed by high night-time evaporation rates that varied concomitant with wind speed. The energy for evaporation was partly supplied by negative sensible and soil heat fluxes (soil thermal properties obviously changed during the rainfall event, but they could not be calibrated for periods shorter than a day), leaving a relatively small energy balance closure gap (~30 W m^{-2}, see Fig. 14).
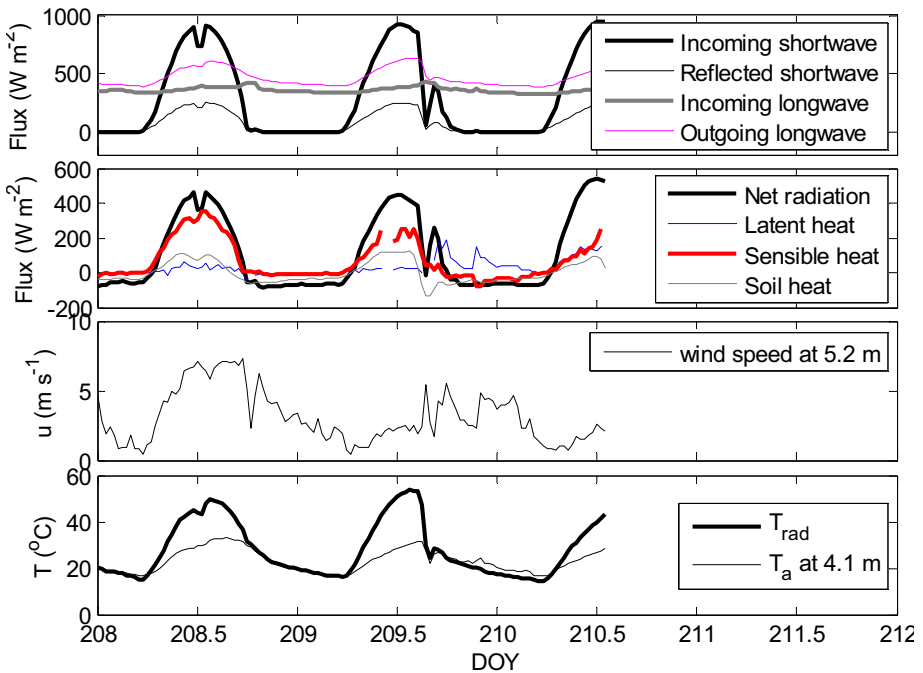
Fig. 14. Time series of radiation components, heat fluxes, wind speed and radiometric surface, and air temperature (at the camelina site on the day before the rainfall event, the day of the rainfall event, and the day following the rainfall event).

5. DISCUSSION

The energy balance closure gap was smallest in the most homogeneous site (camelina), and largest in the most heterogeneous site with limited fetch (vineyard). The closure gap in the camelina site is small compared to most published values (*e.g.*, Wilson *et al.* 2002, Foken 2008), and too small to identify its source. Obvious factors that are known to adversely affect the energy balance (Foken 2008, Liebethal *et al.* 2005) have been ruled out at this site: (i) the calculation of ground heat flux at the surface, (ii) application of frequency response correction of the turbulent fluxes, and (iii) calibration of the radiometer. We considered including heat storage in the vegetation and air layer up to the level of the sensors in the energy balance equation, but calculated heat storage changes appeared to be negligible due to the low biomass and low measurement height. The remaining errors in closure could be due to measurement or representation errors of the turbulent heat fluxes. The EBR suggested a small overestimate of the turbulent fluxes, whereas the linear regression of half hourly estimates suggested a small underestimate. Frank *et al.* (2013) recently showed that the sonic anemometer that was used (CSAT3), due to its design, may underestimate vertical wind speed and thus sensible heat flux by 8%. Although their study was carried out over forest, we could not exclude the possibility that our sensible heat fluxes are underestimated as well.

The small energy balance closure gap at the camelina site gives confidence in the flux tower data. Moreover, the calculated 80% source area of the fluxes did not extend beyond the edges of the camelina field for either of the two measurement heights (not shown) except for a small number of night-time cases, only two of which included an irrigated field. Moreover, the sensible heat flux measurements at both heights were almost equal (Fig. 7). This confirms that the measurements represent the local fluxes for the camelina site. Nevertheless, we cannot rule out that larger scale thermally induced circulations contributed to the locally measured flux. At larger spatial scale, both in horizontal and vertical direction, we expect large eddies to contribute to the advection and circulation of heat due to strong contrasts in vegetation cover, soil moisture, and surface temperatures. The measurements at the camelina site were carried out in a field with nearby irrigated plots, which could cause such mesoscale eddies and a non-zero stationary vertical wind speed (*e.g.*, Foken 2008, Eder *et al.* 2015). The average uncorrected vertical wind speed over the entire period was 4 $cm^2 s^{-1}$ in upward direction, which indicates that the site had either convective rising, or that the anemometer was slightly misaligned.

At the vineyard site, a more detailed footprint calculation is required to obtain local surface fluxes. A first analysis showed that in 90% of the half-

hourly intervals, the 80% upwind footprint area included other fields. In the first 5 days of the measurement campaign, the wind was predominantly from the north and the flux footprint extended to an adjacent irrigated grass field. In calculating energy balance statistics, these data were excluded. Another problem of the footprint calculation is that the models that were used are not valid for footprints that have a variable roughness in space.

At the camelina site, sensible and latent heat flux could accurately be reproduced with the wind profile in combination with Bowen ratios. This was not the case at the reforestation and vineyard sites, where gradients were not always consistent with eddy covariance fluxes (even if considering larger uncertainty in the data due to the fact that the sensors in the vertical profiles at these sites were not inter-calibrated). This indicates that the fluxes at these two sites were not only local fluxes.

The sensible heat flux at the camelina site could be accurately reproduced from the difference between radiometric surface temperature and air temperature, but only when using a considerable excess resistance for heat, kB^{-1}, higher than most reported values (Gökmen *et al.* 2012). The lack of a physical basis for the roughness height for heat z_{0h} makes it a tuning parameter.

References

Bowen, I.S. (1926), The ratio of heat losses by conduction and by evaporation from any water surface, *Phys. Rev.* **27**, 6, 779-787, DOI: 10.1103/PhysRev.27.779.

Cleugh, H.A., R. Leuning, Q. Mu, and S.W. Running (2007), Regional evaporation estimates from flux tower and MODIS satellite data, *Remote Sens. Environ.* **106**, 3, 285-304, DOI: 10.1016/j.rse.2006.07.007.

Corbari, C., D. Masseroni, and M. Mancini (2012), Effetto delle correzioni dei dati misurati da stazioni eddy covariance sulla stima dei flussi evapotraspirativi, *Ital. J. Agrometeorol.* **1**, 35-51 (in Italian).

de Vries, D.A. (1963), Thermal properties of soils. **In:** W.R. van Wijk (ed.), *Physics of Plant Environment*, North-Holland Publ. Co., Amsterdam.

Detto, M., N. Montaldo, J.D. Albertson, M. Mancini, and G. Katul (2006), Soil moisture and vegetation controls on evapotranspiration in a heterogeneous Mediterranean ecosystem on Sardinia, Italy, *Water Resour. Res*. **42**, 8, W08419, DOI: 10.1029/2005WR004693.

Dyer, A.J. (1974), A review of flux-profile relationships, *Bound.-Lay. Meteorol*. **7**, 3, 363-372, DOI: 10.1007/BF00240838.

Eder, F., M. Schmidt, T. Damian, K. Träumner, and M. Mauder (2015), Mesoscale eddies affect near-surface turbulent exchange: evidence from lidar and tower measurements, *J. Appl. Meteorol. Clim.* **54**, 1, 189-206, DOI: 10.1175/JAMC-D-14-0140.1.

Foken, T. (2008), The energy balance closure problem: An overview, *Ecol. Appl.* **18**, 6, 1351-1367, DOI: 10.1890/06-0922.1.

Foken, T., M. Göckede, M. Mauder, L. Mahrt, B. Amiro, and W. Munger (2005), Post-field data quality control. **In:** X. Lee, W. Massman, and B. Law (eds.), *Handbook of Micrometeorology*, Atmospheric and Oceanographic Sciences Library, Vol. 29, Springer Netherlands, 181-208, DOI: 10.1007/1-4020-2265-4_9.

Frank, J.M., W.J. Massman, and B.E. Ewers (2013), Underestimates of sensible heat flux due to vertical velocity measurement errors in non-orthogonal sonic anemometers, *Agr. Forest Meteorol*. **171-172**, 72-81, DOI: 10.1016/j.agrformet.2012.11.005.

Gash, J.H.C. (1987), An analytical framework for extrapolating evaporation measurements by remote sensing surface temperature, *Int. J. Remote Sens.* **8**, 8, 1245-1249, DOI: 10.1080/01431168708954769.

Gökmen, M., Z. Vekerdy, A. Verhoef, W. Verhoef, O. Batelaan, and C. van der Tol (2012), Integration of soil moisture in SEBS for improving evapotranspiration estimation under water stress conditions, *Remote Sens. Environ*. **121**, 261-274, DOI: 10.1016/j.rse.2012.02.003.

Hsieh, C.I., G. Katul, and T.W. Chi (2000), An approximate analytical model for footprint estimation of scalar fluxes in thermally stratified atmospheric flows, *Adv. Water Res.* **23**, 7, 765-772, DOI: 10.1016/S0309-1708(99)00042-1.

Horst, T.W. (1997), A simple formula for attenuation of eddy fluxes measured with first-order-response scalar sensors, *Bound.-Lay. Meteorol*. **82**, 2, 219-233, DOI: 10.1023/A:1000229130034.

Kalma, J.D., T.R. McVicar, and M.F. McCabe (2008), Estimating land surface evaporation: A review of methods using remotely sensed surface temperature data, *Surv. Geophys.* **29**, 4-5, 421-469, DOI: 10.1007/s10712-008-9037-z.

Kustas, W.P., and J.M. Norman (1996), Use of remote sensing for evapotranspiration monitoring over land surfaces, *Hydrol. Sci. J.* **41**, 4, 495-516, DOI: 10.1080/02626669609491522.

Kustas, W.P., K.S. Humes, J.M. Norman, and M.S. Moran (1996), Single- and dual-source modeling of surface energy fluxes with radiometric surface temperature, *J. Appl. Meteorol. Clim.* **35**, 1, 110-121, DOI: 10.1175/1520-0450(1996)035<0110:SADSMO>2.0.CO;2.

Liebethal, C., B. Huwe, and T. Foken (2005), Sensitivity analysis for two ground heat flux calculation approaches, *Agr. Forest Meteorol.* **132**, 3-4, 253-262, DOI: 10.1016/j.agrformet.2005.08.001.

Massman, W.J. (1999), A model study of kB_H^{-1} for vegetated surfaces using 'localized near-field' Lagrangian theory, *J. Hydrol.* **223**, 1-2, 27-43, DOI: 10.1016/S0022-1694(99)00104-3.

Owen, P.R., and W.R. Thomson (1963), Heat transfer across rough surfaces, *J. Fluid Mech.* **15**, 3, 321-334, DOI: 10.1017/S0022112063000288.

Paulson, C.A. (1970), The mathematical representation of wind speed and temperature profiles in the unstable atmospheric surface layer, *J. Appl. Meteorol. Clim.* **9**, 6, 857-861, DOI: 10.1175/1520-0450(1970)009<0857:TMROWS>2.0.CO;2.

Raupach, M.R. (1994), Simplified expressions for vegetation roughness length and zero-plane displacement as functions of canopy height and area index, *Bound.-Lay. Meteorol.* **71**, 1-2, 211-216, DOI: 10.1007/BF00709229.

Schotanus, P., F.T.M. Nieuwstadt, and H.A.R. de Bruin (1983), Temperature measurement with a sonic anemometer and its application to heat and moisture fluxes, *Bound.-Lay. Meteorol.* **26**, 1, 81-93, DOI: 10.1007/BF00164332.

Stewart, J.B., W.P. Kustas, K.S. Humes, W.D. Nichols, M.S. Moran, and H.A.R. de Bruin (1994), Sensible heat flux-radiometric surface temperature relationship for eight semiarid areas, *J. Appl. Meteorol. Clim.* **33**, 9, 1110-1117, DOI: 10.1175/1520-0450(1994)033<1110:SHFRST>2.0.CO;2.

Su, Z., T. Schmugge, W.P. Kustas, and W.J. Massman (2001), An evaluation of two models for estimation of the roughness height for heat transfer between the land surface and the atmosphere, *J. Appl. Meteorol. Clim.* **40**, 11, 1933-1951, DOI: 10.1175/1520-0450(2001)040<1933:AEOTMF>2.0.CO;2.

Su, Z., W. Timmermans, A. Gieske, L. Jia, J.A. Elbers, A. Olioso, J. Timmermans, R. van der Velde, X. Jin, H. van der Kwast, F. Nerry, D. Sabol, J.A. Sobrino, J. Moreno, and R. Bianchi (2008), Quantification of land–atmosphere exchanges of water, energy and carbon dioxide in space and time over the heterogeneous Barrax site, *Int. J. Remote Sens.* **29**, 17-18, 5215-5235, DOI: 10.1080/01431160802326099.

Timmermans, W.J., G. Bertoldi, J.D. Albertson, A. Olioso, Z. Su, and A.S.M. Gieske (2008), Accounting for atmospheric boundary layer variability on flux estimation from RS observations, *Int. J. Remote Sens.* **29**, 17-18, 5275-5290, DOI: 10.1080/01431160802036383.

Timmermans, W.J., C. van der Tol, J. Timmermans, M. Ucer, X. Chen, L. Alonso, J. Moreno, A. Carrara, R. Lopez, F. de la Cruz Tercero, H.L. Corcoles, E. de Miguel, J.A.G. Sanchez, I. Pérez, B. Franch, J.-C.J. Munoz, D. Skokovic, J. Sobrino, G. Soria, A. MacArthur, L. Vescovo, I. Reusen, A. Andreu, A. Burkart, C. Cilia, S. Contreras, C. Corbari, J.F. Calleja, R. Guzinski, C. Hellmann, I. Herrmann, G. Kerr, A.-L. Lazar, B. Leutner, G. Mendiguren, S. Nasilowska, H. Nieto, J. Pachego-Labrador, S. Pulanekar, R. Raj, A. Schikling, B. Siegmann, S. von Bueren, and Z.B. Su (2015), An overview of the Regional Experiments for Land-atmosphere Exchanges 2012 (REFLEX 2012) campaign, *Acta Geophys.* **63**, 6, 1465-1484, DOI: 10.2478/s11600-014-0254-1 (this issue).

van der Tol, C. (2012), Validation of remote sensing of bare soil ground heat flux, *Remote Sens. Environ*. **121**, 275-286, DOI: 10.1016/j.rse.2012.02.009.

Verhoef, A., H.A.R. de Bruin, and B.J.J.M. van den Hurk (1997), Some practical notes on the parameter kB^{-1} for sparse vegetation, *J. Appl. Meteorol. Clim.* **36**, 5, 560-572, DOI: 10.1175/1520-0450(1997)036<0560:SPNOTP>2.0. CO;2.

Webb, E.K., G.I. Pearman, and R. Leuning (1980), Correction of flux measurements for density effects due to heat and water vapour transfer, *Quart. J. Roy. Meteorol. Soc.* **106**, 447, 85-100, DOI: 10.1002/qj.49710644707.

Wilson, K., A. Goldstein, E. Falge, M. Aubinet, D. Baldocchi, P. Berbigier, C. Bernhofer, R. Ceulemans, H. Dolman, C. Field, A. Grelle, A. Ibrom, B.E. Law, A. Kowalski, T. Meyers, J. Moncrieff, R. Monson, W. Oechel, J. Tenhunen, R. Valentini, and S. Verma (2002), Energy balance closure at FLUXNET sites, *Agr. Forest Meteorol.* **113**, 1-4, 223-243, DOI: 10.1016/ S0168-1923(02)00109-0.

Yang, K., T. Koike, and D. Yang (2003), Surface flux parameterization in the Tibetan Plateau, *Bound.-Lay. Meteorol.* **106**, 2, 245-262, DOI: 10.1023/ A:1021152407334.

Influence of Component Temperature Derivation from Dual Angle Thermal Infrared Observations on TSEB Flux Estimates Over an Irrigated Vineyard

Ana ANDREU[1], Wim J. TIMMERMANS[2], Drazen SKOKOVIC[3],
and Maria P. GONZALEZ-DUGO[4]

[1]Instituto de Investigación y Formación Agraria y Pesquera (IFAPA),
Cordoba, Spain; e-mail: ana.andreu.mendez@juntadeandalucia.es

[2]University of Twente, Faculty of Geo-information Science and Earth Observation,
Department of Water Resources, Enschede, The Netherlands;
e-mail: w.j.timmermans@utwente.nl

[3]Global Change Unit (GCU), Department of Earth Physics, University of Valencia,
Valencia, Spain; e-mail: drazen.skokovic@uv.es

[4]Instituto de Investigación y Formación Agraria y Pesquera (IFAPA),
Cordoba, Spain; e-mail: mariap.gonzalez.d@juntadeandalucia.es

A b s t r a c t

A two-source model for deriving surface energy fluxes and their soil and canopy components was evaluated using multi-angle airborne observations. In the original formulation (TSEB1), a single temperature observation, Priestley–Taylor parameterization and the vegetation fraction are used to derive the component fluxes. When temperature observations are made from different angles, soil and canopy temperatures can be extracted directly. Two dual angle model versions are compared *versus* TSEB1: one incorporating the Priestley–Taylor parameterization (TSEB2I) and one using the component temperatures directly (TSEB2D), for which data from airborne campaigns over an agricultural area in Spain are used. Validation of TSEB1 *versus* ground measurements showed RMSD values of 28 and 10 Wm^{-2} for sensible and latent heat

---

fluxes, respectively. Reasonable agreement between TSEB1 and TSEB2I was found, but a rather low correlation between TSEB1 and TSEB2D was observed. The TSEB2D estimates appear to be more realistic under the given conditions.

Key words: Two Source Energy Balance (TSEB) model, component temperatures, resistance schemes, available energy.

1. INTRODUCTION

Quantification of the spatial and temporal variability in hydrological processes and land surface states is of interest on several different disciplines, including agriculture, hydrology, meteorology and climatology. Interconnections and feedbacks between hydrological variables and regional hydrometeorology have led to an increase in the use of satellite remote sensing to determine the water and energy budgets at the Earth's surface. The partitioning of available energy into sensible and latent heat fluxes largely depends on the composition of the observed area, specifically, whether it is vegetated or bare. Due to the heterogeneity of the Earth's surface at most scales, energy-balance models that distinguish between soil/substrate and vegetation contributions to the radiative temperature and radiation/turbulent fluxes have proven to be among the most reliable. A proper partitioning in component fluxes is of importance, not only for its practical consequences, such as the determination of the water-use efficiency of plants, but also because it is important for climate change issues, since the transpiration component shows a strong correlation with carbon sequestration (Scott *et al.* 2006).

During the last few decades, these physically based models have evolved in a quasi-operational mode. In particular, the Two Source Energy Balance model (TSEB) of Norman *et al.* (1995) has been shown to be robust for semi-arid sparse canopy-cover landscapes. Although it is physically based, still a number of assumptions and tabulated input parameters, which are neither easily available nor easily measurable operationally, and their influence on model output over a variety of landcover units need to be evaluated. Such models tend to use resistance schemes in which the turbulent sensible (latent) heat fluxes are determined by the ratio of a temperature (vapor pressure) difference between the overlaying air and the surface, whether soil or canopy, over an aerodynamic resistance to heat (vapor) transport. Since operational remote-sensing observations of vapor pressure are not readily available, the models are usually designed to utilize observations of temperature rather than of vapor pressure. As a result, these resistance schemes are used to derive sensible heat fluxes after which latent heat fluxes are then calculated as a rest-term in the energy balance. In an operational mode, the soil surface temperature, T_S, and canopy temperature, T_C, are usually derived from a single observation of directional radiometric temperature, T_R, in com-

bination with an estimate of the fractional vegetation cover, f_C, at sensor view angle.

In the TSEB model, T_R is calculated from the brightness temperature, which is directly measured by the radiometer, thereby assuming a single directional emissivity that represents soil and vegetation combined. Deriving the soil and canopy component temperatures from f_C and a single T_R observation requires an iterative process, where it is uncertain whether the proper solution is obtained in terms of component temperatures and hence in terms of properly parameterized resistances. Numerous validation studies have shown a good performance of the TSEB model flux output *versus* flux observations (French *et al.* 2005, Gonzalez-Dugo *et al.* 2009, Kustas and Norman 1997, Timmermans *et al.* 2007), which are usually "lumped-together" observations of total H and LE fluxes. Less is known about the validity of the internal model parameters, these being the component temperatures, resistances, and the component flux output. This limits our understanding of the physical processes involved and thus limits model portability (Colaizzi *et al.* 2012a, Kalma *et al.* 2008).

However, when T_R observations made from multiple angles are available, the component temperatures can be derived directly (Kustas and Norman 1997), thereby offering the possibility to assess the validity of the parameterizations used. Some studies have tested the TSEB model by using component temperatures (Colaizzi *et al.* 2012a, Kustas and Norman 1997, Morillas *et al.* 2013). However, a key assumption of the TSEB model and also of other dual source models, is that the effective source/sink for turbulent flux exchange for the entire canopy, as well as for the soil/substrate, can be described by a bulk canopy, or bulk soil/substrate, temperature, and resistance (Colaizzi *et al.* 2012a). Even so, large local differences in observed temperature exist for sunlit and shaded leaves and soil, old and young leaves, and transpiring and non-transpiring leaves (Timmermans J. *et al.* 2008). When locally measured component temperatures such as in Colaizzi *et al.* (2012a) or Morillas *et al.* (2013), or ground-based multiple viewing angle observations such as in Kustas and Norman (1997) are used, they may not represent the bulk canopy and bulk soil temperatures used in the parameterization scheme. Moreover, a significant mismatch between the spatial resolution of the temperature measurements and the size of the flux footprint can cause significant discrepancies between modeled and measured fluxes (Kustas and Norman 1997). Therefore, in the current contribution we preferred to use airborne imagery acquired from viewing angles that differ more than 45° at a resolution that is low enough to obtain "observations" of the representative bulk component temperatures but high enough to capture within-field variation. As such, this study focuses more on inter-model output differences than on absolute validation.

The objective of this study was to determine how physically based retrieval of the representative bulk soil and canopy component temperatures, which are used in the model parameterization, influences estimates of the turbulent fluxes, their components, and model parameters. Thereto, first the performance of the TSEB model as it is commonly used (Anderson *et al.* 1997, French *et al.* 2005, Norman *et al.* 1995) is shown against ground-truth observations of radiation and energy fluxes over the current area. Then soil and canopy component temperatures from dual angle airborne observations were used in dual angle versions of TSEB (Colaizzi *et al.* 2012a, Kustas and Norman 1997). A comparison of the output produced by the different versions of the model is made, followed by a discussion thereof.

2. METHODS AND MATERIALS

2.1 Methods

The dual-source model used in this study is the well-established Two-Source Energy Balance (TSEB) model of Norman *et al.* (1995) which has shown good performance over a wide range of arid and partially-vegetated landscapes (French *et al.* 2005, Gonzalez-Dugo *et al.* 2009, Kustas and Norman 1997, Timmermans *et al.* 2007). Under such circumstances, a dual source model that distinguishes between the soil and vegetation contribution to the turbulent fluxes has clear and well-known advantages over simpler single-source models that treat these contributions in a lumped manner (Huntingford *et al.* 1995, Kustas *et al.* 1996). The TSEB model presents two different versions, according to the assumed resistance network for parameterizing the energy flux exchange, being either in series or in parallel (Norman *et al.* 1995). The series version of the TSEB resistance network allows interactions between soil/substrate and main canopy layer and is therefore particularly useful over relatively dry but relatively densely vegetated areas. Because the vineyard area under study is characterized by just these conditions, use here is made of the series approach only. Although descriptions of the model are available in Norman *et al.* (1995) and Kustas and Norman (1997), the following sections offer a detailed description of the several steps involved in the different versions. This is considered relevant in view of the specific differences in their output, see Section 3.2.

2.1.1 Single-angle model

The single-angle model is the updated version of the Two-Source Energy Balance (TSEB) model (Norman *et al.* 1995), as described by Kustas and Norman (1999) and Li *et al.* (2005). From here on, this scheme will be referred to as TSEB1.

The model assumes that the surface radiometric temperature (T_R) is a combination of soil (T_S) and canopy (T_C) temperatures, weighted by the vegetation fraction (f_C):

$$T_R(\varphi) = \left[f_C(\varphi)T_C^4 + \left(1 - f_C(\varphi)\right)T_S^4 \right]^{(1/4)} , \tag{1}$$

where f_C is affected by the sensor viewing angle (φ). Note that the angular variation of directional emissivity is neglected because variations of less than 0.005 are obtained between viewing angles at nadir and 60° for most vegetated surfaces (Anton and Ross 1987, Kustas and Norman 1997).

Because of the significance in the current study of the vegetation characteristics as seen from different angles we will describe the determination thereof in a bit more detail at this point. The method used to derive the fractional cover at nadir ($\varphi = 0$) follows from Choudhury *et al.* (1994), using a scaled Normalized Difference Vegetation Index (NDVI):

$$f_C(0) = 1 - \left(\frac{NDVI_{max} - NDVI}{NDVI_{max} - NDVI_{min}} \right)^p , \tag{2}$$

where $NDVI_{max}$ and $NDVI_{min}$ represent a surface fully covered by vegetation and completely bare, respectively. Parameter p is the ratio of the leaf angle distribution factor, Λ, to the canopy extinction factor, κ, which is dependent on solar zenith angle ψ (Campbell and Norman 1998). The apparent fractional vegetation cover at viewing angle φ is then obtained by dividing $f_C(0)$ by the cosine of the sensor viewing angle. The Leaf Area Index (LAI), which is used in the estimation of extinction of net radiation and wind speed within the canopy, is related to $f_C(\varphi)$, following Choudhury (1987):

$$LAI = \frac{1 - f_C(\phi)}{\Lambda} . \tag{3}$$

In the case of clumped canopies with partial vegetation cover, such as vineyards and orchards, LAI is multiplied by the so-called clumping factor, $\Omega(\psi)$, which depends on solar zenith angle and vegetation structure. This factor corrects for the reduction in the extinction of the radiation in a clumped canopy as compared to a uniformly distributed one, by multiplying the LAI by the clumping factor. Here we have followed the approach suggested in Kustas and Norman (2000), following:

$$\Omega(\psi) = \frac{\Omega(0)}{\Omega(0) + \left(1 - \Omega(0)\right) \cdot \exp\left(-2.2\psi^P\right)} , \tag{4}$$

where $\Omega(0)$ is the clumping factor at nadir viewing angle, and $P = 3.8 - 0.46\,D$, where D is the ratio of vegetation height to width of the clumps.

The surface energy-balance equation can be formulated for the entire soil-canopy-atmosphere system or for the soil and canopy components separately:

$$Rn_C = LE_C + H_C \ ,$$
(5)

$$Rn_S = LE_S + H_S + G \ .$$
(6)

The partitioning of net radiation, Rn, can be either directly on global Rn (Norman $et\ al.$ 1995), or by formulations for the transmission of direct and diffuse shortwave radiation and for the transmission of longwave radiation through the canopy, as described in Kustas and Norman (1999). In the current contribution we have used the original model description following Norman $et\ al.$ (1995). The spatial variation in the horizontal direction is mainly regulated by fractional vegetation cover and in the vertical (radiation extinction within the canopy) by LAI. Since the radiation formulation follows the so-called "layer-approach" (Lhomme and Chehbouni 1999), a simple summation of the soil and canopy components then yields the total of the flux under consideration.

The soil heat flux is then estimated as a time-dependent function of the net radiation reaching the soil:

$$G = c_g Rn_S \ ,$$
(7)

where c_g is slightly variable with time. Details of the original determination can be found in (Kustas $et\ al.$ 1998). Here it is calibrated against local observations using the measurements from the test sites.

Within the series resistance scheme, the sensible heat fluxes H_C, H_S, and H are expressed as:

$$H_C = \rho_a C_p \left(T_C - T_{AC} \right) / R_X \ ,$$
(8)

$$H_S = \rho_a C_p \left(T_S - T_{AC} \right) / R_S \ ,$$
(9)

$$H = H_C + H_S = \rho_a C_p \left(T_{AC} - T_A \right) / R_A \ ,$$
(10)

where ρ_a is the air density [kg m^{-3}], C_p the air specific heat [J kg^{-1} K^{-1}], T_{AC} is the air temperature in the canopy-air space [K], R_X is the resistance to heat flow of the vegetation leaf boundary layer [s m^{-1}], R_S is the resistance to the heat flow in the boundary layer above the soil [s m^{-1}], R_A is the aerodynamic resistance [s m^{-1}] calculated from the stability-corrected temperature-profile equations (Brutsaert 1982) using Monin–Obhukov Similarity Theory (MOST), and T_A is the air temperature. The procedures to derive T_{AC} as well as the resistance terms R_X and R_S are provided in the Appendix of Norman $et\ al.$ (1995), where the main inputs are wind speed, u [m s^{-1}], the displacement

height, d_0 [m], and roughness length for momentum and heat transport, z_{0M} [m] and z_{0H} [m], respectively. The latter three are estimated following the procedure as described by Massman and Weil (1999).

When estimates of the sensible heat fluxes (H_C and H_S) are known, the latent heat fluxes can be estimated as a rest-term from Eqs. 5 and 6. However, when a radiometric temperature image is available at only one viewing angle, an extra equation is needed in addition to Eq. 1 to solve for T_C and T_S. In the TSEB1 formulation, following Norman *et al.* (1995), this is solved by deriving the canopy latent heat flux using as an initial assumption a potentially transpiring canopy, following the Priestley–Taylor equation (Priestley and Taylor 1972):

$$LE_C = \alpha_{\mathrm{PT}} f_g \left(\frac{\Delta}{\Delta + \gamma} \right) Rn_C \ , \tag{11}$$

where α_{PT} is the Priestley–Taylor coefficient, usually taken as 1.26 [–], f_g is the green vegetation fraction [–], Δ is the slope of the saturation vapor pressure *versus* temperature [kPa·K^{-1}], and γ is the psychrometric constant [kPa·K^{-1}].

In practice, all conductive fluxes, *i.e.*, Rn, Rn_C, Rn_S, and G, are calculated once, following the formulations as given by Norman *et al.* (1995), and remain constant thereafter. Then, the next step is to derive H_C from Eq. 5. A first approximation of T_C, *i.e.*, the average of air temperature T_A and radiometric temperature T_R, is used to derive T_S from Eq. 1. In the series approach, which was used here, a linear approximation of T_C is calculated following the procedure described in the Appendix of Norman *et al.* (1995), using H_C and T_S to arrive at the within-canopy air temperature, T_{AC}. T_{AC} is then used for a first estimation of H_S using Eq. 9. LE_S is finally derived from Eq. 6. If the vegetation is stressed, the Priestley–Taylor approximation, *i.e.*, Eq. 11, overestimates the transpiration of the canopy and negative values of LE_S are computed. This improbable condensation over the soil during daytime indicates the existence of vegetation water stress and it is solved by reducing α_{PT}. An updated, lower, estimate of LE_C is obtained which yields an updated, higher, estimate of H_C through the use of Eq. 5. Next, Eq. 8 provides a new, higher, estimate of T_C, which in turn yields a lower estimate of T_S through Eq. 1, resulting in a lower, updated estimate of H_S. Through the use of Eq. 6 an updated, higher, estimate of LE_S is obtained. This iteration process is continued until $LE_S > 0$.

At this moment, all the fluxes, radiative, conductive and turbulent, and their components, soil and canopy are known, as well as the "equilibrium" soil and canopy component temperatures. However, when multiple viewing angle observations of T_R are available, the soil and canopy temperatures may

be derived directly from the observations. These provide the opportunity to estimate the component sensible heat fluxes from Eqs. 8 and 9, thereby avoiding the need of the above iteration process and as such a check on the physical realism of the model.

2.1.2 Dual-angle model

In the dual-angle approach, a version also described by Kustas and Norman (1997), T_R observations at different viewing angles provide soil and canopy component temperatures. The physical framework of the model remains identical to the single-angle version of TSEB. However, the mathematical framework to determine the turbulent fluxes is slightly different.

The soil and canopy component temperatures were obtained from the simultaneous solution of two equations containing two unknowns, where f_{C1} and f_{C2} and $T_R(\varphi_1)$ and $T_R(\varphi_2)$ are the fractional covers and the radiometric surface temperatures at the first viewing angle, φ_1, and second viewing angle, φ_2. Equation 1 was used for the two flight lines to derive the component soil and canopy temperatures, following:

$$T_S = \left(\frac{f_{C2} T_R^4(\varphi_1) - f_{C1} T_R^4(\varphi_2)}{f_{C2} - f_{C1}} \right)^{(1/4)} , \qquad (12)$$

$$T_C = \left(\frac{T_R^4(\varphi_1) - (1 - f_{C1}) T_S^4}{f_{C1}} \right)^{(1/4)} . \qquad (13)$$

The radiative and conductive fluxes, Rn_S, Rn_C, and G, are estimated following the same parameterization as in TSEB1 and they remain constant during the steps necessary to derive the component turbulent fluxes. Still, different approaches can be followed to arrive at H_S, H_C, LE_S, and LE_C. Two fundamentally different approaches are described in detail in the following sections.

Dual-angle iteration approach

In what is referred to as the dual-angle iteration approach, TSEB2I, the first step concerns the estimation of LE_C and H_C following Eqs. 11 and 5 as in TSEB1. H_C is used in combination with T_C to obtain the within-canopy temperature, T_{AC}, as in TSEB1. Since T_S is known from the observations, it is used with T_{AC} in Eq. 9 to estimate H_S. LE_S is then calculated as a rest-term from Eq. 6. If negative values of LE_S are computed, this problem is solved by reducing α_{PT}, as in TSEB1. An updated, lower, estimate of LE_C is obtained which yields an updated, higher, estimate of H_C through the use of Eq. 5. The updated H_C is again used in combination with T_C to derive an update of T_{AC}, which in turn is used in conjunction with T_S in Eq. 9, to produce

a new estimate of H_S. Again, through the use of Eq. 6 a new estimate of LE_S is obtained. This iteration process is continued until $LE_S > 0$.

Dual-angle component approach

In the dual angle component approach, TSEB2D, the Priestley–Taylor iteration procedure is not used. Instead, the within-canopy temperature, T_{AC}, is estimated directly from the known component temperatures and the resistances, as follows:

$$T_{AC} = \frac{\dfrac{T_A}{R_A} + \dfrac{T_S}{R_S} + \dfrac{T_C}{R_X}}{\dfrac{1}{R_A} + \dfrac{1}{R_S} + \dfrac{1}{R_X}} \; . \tag{14}$$

The component sensible heat fluxes, H_C and H_S, are then calculated directly from Eqs. 8 and 9. Note that the formulation of Eq. 14 is equal to the general expression of the aerodynamic temperature in two-source models (Merlin and Chehbouni 2004, Shuttleworth and Gurney 1990).

The component latent heat fluxes, LE_C and LE_S, are simply calculated as rest-term from Eqs. 5 and 6. If LE_C or LE_S is below 0, then it is set to 0, and H_C or H_S is calculated as a rest-term from Eqs. 5 or 6, respectively. Basically, the TSEB2D approach is the same as the 2ANGLE model described by Kustas and Norman (1997).

2.2 Material

In order to ensure the proper extraction of the bulk soil and canopy component temperatures from dual-angle observations, some minimum difference in viewing angle of these observations is needed. The optimum viewing-angle difference, usually between nadir and a particular zenith viewing angle, depends among other things on pixel resolution, local vegetation cover, and geometry, as well as on component temperature differences. For practical application, differences of some 40° to 60° are generally desirable (Colaizzi *et al.* 2012a, Kustas and Norman 1997, Merlin and Chehbouni 2004, Vining and Blad 1992).

Airborne data that fulfill these requirements were obtained during the EODIX campaign over a vineyard, centered at 39°03′35″ N and 02°06′04″ W, in an agricultural test-site near Barrax, Spain. The area is extremely flat and located at an elevation of 700 m a.s.l. The campaign, carried out in June 2011, was specifically designed to obtain imagery with large differences in viewing angle. Unfortunately, during this campaign no detailed flux and component temperature observations were collected, which made it difficult to validate the model results. Over the vineyard, the only data available for

validation was the water flux measured by a weighing lysimeter. Therefore, also data were used from the REFLEX campaign, which was flown in July 2012 covering the same vineyard and which was designed specifically to advance our understanding of land-atmosphere interaction processes over heterogeneous terrain.

The approach was first to demonstrate proper model performance over the Barrax site, using data from the REFLEX 2012 campaign. Although this "validation", was performed over a much larger area, covering also other land cover units than the vineyard, the main idea was to ensure that the model was providing reliable output for this area. Details of this study are described in Corbari *et al.* (2015) and a summary of the results is provided in Section 3.1. The actual comparison between the different model versions is then done using data from the EODIX campaign only. These data offered the possibility to extract bulk canopy and soil component temperatures for the vineyard, which is located at the center of the site. The procedure is outlined in Section 2.1.2 and the results are shown in Section 3.3. At the time of the campaigns, the vineyard in general is characterized by dry soils and drip-irrigated grape stands. The drip irrigation system is not located directly on the soil, but some cm above it, watering the surface along the tube. As a consequence, to some degree grass is growing under the vine stands and at several locations, also in the corridors. The vineyard can best be described as relatively sparse; grape stands ranging in height from 1.0 to 2.5 m are planted in rows at about 3-meter intervals, but having a relatively dense canopy. This makes the site particularly suitable to test the TSEB series model parameterization, which was specifically designed for this type of landcover (Norman *et al.* 1995). The comparison is done by comparing model output from the single-angle and dual-angle TSEB versions using the data of the EODIX campaign. Since for all TSEB versions the net radiation and soil heat flux parameterizations are identical, the focus in the comparison study is on the turbulent flux output only.

A brief description of the observations and processing done for the input to and validation of the TSEB model is provided below. For a more complete description of the campaign observations see Timmermans *et al.* (2014) and van der Tol *et al.* (2015) for the REFLEX campaign and Mattar *et al.* (2014) for the EODIX campaign.

2.3 Observations and data processing

2.3.1 REFLEX 2012 campaign

Ground-truth data

During the campaign, which took place from 16 to 28 July 2012, three eddy covariance (EC) towers and a large aperture scintillometer (LAS) were in-
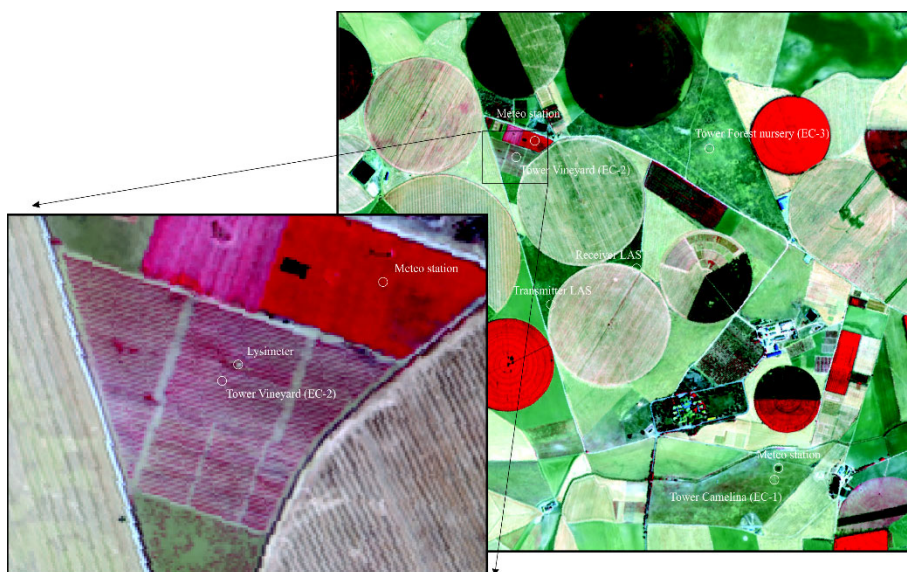
Fig. 1. Site overview with reference stations and flux tower sites. The zoom shows details of the vineyard site with a W-NW to E-SE crop row orientation, and lysimeter and flux tower positions.

stalled over different landcover units. The landcover units comprised a camelina field, a vineyard, a reforestation areak, and a large wheat-stubble field (see Fig. 1). Apart from the turbulent H and LE fluxes, at the flux towers also net radiation (Rn) and soil heat flux (G) and standard meteorological parameters at three different heights were recorded. Required meteorological model inputs concern incoming shortwave radiation and air temperature, relative humidity, and wind speed at a certain reference level; see Corbari *et al.* (2015) for details. Since some crop and tree heights in the area were greater than the measurement level at the reference stations, the required meteorological model input was obtained by the average of the three EC stations at a reference height of 5 m. Although a certain spatial variability in these variables is known to influence flux estimations over such heterogeneous sites (Timmermans W.J. *et al.* 2008) the spatial average (the standard deviation of air temperature was 0.9°, and 0.09 ms^{-1} for wind speed) was considered to be representative of the area with respect to the current model validation.

A detailed analysis of the turbulent flux observations is provided in van der Tol *et al.* (2015), which includes a discussion of the well-known closure problem.

Remote sensing data

Required remote sensing based model inputs covered broadband surface albedo, normalized difference vegetation index, and surface temperature. These were obtained from optical airborne data acquired with the Airborne Hyperspectral Scanner (AHS), a sensor mounted on the Spanish Instituto Nacional de Tecnica Aerospacial (INTA) aircraft platform. An overpass at 09:28 UTC (11:28 local time) on 25 July 2012 was used for the current contribution. At-surface georeferenced reflectances (level 2b), resampled to a 4-meter pixel size, were provided by the INTA Remote Sensing Laboratory that was in charge of post-processing the airborne acquisitions. The at-surface reflectance was validated against field spectroscopy acquired *in situ* over a variety of landcover units, and showed good overall agreement. Details of these observations and post-processing steps are provided in de Miguel *et al.* (2015). Broadband surface albedo and NDVI were then derived from the surface reflectance in specific Red and Near Infrared (NIR) bands of the AHS sensor, following the same procedure as described in Timmermans *et al.* (2011). At-sensor radiances (level 1b) from the thermal AHS channels were processed by the Global Change Unit at the Faculty of Earth Physics at the University of Valencia, Spain, and validated against ground observations performed over several different landcovers. Land surface temperature and emissivity were retrieved simultaneously using the Temperature-Emissivity-Separation algorithm of Gillespie *et al.* (1998), adapted for use with the AHS data as described in Sobrino *et al.* (2009).

2.3.2 EODIX 2011 campaign

Ground-truth data

The necessary meteorological model input data were obtained from the lysimeter station located inside the vineyard, see zoom in Fig. 1. The meteorological observations were acquired at a height of 4 m. They consisted of 15-minute averages of incoming shortwave radiation, $S^{\downarrow}$, and 1-hour averages of air temperature, T_A, relative humidity, R.H., and wind speed, u. The hourly averages were then interpolated to acquire estimates at the airborne overpass time (Table 1).

Table 1

Meteorological model input from the EODIX campaign

Parameter	$S^{\downarrow}$ [Wm^{-2}]	T_A [°C]	R.H. [%]	U [ms^{-1}]
Value	772	23.4	53.0	1.2

Although no rainfall was recorded in the two weeks preceding the experiment, the last irrigation registered on the lysimiter was 20 mm on 7 June, five days before the airborne overpass. However, the irrigation scheme at this experimental test farm is rather irregular, both temporally as well as spatially. As a consequence, considerable variation exists in the degree of canopy stress within the vineyard. Locally stable conditions may occur, given the nature of the vineyard where sometimes hot bare corridors alternate with irrigated vines. On the other hand, also relatively stressed vines exist within the vineyard, due to the irregular irrigation, but also due to a variation in fractional vegetation cover (around 40% on average for the vineyard, but with minimum and maximum values ranging from 15 to 85%, respectively). In the southern part of the vineyard, for example, less mature vine stands occur, characterized by a lower fractional cover of vine stands, but a more frequent irrigation. Typically at these places, but also at other locations within the vineyard, the corridors show the presence of grass, growing on water from the irrigation tubes.

The lysimeter station records hourly actual evaporation rates, which are interpolated for the overpass time of the airplane. The observation (124 Wm^{-2}) was used as an indication of the model performance, testing to which degree the estimations of LE fluxes were realistic and physically meaningful. A note has to be made with respect to dew which is recorded by the lysimiter almost all mornings in the period of the campaign, typically a few hours before the flight. Vaporization of this dew, mainly from the substrate, may also contribute to the LE flux during the flight overpass.

Remote-sensing data

Airborne optical imagery used to analyze the performance of the different model versions was also obtained from the Airborne Hyperspectral Scanner (AHS) operated by INTA. Two parallel flight lines acquired at 09:00 and 09:20 UTC on 12 June 2011 were utilized for this purpose. Local time is following CET, which is two hours later, but since the geographic position of the area is West, the true solar time is closer to 1 hour later than UTC. The flight lines were chosen such that they were parallel to each other and also parallel to the row orientation of the vineyard, in order to minimize potential local differences in shadowing effects due to differences in viewing azimuth. The campaign was specifically designed to obtain large differences in viewing angles. In order to achieve view zenith angles close to 60°, a wedge was placed under the sensor, to tilt it during the flight (Mattar *et al.* 2014). This produced a nadir viewing angle over the vineyard for the flight line acquired at 09:00 and a zenith viewing angle of 57° over the vineyard for the flight line obtained at 09:20.

Required general model inputs, broadband surface albedo, NDVI and surface temperature were obtained from the nadir flight in exactly the same manner as for the REFLEX 2012 campaign and are therefore not described here again. However, an ASD spectrometer was used for *in situ* measurements of surface reflectance and a CIMEL CE312-2 and IR120 radiometer for thermal emission over a large number of selected sites encompassing different landcover units. An RMSE of 0.03 [–] was found for reflectance and an RSME of 1.5 [K] for land surface temperature, equal to the values found in previous campaigns over the same area using the same sensor (Mattar *et al*. 2014, Sobrino *et al*. 2006, 2009).

In addition, the required bulk soil and canopy component temperature observations were obtained, using Eqs. 12 and 13, from the two parallel flight lines, which were characterized by viewing zenith angle differences over the vineyard of around 57°. In order to take the small time difference of 20 minutes between the two successive flight lines into account, a correction of T_R was made, using the ratio of $T_R(\varphi_1)/T_R(\varphi_2)$ taken from a homogeneously vegetated area (dense grass cover) just north of the vineyard. However, the differences obtained were almost negligible.

3. RESULTS AND DISCUSSION

3.1 Validation of single-angle model over Barrax (REFLEX 2012 campaign)

TSEB model output for *Rn*, *G*, *H*, and *LE* as derived from the AHS overpass at 09:28 UTC (11:28 local time) on 25 July 2012, was validated against ground observations over four different landcover units. For this purpose, the so-called field-of-view of the local sensors needs to be determined. This is especially important when dealing with high-resolution imagery as is the case in the underlying study. For the net radiation sensor, 99% of the observations originate from a circle whose diameter is 10 times the sensor height (*i.e.*, 5 m), although ground surfaces closer to the sensor have a higher weighting. A window of 10×10 pixels (*i.e.*, 40×40 m) was selected around the location of the observation. The same was done for the soil heat flux observations, which are characterized by a high spatial variation. To at least take this effect into account, we chose a similar window as for the net radiation observations. For the turbulent fluxes, a different strategy is followed. The "field-of-view", or footprint (Vesala *et al.* 2008), of these sensors depend on terrain characteristics, wind speed, and wind direction. The procedure outlined in Timmermans *et al.* (2009) is used to calculate the footprints of the observation towers at the moment of airborne overpass. Footprint-weighted averages of the model output for *H* and *LE* were then compared to the ground observations.

Model performance was evaluated using difference statistics comprising of the mean absolute difference (MAD), the mean absolute error (MAE), and the root mean square difference (RMSD), see Table 2.

Table 2

Difference statistics for the four observation sites

Statistics	H	LE	G	Rn
MAD [Wm^{-2}]	22.5	8.7	85.0	51.5
MAE [%]	13.9	29.4	51.2	13.6
RMSD [Wm^{-2}]	28.0	10.0	87.2	58.3

Although only limited ground observations were available for this particular study, a reasonably good agreement between observed and modelled fluxes is noted, especially for the turbulent fluxes. An analysis of the model performance per landcover and per flux component is beyond the scope of the current contribution, but a detailed discussion and tower footprints can be found in Corbari *et al.* (2015). For our study, we regard the overall model performance of TSEB1 with respect to the estimation of both radiative and especially turbulent fluxes over this site as reliable.

3.2 Soil and canopy component temperatures

The nadir T_R and f_C maps as well as the component temperature maps are shown in Fig. 2.

As can be noticed, and also seen in the zoom of Fig. 1, two main corridors exist in the vineyard, which are characterized by a very low fractional cover. As they are oriented perpendicularly to the flight lines, the difference in fractional cover between the two flight lines was minimal. Since this difference is in the denominator of Eq. 12, the determination of T_S can become very sensitive to errors. These pixels, as well as other pixels where the difference in fractional cover was minimal, were therefore excluded from the analysis.

In a spatial context, clearly the parts in the vineyard that are characterized by a higher f_C show a lower T_R, and *vice versa*, as may be expected. Another clear phenomenon throughout the vineyard is the lower T_S at high f_C, and *vice versa*. This is primarily caused by the higher radiation extinction within the canopy (shadow), resulting in a lesser warming up of the soil/substrate during the morning hours. Therefore, if homogenous soil conditions are assumed and T_R is constant, a higher f_C will result in a lower T_S and, according to Eq. 1, thus in a higher T_C. Despite the fact that soil conditions and T_R are not homogeneous throughout the vineyard, this (*i.e.*, a lower
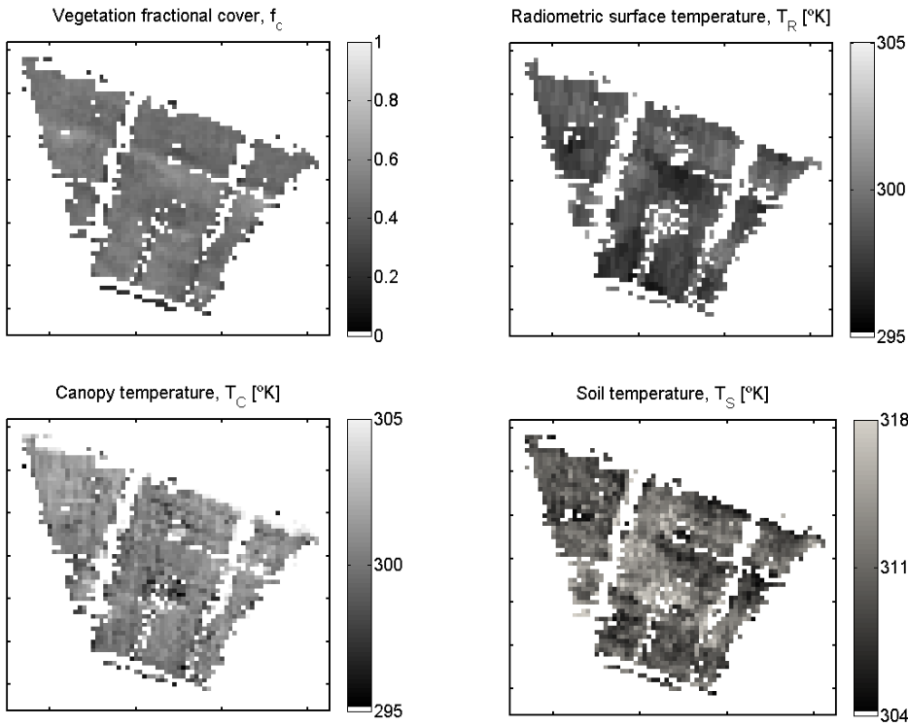
Fig. 2. Retrieved f_C, T_R, T_C, and T_S maps over the Barrax site for 12 June 2011 (EODIX campaign).

T_S is accompanied by a higher T_C and *vice versa*) is what is seen here to a certain extent. At a first instance, this does not seem physically very realistic, since relatively high T_C and relatively low T_S would indicate stressed vegetation over a relatively cold soil and *vice versa*. However, given the variation in characteristics of the vineyard, where locally in the corridors shallow rooted grass is fed by water from the irrigation tubes, situations with stressed vines and low temperatures for the soil/substrate do occur. The opposite situation, *i.e.*, unstressed vegetation occurring over a relatively hot soil/substrate, is rather common in a drip-irrigated system. Which situation prevails and whether this is realistic in the current situation is discussed in Section 3.3.

In an absolute sense, the bulk soil and canopy component temperatures obtained from the dual angle airborne observations over the vineyard showed average values of 310.6 and 300.7 K, respectively, with standard deviations of 0.62 for the soil and 0.30 for the canopy. Although these "observed" temperatures are actually derived from Eqs. 12 and 13, and as such are not actual observations of T_S and T_C, they will be referred to as "ob-

served" from here onwards, to differentiate them from soil and canopy temperatures as modelled by TSEB1. The soil temperatures ranged from 303.8 to 318.1 K, while observed canopy temperatures were between 298.0 and 302.6 K. Unfortunately, during the EODIX 2011 campaign, no detailed ground observations of soil and leave component temperatures were available. However, given an observed air temperature of 296.5 K and a vapor pressure deficit of 1.2 kPa the observations are in agreement with theoretical limits as defined by Jackson *et al.* (1981) and Gardner *et al.* (1992), or more recently by Colaizzi *et al.* (2012b). They report that typical values for foliage temperatures under these circumstances may range from 1.5 K below air temperature for potentially transpiring crops to 5.0 K above air temperature for non-transpiring crops, although it is stated that measurements may occasionally exceed these limits.

Similar observations were made by Timmermans J. *et al.* (2008) during the Sen2Flex campaign over the Barrax vineyard. Apart from measuring sunlit and shaded soil temperature, they used contact probes to measure individual leaf temperatures of sunlit and shadowed, old and young leaves, at different heights in the canopy. They found within-canopy differences in leaf temperature, ranging from 5 K below air temperature to 6 K above air temperature in late morning, and reported standard deviations as large as 3.1 K for soil and 1.3 K for the canopy component temperatures, within a 5 m radius. The canopy temperatures observed in the current study are obviously biased towards the upper theoretical limit with respect to air temperature. This may indicate that, though irrigated, the crops are transpiring at a subpotential rate.

A comparison of the component temperatures with modelled values of soil and canopy temperatures obtained from TSEB1 is provided in Fig. 3.
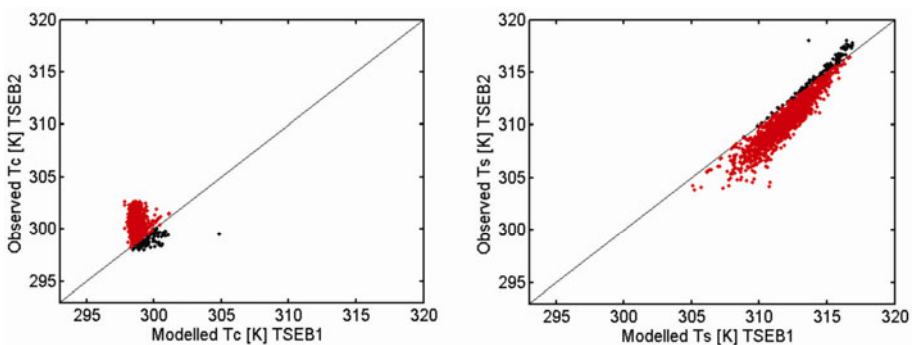
Fig. 3. Observed *versus* estimated component temperatures for 12 June 2011. In red/orange pixels are shown where T_S observed < T_S modelled and/or T_C observed > T_C modelled.

For a large part of the vineyard, the modelled values of T_C are lower than observations (298.7 K *versus* 300.7 K on average, respectively) and in much of the vineyard the values of modelled T_S are higher than observed (312.1 K *versus* 310.6 K on average, respectively). Because of the importance of this phenomenon for this study, the pixels where this occurs are displayed in red (or orange) in Fig. 3 and in following sections. Apart from the average differences, the standard deviation in the modelled values of both T_C and T_S is smaller than for the observations. Observed T_C shows a standard deviation of 0.30 K *versus* a standard deviation of 0.20 K for the modelled values. For T_S the standard deviations for observations and modelled values are 0.62 K and 0.49 K, respectively.

3.3 Inter-comparison between single-angle and dual-angle models (EODIX 2011 campaign)

3.3.1 Single-angle (TSEB1) and dual-angle iteration approach (TSEB2I)

Model output from TSEB1 is plotted *versus* TSEB2I output for the turbulent fluxes in Fig. 4. Although a reasonable agreement and clear correlation, *R*,
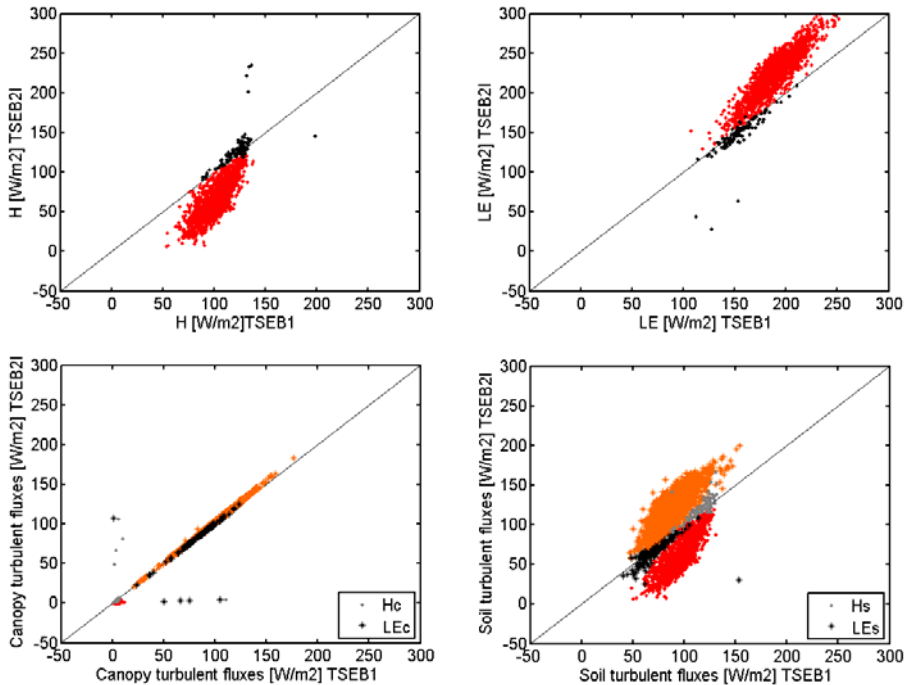
Fig. 4. Turbulent fluxes and their components (lower panels) from TSEB1 *versus* TSEB2I. In red/orange pixels are shown where T_S observed < T_S modelled and/or T_C observed > T_C modelled.

between the two model versions (R is equal to 0.91 for LE and 0.82 for H) is noted in this figure, there are also clear differences.

A mean difference of -31.9 Wm^{-2} and RMSD of 32.9 Wm^{-2} of sensible heat flux by TSEB2I with respect to TSEB1 output is noted and a similar (available energy, $Rn - G$, is the same for both models) over-estimation, and RMSD of latent heat flux by TSEB2I with respect to TSEB1 can be seen. An explanation for this is found by a closer examination of the component flux outputs of both model versions, which are shown in Fig. 4. Model output statistics, including those from the TSEB2D model version, are presented in Table 3 in the next section.

Table 3

Model output statistics for TSEB1 and TSEB2I:
mean $(\overline{x})$ and standard deviation (σ).

Model	H		H_C		H_S		LE		LE_C		LE_S	
	$\overline{x}$	σ	$\overline{x}$	σ	$\overline{x}$	σ	$\overline{x}$	σ	$\overline{x}$	σ	$\overline{x}$	σ
TSEB1	102	4.0	5	2.7	97	3.7	185	6.8	97	6.8	88	4.2
TSEB2I	68	7.7	3	4.2	66	7.0	219	10.8	100	7.5	119	7.0
TSEB2D	142	5.2	69	10.0	73	6.6	145	5.7	34	8.8	112	6.7

In the left panel of Fig. 4 the canopy component fluxes of TSEB1 are plotted against those of TSEB2I, and in the right panel the soil components are shown.

The canopy component fluxes of TSEB1 and TSEB2I are identical for almost all pixels in the vineyard. This is due to the Priestley–Taylor iteration procedure that was used here in both versions of the model. If the first estimates of T_S, in TSEB1, or observations of T_S, in TSEB2I, yield an H_S that is smaller than $Rn_S - G$, then the first estimate of $LE_S > 0$. This is the situation for nearly all points, which means that the two versions yield the same values for LE_C and H_C fluxes under these circumstances.

Since for almost all pixels the canopy component fluxes are identical for the two versions of the model and LE_S is determined as a rest-term, the differences for H and LE are entirely regulated by the differences for H_S. The TSEB2I model output for H_S is almost everywhere smaller than in the TSEB1 version, see Fig. 4 right panel. Examination of Eq. 9 reveals that differences in H_S may be invoked by differences in T_{AC}, in R_S or in different values for T_S.

Many of the observed values of T_C are larger than the TSEB1 model output for T_C, see Fig. 3. Equation 1 shows that for T_S the opposite then must hold true, which is confirmed in the right panel of Fig. 3. Lower values of T_S in TSEB2I potentially yield lower values for H_S.

Model differences for R_S are mainly regulated by differences in the coefficient a in T_C, following Eq. 5 in Kustas and Norman (1999). Larger T_C values in TSEB2I, and thus lower T_S values, result in lower values for a' and thus in higher R_S values, since wind speed values do not differ significantly between model versions. Higher R_S values potentially yield lower values for H_S in TSEB2I as well.

Within canopy, air temperature, T_{AC}, is obtained from Eq. 8. Since values for R_X, mainly driven by wind speed, and H_C are similar in both versions of the model, higher values of T_C in TSEB2I also yield higher values of T_{AC} in TSEB2I. Larger values of T_{AC} potentially yield lower values of H_S in TSEB2I as compared to TSEB1.

The model differences for R_S and T_{AC} described above are illustrated in Fig. 5. In the current contribution we have used the modified formulation for R_S, as given in Eq. 5 in Kustas and Norman (1999). Using the original R_S formulation (Norman *et al.* 1995), which is independent of the difference between T_S and T_C, reduced differences for R_S, but did not significantly influence model differences for H_S output. Since H_C is negligible for almost entire vineyard in both TSEB1 and TSEB2I parameterizations, T_{AC} and T_C are almost identical, see Eq. 8. Therefore, the shape of the right panel of Fig. 5 is rather similar to the left panel of Fig. 3.

Resuming, larger values of observed T_C as compared to modelled T_C in TSEB1 for all three parameters that have a direct influence on H_S yield lower values of H_S. This is confirmed by the red pixels in the lower right panel (and thus upper left panel) of Fig. 4, which are all below the 1:1 line. On the other hand, if lower values of T_C were observed than for TSEB1-modelled T_C, this would yield higher values of H_S in TSEB2I than in TSEB1. Since many of the observed values of T_C were higher than those of the modelled T_C, the dual angle model output for H_S, and thus for H, is lower.
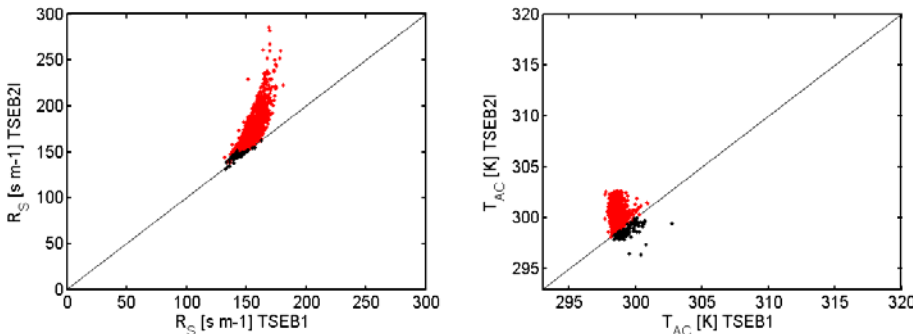
Fig. 5. Left panel R_S, right panel T_{AC}.

3.3.2 Single-angle (TSEB1) and dual-angle component approach (TSEB2D)

The model output from TSEB1 is plotted *versus* TSEB2D output for the turbulent fluxes in Fig. 6. Agreement and correlation between the two models is less than between TSEB1 and TSEB2I. Correlation, *R*, between the two model versions is equal to 0.55 for *LE* and 0.30 for *H*, whereas the mean differences and RMSD between TSEB2D and TSEB1 are +39.4 Wm^{-2} and 40.2 Wm^{-2}, respectively, for *H*. Again the difference statistics for *LE* are equal and opposite to those of *H*. Interestingly, the mean difference has the opposite sign as compared to TSEB2I. Once again, an explanation is found by a closer examination of the component flux outputs of both model versions, as shown in Fig. 6. Model output statistics are presented in Table 3.

For the soil component fluxes, shown in the right panel of Fig. 6, a similar reasoning may be followed as described in the last paragraph of Section 3.3.1. Therefore, the right panel of Fig. 6 is very similar to the right panel of Fig. 4.
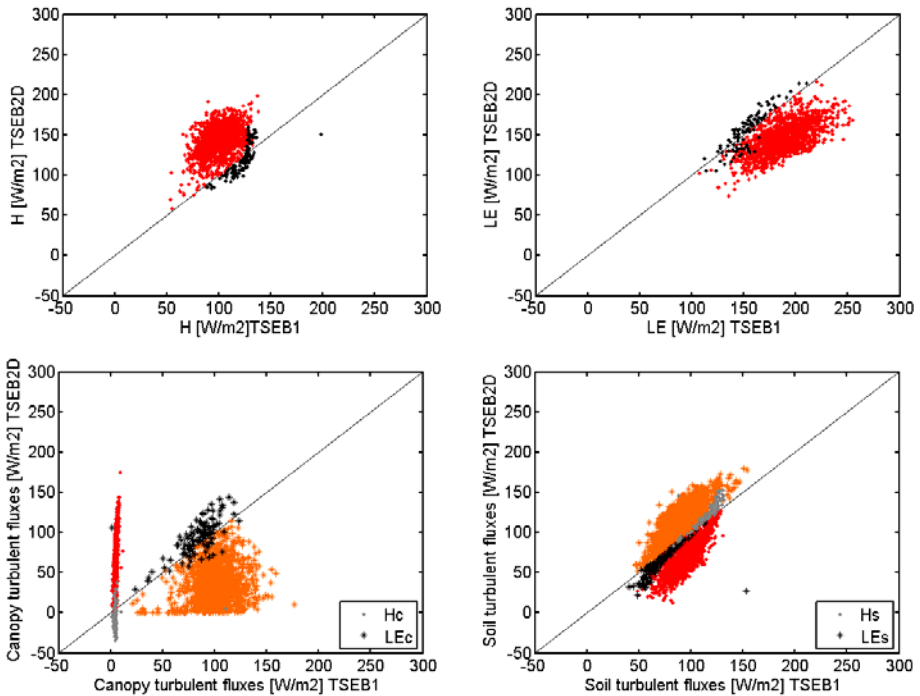
Fig. 6. Turbulent fluxes and their components (lower panels) from TSEB1 *versus* TSEB2D. In red/orange pixels are shown where T_S observed < T_S modelled and/or T_C observed > T_C modelled.

However, a striking difference between the two model versions can be observed with respect to the canopy component fluxes. In the TSEB2D approach, values for H_C range from –35 to 175 W·m^{-2}. However, in the TSEB1 approach, for almost the entire vineyard, the canopy is transpiring at the potential rate, resulting in negligible values for H_C under the current circumstances.

In the absence of stressed vegetation, the first estimate of the partitioning of Rn_C into LE_C and H_C in TSEB1 is determined entirely by the slope of the saturation vapor pressure, Δ, which depends solely on air temperature. In the temperature range between 25 and 35°C, which are typical summertime values at this latitude, the first estimate of the portion of Rn_C that is consumed by latent heat exchange ranges from 95 to 105%. This leaves only negligible amounts of energy available for sensible heat exchange between the canopy and the air. Under TSEB1, these first estimates will not change as long as the first estimate of the soil component of the sensible heat flux, H_{S-1}, is smaller than the available amount of energy for the soil, *i.e.*, $Rn_S - G$. In other words, these first estimates will not change as long as LE_{S-1} is larger than 0. This is the case for almost all pixels in the vineyard.

Following Eq. 8, negligible sensible flux over the canopy results in a within-canopy air temperature very similar to the canopy temperature. One could reason that in such a case the sensible heat flux over the soil is driven by the difference between T_S and T_C. Given that the first estimate of T_C in TSEB1 is the average between air temperature and radiometric surface temperature, this means that the first estimate of H_S is driven by the difference between air and radiometric surface temperature as a function of fractional canopy cover, f_C, over the surface resistance. Using this information in the first estimate of LE_S provides a simple first check whether given conditions will predict water-stressed canopy conditions. Under the current conditions, this first estimate of LE_S is positive everywhere, meaning no lowering of α_{PT} in Eq. 11 occurred at any location. Hence the canopy sensible heat flux estimates in TSEB1 (as for TSEB2I) are negligible (Table 3). This is remarkable, given that the observed canopy component temperatures are "biased towards the upper theoretical limit with respect to air temperature", indicating potentially relatively high canopy sensible heat fluxes. It should be noted at this point that for TSEB1 (and for TSEB2I) to predict stressed conditions LE_S has to be zero. Therefore, situations where the upper soil is wet (due to dew, or just after a rain or irrigation event) and plants (which have their roots at a deeper and potentially drier soil layer) are stressed, cannot be modelled by TSEB1 nor TSEB2I. This is a drawback of the model for agricultural applications.

Contrary to TSEB1 and TSEB2I, in TSEB2D the canopy turbulent fluxes, H_C and LE_C, are not estimated from Rn_C, but from the canopy tempera-

tures directly. As such, a potential error in Rn_C will affect TSEB1-H_C and TSEB2I-H_C, but will not affect TSEB2D-H_C. The TSEB2D estimates for canopy sensible heat fluxes, that range from –35 to 175 W·m^{-2}, are on average 69 W·m^{-2} and show a standard deviation equal to 10.0 W·m^{-2}. This relatively large range is also observed by Kustas and Norman (1997) who state that in general an approach that uses the component temperatures directly produces considerable scatter. Of course, we do not have component flux observations at the scale of individual vines, but given the observed range in canopy temperatures a certain scatter in canopy sensible heat fluxes may be expected. This is in accordance with the nature of this vineyard, where both full-grown mature vine stands exist next to younger vine stands with a lower fractional vegetation cover and a higher irrigation supply. Although no individual canopy flux observations are available, the range in TSEB2D model output therefore seems realistic. The larger rate of latent heat from the soil could be related with the dew registered on the lysimeter as mentioned earlier.

In TSEB2D, the canopy sensible heat fluxes were estimated following Eq. 8, where ρ_a, C_p, and T_C are the observed parameters, R_X is estimated as given in Eq. A.8 in Norman *et al.* (1995) and T_{AC} is estimated following Eq. 14. Since the main variation in R_X originates from wind speed just above the canopy, no large differences between TSEB1 and TSEB2D are noted, see the upper left panel of Fig. 7. Given the large spread in H_C for TSEB2D one might expect an effect on T_{AC} as well. This effect, which is a reduction in standard deviation and relatively lower values, is shown in the upper right panel of Fig. 7. T_{AC} is derived not only from air and component temperatures but also depends directly on the resistances (Eq. 14). How they relate to the soil and aerodynamic resistances in TSEB1 is plotted in the lower panels of Fig. 7. Larger values and larger standard deviation for R_S, similar to TSEB2I, are seen for TSEB2D as compared to TSEB1. To a lesser extent, the opposite is seen for R_A, lower standard deviation and partly lower values in TSEB2D. Apparently, the interplay between component temperatures and resistances Eq. 14 has a compensating, lowering effect on T_{AC} here.

Since T_{AC} depends not only on observed air and component temperatures but on all resistances as well, the different resistance parameterizations are of crucial importance for obtaining accurate component flux estimates here. Validation of these parameterizations for the current study would have involved further experimental observations of within- and above-canopy wind, temperature, and flux profiles. However, this is beyond the scope of the current study, whose objective was merely to investigate the effect of using observed component temperatures instead of model-derived component temperatures on model output.
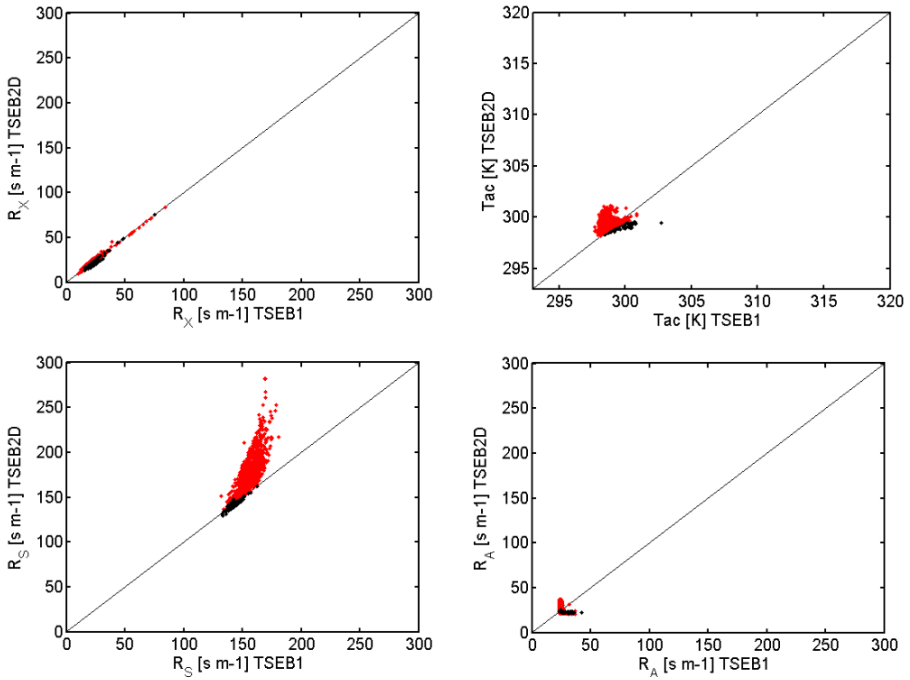
Fig. 7. Comparison between TSEB1 and TSEB2D for the within-canopy temperature, T_{AC}, and the resistances, R_X, R_S, and R_A.

3.3.3 Concluding remarks

Summarizing, using the observed component temperatures in TSEB2D results in higher values for H, and lower values for LE, as compared to TSEB1 under current conditions. The opposite holds true for TSEB2I; here, using the observed component temperatures results in lower values for H and higher values for LE.

The latter is explained entirely by the soil components for TSEB1 and TSEB2I, as described extensively in Section 3.3.1. The soil components for TSEB2I and TSEB2D are estimated in a similar manner. Both use the observed T_S, resulting in a lower H_S estimate for both models with respect to TSEB1. Since no PT-iteration took place, no "correction" was performed on LE_S in TSEB2I, hence the lower right panels of Figs. 4 and 6 have a very similar shape. The (small) difference in magnitude of the soil fluxes of TSEB2I and TSEB2D is regulated mainly by the difference in magnitude of T_{AC} because R_S for the two models is almost identical since wind speed values do not differ significantly between model versions.

Because the estimations of H fluxes from TSEB2D on average are higher than those of TSEB1, the under-estimation of H_S by TSEB2D with respect to

TSEB1 has to be more than compensated by the over-estimation of H_C. The average difference between modelled and observed canopy temperatures is 2.0 °K, whereas for the soil temperatures this is only 1.5 K, meaning that potentially the effect of using observed component temperatures on H_S is smaller than on H_C. This effect is even emphasized by the resistances, because R_S becomes larger when using the observed component temperatures, whereas R_X remains (almost) unchanged. Therefore, the estimates of H from TSEB2D are higher than those of TSEB1 when T_C observed is larger than T_C modelled. This is reflected by the red pixels in the upper left panel of Fig. 6, which are all above the 1:1 line.

Now, the question remains which of the model versions performs better. Unfortunately we do not have (component) flux measurements. However, an indication of the model performance may be obtained from Table 4, where TSEB1, TSEB2I, and TSEB2D model outputs for *LE* are compared with the lysimeter measurements. The best fit corresponds to the TSEB2D output, although the agreement with TSEB1 is still within generally accepted ranges. The TSEB2I output shows the largest discrepancy, suggesting that using the Priestley–Taylor approach combined with observed component temperatures performs worse than using the Priestley–Taylor approach only.

Table 4

LE model results for TSEB1, TSEB2I, and TSEB2D
versus the lysimeter observation

Latent heat flux [Wm^{-2}]	Lysimeter	TSEB1	TSEB2I	TSEB2D
	124	163	201	125

4. SUMMARY

Validation of the widely used single-angle model, TSEB1, over a very heterogeneous agricultural area in a semi-arid environment showed good results that are comparable to previous validations work done for the model. Turbulent flux exchanges showed a particularly good fit with respect to ground observations.

Dual-angle measurements yielded observations of soil and canopy component temperatures that showed a larger spread than modelled values for T_S and T_C. No ground observations of component temperatures were made during the overpass but values showed very similar responses compared to observations made during previous and comparable campaigns and were within theoretical limits. Values obtained for canopy temperature indicated relatively stressed vegetation stands. This was not confirmed by results of the TSEB1 model, which generated values for T_C that were generally lower than observations and T_S that were generally higher than observations.

The output of two types of the dual angle version of TSEB, comparable to those described in Kustas and Norman (1997) and Colaizzi *et al.* (2012a), was compared with the output of the single-angle model version. The first version, TSEB2I, contains a similar iteration procedure to that of the single-angle version, invoking a step-wise lowering of the Priestley–Taylor coefficient. The second version, TSEB2D, without iteration procedure, utilizes the observed component temperatures to estimate component sensible heat fluxes directly.

Reasonable agreement and correlations between TSEB1 and TSEB2I model outputs for the turbulent fluxes were found. TSEB1 generates slightly lower values for LE and slightly higher values for H than TSEB2I. This is entirely regulated by the soil component of the fluxes, since the canopy flux estimates of both model versions are similar due to the iteration procedure used in both model versions. This procedure yields a potentially transpiration canopy in over almost the entire vineyard under the current conditions. The higher values for T_S obtained in TSEB1 as compared to observed values for T_S always result in higher estimates of H_S in the current parameterization. LE_S is calculated as a rest-term, so TSEB1 estimates are lower than estimates of TSEB2I. TSEB1 results for H are therefore higher than for TSEB2I and TSEB1 results for LE are lower than for TSEB2I.

There is considerably less agreement between the TSEB1 and TSEB2D model outputs. Since the soil components are estimated in a similar manner as for TSEB2I, the reason for the poorer agreement lies in the estimation of the canopy component fluxes. Under the current conditions, TSEB1 predicts potential transpiration rates for the entire vineyard, which yields negligible H_C estimates overall. However, using observed T_C in TSEB2D to directly estimate H_C yields values that range from –35 to 175 W·m^{-2}. Even though no ground observations are available for these component fluxes, these values seem to be more realistic under the given conditions. Moreover, local circumstances indicated the potential existence of stressed vegetation co-existing with evaporating soil, or substrate, which is a condition that cannot be modelled by TSEB1 nor TSEB2I.

R e f e r e n c e s

Anderson, M.C., J.M. Norman, G.R. Diak, W.P. Kustas, and J.R. Mecikalski (1997), A two-source time-integrated model for estimating surface fluxes using thermal infrared remote sensing, *Remote Sens. Environ.* **60**, 2, 195-216, DOI: 10.1016/S0034-4257(96)00215-5.

Anton, J.A., and J.K. Ross (1987), Emissivity of the vegetation-soil system, *Sov. J. Remote Sens.* **5**, 49-55 (in Russian with English summary).

Brutsaert, W. (1982), *Evaporation into the Atmosphere. Theory, History, and Applications*, Springer Science & Business Media, Dordrecht, DOI: 10.1007/978-94-017-1497-6, 299 pp.

Campbell, G.S., and J.M. Norman (eds.) (1998), *An Introduction to Environmental Biophysics*, 2nd ed., Springer, New York.

Choudhury, B.J. (1987), Relationships between vegetation indices, radiation absorption, and net photosynthesis evaluated by a sensitivity analysis, *Remote Sens. Environ.* **22**, 2, 209-233, DOI: 10.1016/0034-4257(87)90059-9.

Choudhury, B.J., N.U. Ahmed, S.B. Idso, R.J. Reginato, and C.S.T. Daughtry (1994), Relations between evaporation coefficients and vegetation indices studied by model simulations, *Remote Sens. Environ.* **50**, 1, 1-17, DOI: 10.1016/0034-4257(94)90090-6.

Colaizzi, P.D., W.P. Kustas, M.C. Anderson, N. Agam, J.A. Tolk, S.R. Evett, T.A. Howell, P.H. Gowda, and S.A. O'Shaughnessy (2012a), Two-source energy balance model estimates of evapotranspiration using component and composite surface temperatures, *Adv. Water Resour.* **50**, 134-151, DOI: 10.1016/j.advwatres.2012.06.004.

Colaizzi, P.D., S.R. Evett, S.A. O'Shaughnessy, and T.A. Howell (2012b), Using plant canopy temperature to improve irrigated crop management. **In:** *Proc. 24th Annual Central Plains Irrigation Conf., 21-22 February 2012*, Colby, USA, 203-223.

Corbari, C., W. Timmermans, and A. Andreu (2015), Intercomparison of surface energy fluxes estimates from the FEST-EWB and TSEB models over the heterogeneous REFLEX 2012 site (Barrax, Spain), *Acta Geophys.* **63**, 6, 1609-1638, DOI: 10.2478/s11600-014-0258-x (this issue).

de Miguel, E., M. Jiménez, I. Pérez, Ó.G. de la Camara., F. Muñoz, and J.A. Gómez-Sánchez (2015), AHS and CASI processing for the REFLEX

remote sensing campaign: methods and results, *Acta Geophys.* **63**, 6, 1485-1498, DOI: 10.1515/acgeo-2015-0031 (this issue).

French, A.N., F. Jacob, M.C. Anderson, W.P. Kustas , W. Timmermans, A. Gieske, Z. Su, H. Su, M.F. McCabe, F. Li, J. Prueger, and N. Brunsell (2005), Surface energy fluxes with the Advanced Spaceborne Thermal Emission and Reflection Radiometer (ASTER) at the Iowa 2002 SMACEX site (USA), *Remote Sens. Environ.* **99**, 1-2, 55-65, DOI: 10.1016/j.rse.2005.05.015.

Gardner, B.R., D.C. Nielsen, and C.C. Shock (1992), Infrared thermometry and the Crop Water Stress Index. I. History, theory, and baselines, *J. Prod. Agric.* **5**, 4, 462-466, DOI: 10.2134/jpa1992.0462.

Gillespie, A., S. Rokugawa, T. Matsunaga, J.S. Cothern, S. Hook, and A.B. Kahle (1998), A temperature and emissivity separation algorithm for Advanced Spaceborne Thermal Emission and Reflection Radiometer (ASTER) images, *IEEE Trans. Geosci. Remote Sens.* **36**, 4, 1113-1126, DOI: 10.1109/36.700995.

Gonzalez-Dugo, M.P., C.M.U. Neale, L. Mateos, W.P. Kustas, J.H. Prueger, M.C. Anderson, and F. Li (2009), A comparison of operational remote sensing-based models for estimating crop evapotranspiration, *Agr. Forest Meteorol.* **149**, 11, 1843-1853, DOI: 10.1016/j.agrformet.2009.06.012.

Huntingford, C., S.J. Allen, and R.J. Harding (1995), An intercomparison of single and dual-source vegetation-atmosphere transfer models applied to transpiration from Sahelian savannah, *Bound.-Lay. Meteorol.* **74**, 4, 397-418, DOI: 10.1007/BF00712380.

Jackson, R.D., S.B. Idso, R.J. Reginato, and P.J. Pinter Jr. (1981), Canopy temperature as a crop water stress indicator, *Water Resour. Res.* **17**, 4, 1133-1138, DOI: 10.1029/WR017i004p01133.

Kalma, J.D., T.R. McVicar, and M.F. McCabe (2008), Estimating land surface evaporation: A review of methods using remotely sensed surface temperature, data, *Surv. Geophys.* **29**, 4-5, 421-469, DOI: 10.1007/s10712-008-9037-z.

Kustas, W.P., and J.M. Norman (1997), A two-source approach for estimating turbulent fluxes using multiple angle thermal infrared observations, *Water Resour. Res.* **33**, 6, 1495-1508, DOI: 10.1029/97WR00704.

Kustas, W.P., and J.M. Norman (1999), Evaluation of soil and vegetation heat flux predictions using a simple two-source model with radiometric temperatures for partial canopy cover, *Agr. Forest Meteorol.* **94**, 1, 13-29, DOI: 10.1016/S0168-1923(99)00005-2.

Kustas, W.P., and J.M. Norman (2000), A two-source energy balance approach using directional radiometric temperature observations for sparse canopy covered surfaces, *Agron. J.* **92**, 5, 847-854, DOI: 10.2134/agronj2000.925847x.

Kustas, W.P., D.I. Stannard, and K.J. Allwine (1996), Variability in surface energy flux partitioning during Washita '92: Resulting effects on Penman–

Monteith and Priestley–Taylor parameters, *Agr. Forest Meteorol*. **82**, 1-4, 171-193, DOI: 10.1016/0168-1923(96)02334-9.

Kustas, W.P., X. Zhan, and T.J. Schmugge (1998), Combining optical and microwave remote sensing for mapping energy fluxes in a semiarid watershed, *Remote Sens. Environ*. **64**, 2, 116-131, DOI: 10.1016/S0034-4257(97)00176-4.

Lhomme, J.P., and A. Chehbouni (1999), Comments on dual-source vegetation-atmosphere transfer models, *Agr. Forest Meteorol*. **94**, 3-4, 269-273, DOI: 10.1016/S0168-1923(98)00109-9.

Li, F., W.P. Kustas, J.H. Prueger, C.M.U. Neale, and T.J. Jackson (2005), Utility of remote sensing-based two-source energy balance model under low- and high-vegetation cover conditions, *J. Hydrometeor*. **6**, 6, 878-891, DOI: 10.1175/JHM464.1.

Massman, W.J., and J.C. Weil (1999), An analytical one-dimensional second-order closure model of turbulence statistics and the Lagrangian time scale within and above plant canopies of arbitrary structure, *Bound.-Lay. Meteorol*. **91**, 1, 81-107, DOI: 10.1023/A:1001810204560.

Mattar, C., B. Franch, J.A. Sobrino, C. Corbari, J.C. Jiménez-Muñoz, L. Olivera-Guerra, D. Skokovic, G. Sória, R. Oltra-Carriò, Y. Julien, and M. Mancini (2014), Impacts of the broadband albedo on actual evapotranspiration estimated by S-SEBI model over an agricultural area, *Remote Sens. Environ*. **147**, 23-42, DOI: 10.1016/j.rse.2014.02.011.

Merlin, O., and A. Chehbouni (2004), Different approaches in estimating heat flux using dual angle observations of radiative surface temperature, *Int. J. Remote Sens*. **25**, 1, 275-289, DOI: 10.1080/0143116031000116408.

Morillas, L., M. García, H. Nieto, L. Villagarcia, I. Sandholt, M.P. Gonzalez-Dugo, P.J. Zarco-Tejada, and F. Domingo (2013), Using radiometric surface temperature for surface energy flux estimation in Mediterranean drylands from a two-source perspective, *Remote Sens. Environ*. **136**, 234-246, DOI: 10.1016/j.rse.2013.05.010.

Norman, J.M., W.P. Kustas, and K.S. Humes (1995), Source approach for estimating soil and vegetation energy fluxes in observations of directional radiometric surface temperature, *Agr. Forest Meteorol*. **77**, 3-4, 263-293, DOI: 10.1016/0168-1923(95)02265-Y.

Priestley, C.H.B., and R.J. Taylor (1972), On the assessment of surface heat flux and evaporation using large-scale parameters, *Mon. Weather Rev*. **100**, 2, 81-92, DOI: 10.1175/1520-0493(1972)100<0081:OTAOSH>2.3.CO;2.

Scott, R.L., T.E. Huxman, W.L. Cable, and W.E. Emmerich (2006), Partitioning of evapotranspiration and its relation to carbon dioxide exchange in a Chihuahuan Desert shrubland, *Hydrol. Process*. **20**, 15, 3227-3243, DOI: 10.1002/hyp.6329.

Shuttleworth, W.J., and R.J. Gurney (1990), The theoretical relationship between foliage temperature and canopy resistance in sparse crops, *Quart. J. Roy. Meteorol. Soc.* **116**, 492, 497-519, DOI: 10.1002/qj.49711649213.

Sobrino, J.A., J.C. Jiménez-Muñoz, P.J. Zarco-Tejada, G. Sepulcre-Cantò, and E. de Miguel (2006), Land surface temperature derived from airborne hyperspectral scanner thermal infrared data, *Remote Sens. Environ.* **102**, 1-2, 99-115, DOI: 10.1016/j.rse.2006.02.001.

Sobrino, J.A., J.C. Jiménez-Muñoz, P.J. Zarco-Tejada, G. Sepulcre-Cantó, E. de Miguel, G. Sòria, M. Romaguera, Y. Julien, J. Cuenca, V. Hidalgo, B. Franch, C. Mattar, L. Morales, A. Gillespie, D. Sabol, L. Balick, Z. Su, L. Jia, A. Gieske, W.J. Timmermans, A. Olioso, F. Nerry, L. Guanter, J. Moreno, and Q. Shen (2009), Thermal remote sensing from Airborne Hyperspectral Scanner data in the framework of the SPARC and SEN2FLEX projects: an overview, *Hydrol. Earth Syst. Sci.* **13**, 2031-2037, DOI: 10.5194/hess-13-2031-2009.

Timmermans, J., C. van der Tol, W. Verhoef, and Z. Su (2008), Contact and directional radiative temperature measurements of sunlit and shaded land surface components during the SEN2FLEX 2005 campaign, *Int. J. Remote Sens.* **29**, 17-18, 5183-5192, DOI: 10.1080/01431160802036599.

Timmermans, W.J., W.P. Kustas, M.C. Anderson, and A.N. French (2007), An intercomparison of the Surface Energy Balance Algorithm for Land (SEBAL) and the Two-Source Energy Balance (TSEB) modeling schemes, *Remote Sens. Environ.* **108**, 4, 369-384, DOI: 10.1016/j.rse.2006.11.028.

Timmermans, W.J., G. Bertoldi, J.D. Albertson, A. Olioso, Z. Su, and A.S.M. Gieske (2008), Accounting for atmospheric boundary layer variability on flux estimation from RS observations, *Int. J. Remote Sens.* **29**, 17-18, 5275-5290, DOI: 10.1080/01431160802036383.

Timmermans, W.J., Z. Su, and A. Olioso (2009), Footprint issues in scintillometry over heterogeneous landscapes, *Hydrol. Earth Syst. Sci.* **13**, 2179-2190, DOI: 10.5194/hess-13-2179-2009.

Timmermans, W.J., J.C. Jiménez-Muñoz, V. Hidalgo, K. Richter, J.A. Sobrino, G. d'Urso, F. Mattia, G. Satalino, E. De Lathauwer, and V.R.N. Pauwels (2011), Estimation of the spatially distributed surface energy budget for AgriSAR 2006, Part I: Remote sensing model intercomparison, *IEEE J. STARS* **4**, 2, 465-481, DOI: 10.1109/JSTARS.2010.2098019.

Timmermans, W.J., C. van der Tol, J. Timmermans, M. Ucer, X. Chen, L. Alonso, J. Moreno, A. Carrara, R. Lopez, F. de la Cruz Tercero, H.L. Corcoles, E. de Miguel, J.A.G. Sanchez, I. Pérez, B. Franch, J.-C.J. Munoz, D. Skokovic, J. Sobrino, G. Soria, A. MacArthur, L. Vescovo, I. Reusen, A. Andreu, A. Burkart, C. Cilia, S. Contreras, C. Corbari, J.F. Calleja, R. Guzinski, C. Hellmann, I. Herrmann, G. Kerr, A.-L. Lazar, B. Leutner, G. Mendiguren, S. Nasilowska, H. Nieto, J. Pachego-Labrador, S. Pulanekar, R. Raj, A. Schikling, B. Siegmann, S. von Bueren, and Z. Su (2015), An overview of the Regional Experiments for Land-atmosphere Exchanges

2012 (REFLEX 2012) campaign, *Acta Geophys.* **63**, 6, 1465-1484, DOI: 10.2478/s11600-014-0254-1 (this issue).

van der Tol, C., W. Timmermans, C. Corbari, A. Carrara, J. Timmermans, and Z. Su (2015), An analysis of turbulent heat fluxes and the energy balance during the REFLEX campaign, *Acta Geophys.* **63**, 6, 1516-1539, DOI: 10.1515/acgeo-2015-0061 (this issue).

Vesala, T., N. Kljun, U. Rannik, J. Rinne, A. Sogachev, T. Markkanen, K. Sabelfeld, T. Foken, and M.Y. Leclerc (2008), Flux and concentration footprint modelling: State of the art, *Environ. Poll.* **152**, 3, 653-666, DOI: 10.1016/j.envpol.2007.06.070.

Vining, R.C., and B.L. Blad (1992), Estimation of sensible heat flux from remotely sensed canopy temperatures, *J. Geophys. Res.* **97**, D17, 18951-18954, DOI: 10.1029/92JD01626.

Utility of an Automated Thermal-Based Approach for Monitoring Evapotranspiration

Wim J. TIMMERMANS[1], William P. KUSTAS[2], and Ana ANDREU[3]

[1]University of Twente, Faculty of Geo-information Science and Earth Observation, Department of Water Resources, Enschede, The Netherlands; e-mail: w.j.timmermans@utwente.nl

[2]Hydrology and Remote Sensing Laboratory, USDA/ARS, Beltsville, MD, USA

[3]Instituto de Investigación y Formación Agraria y Pesquera (IFAPA), Cordoba, Spain

A b s t r a c t

A very simple remote sensing-based model for water use monitoring is presented. The model acronym DATTUTDUT (Deriving Atmosphere Turbulent Transport Useful To Dummies Using Temperature) is a Dutch word which loosely translates as "it's unbelievable that it works". DATTUTDUT is fully automated and only requires a surface temperature map, making it simple to use and providing a rapid estimate of spatially-distributed fluxes. The algorithm is first tested over a range of environmental and land-cover conditions using data from four short-term field experiments and then evaluated over a growing season in an agricultural region. Flux model output is in satisfactory agreement with observations and established remote sensing-based models, except under dry and partial canopy cover conditions. This suggests that DATTUTDUT has utility in identifying relative water use and as an operational tool providing initial estimates of *ET* anomalies in data-poor regions that would be confirmed using more robust modeling techniques.

Key words: remote sensing, water use monitoring, temperature index scheme, automated, operational.

1. INTRODUCTION

Knowledge of the surface energy balance is of prime interest to the fields of meteorology, hydrology, and agronomy. Examples range from General Circulation Models (GCMs) for weather prediction and climate change to impacts of water use in threatened ecosystems, as well as the determination of crop water use, stress, and yield in agro-ecosystems. Numerous Soil-Vegetation-Atmosphere Transfer (SVAT) schemes have been developed in recent years with varying complexity. However, complex model parameterization is rarely possible at appropriate spatial or temporal resolution to adequately represent regional or global scale turbulent heat exchange (Goetz *et al.* 1999). Moreover, operational models for evapotranspiration (*ET*) estimation, using ground-based observations, have shown varying degrees of success (Parlange *et al.* 1995).

Satellite remote sensing potentially offers the possibility of collecting input data at a suitable temporal and spatial scale for regional applications. However, satellite observations cannot provide spatially distributed atmospheric variables, often required by SVAT schemes. These inputs include solar radiation, wind speed, air temperature, and vapor pressure over large heterogeneous areas (Jiang and Islam 2001). Consequently, several studies have proposed the combined use of remotely sensed with SVAT approaches that require minimal ground data (Anderson *et al.* 1997, Bastiaanssen *et al.* 1998, Norman *et al.* 1995, Roerink *et al.* 2000, Senay *et al.* 2013, Su 2002) or derive key meteorological data from the remotely sensed observations (Prihodko and Goward 1997, Prince *et al.* 1998). Generally, the surface energy balance equation is used to estimate actual evapotranspiration as a residual term (Jiang and Islam 2001). However, reliable estimation of surface energy balance components from remotely sensed observations typically requires land cover information about surface properties (*i.e.*, land use/vegetation type, surface roughness, fractional vegetation cover) and a physically-based SVAT scheme having land surface parameterization of the turbulent energy exchange. For operational use of these models, generally a fair degree of model expertise by the operator is needed as well.

Table 1 lists the input parameters and model user expertise on decisions that are necessary to apply the Two-Source Energy Balance (TSEB) model (Norman *et al.* 1995) and related Atmosphere Land Exchange Inverse (ALEXI) approach (Anderson *et al.* 1997, 2005), the Surface Energy Balance System (SEBS) model (Su 2002), the Surface Energy Balance Algorithm for Land (SEBAL) model (Bastiaanssen *et al.* 1998) and the Simplified Surface Energy Balance for operational applications (SSEBop) model (Senay *et al.* 2013) as compared to the current algorithm, DATTUTDUT. The table lists the main model inputs required by the differ-

ent models, although sensitivity to these inputs significantly varies. For example, only nominal estimates of the meteorological input (wind speed, air temperature, and relative humidity) listed under the SEBAL algorithm are needed; the algorithm's internal calibration process circumvents the need for accurate values. Similarly for the NDVI end-member selection for the TSEB and SEBS models is one of a number of possible methodologies used in determining fractional vegetation cover (Carlson and Ripley 1997, Choudhury *et al.* 1994).

Table 1

Main model input required by
TSEB, ALEXI, SEBS, SEBAL, SSEBop, and DATTUTDUT

Necessary input	TSEB	ALEXI	SEBS	SEBAL	SSEBop	DATTU-TDUT
In situ / Ancillary data:						
Solar radiation, or:	√	√	√	√		
Atmospheric transmittance, or	√	√	√	√		
Elevation					√	
Atmospheric pressure	√		√			
Wind speed	√	√	√	√		
Air temperature	√		√	√	√	
Relative humidity	√		√	√		
Sensor viewing angle	√	√				
Radiosounding		√				
Reference *ET*					√	
Remote sensing / Spatial data:						
Reflectance			√	√	√	
NDVI/LAI	√	√	√	√	√	
Surface temperature	√	√	√	√	√	√
Landcover, or:	√	√				
Aerodynamic properties	√	√	√			
User expertise:						
Wet pixel selection				√		
Dry pixel selection				√		
NDVI end-member bare soil	√		√			
NDVI end-member full vegetation	√		√			

In general, the more complex the model formulations of the land surface-atmosphere exchange, the more information/input variables are required. With reliable inputs, often the more sophisticated models provide more reliable estimates under a wider range of environmental conditions. However, when monitoring over regions having little ground information or ancillary observations of meteorological conditions, the inputs required by more sophisticated models are not available or unreliable, causing significant uncertainty in model output. Under such conditions, a simple modeling approach requiring minimal ancillary inputs could prove to be fairly robust, particularly for long-term water use monitoring where errors in short-term (daily) *ET* are often modulated, for example when evaluated as cumulative *ET* over a growing season. This is the rationale for developing a very simple model for routine monitoring of the surface energy balance, with emphasis on an operational system requiring no user expertise. The "Deriving Atmosphere Turbulent Transport Useful To Dummies Using Temperature (DATTUTDUT)" algorithm does not need any ancillary data and only requires a surface temperature image. Furthermore, the algorithm in theory does not need any user inference and is fully automated, provided a cloud-free and atmospherically corrected radiometric surface temperature image is available.

The main objective of this paper is to present an operational and automated remote sensing-based system requiring no calibration and suitable for monitoring spatially distributed water and heat fluxes and demonstrate advantages and limitations of using a very simple temperature-based approach. In Section 2, the formulations and their physical basis are presented and justification for simplifications is discussed. Then, in Section 3, the performance of the proposed model is analyzed. Three different comparison protocols are followed to demonstrate different aspects of the models utility. First the ability of reproducing local energy fluxes in relation to results from well-established and more complex remote sensing-based modeling schemes over a range of environmental and climatologic conditions is presented. Secondly, a spatial model inter-comparison over a very heterogeneous area is carried out to evaluate extreme conditions and performance across a landscape. A third, temporal, evaluation then concerns the performance in estimating actual evapotranspiration over a growing season. In Section 4 a discussion of the results of the different evaluations follows, after which the concluding remarks are provided in Section 5. The validation data for the evaluations come from large scale interdisciplinary experiments conducted in a semi-arid rangeland region – Monsoon'90 (Kustas *et al.* 1994a), a winter wheat/ grazing-lands site − Southern Great Plains'97 (Jackson *et al.* 1999), a corn and soybean production region − SMEX/SMACEX'02 (Kustas *et al.* 2005), an agricultural test site − REFLEX'12 (Timmermans *et al.* 2014), and an irri-

gated agricultural site within an arid region – Gediz'98 (Kite and Droogers 2000).

2. MODEL FORMULATION

2.1 Instantaneous fluxes

Generally, remote sensing-based SVAT schemes use instantaneous observations of the land surface to provide estimates of instantaneous net radiation, R_N, soil, G, sensible, H, and latent, λE, heat fluxes (all in $\mathrm{W\,m^{-2}}$) by solving the energy balance equation

$$R_N = G + H + \lambda E \ , \tag{1}$$

where λ represents the latent heat of vaporization [$\mathrm{J\,kg^{-1}}$] and E is the amount of evaporated water [kg]. The net radiation is usually estimated by dividing it into its components:

$$R_N = R_S^\downarrow + R_S^\uparrow + R_L^\downarrow + R_L^\uparrow = \left(1 - \rho_0\right) \cdot R_S^\downarrow + \varepsilon_0 \cdot \varepsilon_a \cdot \sigma \cdot T_a^4 - \varepsilon_0 \cdot \sigma \cdot T_0^4 \ , \tag{2}$$

where R stands for radiation, and the subscripts N, S, and L refer to net, shortwave, and longwave, and the superscripted arrows indicate incoming (downward) and outgoing (upward) flux directions. Temperature (K) is represented by T, whereas the Greek symbols ρ, ε, and σ represent albedo (–), emissivity (–), and the Stefan–Boltzmann constant ($5.6697 \times 10^{-8}\,\mathrm{W\,m^{-2}\,K^{-4}}$), respectively. Subscripts 0 and a refer to surface and atmospheric level. Typically in these SVAT schemes the soil heat flux is estimated as a semi-empirical ratio to net radiation, using a constant ratio or a function of vegetation indices (Bateni *et al.* 2014). The available energy, R_N-G, is then distributed over the turbulent fluxes, H and λE, by either using the radiometric surface temperature to calculate H and then obtain λE as a residual of the energy balance equation (Bastiaanssen *et al.* 1998, Norman *et al.* 1995, Su 2002), or by incorporating the effect of vapor pressure deficit to estimate crop water use or a stress index (Jackson *et al.* 1981, Menenti and Choudhury 1993).

In the current approach we attempt to solve Eqs. 1 and 2 in an automated manner by parameterizing all variables using only T_0 and its end-members, T_{min} and T_{max} as an input. These temperature extremes are derived from the image itself, which should be cloud free and have constant atmospheric conditions.

The surface albedo has been reported to vary with surface temperature depending on moisture conditions by several authors (Bastiaanssen *et al.* 1998, Jacob *et al.* 2002). Other approaches assume nominal values for soil and vegetation reflective properties (French *et al.* 2003, Kustas and Norman

1999). Here, the surface albedo is thought to vary linearly with radiometric surface temperature between 0.05 and 0.25, following

$$\rho_0 = 0.05 + \left(\frac{T_0 - T_{\min}}{T_{\max} - T_{\min}} \right) \cdot 0.2 \; . \tag{3}$$

These somewhat arbitrary values are taken from Brutsaert (1982) and Garratt (1992); the basic assumption is that dark densely vegetated objects appear cooler and bright bare objects such as soils and rock outcrops generally appear hot.

The shortwave incoming radiation follows from

$$R_S^{\downarrow} = \tau \cdot S_{\text{exo}} \; , \tag{4}$$

where τ represents the shortwave atmospheric transmissivity [–] and S_{exo} [W m^{-2}] is the exo-atmospheric shortwave radiation which depends only on the sun-earth geometry (Campbell and Norman 1998, Monteith and Unsworth 1990).

To facilitate a fully automatic and fast operational scheme, nominal values are taken for transmissivity and emissivity values. For clear sky conditions, Burridge and Gadd (1974) presented a very simple parameterization for instantaneous shortwave atmospheric transmissivity [–], following

$$\tau = 0.6 + 0.2 \cdot \sin(\alpha) \; , \tag{5}$$

where α represents the solar elevation angle [rad], useful when dealing with large image scenes where solar angles are not constant. However, for simplicity here a constant value of 0.7 is taken for the atmospheric transmissivity. Numerous empirical relations are reported for apparent atmospheric emissivity (Brutsaert 1982). If the following, approximation of Bastiaanssen *et al.* (1998) is adopted

$$\varepsilon_a = 1.08 \cdot (-\ln \tau)^{0.265} \tag{6}$$

and, in combination with an atmospheric transmissivity of 0.7, an apparent atmospheric emissivity of about 0.8 is obtained. Since most natural objects emit radiation at least at an efficiency of 96% (Garratt 1992) the surface emissivity [–] is taken equal to unity. Taking the air temperature equal to $T_{\min}$ in combination with these nominal values for emissivity, all radiation components can now be determined following Eq. 2.

The ratio between soil heat flux and net radiation, G [–], is reported to vary from 0.05 for fully vegetated areas (Choudhury 1987, Monteith and Unsworth 1990) to 0.45 for bare soil (Brutsaert 1982, Choudhury 1987). In a

similar fashion as for the surface albedo, a linear relation with radiometric surface temperature is assumed:

$$\Gamma = \frac{G}{R_n} = 0.05 + \left(\frac{T_0 - T_{min}}{T_{max} - T_{min}} \right) \cdot 0.4 \ . \tag{7}$$

The underlying assumption is again that dark densely vegetated areas appear cooler (Bastiaanssen *et al.* 1998, Menenti and Choudhury 1993, Roerink *et al.* 2000) and over densely vegetated areas a smaller part of the net radiation is reaching the surface. Bare soil generally appears hotter and over these areas a larger part of the net radiation will be available to heat the soil surface.

A common feature of thermal-based methods is that radiometric surface temperature is the key remotely-sensed parameter partitioning the available energy between sensible and latent heat. This is also reflected in several sensitivity studies (Anderson *et al.* 1997, Bastiaanssen 1995, Kustas and Norman 1999) and especially in model inter-comparisons (Zhan *et al.* 1996) where surface temperature clearly is the input variable that has the largest impact on model output. It is also important to note that surface layer air temperature is also a critical variable for many of the models that require a surface-air temperature gradient unless there is a built-in procedure that removes or minimizes this requirement (Anderson *et al.* 2007, Timmermans *et al.* 2007). A modeling framework that minimizes the effect of errors in surface and surface layer air temperatures on the calculation of the turbulent fluxes was proposed by Bastiaanssen *et al.* (1998). Their methodology, SEBAL, basically assumes linearity between surface-air temperature differences and surface temperature whose slope is defined by dry and wet areas (hydrologic extremes or end-members) within the scene having maximum and minimum surface temperatures and heat fluxes, *H* and *LE*, determined from the energy balance equation (Eq. 1). When evaluating such a technique, along with other traditional remote sensing-based SVAT models, French *et al.* (2005b) and Timmermans *et al.* (2007) found that the linearity assumption in the SEBAL scheme is not universally valid, a phenomenon also recognized by Bastiaanssen *et al.* (1998) in their original paper. However, this relation has utility in providing an internal calibration for effectively partitioning the available energy between *H* and *LE* over the scene as long as there is no significant land cover differences (*i.e.*, agricultural *versus* forested areas) within the scene which would have a major impact of aerodynamic properties (Norman *et al.* 2006). In SEBAL the assumption is made that at a certain maximum radiometric surface temperature the latent heat flux is zero, whereas sensible heat flux is at its minimum rate at a certain minimum radiometric surface temperature. However, instead of using flux inversion at the

extremes which requires iterative processes to determine the resistance-heat flux relation, here a simple linear relation between evaporative fraction (Λ) and surface temperature extremes is assumed:

$$\Lambda = \frac{\lambda E}{\lambda E + H} = \frac{\lambda E}{R_n - G} = \frac{T_{max} - T_0}{T_{max} - T_{min}} \ . \tag{8}$$

There needs to be hydrological contrast in the image, meaning that both the wet and dry conditions are present in the image scene; a necessary condition for methods that are trying to derive the turbulent fluxes from hydrological contrast (Bastiaanssen *et al.* 1998, Menenti and Choudhury 1993, Pelgrum and Bastiaanssen 1996, Roerink *et al.* 2000). The maximum temperature, T_{max}, is taken as the hottest pixel in the image, whereas the minimum temperature, T_{min} [K], is taken as the 0.5% lowest temperature in the image. The reason for not taking the lowest temperature in the image is to avoid extreme conditions (open water) and to take that part of the image that is transpiring at a potential rate. Following Tasumi *et al.* (2000), the hottest location in the image is used to determine T_{max} in Eq. 8. Similar approaches based on the same physical principle have been proposed since the early days of operational thermal infrared remote sensing (Jackson *et al.* 1981, Jiang and Islam 2001, Roerink *et al.* 2000). However, the main differences with the current approach are that DATTUTDUT is tuning-free, fully automated, and only requires an LST image as input.

2.2 Daily estimates

Extending essentially instantaneous fluxes from a satellite "snapshot" observation to daily values either involves multi-temporal observations such as from geostationary satellite observations (Anderson *et al.* 1997, Mecikalski *et al.* 1999, Norman *et al.* 2000) or assuming a constant energy partitioning over the daytime period. By assuming self-preservation (conservative relative partition of the energy flux among its components) in the diurnal evolution of the energy balance, Λ can be taken as constant throughout the day. It has been demonstrated that this assumption holds for environmental conditions where soil moisture does not change significantly (Crago 1996, Kustas *et al.* 1994b, Nichols and Cuenca 1993, Shuttleworth *et al.* 1989). This assumption is also used in other models, such as SEBAL (Bastiaanssen *et al.* 1998) and S-SEBI (Roerink *et al.* 2000).

Since geostationary satellites only provide useful data for mid-latitudes at a rather low spatial resolution ($\sim$ 5-10 km) and also because of a need for a simplified approach, hence minimum computational requirements, here the assumption of constant evaporative fraction over the daytime period is adopted. However, the recent work has shown that this assumption might be

violated under certain conditions (Chehbouni *et al.* 2008, Delogu *et al.* 2012, Gentine *et al.* 2007) and a recent study suggests using at-surface solar radiation is the most robust for up-scaling instantaneous *ET* over a range of environmental conditions (Cammalleri *et al.* 2014). Nevertheless, this approach provides reasonable estimation of daily amounts of evapotranspiration from the instantaneous estimates during the daytime (Brutsaert and Chen 1996).

Since the evaporative fraction is estimated from Eq. 8 and the soil heat flux is assumed to cancel on a daily basis, one only needs an estimate of the daily amount of net radiation to obtain the daily amount of latent heat, λE_{24}, both in MJ m^{-2};

$$\Lambda_i = \Lambda_{24} = \frac{\lambda E_i}{\lambda E_i + H_i} = \frac{\lambda E_{24}}{\lambda E_{24} + H_{24}} = \frac{\lambda E_{24}}{R_{n,24} - G_{24}} = \frac{\lambda E_{24}}{R_{n,24}} \ . \tag{9}$$

The daily amount of net radiation $R_{n,24}$ [MJ m^{-2}] is calculated following:

$$R_{n,24} = S_{n,24} + L_{n,24} \ , \tag{10}$$

where *S* and *L* represent shortwave and longwave radiation, whereas the subscripts *n* and 24 stand for net and 24 hours, respectively. Several methods exist for estimating both components. Here the daily shortwave radiation [MJ] is estimated following:

$$S_{n,24} = \left(1 - \rho_{0,24}\right) \cdot \tau_{24} \cdot S_{\text{exo},24} \ , \tag{11}$$

where the daily exo-atmospheric radiation [MJ m^{-2}], $S_{\text{exo},24}$, depends only on trigonometric astronomic relations, readily available from handbooks (Campbell and Norman 1998, Duffie and Beckman 1991, Monteith and Unsworth 1990) or by integrating the exo-atmospheric radiation from sunrise to sunset. Daily average surface albedo, $\rho_{0,24}$, is obtained from multiplying the instantaneous value with a constant *c* [–]. According to Menenti *et al.* (1989) *c* may be taken equal to 1.1 when compared to typical daytime surface albedo values. Daily average transmissivity values [–], τ_{24}, may be obtained from several sources. Here we adopted the instantaneous value under the assumption of a cloud free day.

For the longwave components a semi-empirical relation developed by de Bruin (1987) for daily average net longwave radiation, $L_{n,24\text{-avg}}$ [W m^{-2}], is used:

$$L_{n,24-\text{avg}} = -110 \cdot \tau_{24} \ . \tag{12}$$

To convert this quantity to daily net longwave radiation, in MJ m^{-2}, it needs to be multiplied with the daylength (s). The daily net longwave radiation is assumed constant over the scene.

In order to obtain daily amounts of water evaporated and transpired, E_{24} [kg m^{-2}], the daily total of latent heat, λE_{24}, needs be corrected for the latent heat of vaporization, λ [MJ kg^{-1}]. This latent heat of vaporization depends to some extent on air temperature, for which T_{min} is taken:

$$\lambda = 2.501 - 0.002361 \cdot \left(T_{min} - 273.15 \right) . \tag{13}$$

Although we developed the scheme to be fully automated and also such that no ancillary data is needed, it is obvious that if additional data are available these may be applied accordingly. Since the algorithm is physically based, use of these ancillary data should potentially further improve the algorithm performance.

3. MODEL PERFORMANCE

To demonstrate different aspects of the models' utility, three different comparison protocols are followed. First, the ability of estimating local energy fluxes is presented. In order to ensure both a range of environmental and climatic conditions as well as sufficient ground truth data, four study areas having extensive field observations were selected for evaluating DATTUTDUT output and to compare results with published results using more established and more complex remote sensing-based energy balance models (French *et al.* 2005b, Timmermans *et al.* 2007, 2014). The other remote sensing energy balance modeling approaches applied to these data sets are SEBAL as originally formulated in Bastiaanssen *et al.* (1998) and two versions of the TSEB (Norman *et al.* 1995). One version uses local meteorological observations (French *et al.* 2003, Kustas and Norman 1997) and was applied to the Monsoon'90, SGP'97, and REFLEX'12 experiments. The other version, ALEXI, is a time-integrated approach with TSEB coupled to an atmospheric boundary layer growth model and requiring thermal-IR observations at two instances in the early and mid-morning period (Anderson *et al.* 1997, French *et al.* 2005b) and was applied to the SMACEX'02 experimental site.

Secondly, a spatial model inter-comparison between DATTUTDUT and the SEBAL and TSEB algorithms over a very heterogeneous area is carried out to evaluate extreme conditions and model performance across a landscape. Data from the REFLEX'12 experiment (Timmermans *et al.* 2014) over an agricultural test-site near Barrax, Spain, is used here since the area is characterized by the co-existence of dry and hot bare soil and a variety of well-watered crops.

Thirdly, with a fully automated algorithm using midday surface temperature that does not require ancillary data on land use, fractional vegetation cover or meteorological inputs, just hydrological extremes (wet and dry pix-

el) within the scene for estimating surface energy balance, the challenge remains to demonstrate its utility for operational monitoring of longer-term water use. This is done by applying the scheme to data collected at two sites during the joint International Water Management Institute (IWMI)/General Directorate of Rural Services, Government of Turkey (GDRS) study of the Gediz River Basin, as described in Kite and Droogers (2000). The DATTUTDUT algorithm is evaluated against published results from other methodologies. However, in this case the purpose is to evaluate its utility for operational water use monitoring purposes.

3.1 Data description

Monsoon'90

The Monsoon'90 field experiment is described in Kustas *et al.* (1994a), and covers a semiarid rangeland in the Walnut Gulch Experimental Watershed near Tucson, Arizona. The remote sensing data used in this analysis were acquired with the NS001 sensor mounted in a NASA C-130 aircraft. The NS001 instrument has eight bands, of which seven correspond to the Landsat Thematic Mapper instrument. This provided aircraft-based VIS, NIR, and TIR measurements from three days during early August 1990 are used, representing dry (DOY 213), intermediate (DOY 221), and wet (DOY 216) conditions. Land cover data, necessary for the TSEB algorithm, was taken from classifying Landsat TM data of September 1990. A detailed description of the dataset used is provided in Humes *et al.* (1994), with the note that here data from DOY 213 is used instead of the data from DOY 209 used in that particular study. There were eight flux tower sites distributed over the watershed covering the main land cover types. Details of the tower measurements are given in Kustas *et al.* (1994a).

SGP'97

The Southern Great Plains'97 (SGP'97) experiment is summarized by Jackson *et al.* (1999). The data set included VIS, NIR, and TIR remote measurements over the EL Reno, Oklahoma, site and comprised fallow and tilled winter wheat and grassland/pasture fields. Data collected were from the Thermal Infrared Multi-spectral Scanner (TIMS) and the Thematic Mapper Simulator (TMS) airborne instruments. Data from two days during the summer of 1997, representing wet (DOY 180) and dry (DOY 183) conditions, are used at a spatial resolution of 15 m, covering agricultural fields (both bare and vegetated) and natural riparian areas. The land use data originates from 30 m resolution imagery, based on the combination of known ground conditions and Landsat TM imagery from DOY 205 that same year. Details of the processing of the remote sensing imagery can be found in

French *et al.* (2003). There were four flux towers covering the main land cover types. Details of the tower measurements are given in Twine *et al.* (2000).

SMACEX'02

The Soil Moisture Atmosphere Coupling Experiment 2002 (SMACEX'02) data set described by Kustas *et al.* (2005) was collected over an experimental watershed in central Iowa, USA, an upper Midwest corn and soybean production region. The experiment took place during the 2002 growing season. An ASTER image collected on DOY 182 (1 July 2002) was used. The landcover map was derived from a supervised classification of Landsat imagery and ground truth observations carried out in June and July. Flux tower measurements were available from 10 locations distributed over the study area to obtain representative areal sampling (Prueger *et al.* 2005).

REFLEX'12

The REFLEX'12 campaign was an airborne campaign to support the understanding of land-atmosphere interaction processes (Timmermans *et al.* 2014). The experiment was carried out over the Las Tiesas Experimental Farm test site near Barrax in the La Mancha region in Spain, maintained by the Provincial Technical Agronomical Institute (ITAP). The campaign took place during 10 days in the end of July 2012, when the non-irrigated parts of the area are characterized by extremely dry conditions. Airborne imagery from the Airborne Hyperspectral Sensor (AHS) obtained during DOY 207 (de Miguel *et al.* 2015) was used in this analysis. Flux tower observations and a Large Aperture Scintillometer (LAS) covering four sites with distinctly different landcover provided the ground truth (van der Tol *et al.* 2014).

GEDIZ'98

The intercomparison study over an irrigated area in the Gediz River Basin in Western Turkey is described in detail in Kite and Droogers (2000). For the analysis used here a total of 73 level-1B NOAA-AVHRR images were downloaded from the internet and pre-processed into surface reflectance and surface temperature images. The procedures followed are described in detail in Gieske and Meijninger (2005). Flux observations were available from two locations within the study region. A Large Aperture Scintillometer (LAS) was deployed over a valley in the Gediz River Basin in Western Turkey. The pathlength of the scintillometer was 2.7 km and provided surface fluxes at a scale comparable to the AVHRR imagery. The land use in the valley was heterogeneous, consisting of 60% of raison grape, 15% cotton, 15% of fruit trees, 5% pasture, and 5% of mixed tree species. The second location con-

sisted of an irrigated cotton field, located west of Menemen, in a cotton production region, homogeneous at the AVHRR pixel scale. Fluxes at this location were obtained from a fast-response temperature sensor using the temperature variance method (de Bruin 1994). In addition, net radiation, soil heat flux, and additional meteorological measurements were obtained at this location (Meijninger and de Bruin 2000).

3.2 Local model evaluation *versus* ground observations

The main assumption in the current algorithm concerns the linearity between "instantaneous" scaled temperature and half-hourly evaporative fraction via Eq. 8. The datasets described above provided the opportunity to validate that assumption. In Figure 1 the observed evaporative fraction (Λ) is plotted *versus* the scaled temperature, as defined in Eq. 8 for all four experiments. The RMSD-value (see Table 2 for definition) between the observations and model estimates for the four experiments is approximately 0.13. A linear regression with an R^2 equal to 0.65 (0.81 and 0.62 for TSEB and SEBAL, respectively) was found with a slope of 0.71 (0.98 and 0.79 for TSEB and SEBAL, respectively) and an intercept of 0.22 (0.02 and 0.10 for TSEB and SEBAL, respectively). A slope close to unity with a small intercept provides support for the use of Eq. 8 for these landscapes. Note that there was no model tuning in applying the DATTUTDUT algorithm.
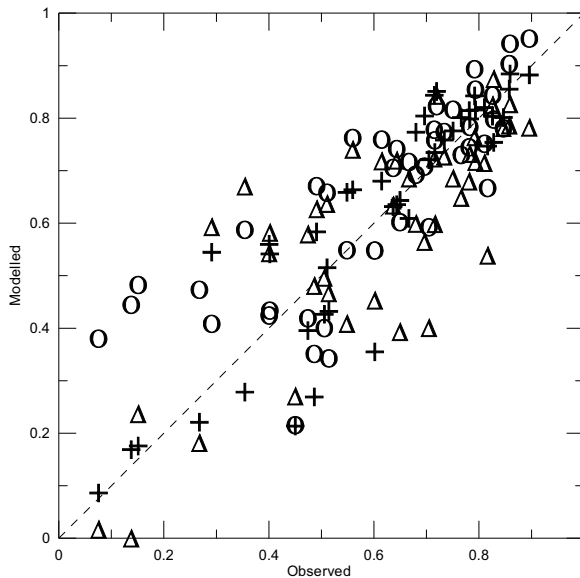
Fig. 1. Observed *versus* modeled evaporative fraction for all four experiments, using DATTUTDUT (O), SEBAL (Δ), and TSEB (+).

The scatter between DATTUTDUT-derived Λ and observations increases significantly with increasing dry or stressed conditions (*i.e.*, lower Λ values). On the other hand, the trend for SEBAL is a relatively large dispersion around intermediate values of Λ, whereas this is less so with the TSEB approach. The extremely stressed cases (Λ < 0.3) originate from sites in the REFLEX'12 dataset which were sparsely vegetated. Removing these observations from the analysis for the DATTUTDUT model resulted in a minor increase in R^2 from 0.65 to 0.68. However, more importantly, the slope and intercept changed from 0.71 and 0.22 to 0.94 and 0.06, respectively. While the REFLEX'12 conditions may be considered rather extreme in terms of vegetation stress and heterogeneity in canopy cover, reliable estimates under such conditions are necessary for accurately monitoring the spatial and temporal variations in fluxes across many landscapes.

The results for the four energy balance components for the three models are illustrated in Fig. 2 and performance of the models is evaluated using difference statistics by Willmott (1984). Table 2 lists the definitions and the quantities of the various difference statistics for the surface energy balance components as well as for the evaporative fraction. These include the RMSD, the mean absolute difference (MAD), and the mean absolute percent difference (MAPD). There is no distinction made between the four experimental datasets, and the figure indicates that the scatter with the measurements is generally greater with DATTUTDUT and SEBAL than with TSEB. In particular, the net radiation estimates of the DATTUTDUT algorithm tend to have greater discrepancies with the observations, which are more prominent at the lower values. The mean difference between observation and prediction for R_N were about 10 and 30 $W\,m^{-2}$ for TSEB and SEBAL, respectively, and around 45 $W\,m^{-2}$ for DATTUTDUT. With respect to the predicted soil heat fluxes, also the largest discrepancies with observations
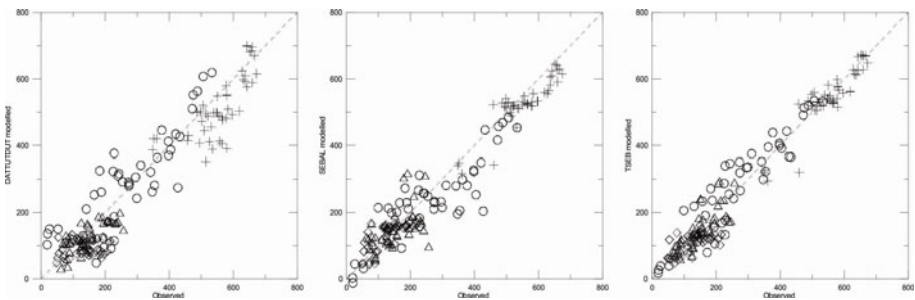
Fig. 2. Modeled and observed instantaneous energy balance components of *Rn* (+), *G* (◊), *H* (Δ), and *LE* (○) in $W\,m^{-2}$ for the Monsoon'90 (DOY 213, 216, and 221), SGP'97 (DOY 180 and 183), SMACEX (DOY 182), and REFLEX'12 (DOY 207) sites, for the three models.

Table 2

Description of statistics and quantitative measures of model performance for SEBAL (S), TSEB (T), and DATTUTDUT (D)

Variable	Description	Equation	Rn			G			H			LE			Λ		
			S	T	D	S	T	D	S	T	D	S	T	D	S	T	D
N	Number of observations		44	44	44	44	44	44	44	44	44	44	44	44	44	44	44
$\langle O \rangle$	Mean of the observation [W m^{-2}]	$\dfrac{1}{n}\sum_{i=1}^{n} O_i$	556	556	556	132	132	132	147	147	147	274	274	274	0.61	0.61	0.61
$\langle P \rangle$	Mean of prediction [W m^{-2}]	$\dfrac{1}{n}\sum_{i=1}^{n} P_i$	528	548	510	135	113	91	148	147	128	245	287	293	0.59	0.62	0.65
So	Standard deviation of observation [W m^{-2}]	$\left[\sum_{i=1}^{n}\dfrac{(O_i - \langle O \rangle)^2}{n-1}\right]^{1/2}$	81	81	81	47	47	47	55	55	55	135	135	135	0.21	0.21	0.21
Sp	Standard deviation of prediction [W m^{-2}]	$\left[\sum_{i=1}^{n}\dfrac{(P_i - \langle P \rangle)^2}{n-1}\right]^{1/2}$	75	90	94	40	30	23	58	62	42	115	142	146	0.21	0.23	0.18
MAD	Mean absolute difference [W m^{-2}]	$\dfrac{1}{n}\sum_{i=1}^{n}\lvert P_i - O_i \rvert$	37	28	62	25	30	52	42	26	33	61	45	64	0.11	0.07	0.10
MAPD	Mean absolute percent difference [W m^{-2}]	$\dfrac{100}{\langle O \rangle}\left(\dfrac{1}{n}\sum_{i=1}^{n}\lvert P_i - O_i \rvert\right)$	7	5	11	19	23	40	28	18	22	22	16	23	18	12	17
RMSD	Root-mean-square difference [W m^{-2}]	$\left[\dfrac{1}{n}\sum_{i=1}^{n}(P_i - O_i)^2\right]^{1/2}$	45	37	77	31	40	64	54	35	39	75	55	78	0.14	0.10	0.13

are noted for the DATTUTDUT scheme, an under-estimation of around 40 W m^{-2}, partly because of its direct linkage with R_N. However, the main objective here is to demonstrate the utility of the current scheme for determining spatially distributed water and heat fluxes, which are governed by the amount of available energy, $R_N - G$. Since over- and under-estimations of R_N and G are generally paired, there is reasonable agreement in modeled and observed available energy.

Mean biases between observation and prediction for sensible heat flux were negligible for TSEB and SEBAL and nearly 20 W m^{-2} for the DATTUTDUT scheme. Biases in latent heat flux were lowest for TSEB (~15 W m^{-2}), 20 W m^{-2} for DATTUTDUT, and highest for SEBAL at ~30 W m^{-2}. The RMSD-values for the three models range from 35 to 55 W m^{-2} for H and from 55 to 80 W m^{-2} for λE. A point worth mentioning here is that significant energy balance closure gaps (~100 W m^{-2}) were sometimes evident in the flux tower data (Prueger *et al.* 2005, Twine *et al.* 2000, van der Tol *et al.* 2014). Although the measurements were corrected for lack of energy balance closure, following French *et al.* (2005a, b), the model-measurement differences do include the scatter attributed to uncertainty/energy balance closure errors in the flux observations.

The described predictions of H and λE translate directly into Λ, and because of its relevance for the current approach the performance statistics for Λ are shown in Table 2 as well. All three models show an almost perfect match between the mean observed and mean predicted value, where the discrepancy of DATTUTDUT is largest but still minimal at 4%. This is mainly caused by the aforementioned deviations between observations and predictions of the turbulent fluxes at dry and sparsely vegetated locations. RMSD-values for TSEB are 0.10, whereas SEBAL and DATTUTDUT show values of 0.14 and 0.13, respectively.

3.3 Spatial model evaluation

The Barrax area is characterized by rather extreme conditions covering the full range in fractional vegetation cover as well as in moisture conditions, rendering sensible heat fluxes ranging from stable conditions to values as high as 400 W m^{-2} (Timmermans *et al.* 2008). Therefore, the REFLEX campaign offered an excellent opportunity to analyze spatial differences in model output.

Maps of model output for evaporative fraction are shown in the upper panels of Fig. 3 for TSEB, SEBAL, and DATTUTDUT. The patterns in evaporative fraction are similar for all three models. Spatial correlation between DAUTTUTDUT and TSEB is 0.92, between DATTUTDUT and SEBAL it is 0.40, and between TSEB and SEBAL this equals 0.38. The rela-
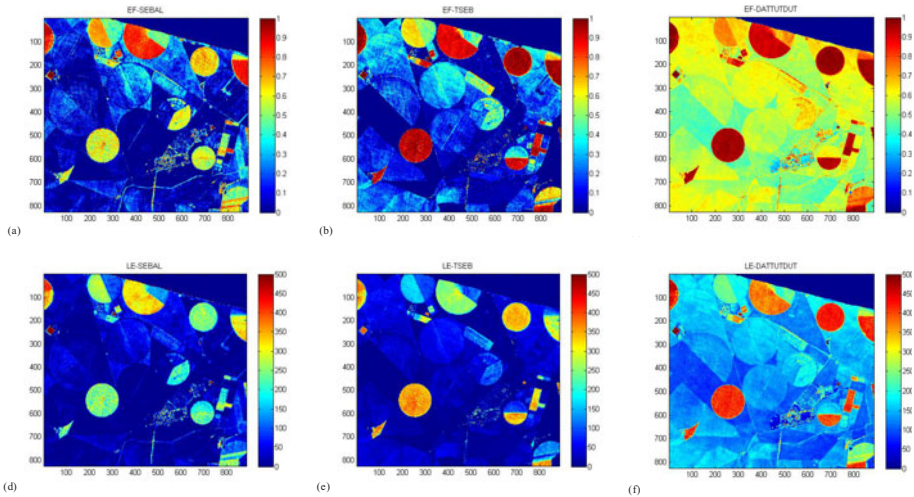
Fig. 3. Distribution of model output for *EF* and *LE* for all three models.

tively low correlation between SEBAL and TSEB is mainly caused by the difference in estimation of surface roughness length for momentum, as noted by Timmermans *et al.* (2007), and will not be discussed further here. The relatively high correlation between TSEB and DATTUTDUT is encouraging, given the simplicity of the latter. However, despite the rather good spatial agreement of evaporative fraction between the three models, especially between TSEB and DATTUTDUT, there are absolute differences of up to 0.50 [–] for some areas (see Table 3). How these translate into absolute values of latent heat flux is shown in the lower panels of Fig. 3; over certain areas differences of up to $150\,\mathrm{W\,m^{-2}}$ are noted. These are significant differences, similar to those reported by Timmermans *et al.* (2007) between SEBAL and TSEB model output of sensible heat flux.

For the relatively wet, thus irrigated, areas the three schemes show a rather similar response, which is also reflected in Table 3. For the drier, non-irrigated, parts of the area the DATTUTDUT scheme shows considerably higher values for Λ as compared to SEBAL and TSEB. This is also reflected in Fig. 1, where the 4 driest observations originate from the REFLEX'12 campaign, over a vineyard, a wheat stubble field, a forest nursery, and a camelina field (Andreu *et al.* 2015). SEBAL and TSEB show reasonable to good performance for these sites *versus* observations, whereas the simple scheme has clear problems producing the proper output under these circumstances. Apart from the earlier-mentioned issue of not parameterizing the aerodynamic roughness effects by DATTUTDUT, which is especially noticed in dry and aerodynamically rough areas, another issue here is the high spatial resolution of the REFLEX'12 imagery in combination with the auto-

LST and evaporative fraction averaged for the main landcover units

Landcover	LST [K]		Evaporative fraction [–]			
	Avg.	St. dev.	SEBAL	TSEB	DATTUTDUT	
					Original	Adjusted
Bare pasture	315.9	2.7	0.09	0.01	0.49	0.00
Barley stubble	312.3	1.7	0.14	0.29	0.59	0.19
Building	312.4	6.3	0.08	0.08	0.59	0.19
Camelina	315.9	1.6	−0.09	0.04	0.49	−0.00
Corn	299.5	1.9	0.60	0.91	0.95	0.87
Crops	310.3	4.1	0.23	0.41	0.65	0.30
Fallow land	315.7	2.7	0.13	0.01	0.50	0.01
Forest nursery	314.7	1.7	0.21	0.04	0.53	0.06
Grass	301.8	2.7	0.57	0.89	0.88	0.74
Harvested cropland	312.3	1.9	−0.08	0.20	0.59	0.19
Open water	296.9	5.0	0.95	1.07	1.02	1.00
Orchard	314.5	5.0	0.07	0.10	0.53	0.08
Poppy	309.2	2.1	0.63	0.51	0.68	0.35
Sunflower	301.4	3.6	0.78	0.84	0.89	0.76
Vineyard	312.8	1.8	0.13	0.06	0.58	0.16
Wheat stubble	313.1	1.3	−0.07	0.20	0.57	0.15

mated end-member selection, T_{min} and T_{max}. The latter issue causes an increase in the sensitivity of DATTUTDUT to variability in the heat fluxes under dry conditions.

The spatial resolution equals 4.0 m and therefore a high within-field variation of land surface temperature is observed (Table 3). In addition, there is a large number of fields of different landcover that were dry and hot at the time of image acquisition. Consequently, the histogram distribution of LST, middle panel of Fig. 4, has an exceptionally long tail on the high end. Selecting the hottest pixel in the image to represent T_{max} in Eq. 8, under these conditions, results in a significant portion of the image yielding too high evaporative fraction estimates from DATTUTDUT.

It is beyond the scope of the current contribution to perform a detailed sensitivity analysis on the selection of the end-members in the line of Timmermans *et al.* (2007). However, in the LST histogram in Fig. 4 the absolute minimum (0.0%) and maximum (100.0%) are indicated as well as the 0.5 and 99.5% – minimum and maximum values of LST. The DATTUTDUT model uses the 0.5 and 100.0% values for T_{min} and T_{max}, which are 297.6 and 333.7 K, respectively.
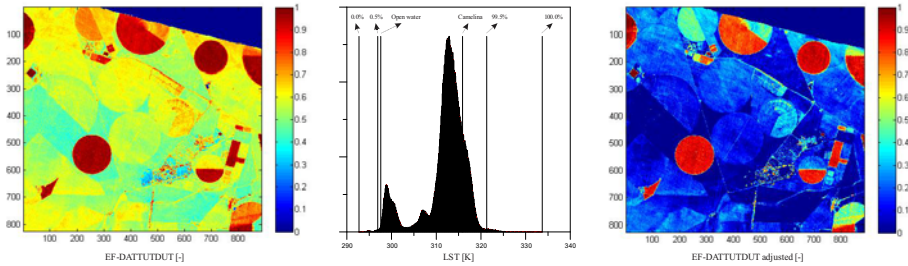
Fig. 4. Influence of end-member selection on model output.

To demonstrate the effect of end-member selection on spatial model results T_{min} and T_{max} are selected based on the minimum and maximum LST averaged per landcover unit (Table 3). In the left and right panel of Fig. 4 the model output for Λ is shown for the original model run and for the adjusted end-members, respectively, whereas the average results grouped per landcover type are shown in the right-most column of Table 3. A considerable improvement in spatial agreement is seen after this adjustment. With the exception of built-up areas (buildings) and poppy landcover units, the DATTUTDUT model results are comparable to the more physically-based approaches (see Table 3). This indicates that over problematic, *i.e.*, dry and sparsely vegetated, areas model results may improve considerably after adjusting the end-member values based on landcover. A procedure could be developed based on landcover information to ensure proper linking between T_{min} and T_{max} and the hydrological extremes (wet and dry conditions), a technique also used in other index-type of models (Kalma *et al.* 2008). However, in this paper the objective is to demonstrate the utility of a completely automated approach without user adjustments for monitoring evapotranspiration.

3.4 Temporal model evaluation

The daily average net radiation from the SEBAL and DATTUTDUT schemes is compared with the ground observations in Fig. 5. Although the procedure used in Gieske and Meijninger (2005) to derive daily average net radiation is not exclusively related to the SEBAL algorithm, for simplicity the results are referred to as SEBAL estimates. For both schemes the R_N estimates shown are taken from the pixel at the cotton site, where the weather station is situated. Both models seem to follow the temporal trend and magnitudes of the observations rather well, although SEBAL shows slightly higher estimates at the beginning of the season whereas DATTUDUT shows slightly higher values towards the end of the season. The overall general agreement is supported by the relatively low RMSD value between modeled
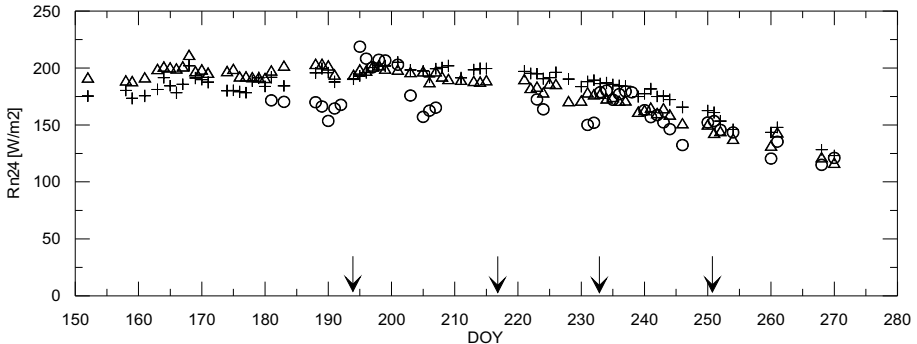
Fig. 5. Daily values of net radiation for the cotton site plotted against day number. AVHRR-DATTUTDUT values (+) and SEBAL estimates (Δ) are compared with those determined with the weather station (○) on the cotton field.

and measured daily R_n which is ~20 W m^{-2} (MAPD ~10%), for both the SEBAL and DATTUTDUT algorithms.

Following irrigation, indicated by arrows in Fig. 5, the ground observations show an increase in net radiation, due to a decrease in both albedo and surface temperature. However, this effect is not clearly seen in the satellite approaches where only a minor increase is computed which is slightly more pronounced for the DATTUTDUT estimates.

The turbulent flux observations are areal averages which depend on windspeed, wind direction, and aerodynamic properties of the upwind landscape and can be determined using the so-called footprint calculations (Schmid 1994, Timmermans *et al.* 2009). Due to the absence of detailed wind direction and wind speed information in the current study the average of a four-pixel window is taken over the cotton site. A similar four-pixel window is taken in the center of the heterogeneous valley in the middle of the scintillometer transect since this is the area contributing the most to the observed signal. In Figure 6, the estimated evaporative fractions from both remote sensing techniques are compared for the homogeneous cotton site and the heterogeneous valley site, Fig. 6a and b, respectively. In addition, an inter-comparison of model output of the time evolution of evaporative fraction over the growing season is shown in Fig. 6c and d. It is clearly seen that correlation in model output for the cotton site is much higher than for the valley site (R^2 is 0.915 and 0.054, respectively). For the valley site there is actually a negative correlation-although it is statistically not significantly different from zero. Over this site, evaporative fraction estimates from SEBAL increase slightly over the season, whereas DATTUTDUT output has a decreasing trend over the season.
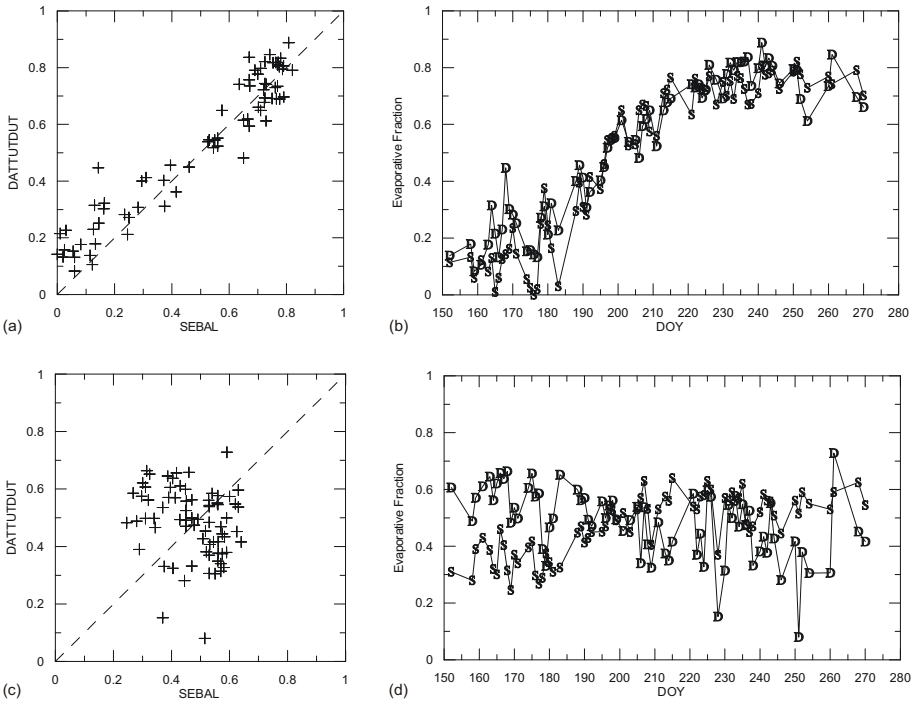
Fig. 6. DATTUTDUT (D-symbol) *versus* SEBAL (S-symbol) evaporative fraction estimates for the cotton (upper panels) and the valley site (lower panels).

A comparison of model output with observations of daily *ET*, for both methods estimated using Eq. 9, is illustrated for both sites in Fig. 7. In Figure 7a-c results are displayed for the cotton site and in Fig. 7d-f, results are shown for the valley location. Following Gieske and Meijninger (2005) the LAS data is combined with the AVHRR-derived daily R_N estimates to derive daily amounts of *ET* from Eq. 9.

In the model-measurement comparisons of daily *ET* displayed in Fig. 7, both models tend to underestimate the ground observations for both sites, with SEBAL output showing significantly greater bias. This effect is particularly evident in the beginning of the season, as seen in Fig. 7c and f and even more clear in Fig. 6b and d where DATTUTDUT estimates of evaporative fraction are higher than those of SEBAL. The better performance of the DATTUTDAT scheme over the growing season is supported by the difference statistics for the cotton site, which yielded RMSD values of 1.7 and 1.3 mm day^{-1} (MAPD values of 35 and 28%) for SEBAL and DATTUTDUT, respectively.
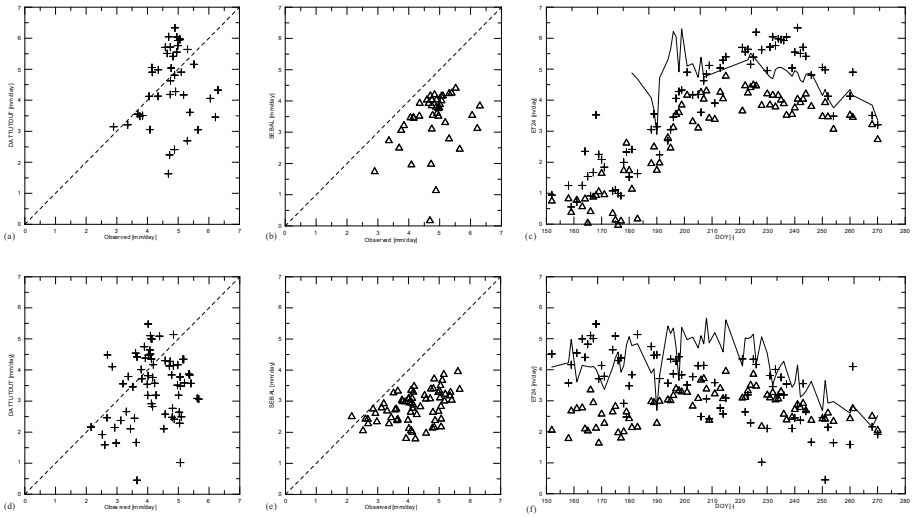
Fig. 7. Daily amounts of evapotranspiration, *ET* [mm/day], over the cotton (a-c) and valley site (d-f). For panels a, b, d, and f, model results *versus* observations are illustrated. For panels c and f, the observations (–) as well as the SEBAL (∆) and DATTUTDUT (+) results are plotted temporally over the course of the growing season.

Over the valley site, the RMSD values for SEBAL and DATTUTDUT are rather similar, namely ~1.5 mm day^{-1} with MAPD value of ~35%. In Figure 7f, the DATTUTDUT and the ground observations follow a similar temporal trend, but DATTUTDUT slightly underestimates the daily amounts in the second half of the growing season with respect to ground observations. On the other hand, SEBAL estimates show little temporal variation over the season. Since the net radiation estimation from both models is rather similar over the growing season for this site (correlation coefficient r^2 is equal to 0.8), the difference in *ET* estimates has to originate from the different estimates of the evaporative fraction. Generally, in the second half of the growing season the two methods are in better agreement with the observations, although there is a slight underestimation by both remote sensing-based approaches with respect to the measurements over the valley site.

Cumulative *ET* values are shown in Fig. 8 for the cotton site as presented by Gieske and Meijninger (2005) using the ground observations and SEBAL output for the monitoring period spanning a rain free period from DOY 150 to 270 (30 May until 28 September 1998). Using a simple water budget, by differencing the total irrigation and percolation provides an independent indication of the cumulative *ET* in this period. Droogers and Bastiaanssen (2002) reported a total of 545 mm supplied for irrigation in this period and a
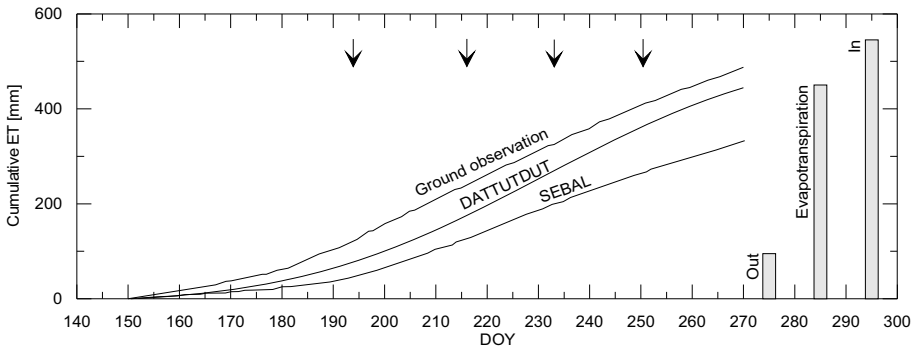
Fig. 8. Cumulative *ET* values derived from the temperature variance observations and from DATTUTDUT and SEBAL over the irrigated cotton site. The figure also displays the totals resulting from a simple water budget calculation where "In" represents the total amount of irrigation and "Out" is the total outgoing bottom flux or percolation for the monitoring period and the "Evapotranspiration" = In-Out.

yearly percolation of 284 mm, continuously downward throughout the year. Assuming equally distributed percolation over the year yields a total water use for the monitoring period of 452 mm. However, since figures for grape landcover indicated less percolation, and at times even capillary rise during the growing season, this figure might be slightly higher. The components of the simple water budget are also shown in Fig. 8, where "In" represents the total amount of irrigation and "Out" stands for the total outgoing bottom flux or percolation for the monitoring period.

Plotting cumulative *ET* modulates some of the scatter and errors in daily *ET*, and makes clearer the systematic bias between the models and observations (Gieske and Meijninger 2005). Comparing the two remote sensing models, and the simple water balance method with the ground measurements, yields underestimates of 44, 155 and 38 mm with DATTUTDUT, SEBAL and simple water balance methods, respectively. Relative to cumulative *ET* for the monitoring period this yields MAPD values between *ET* observations and DATTUTDUT, SEBAL, and simple water balance estimates of 9, 32, and 8%, respectively.

The underestimation of *ET* during the growing season by the remote sensing methods is a concern and needs to be investigated in greater detail. With regard to the trends, it appears that both remote sensing based methods respond fairly well to the start of the growing season (irrigation days are indicated by arrows). However, the DATTUTDUT method yields the greatest rise (slope) during the main irrigation period (roughly from DOY 210 to 250), possibly indicating a better performance under these conditions.

4. DISCUSSION

In a remote sensing model intercomparison study, Timmermans *et al.* (2007) documented the poor performance in estimating heat fluxes when applying a version of SEBAL over dry and sparsely vegetated conditions. Similarly, an intercomparison study by Choi *et al.* (2009) over the SMEX/SMACEX'02 study region found significant discrepancies in modeled turbulent heat flux patterns between TSEB and the Mapping EvapoTranspiration at high Resolution using Internalized Calibration (METRIC) approach, a derivative of SEBAL, that were largely correlated with vegetation density. Generally, the largest discrepancies, primarily a bias in H, between these two models occurred in areas with partial vegetation cover. A similar result is noted in the current study.

   The reported disagreement in R_N for DATTUTDUT has several reasons which are counter-acting in both the shortwave and the longwave radiation components. Unfortunately, only a limited number of radiation component observations are available for the datasets used. Mainly net radiometers and pyranometers were used to measure R_N and $R_S^{\downarrow}$ whereas only at a few sites albedo measurements were carried out. Concerning the incoming radiation components, the SEBAL and TSEB algorithms use observations of $R_S^{\downarrow}$, whereas DATTUTDUT assumes a constant transmissivity of 0.7 [–] in combination with the exo-atmospheric radiation. The average observed transmissivity for the dataset used was 0.79 [–], yielding an average underestimation around $70\ \mathrm{W\,m^{-2}}$ at the average observed $R_S^{\downarrow}$ (*i.e.*, $800\ \mathrm{W\,m^{-2}}$). On the other hand, using the set transmissivity to derive an atmospheric emissivity using Eq. 6 yields an over-estimation of some $40\ \mathrm{W\,m^{-2}}$ at an average air temperature of around 300 K for $R_L^{\downarrow}$. With respect to the outgoing radiation components, the DATTUTDUT assumptions also generally result in compensating errors. At the few sites where albedo was measured, 6 in total, the TSEB and SEBAL algorithms showed a near-perfect fit with the observations, whereas the DATTUTDUT scheme showed an under-estimation of around 50%. With average values of $R_S^{\downarrow}$ and albedo (*i.e.*, 0.2 [–]) this yields an over-estimation of R_N around $80\ \mathrm{W\,m^{-2}}$. Using a surface emissivity equal to unity with an average high-end surface temperature of around 315 K, an over-estimation of $R_L^{\uparrow}$ of about $30\ \mathrm{W\,m^{-2}}$ is noted as compared to using typical bare soil emissivities of 0.95 [–]. Although the average net effect is rather limited, around $20\ \mathrm{W\,m^{-2}}$, largest deviations are noted over hot and dry, sparsely vegetated areas. The incoming radiation components are spatially rather homogeneous but at these dry and sparsely vegetated locations the outgoing radiation components are largest. Therefore, under these circumstances, the DATTUTDUT assumptions of unity surface emissivity and linearity between albedo and temperature produce the largest discrepan-

cies, *i.e.*, an under-estimation, with both the SEBAL and TSEB output as well as with the observations of R_N.

As mentioned before, a large part of the discrepancy between the modelled and observed values for G is caused by the direct linkage of G with R_N. A second reason might be an over-simplification of the relation between G and R_N used here; see Eq. 7. Assuming the surface temperature is the only indicator that determines how much radiation is penetrating through the vegetation and reaching the soil is not only an oversimplified metric for determining vegetation density but also gives erroneous results under wet surface soil moisture conditions. Consequently, the standard deviation of the predicted G values is considerably lower than that of the observations, although to a lesser extent this is also noted for TSEB and SEBAL. A relatively flat response and under-estimation for soil heat fluxes is a phenomenon seen more often in remote sensing-based SVAT models (Jacob *et al.* 2002, Timmermans *et al.* 2007). This, despite attempts to incorporate the dynamic behavior of the G ratio by either introducing a time-dependence (Kustas *et al.* 1998, Santanello and Freidl 2003), or by incorporating the surface temperature in a semi-empirical manner (Bastiaanssen *et al.* 1998).

Concerning the turbulent fluxes, in past studies, for midday convective conditions, typically an RMSD-value between modeled and measured turbulent heat fluxes of approximately 50 W m^{-2} or less and/or MAPD-value of less than 20% is considered acceptable agreement (Hanna and Chang 1992, Kalma *et al.* 2008, Kustas and Norman 2000, Twine *et al.* 2000). This level of agreement considers the fact that energy closure problems (Oncley *et al.* 2002) and uncertainties in footprint analysis (Foken and Leclerc 2004, Hoedjes *et al.* 2007, Timmermans *et al.* 2009) cause uncertainties in H and λE tower measurements that are often similar in magnitude to model-measurement differences of ~50 W m^{-2}. In Table 2, the difference statistics for the TSEB scheme meet these error criteria, while the errors using DATTUTDUT and SEBAL do not. Nevertheless, the simpler schemes requiring less input data and expertise to run (particularly DATTUTDUT) still give useful H and λE estimates except under dry and sparsely vegetated conditions.

The DATTUTDUT approach uses the evaporative fraction concept in combination with daily R_N estimates to produce daily ET values. Therefore the absolute discrepancies in H and λE become less critical, which was also noted in the temporal evaluation of the model. The general trend of observed daily ET values over a growing season for two sites in Turkey is reproduced reasonably well, with DATTUTDUT outperforming the SEBAL scheme.

Root Mean Squared Differences between both satellite-based model estimates and observed daily R_N over the growing season were mainly caused by the difference in the scale of observations. The net radiation, measured at

2.5 m, was representative at the local or patch scale which are on the order of 150 m^2. Although the observation site, which was located in a 300×500 m^2 cotton field surrounded by other cotton fields, was homogeneous at the AVHRR resolution with respect to land use, the irrigation pattern varied for each farm (Kite and Droogers 2000). This may explain the more smooth response of the satellite-based approaches for net radiation as compared to the ground observations, which were more strongly influenced by irrigation activity.

Despite the simplification of using a constant atmospheric transmissivity over the growing season, the RMSD values for daily R_N were only around 20 W m^{-2}. Substituting a variable transmissivity over the season, using Eq. 5, did not significantly improve the DATTUTDUT results. An average increase over the season of 3% in R_N was noted, which was mainly caused by deviations toward the end of the season, which were up to a maximum of 8.5%. Over the cotton site this caused a deterioration in RMSD for daily ET from 1.31 to 1.38 mm day^{-1} and for the valley site a slight improvement from 1.45 to 1.41 mm day^{-1}.

A potentially larger source of error in both SEBAL and DATTUTDUT is the selection of the extreme pixels, as also noted in the spatial intercomparison. According to Meijninger (2003), the selection of the dry pixels in the initial, non-irrigated period, may be tenuous due to the difficulty in finding representative dry pixels under regionally humid and wet surface conditions that typically exist in the early period of the growing season here. Under such circumstances, selecting dry pixels that in reality do not represent the true dry extreme, and hence the "dry pixel" $ET > 0$, causes a bias (underestimation of ET) for other pixels in the scene as these techniques force more of the available energy to be partitioned into H instead of LE. There is slightly less of a bias issue or underestimation for the DATTUTDUT scheme because the selection of the dry pixel is automated and always is the highest temperature value in the image.

An example of the issue in assigning wet and dry pixel temperatures is provided in Fig. 9, where two-dimensional scatterplots of surface temperature *versus* albedo are shown for a day early in the season (DOY 167) and one later in the growing season (DOY 196) accompanied by the frequency distribution of the surface temperature. The solid lines indicate the wet and dry pixel temperature automatically selected by the DATTUTDUT algorithm, where the shaded area in the frequency distribution represents 0.5% of the total area determining the wet pixel selection. The dotted lines indicate the area where the dry pixel is most likely to be selected following the standard SEBAL procedure. Note that selecting a proper dry pixel for the SEBAL procedure from the scatterplot in Fig. 9b is more straightforward than in the case of Fig. 9a.
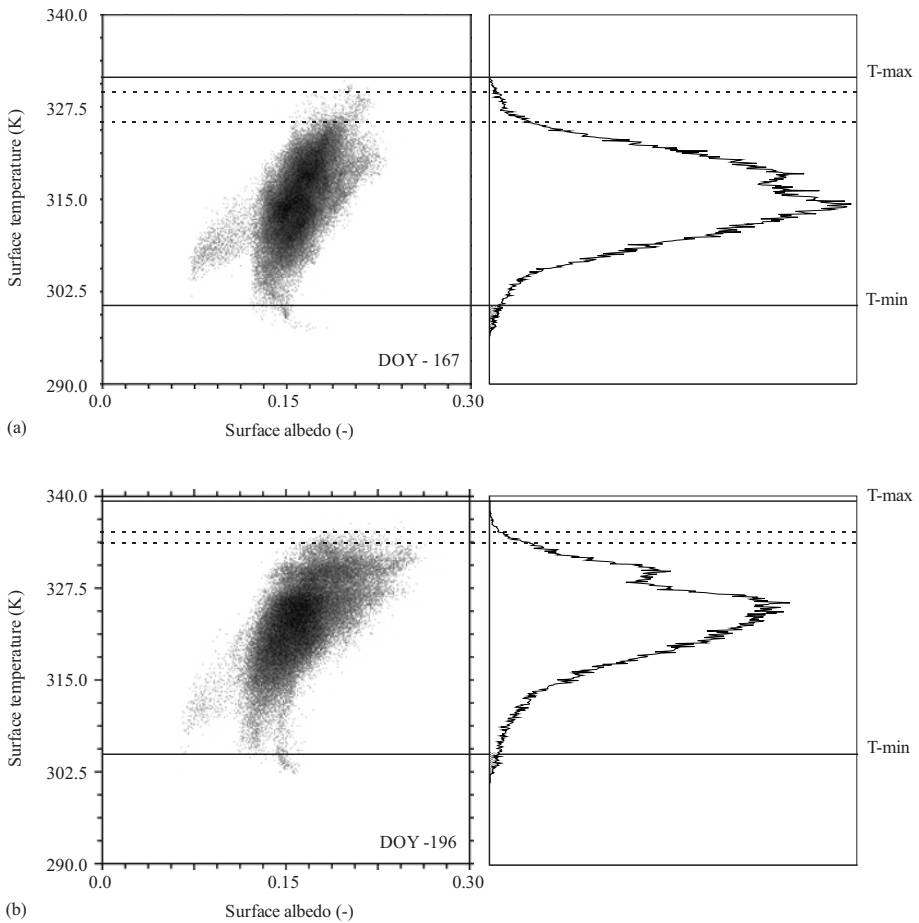
Fig. 9. Two-dimensional scatterplots of surface temperature *versus* surface albedo for an early season day (DOY 167) and a mid-season day (DOY 196) image. The solid lines indicate the wet a (T_{min}) and dry (T_{max}) pixel temperature automatically selected by the DATTUTDUT algorithm, where the shaded area in the frequency distribution represents 0.5% of the total area determining the wet pixel selection. The dotted lines indicate the likely T_{max} values for the dry pixel following the standard SEBAL procedure.

Although this procedure is automated in the case of DATTUTDUT, this does point out a limitation of these types of schemes, namely that a wet and a dry pixel are required within the scene. The existence of wet and dry pixels may not be present, and also will be pixel-resolution dependent, as also illustrated in Section 3.3.

With respect to daily *ET*, for the cotton site both satellite methods and the observations showed a similar behavior over the study period; see

Fig. 7c. During the first half of the season, observations yield the highest *ET* values, SEBAL the lowest and with the DATTUTDUT estimates somewhere in between. Apart from the temperature selection procedure this may be caused by a fairly large negative soil heat flux observed during the first days after irrigation. Since the satellite based methods assume a negligible daily soil heat flux, both turbulent fluxes will be under-estimated, since daily available energy ($Rn_{24} - G_{24}$) is under-estimated. From roughly DOY 225 to 245 DATTUTDUT is overestimating and SEBAL is underestimating the observed *ET* by similar magnitudes. There is no obvious explanation for this result. From DOY 245 until 270, which is the end of the growing season, DATTUTDUT is in close agreement with the observation, whereas SEBAL slightly underestimates the daily *ET*.

The reported RMSD values for daily *ET* seem rather large, but Kite and Droogers (2000) showed similar discrepancies for two selected days (DOY 177 and 241) using 9 different methods of estimating daily *ET*. Average *ET* values over the cotton site for the two days were 3.5 and 4.6 mm day^{-1}, respectively, whereas standard deviations among the different methods were as high as 1.6 and 1.1 mm day^{-1}. The *ET* values from SEBAL and DATTUTDUT for the two days were 0.1 and 0.8 for DOY 177 and 6.3 and 4.1 for DOY 241, respectively. For DOY 241, the two model estimates fall within the variation of other methods, but for the start of the season (DOY 177) both models showed an under-estimation, which is attributed to the assumption of negligible soil heat flux described above. The average *ET* value computed by Kite and Droogers (2000) for the valley site was ~4.0 mm day^{-1} with standard deviation of 1.0 mm day^{-1} for both DOY 177 and 241. Daily *ET* from SEBAL and DATTUTDUT for these days are 1.8 and 4.4 mm for DOY 177 and 3.0 and 2.8 mm for DOY 241. Again for DOY 241 both models fall within the variation of other methods while there is a slight under-estimation for DOY 177.

Model validation is usually performed using a handful of tower-based flux observations which are usually situated in homogeneous sites and as such typically are not representative of extreme or unique conditions. As such, assessing model performance with measurements at several selected sites does not guarantee that a model will provide reliable flux estimates over the whole scene, particularly in heterogeneous landscapes (Timmermans *et al.* 2007). Therefore, a spatial model evaluation was carried out over the Barrax site. Sensitivity to the selection of proper temperature end-members was demonstrated and results suggested a procedure might be developed to ensure proper linking between T_{min} and T_{max} and the hydrologic extremes. However, forested areas can have high sensible heat fluxes and low surface-air temperature difference due to a very low aerodynamic resistance. This situation will not be properly accommodated by a model that

does not parameterize aerodynamic roughness effects on the flux-gradient relationship. To investigate model performance and assumptions under such conditions requires a study described in Norman *et al.* (2006) that involves an inter-comparison and analysis of fluxes generated by different remote sensing-based modeling approaches in comparison to detailed simulations for a full range in hydrologic and aerodynamic conditions using a complex multi-source soil-plant-environment model. Simulations from a detailed SVAT from a study evaluating the effects of sub-pixel variability by Kustas and Norman (2000) could serve as a test case. However, this is beyond the scope of the current contribution, which is focused demonstrating the model utility covering a wide range in fractional vegetation cover, soil moisture, and meteorological conditions.

In summary, the simple schemes requiring less input data and expertise to run (particularly DATTUTDUT) still give useful H and λE estimates except under very dry and sparsely vegetated conditions. The difference in model performance between TSEB, SEBAL, and DATTUTDUT over such locations may have different reasons, such as the explicit use of climatic data in TSEB and SEBAL and not in DATTUTDUT, or the way aerodynamic properties are prescribed, one-source for SEBAL, two-source for TSEB, and not for DATTUTDUT, effects which have been examined by many others (Choi *et al.* 2009, French *et al.* 2005b, Timmermans *et al.* 2007). However, since the discrepancies with local flux observations for DATTUTDUT mainly occur over dry and sparsely vegetated areas, we firmly believe the underestimation of R_N combined with the selection of T_{max} using high resolution imagery, at these locations are the main reasons. At these locations the latent heat flux is set to zero. Would the estimate of available energy have been higher at these locations, the majority of the available energy would have been attributed to the sensible heat flux, which would reduce the evaporative fraction.

5. CONCLUDING REMARKS

In this study a remote sensing-based framework (DATTUTDUT) is developed for the automated estimation of surface energy balance components from remotely sensed radiometric surface temperature only. The method can be used to derive a spatially distributed map of actual evapotranspiration over large heterogeneous areas, provided that hydrologic extremes or wet and dry conditions are present.

Maps of surface energy balance components using the current approach were compared to ground observations and two other more complex remote sensing-based land surface models that have been validated numerous times in the literature. The inter-comparisons were made using large scale field experimental data collected over heterogeneous landscapes under a wide

range of environmental conditions. This simple and fully automated scheme was shown to provide estimates of the available energy (net radiation less soil heat flux) and turbulent (sensible and latent heat) fluxes comparable to these established and more complex remote sensing-based schemes, but only under less extreme and heterogeneous environmental conditions. Discrepancies with observations were significant using either SEBAL, version of Bastiaanssen *et al.* (1998), or DATTUTDUT approaches under dry sparsely vegetated areas.

The DATTUTDUT scheme was also applied to an irrigated site for the purposes of evaluating its utility for seasonal monitoring of crop water use. The scheme provided estimates of daily *ET* that generally underestimate the observations with significant scatter. Clearly there are environmental conditions (both hydrometeorological and land cover/land use) that limit the utility of both the DATTUTDUT and SEBAL schemes. For example, early in the growing season wet and dry pixels are difficult to identify and when the region is under water stressed conditions, this procedure is also less reliable unless land use is considered in defining T_{max} (see Table 3). Moreover, the DATTUTDUT scheme cannot account for the effect of significant variation of aerodynamic properties of the landscape, which can have a dramatic impact on the flux-gradient relationship (Norman *et al.* 2006). However, given the simplicity of the algorithm and its ease of use, the proposed model has utility in identifying areas of high and low water use even if the *ET* magnitudes are error-prone (see Fig. 3) and therefore could be an operational tool for rapid monitoring of relative water use or plant stress conditions in regions having little ground information. Once such areas of relatively low and high *ET* are identified, more physically-based models such as ALEXI/DisALEXI (Anderson *et al*. 2011) could be run to more reliably quantify the *ET*/stress conditions.

To gain a greater sense of the level of uncertainty in *ET* mapping and monitoring using the current approach, model inter-comparison studies of the type conducted by Timmermans *et al.* (2007) between the DATTUTDUT scheme and more established remote-sensing based approaches, such as ALEXI/DisALEXI and SEBAL but also for other simple index methods such as S-SEBI and SSEBop, are planned for a variety of landscapes containing a wide range in land use/vegetation cover and environmental conditions.

References

Anderson, M.C., J.M. Norman, G.R. Diak, W.P. Kustas, and J.R. Mecikalski (1997), A two-source time-integrated model for estimating surface fluxes using thermal infrared remote sensing, *Remote Sens. Environ.* **60**, 2, 195-216, DOI: 10.1016/S0034-4257(96)00215-5.

Anderson, M.C., J.M. Norman, W.P. Kustas, F. Li, J.H. Prueger, and J.R. Mecikalski (2005), Effects of vegetation clumping on two-source model estimates of surface energy fluxes from an agricultural landscape during SMACEX, *J. Hydrometeor.* **6**, 6, 892-909, DOI: 10.1175/JHM465.1.

Anderson, M.C., W.P. Kustas, and J.M. Norman (2007), Upscaling flux observations from local to continental scales using thermal remote sensing, *Agron. J.* **99**, 1, 240-254, DOI: 10.2134/agronj2005.0096S.

Anderson, M.C., W.P. Kustas, J.M. Norman, C.R. Hain, J.R. Mecikalski, L. Schultz, M.P. González-Dugo, C. Cammalleri, G. d'Urso, A. Pimstein, and F. Gao (2011), Mapping daily evapotranspiration at field to continental scales using geostationary and polar orbiting satellite imagery, *Hydrol. Earth Syst. Sci.* **15**, 223-239, DOI: 10.5194/hess-15-223-2011.

Andreu, A., W.J. Timmermans, D. Skokovic, and M.P. Gonzalez-Dugo (2015), Influence of component temperature derivation from dual angle thermal infrared observations on TSEB flux estimates over an irrigated vineyard, *Acta Geophys.* **63**, 6, 1540-1570, DOI: 10.1515/acgeo-2015-0037 (this issue).

Bastiaanssen, W.G.M. (1995), Regionalization of surface flux densities and moisture indicators in composite terrain: a remote sensing approach under clear skies in Mediterranean climates, Ph.D. Thesis, Wageningen Agricultural University, Wageningen, The Netherlands, 273 pp.

Bastiaanssen, W.G.M., M. Menenti, R.A. Feddes, and A.A.M. Holtslag (1998), A remote sensing surface energy balance algorithm for land (SEBAL). 1. Formulation, *J. Hydrol.* **212-213**, 198-212, DOI: 10.1016/S0022-1694(98)00253-4.

Bateni, S.M., D. Entekhabi, S. Margulis, F. Castelli, and L. Kergoat (2014), Coupled estimation of surface heat fluxes and vegetation dynamics from remotely

sensed land surface temperature and fraction of photosynthetically active radiation, *Water Resour. Res*. **50**, 11, 8420-8440, DOI: 10.1002/2013WR014573.

Brutsaert, W. (1982), *Evaporation into the Atmosphere. Theory, History, and Applications*, Reidel, Dordrecht, 299 pp.

Brutsaert, W., and D. Chen (1996), Diurnal variation of surface fluxes during thorough drying (or severe drought) of natural prairie, *Water Resour. Res.* **32**, 7, 2013-2019, DOI: 10.1029/96WR00995.

Burridge, D.M., and A.J. Gadd (1974), The Meteorological Office operational 10-level numerical weather prediction model (December 1974), Tech. Notes 12 and 48, British Meteorological Office, Bracknell, England, 57 pp.

Cammalleri, C., M.C. Anderson, and W.P. Kustas (2014), Upscaling of evapotranspiration fluxes from instantaneous to daytime scales for thermal remote sensing applications, *Hydrol. Earth Syst. Sci.* **18**, 1885-1894, DOI: 10.5194/hess-18-1885-2014.

Campbell, G.S., and J.M. Norman (1998), *An Introduction to Environmental Biophysics*, 2nd ed., Springer, New York, 286 pp., DOI: 10.1007/978-1-4612-1626-1.

Carlson, T.N., and D.A. Ripley (1997), On the relation between NDVI, fractional vegetation cover, and leaf area index, *Remote Sens. Environ.* **62**, 3, 241-252, DOI: 10.1016/S0034-4257(97)00104-1.

Chehbouni, A., J.C.B. Hoedjes, J.-C. Rodriguez, C.J. Watts, J. Garatuza, F. Jacob, and Y.H. Kerr (2008), Using remotely sensed data to estimate area-averaged daily surface fluxes over a semi-arid mixed agricultural land, *Agr. Forest Meteorol.* **148**, 3, 330-342, DOI: 10.1016/j.agrformet.2007.09.014.

Choi, M., W.P. Kustas, M.C. Anderson, R.G. Allen, F. Li, and J.H. Kjaersgaard (2009), An intercomparison of three remote sensing-based surface energy balance algorithms over a corn and soybean production region (Iowa, U.S.) during SMACEX, *Agr. Forest Meteorol.* **149**, 12, 2082-2097, DOI: 10.1016/j.agrformet.2009.07.002.

Choudhury, B.J. (1987), Relationships between vegetation indices, radiation absorption, and net photosynthesis evaluated by a sensitivity analysis, *Remote Sens. Environ.* **22**, 2, 209-233, DOI: 10.1016/0034-4257(87)90059-9.

Choudhury, B.J., N.U. Ahmed, S.B. Idso, R.J. Reginato, and C.S.T. Daughtry (1994), Relations between evaporation coefficients and vegetation indices studied by model simulations, *Remote. Sens. Environ.* **50**, 1, 1-17, DOI: 10.1016/0034-4257(94)90090-6.

Crago, R.D. (1996), Conservation and variability of the evaporative fraction during the daytime, *J. Hydrol.* **180**, 1-4, 173-194, DOI: 10.1016/0022-1694(95)02903-6.

de Bruin, H.A.R. (1987), From Penman to Makkink. **In:** J.C. Hooghart (ed.), *"Evaporation and Weather" Proceedings and Information, 25 March 1987,*

Hague, Netherlands, TNO Committee on Hydrological Research, Vol. 39, 5-31.

de Bruin, H.A.R. (1994), Analytic solutions of the equations governing the temperature fluctuation method, *Bound.-Lay. Meteorol.* **68**, 4, 427-432, DOI: 10.1007/BF00706800.

de Miguel, E., M. Jiménez, I. Pérez, Ó.G. de la Cámara, F. Muñoz, and J.A. Gómez-Sánchez (2015), AHS and CASI processing for the REFLEX remote sensing campaign: methods and results, *Acta Geophys.* **63**, 6, 1485-1498, DOI: 10.1515/ acgeo-2015-0031 (this issue).

Delogu, E.,G. Boulet, A. Olioso, B. Coudert, J. Chirouze, E. Ceschia, V. le Dantec, O. Marloie, G. Chehbouni, and J.-P. Lagouarde (2012), Reconstruction of temporal variations of evapotranspiration using instantaneous estimates at the time of satellite overpass, *Hydrol. Earth Syst Sci.* **16**, 2995-3010, DOI: 10.5194/hess-16-2995-2012.

Droogers, P., and W. Bastiaanssen (2002), Irrigation performance using hydrological and remote sensing modeling, *J. Irrig. Drain. Eng. ASCE* **128**, 1, 11-18, DOI: 10.1061/(ASCE)0733-9437(2002)128:1(11).

Duffie, J.A., and W.A. Beckman (1991), *Solar Engineering of Thermal Processes*, 2nd ed., John Wiley & Sons, New York, 944 pp.

Foken, T., and M.Y. Leclerc (2004), Methods and limitations in validation of footprint models, *Agr. Forest Meteorol.* **127**, 3-4, 223-234, DOI: 10.1016/ j.agrformet.2004.07.015.

French, A.N., T.J. Schmugge, W.P. Kustas, K.L. Brubaker, and J. Prueger (2003), Surface energy fluxes over El Reno, Oklahoma, using high-resolution remotely sensed data, *Water Resour. Res.* **39**, 6, 1164, DOI: 10.1029/ 2002WR001734.

French, A.N., F. Jacob, M.C. Anderson, W.P. Kustas, W. Timmermans, A. Gieske, Z. Su, H. Su, M.F. McCabe, F. Li, J. Prueger, and N. Brunsell (2005a), Corrigendum to "Surface energy fluxes with the Advanced Spaceborne Thermal Emission and Reflection radiometer (ASTER) at the Iowa 2002 SMACEX site (USA)" [Remote Sensing of Environment 2005 99/1-2; 55-65], *Remote Sens. Environ.* **99**, 4, 471, DOI: 10.1016/j.rse.2005.10.001.

French, A.N., F. Jacob, M.C. Anderson, W.P. Kustas, W. Timmermans, A. Gieske, Z. Su, H. Su, M.F. McCabe, F. Li, J. Prueger, and N. Brunsell (2005b), Surface energy fluxes with the Advanced Spaceborne Thermal Emission and Reflection radiometer (ASTER) at the Iowa 2002 SMACEX site (USA), *Remote Sens. Environ.* **99**, 1-2, 55-65, DOI: 10.1016/j.rse.2005. 05.015.

Garratt, J.R. (1992), *The Atmospheric Boundary Layer*, Cambridge University Press, Cambridge.

Gentine, P., D. Entekhabi, A. Chehbouni, G. Boulet, and B. Duchemin (2007), Analysis of evaporative fraction diurnal behaviour, *Agr. Forest Meteorol.* **143**, 1-2, 13-29, DOI: 10.1016/j.agrformet.2006.11.002.

Gieske, A., and W. Meijninger (2005), High density NOAA time series of ET in the Gediz Basin, Turkey, *Irrig. Drain. Syst*. **19**, 3-4, 285-299, DOI: 10.1007/s10795-005-5191-3.

Goetz, S.J., S.D. Prince, S.N. Goward, M.M. Thawley, and J. Small (1999), Satellite remote sensing of primary production: an improved production efficiency modeling approach, *Ecol. Model*. **122**, 3, 239-255, DOI: 10.1016/S0304-3800(99)00140-4.

Hanna, S.R., and J.C. Chang (1992), Boundary-layer parameterizations for applied dispersion modeling over urban areas, *Bound.-Lay. Meteorol.* **58**, 3, 229-259, DOI: 10.1007/BF02033826.

Hoedjes, J.C.B., A. Chehbouni, J. Ezzahar, R. Escadafal, and H.A.R. de Bruin (2007), Comparison of large aperture scintillometer and eddy covariance measurements: Can thermal infrared data be used to capture footprint-induced differences? *J. Hydrometeorol*. **8**, 2, 144-159, DOI: 10.1175/JHM561.1.

Humes, K.S., W.P. Kustas, and M.S. Moran (1994), Use of remote sensing and reference site measurements to estimate instantaneous surface energy balance components over a semiarid rangeland watershed, *Water Resour. Res*. **30**, 5, 1363-1373, DOI: 10.1029/93WR03082.

Jackson, R.D., S.B. Idso, R.J. Reginato, and P.J. Pinter Jr. (1981), Canopy temperature as a crop water stress indicator, *Water Resour. Res*. **17**, 4, 1133-1138, DOI: 10.1029/WR017i004p01133.

Jackson, T.J., D.M. le Vine, A.Y. Hsu, A. Oldak, P.J. Starks, C.T. Swift, J.D. Isham, and M. Haken (1999), Soil moisture mapping at regional scales using microwave radiometry: the Southern Great Plains hydrology experiment, *IEEE Trans. Geosci. Remote. Sens*. **37**, 5, 2136-2151, DOI: 10.1109/36.789610.

Jacob, F., A. Olioso, X.F. Gu, Z. Su, and B. Seguin (2002), Mapping surface fluxes using airborne visible, near infrared, thermal infrared remote sensing data and a spatialized surface energy balance model, *Agronomie* **22**, 6, 669-680, DOI: 10.1051/agro:2002053.

Jiang, L., and S. Islam (2001), Estimation of surface evaporation map over Southern Great Plains using remote sensing data, *Water Resour. Res.* **37**, 2, 329-340, DOI: 10.1029/2000WR900255.

Kalma, J.D., T.R. McVicar, and M.F. McCabe (2008), Estimating land surface evaporation: A review of methods using remotely sensed surface temperature data, *Surv. Geophys*. **29**, 4-5, 421-469, DOI: 10.1007/s10712-008-9037-z.

Kite, G.W., and P. Droogers (2000), Comparing evapotranspiration estimates from satellites, hydrological models and field data, *J. Hydrol.* **229**, 1-2, 3-18, DOI: 10.1016/S0022-1694(99)00195-X.

Kustas, W.P., and J.M. Norman (1997), A two-source approach for estimating turbulent fluxes using multiple angle thermal infrared observations, *Water Resour. Res*. **33**, 6, 1495-1508, DOI: 10.1029/97WR00704.

Kustas, W.P., and J.M. Norman (1999), Evaluation of soil and vegetation heat flux predictions using a simple two-source model with radiometric temperatures for partial canopy cover, *Agr. Forest Meteorol*. **94**, 1, 13-29, DOI: 10.1016/S0168-1923(99)00005-2.

Kustas, W.P., and J.M. Norman (2000), Evaluating the effects of subpixel heterogeneity on pixel average fluxes, *Remote Sens. Environ*. **74**, 3, 327-342, DOI: 10.1016/S0034-4257(99)00081-4.

Kustas, W.P., M.S. Moran, K.S. Humes, D.I. Stannard, P.J. Pinter Jr., L.E. Hipps, E. Swiatek, and D.C. Goodrich (1994a), Surface energy balance estimates at local and regional scales using optical remote sensing from an aircraft platform and atmospheric data collected over semiarid rangelands, *Water Resour. Res*. **30**, 5, 1241-1259, DOI: 10.1029/93WR03038.

Kustas, W.P., E.M. Perry, P.C. Doraiswamy, and M.S. Moran (1994b), Using satellite remote sensing (to extrapolate evapotranspiration estimates in time and space over a semiarid Rangeland basin), *Remote Sens. Environ*. **49**, 3, 275-286, DOI: 10.1016/0034-4257(94)90022-1.

Kustas, W.P., X. Zhan, and T.J. Schmugge (1998), Combining optical and microwave remote sensing for mapping energy fluxes in a semiarid watershed, *Remote Sens. Environ*. **64**, 2, 116-131, DOI: 10.1016/S0034-4257(97)00176-4.

Kustas, W.P., J.L. Hatfield, and J.H. Prueger (2005), The Soil-Moisture-Atmosphere Couopling Experiment (SMACEX): background, hydrometeorological conditions, and preliminary findings, *J. Hydrometeorol*. **6**, 6, 791-804, DOI: 10.1175/JHM456.1.

Mecikalski, J.R., G.R. Diak, M.C. Anderson, and J.M. Norman (1999), Estimating fluxes on continental scales using remotely sensed data in an atmospheric-land exchange model, *J. Appl. Meteorol*. **38**, 9, 1352-1369, DOI: 10.1175/1520-0450(1999)038<1352:EFOCSU>2.0.CO;2.

Meijninger, W.M.L. (2003), Surface fluxes over natural landscapes using scintillometry, Ph.D. Thesis, Wageningen University, Wageningen, The Netherlands.

Meijninger, W.M.L., and H.A.R. de Bruin (2000), The sensible heat fluxes over irrigated areas in western Turkey determined with a large aperture scintillometer, *J. Hydrol*. **229**, 1-2, 42-49, DOI: 10.1016/S0022-1694(99)00197-3.

Menenti, M., and B.J. Choudhury (1993), Parameterization of land surface evaporation by means of location dependant potential evaporation and surface temperature range. **In:** H.J. Bolle, R.A.Feddes, and J.D. Kalma (eds.), *Proc. Int. Symp. "Exchange Processes at the Land surface for a range of space and time scales", 13-16 July 1993, Yokohama, Japan.*

Menenti, M., W.G.M. Bastiaanssen, and D. van Eick (1989), Determination of surface hemispherical reflectance with Thematic Mapper data, *Remote Sens. Environ.* **28**, 327-337, DOI: 10.1016/0034-4257(89)90124-7.

Monteith, J.L., and M.H. Unsworth (1990), *Principles of Environmental Physics*, Edward Arnold Publishers, London, 291 pp.

Nichols, W.E., and R.H. Cuenca (1993), Evaluation of the evaporative fraction for parameterization of the surface energy balance, *Water Resour. Res.* **29**, 11, 3681-3690, DOI: 10.1029/93WR01958.

Norman, J.M., W.P. Kustas, and K.S. Humes (1995), Source approach for estimating soil and vegetation energy fluxes in observations of directional radiometric surface temperature, *Agr. Forest Meteorol.* **77**, 3-4, 263-293, DOI: 10.1016/0168-1923(95)02265-Y.

Norman, J.M., W.P. Kustas, J.H. Prueger, and G.R. Diak (2000), Surface flux estimation using radiometric temperature: A dual-temperature-difference method to minimize measurement errors, *Water Resour. Res.* **36**, 8, 2263-2274, DOI: 10.1029/2000WR900033.

Norman, J.M., M.C. Anderson, and W.P. Kustas (2006), Are single-source, remote-sensing surface-flux models too simple?, *AIP Conf. Proc.* **852**, 170, DOI: 10.1063/1.2349341.

Oncley, S.P., T. Foken, R. Vogt, C. Bernhofer, W. Kohsiek, H. Liu, A. Pitacco, D. Grantz, L. Ribeiro, and T. Weidinger (2002), The energy balance experiment EBEX-2000. **In:** *Proc. 15th Conf. on Boundary Layers and Turbulence, American Meteorological Society (AMS), 15-19 July 2002, Wageningen University, Wageningen, The Netherlands*.

Parlange, M.B., W.E. Eichinger, and J.D. Albertson (1995), Regional scale evaporation and the atmospheric boundary layer, *Rev. Geophys.* **33**, 1, 99-124, DOI: 10.1029/94RG03112.

Pelgrum, H., and W.G.M. Bastiaanssen (1996), An intercomparison of techniques to determine the area-averaged latent heat flux from individual in situ observations: A remote sensing approach using the European Field Experiment in a Desertification-Threatened Area data, *Water Resour. Res.* **32**, 9, 2775-2786, DOI: 10.1029/96WR01396.

Prihodko, L., and S.N. Goward (1997), Estimation of air temperature from remotely sensed surface observations, *Remote Sens. Environ.* **60**, 3, 335-346, DOI: 10.1016/S0034-4257(96)00216-7.

Prince, S.D., S.J. Goetz, R.O. Dubayah, K.P. Czajkowski, and M. Thawley (1998), Inference of surface and air temperature, atmospheric precipitable water and vapor pressure deficit using Advanced Very High-Resolution Radiometer satellite observations: comparison with field observations, *J. Hydrol.* **212-213**, 230-249, DOI: 10.1016/S0022-1694(98)00210-8.

Prueger, J.H., J.L. Hatfield, T.B. Parkin W.P. Kustas, L.E. Hipps, C.M.U. Neale, J.I. MacPherson, W.E. Eichinger, and D.I. Cooper (2005), Tower and aircraft eddy covariance measurements of water vapor, energy, and carbon

dioxide fluxes during SMACEX, *J. Hydrometeorol.* **6**, 6, 954-960, DOI: 10.1175/JHM457.1.

Roerink, G.J., Z. Su, and M. Menenti (2000), S-SEBI: A simple remote sensing algorithm to estimate the surface energy balance, *Phys. Chem. Earth B* **25**, 2, 147-157, DOI: 10.1016/S1464-1909(99)00128-8.

Santanello, J.A., and M.A. Friedl (2003), Diurnal covariation in soil heat flux and net radiation, *J. Appl. Meteorol.* **42**, 6, 851-862, DOI: 10.1175/1520-0450(2003)042<0851:DCISHF> 2.0.CO;2.

Schmid, H.P. (1994), Source areas for scalars and scalar fluxes, *Bound.-Lay. Meteorol.* **67**, 3, 293-318, DOI: 10.1007/BF00713146.

Senay, G.B., S. Bohms, R.K. Singh, P.H. Gowda, N.M. Velpuri, H. Alemu, and J.P. Verdin (2013), Operational evapotranspiration mapping using remote sensing and weather datasets: A new parameterization for the SSEB approach, *J. Am. Water Resour. Assoc.* **49**, 3, 577-591, DOI: 10.1111/jawr. 12057.

Shuttleworth, W.J., R.J. Gurney, A.Y. Hsu, and J.P. Ormsby (1989), FIFE: The variation in energy partition at surface flux sites, *IAHS Publ.* **186**, 67-74.

Su, Z. (2002), The Surface Energy Balance System (SEBS) for estimation of turbulent heat fluxes, *Hydrol. Earth Syst. Sci.* **6**, 1, 85-100, DOI: 10.5194/ hess-6-85-2002.

Tasumi, M., R.G. Allen, and W.G.M. Bastiaanssen (2000), The theoretical basis of SEBAL. **In:** A. Morse, T.Tasumi, G.A. Richard, and J.K. William (eds.), *Application of the SEBAL Methodology for Estimating Consumptive Use of Water and Stream flow Depletion in the Bear River Basin of Idaho through Remote Sensing*, Final report, Department of Biological and Agriculture Engineering, University of Idaho, Moscow, USA, 46-69.

Timmermans, W.J., W.P. Kustas, M.C. Anderson, and A.N. French (2007), An intercomparison of the Surface Energy Balance Algorithm for Land (SEBAL) and the Two-Source Energy Balance (TSEB) modeling schemes, *Remote Sens. Environ.* **108**, 4, 369-384, DOI: 10.1016/j.rse.2006.11.028.

Timmermans, W.J., G. Bertoldi, J.D. Albertson, A. Olioso, Z. Su, and A.S.M. Gieske (2008), Accounting for atmospheric boundary layer variability on flux estimation from RS observations, *Int. J. Remote Sens.* **29**, 17-18, 5275-5290, DOI: 10.1080/01431160802036383.

Timmermans, W.J., Z. Su, and A. Olioso (2009), Footprint issues in scintillometry over heterogeneous landscapes, *Hydrol. Earth Syst. Sci.* **13**, 2179-2190, DOI: 10.5194/hess-13-2179-2009.

Timmermans, W.J., C. van der Tol, J. Timmermans, M. Ucer, X. Chen, L. Alonso, J. Moreno, A. Carrara, R. Lopez, F. de la Cruz Tercero, H.L. Corcoles, E. de Miguel, J.A.G. Sanchez, I. Pérez, B. Franch, J.-C.J. Munoz, D. Skokovic, J. Sobrino, G. Soria, A. MacArthur, L. Vescovo, I. Reusen, A. Andreu, A. Burkart, C. Cilia, S. Contreras, C. Corbari, J.F. Calleja, R. Guzinski, C. Hellmann, I. Herrmann, G. Kerr, A.-L. Lazar, B. Leutner,

G. Mendiguren, S. Nasilowska, H. Nieto, J. Pachego-Labrador, S. Pulane-kar, R. Raj, A. Schikling, B. Siegmann, S. von Bueren, and Z.B. Su (2015), An overview of the Regional Experiments For Land-atmosphere Exchanges 2012 (REFLEX 2012) campaign, *Acta Geophys.* **63**, 6, 1465-1484, DOI: 10.2478/s11600-014-0254-1 (this issue).

Twine, T.E., W.P. Kustas, J.M. Norman, D.R. Cook, P.R. Houser, T.P. Meyers, J.H. Prueger, P.J. Starks, and M.L. Wesely (2000), Correcting eddy-covariance flux underestimates over a grassland, *Agr. Forest Meteorol*. **103**, 3, 279-300, DOI: 10.1016/S0168-1923(00)00123-4.

van der Tol, C., W.J. Timmermans, C. Corbari, A. Carrara, J. Timmermans, and Z. Su (2014), An analysis of turbulent heat fluxes and the energy balance during the REFLEX campaign, *Acta Geophys*. **63**, 6, 1516-1539, DOI: 10.1515/acgeo-2015-0061 (this issue).

Willmott, C.J. (1984), On the evaluation of model performance in physical geography. **In:** G.L. Gaile and C.J. Willmott (eds.), *Spatial Statistics and Models*, Theory and Decision Library, Vol. 40, Reidel Publ., Boston, 443-460.

Zhan, X., W.P. Kustas, and K.S. Humes (1996), An intercomparison study on models of sensible heat flux over partial canopy surfaces with remotely sensed surface temperature, *Remote Sens. Environ*. **58**, 3, 242-256, DOI: 10.1016/S0034-4257(96)00049-1.

Intercomparison of Surface Energy Fluxes Estimates from the FEST-EWB and TSEB Models over the Heterogeneous REFLEX 2012 Site (Barrax, Spain)

Chiara CORBARI[1], Wim TIMMERMANS[2], and Ana ANDREU[3]

[1]Politecnico di Milano, Department of Civil and Environmental Engineering, Milano, Italy; e-mail: chiara.corbari@polimi.it (corresponding author)

[2]University of Twente, Faculty of Geo-information Science and Earth Observation, Department of Water Resources, Enschede, The Netherlands e-mail: w.j.timmermans@utwente.nl

[3]Instituto de Investigación y Formación Agraria y Pesquera (IFAPA), Sevilla, Spain e-mail: ana.andreu.mendez@juntadeandalucia.es

A b s t r a c t

An intercomparison between the Energy Water Balance model (FEST-EWB) and the Two-Source Energy Balance model (TSEB) is performed over a heterogeneous agricultural area. TSEB is a residual model which uses Land Surface Temperature (LST) from remote sensing as a main input parameter so that energy fluxes are computed instantaneously at the time of data acquisition. FEST-EWB is a hydrological model that predicts soil moisture and the surface energy fluxes on a continuous basis. LST is then a modelled variable. Ground and remote sensing data from the Regional Experiments For Land-atmosphere Exchanges (REFLEX) campaign in 2012 in Barrax gave the opportunity to validate and compare spatially distributed energy fluxes. The output of both models matches the ground observations quite well. However, a spatial analysis reveals significant differences between the two approaches for latent and sensible heat fluxes over relatively small fields characterized by high heterogeneity in vegetation cover.

Key words: energy balance model, water and energy balance model, remote sensing.

1.   INTRODUCTION

Evapotranspiration (*ET*) is one of the most important variables in many fields such as hydrology, climatology, forest agronomy and plant physiology, and the partitioning between sensible (*H*) and latent (*LE*) heat fluxes is fundamental for the definition of crop water requirements. For irrigation practices, near-real time knowledge on soil water availability at the local and regional scale is of extreme importance in areas characterized by water scarcity.

In the past years a large number of land surface models, often called Soil-Vegetation-Atmosphere Transfer Schemes (SVAT), have been developed. However, approaches with substantial differences are included. Two main categories can be identified.

The first category concerns the so-called residual approaches which use Land Surface Temperature (LST) from remote sensing as their main input parameter. As such, energy fluxes are computed instantaneously at the time of data acquisition. Extrapolation to daily estimates, necessary for operational irrigation practice or proper water management, is generally performed by either the use of the concept of constant evaporative fraction (*i.e.*, $LE/(LE + H)$) or by using a higher temporal sampling (Chehbouni *et al.* 2008). The residual approaches are usually divided in one-source and two-source schemes, depending on the differentiation of the vegetation and bare soil contribution to the energy fluxes or treating them in a lumped manner. The Surface Energy Balance Model (SEBAL; Bastiaanssen *et al.* 1998), the Surface Energy Balance System (SEBS; Su 2002), and the Simplified Surface Energy Balance Index (S-SEBI; Roerink *et al.* 2000) treat the soil and vegetation contribution in a lumped manner, whereas the Two-Source Energy Balance (TSEB; Norman *et al.* 1995) is an example of the so-called dual source approach.

The second category of models includes coupled energy water balance schemes that predict soil moisture dynamics and usually river runoff as well as the surface energy fluxes on a continuous basis. Therefore, they are usually more complex and over-parameterized and LST is then a modelled variable instead of an input variable. Examples of these models are the Variable Infiltration Capacity (VIC) (Liang *et al.* 1994), the TOPmodel based Land Atmosphere Transfer Scheme (TOPLATS) (Famiglietti and Wood 1994), the Common Land model (CLM) (Dai *et al.* 2003), and the Flash-flood Event-based Spatially-distributed rainfall-runoff Transformation – Energy Water Balance (FEST-EWB) (Corbari *et al.* 2011). These types of model can overcome the limitations related to cloud coverage typical of thermal infrared satellite images and moreover provide continuous estimates of evapotranspiration and also of soil moisture. Of course, some limitations are present in

these models linked to the modelling of irrigation, lateral flows and ground-water, which are difficult to parameterize. Another limitation is the need of many hydraulic soil input parameters that are often not easily available at large scales, nor at high spatial resolution, even though they have an important role in the computation of the principal mass and energy fluxes.

Among the models that need remotely sensed LST as an input, a discussion is open in literature between the reliability of one-source or two-source models. In fact, in areas with sparse vegetation, a two-source model shows better performance as compared to a one-source model. However, different authors have found that with a proper calibration even a one-source model can correctly reproduce the energy fluxes (Bastiaanssen *et al.* 1998, Kustas *et al.* 1996) although a local calibration is not always possible (Su *et al.* 2001, Kustas *et al.* 2006, Cammalleri *et al.* 2012). Model suitability generally is a trade-off between easiness in use and data availability on one hand and required accuracy on the other hand.

Distributed hydrological models are usually more complex and over-parameterized with respect to remote sensing based SVAT models. This requires an accurate calibration procedure that generally depends on comparison between simulated and observed discharges at the available river cross-sections (Famiglietti and Wood 1994, Brath *et al.* 2004, Rabuffetti *et al.* 2008). Nowadays, little efforts have been focused on understanding whether remotely sensed LST can be used to calibrate and validate hydrological models parameters (Franks and Beven 1999, Crow *et al.* 2003, Gutmann and Small 2010, Corbari and Mancini 2013, Corbari *et al.* 2015).

Both types of models have been extensively validated in different climatic and soil/vegetation conditions against ground and/or remotely sensed data. However, few intercomparisons between energy balance models are made that quantify model reliability in evapotranspiration estimation in areas with heterogeneous vegetation and soil moisture conditions (Gonzalez-Dugo *et al.* 2009, Timmermans *et al.* 2007, French *et al.* 2005) or between hydrological models (Wood *et al.* 1998). Even less studies have compared these two types of models that both predict energy fluxes (Crow *et al.* 2005, Corbari *et al.* 2013), most probably due to the rather different methodologies used. The study of Crow *et al.* (2008) also tried to integrate these two types of models through assimilation of one into the other.

Most of the validation experiments usually demonstrate that these models produce reliable energy fluxes compared to ground measurements, but their accuracy at a regional scale is more difficult to demonstrate. It is therefore difficult to select the most suitable model for energy flux predictions which increases the need for further comparisons between different types of models.

In this paper, energy fluxes from a two-source model based on remotely sensed LST (TSEB) and from a continuous distributed hydrological model based on coupled water and energy balances (FEST-EWB) are compared in a spatial manner to understand their reliability and differences under different soil moisture and vegetation conditions. Both models are also validated against ground observed energy fluxes from eddy covariance stations and a scintillometer.

The area used for this comparison is the agricultural test site of Barrax (Spain) where the so-called Regional Experiments For Land-atmosphere Exchanges (REFLEX) campaign is carried out. In this framework an extensive amount of ground and airborne data have been acquired during the second half of July 2012.

The objective of this paper is to evaluate the reliability of each model and an attempt to understand under which vegetation and soil moisture conditions each model works better, given the relevant differences in the computation schemes.

2. MODELS DESCRIPTION

The FEST-EWB and TSEB models use different approaches to calculate surface energy fluxes which will be described in details in the following sections. FEST-EWB is a continuous energy and water balance model (Corbari *et al.* 2011), while TSEB, as originally formulated (Norman *et al.* 1995), is a two-source energy balance model designed for the use with instantaneous remote sensing observations.

2.1 FEST-EWB

FEST-EWB is a distributed hydrological energy water balance model (Corbari *et al.* 2010, 2011, 2013a) developed from the FEST-WB model (Mancini 1990, Rabuffetti *et al.* 2008). FEST-EWB computes the main processes of the hydrological cycle: evapotranspiration, infiltration, surface runoff, flow routing, subsurface flow (Ravazzani *et al.* 2011), snow dynamics (Corbari *et al.* 2009). The computation domain is discretized with a mesh of regular square cells in which every parameter is defined or calculated.

The input requirements (Table 1) of the model are comprised of:
- ❑   meteorological variables,
- ❑   distributed soil and vegetation parameters,
- ❑   a Digital Elevation Model (DEM),
- ❑   a Landuse/landcover map.

The core of the model is the system between the water and energy balance equations (Eqs. 1 and 2 below) which are linked through evapotranspiration. In short, the energy balance is solved by looking for a Representative

Equilibrium Temperature (RET), that is, the land surface temperature that closes the energy balance equation. This equilibrium surface temperature, which is an internal model variable, is comparable to the land surface temperature as retrieved from remote sensing data.

The soil moisture evolution for a given cell at position i,j is described by the energy and water balance equations:

$$Rn_{i,j} - G_{i,j} - H_{i,j} - LE_{i,j} = 0 , \tag{1}$$

$$\frac{\partial SM_{i,j}}{\partial t} = \frac{1}{dz_{i,j}} \left(P_{i,j} - R_{i,j} - PE_{i,j} - ET_{i,j} \right) , \tag{2}$$

where P is the precipitation rate [mm h^{-1}], R is the runoff flux [mm h^{-1}], PE is the drainage flux [mm h^{-1}], ET is the evapotranspiration rate [mm h^{-1}], z is the soil depth [m], Rn [W m^{-2}] is the net radiation, G [W m^{-2}] is the soil heat flux, H [W m^{-2}], and LE [W m^{-2}] are, respectively, the sensible heat and latent heat fluxes. All these terms of the system are functions of the input soil and vegetation parameters.

In particular, ET is linked to the latent heat flux through the latent heat of vaporization (λ) and the water density (ρ_w):

$$LE = \lambda \rho_w ET . \tag{3}$$

The latent heat flux, as reported in Corbari *et al.* (2011), is then computed as

$$LE = \frac{\rho_a c_p}{\gamma} \left(e^* - e_a \right) \left[\frac{f_v}{(r_a + r_c)} + \frac{1 - f_v}{(r_{abs} + r_{soil})} \right] , \tag{4}$$

where ρ_a is the air density, γ is the psychometric constant [Pa° C^{-1}], f_v is the vegetation fraction, and c_p is the specific heat of humid air [MJ kg^{-1} K^{-1}]. The saturation vapour pressure (e^*) is computed as a function of RET (Brutsaert 2005) and the vapour pressure (e_a) is a function of air temperature. The canopy resistance (r_c) is expressed following Jarvis (1976), while the soil resistance (r_{soil}) follows Sun (1982). The aerodynamic resistance (r_a for vegetation and r_{abs} for bare soil) is computed using the model from Thom (1975).

The sensible heat flux is computed as

$$H = \rho_a c_p \left(RET - T_a \right) \left[\frac{(1 - f_v)}{r_{abs}} + \frac{f_v}{r_a} \right] , \tag{5}$$

where T_a is the air temperature [K].

The net radiation is computed as the algebraic sum of the incoming and outgoing short wave and long wave radiation:

$$Rn = R_s (1 - \alpha) + \varepsilon_s \varepsilon_c \sigma (T_a^4) - \varepsilon_s \sigma (RET^4) , \tag{6}$$

where R_s is the incoming shortwave radiation [W m^{-2}], α is albedo, ε_c is the atmosphere emissivity, ε_s is the surface emissivity, and σ is the Stefan–Boltzmann constant [W m^{-2} K^{-4}].

The soil heat flux is the heat exchanged by conduction with the sub-surface soil and it is evaluated as

$$G = \left(\frac{\lambda}{dz} \right) \left(\text{RET} - T_{\text{soil}} \right),$$ (7)

where λ is soil thermal conductivity [W m^{-1} K^{-1}] and T_{soil} is soil temperature [K] at 10 cm depth (McCumber and Pielke 1981).

All the terms of the energy balance depend on RET, so the energy balance equation can be solved by looking for the thermodynamic equilibrium temperature that closes the equation. A Newton–Raphson scheme is used to solve this iteration process.

FEST-EWB was previously validated against energy and mass exchange measurements acquired by an eddy covariance station (Corbari *et al.* 2011) and also against ground and remote sensing information at agricultural district scale (Corbari *et al.* 2010).

2.2 The Two-Source Energy Balance (TSEB)

The Two-Source Energy Balance (TSEB), model of Norman *et al.* (1995) and Kustas and Norman (1999) has shown good performances for a wide range of arid and partially-vegetated landscapes (Timmermans *et al.* 2007, Gonzalez-Dugo 2009). Under such circumstances, a dual source model that distinguishes between the soil and vegetation contribution to the turbulent fluxes has clear and well-known advantages over simpler single-source models that treat these contributions in a lumped manner (Huntingford *et al.* 1995, Kustas *et al.* 1996). In the current contribution, the so-called series parameterization version of TSEB (Norman *et al.* 1995) is followed, allowing the interaction between soil and canopy. The input requirements of the model are summarized in Table 1.

The model assumes that the surface radiometric temperature (T_{RAD}) is a combination of soil (T_S) and canopy (T_C) temperatures, weighted by the vegetation fraction:

$$T_R(\phi) = \left\{ f_v(\phi) T_C^4 + \left[1 - f_v(\phi) \right] T_S^4 \right\}^{1/4},$$ (8)

where f_v is affected by the sensor viewing angle (ϕ). The surface energy-balance equation can be formulated for the whole soil-canopy-atmosphere system, or for the soil and canopy components separately:

$$Rn_c = LE_c + H_c,$$ (9)

The input requirements of the FEST-EWB and TSEB models

Observation	FEST-EWB	TSEB
Air temperature [K]	x	x
Windspeed [m s^{-1}]	x	x
Air pressure [mbar]	x	x
Relative humidity [–]	x	x
R_S [W m^{-2}]	x	x
Irrigation volume	x	
Sensor viewing angle [°]		x
NDVI (fCover, LAI)	x	x
Surface temperature		x
Emissivity	x	x
Landcover or aerodynamic properties	x	x
Soil parameters (saturated hydraulic conductivity, field capacity, wilting point, residual and saturated soil water content, soil depth)	x	

$$Rn_S = LE_S + H_S + G . \tag{10}$$

The original formulations for Rn, Rn_c, Rn_s, and G can be found in Norman *et al.* (1995) and Kustas and Norman (1999). Since the radiation formulation follows the so-called "layer-approach" (Lhomme and Chehbouni 1999), a simple summation of the soil and canopy components yields the total flux

$$Rn = Rn_c + Rn_s , \tag{11}$$

$$H = H_c + H_s , \tag{12}$$

$$LE = LE_c + LE_s . \tag{13}$$

The model is developed originally for uniformly distributed crops. In the case of clumped canopies with partial vegetation cover, such as vineyards and orchards, the parameterizations are corrected by the so-called clumping factor (Anderson *et al.* 2005). This factor corrects for the reduction in the extinction of the radiation in a clumped canopy as compared to a uniformly distributed one. The soil heat flux is then estimated as a time-dependent function of the net radiation reaching the soil, following:

$$G = c_g \, Rn_s , \tag{14}$$

where c_g is slightly variable with time. Details on the original determination can be found in Kustas *et al.* (1998). However, here it is calibrated *versus* local observations using the measurements from the test sites (see Section 4.1.2).

Within the series resistance scheme, the sensible heat fluxes H_c, H_s, and H are expressed as

$$H_c = \rho_a c_p (T_C - T_{AC}) / r_x ,$$ (15)

$$H_s = \rho_a c_p (T_S - T_{AC}) / r_s ,$$ (16)

$$H = H_s + H_c = H_c = \rho_a c_p (T_{AC} - T_a) / r_a ,$$ (17)

where T_{AC} is the air temperature in the canopy air space [K], r_x is the resistance to heat flow of the vegetation leaf boundary layer [s m^{-1}], r_s is the resistance to the heat flow in the boundary layer above the soil [s m^{-1}], whereas r_a is the aerodynamic resistance calculated from the stability corrected temperature profile equations (Brutsaert 1982), using Monin-Obukhov Similarity Theory (MOST). The exact procedures to calculate r_x, r_s, and r_a are described in detail by Norman *et al.* (1995).

The canopy latent heat flux is derived using as an initial assumption a potential canopy transpiration, following the Priestley–Taylor equation:

$$LE_c = \alpha_{PT} f_g \left[\Delta / (\Delta + \gamma) \right] Rn_c ,$$ (18)

where α_{PT} is the Priestley–Taylor coefficient (usually taken as 1.26), f_g is the green vegetation fraction, and Δ is the slope of the saturation vapor pressure *versus* temperature. If the vegetation is stressed, the Priestley–Taylor approximation overestimates the transpiration of the canopy and negative values of LE_S are computed. This improbable condensation over the soil during the daytime indicates the existence of vegetation water stress and it is solved by iteratively reducing α_{PT} and assuming LE_S equal to zero.

3. STUDY SITE

The study area is the agricultural area of Barrax in the centre of Spain (39°3′N, 2°6′W, 700 m a.s.l.) characterized by an alternation of irrigated and dry cultivated area, containing crops such as corn, barley, sunflower, alfalfa, and onions (Fig. 1). The climate is typically Mediterranean with vernal and autumnal rainfall, with an annual average of 400 mm, making it one of the driest areas in Europe.

Between 16 to 28 July 2012, the Regional Experiments For Land-atmosphere Exchanges (REFLEX) 2012 campaign has been carried out, where remote sensing and ground measurements used in this study have been collected (Timmermans *et al.* 2014). Hyper-spectral and thermal
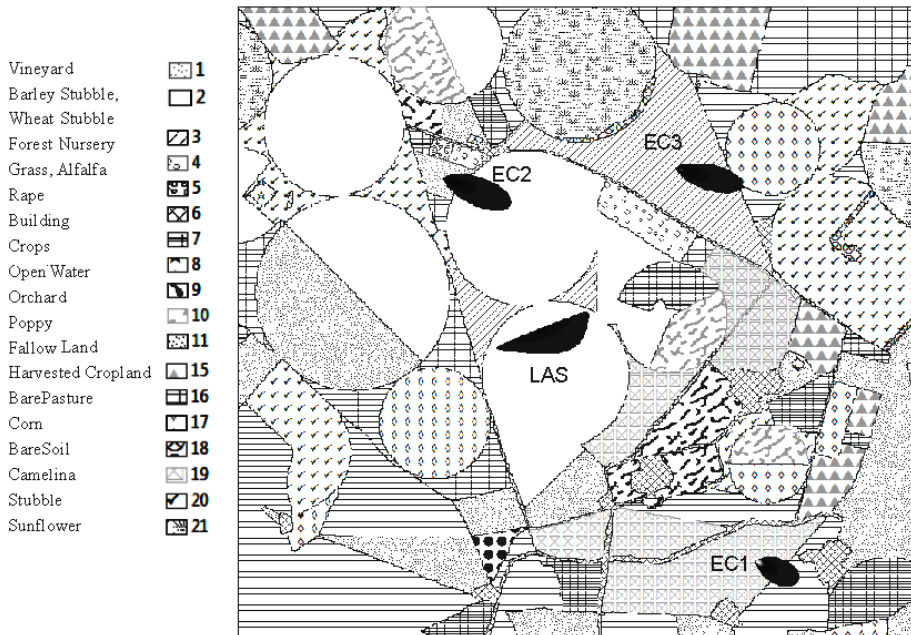
Fig. 1. Barrax agricultural area, land use, and footprint functions for 25 July at 9:28 UTC.

airborne images have been acquired during two days where for the entire period three eddy covariance towers and a large aperture scintillometer (LAS) have been installed. In selected points also some biophysical measurements have been carried out over different land-cover units comprising of Fractional Vegetation Cover (FVC), Leaf Area Index (LAI), Photosynthetically Active Radiation (PAR), and soil moisture (SM).

During the campaign, a large part of the crops were already harvested with the exception of maize, vineyard, sunflower, orchards, and forest nursery (see Fig. 1).

3.1 Ground data

Three micrometeorological towers and LAS sampled water and energy fluxes during the field campaign over different crop types. The first station (EC1) was located in a camelina field, the second one (EC2) in a small vineyard, and the third (EC3) in a forest nursery. The LAS was installed in a wheat-stubble field (van der Tol *et al.* 2015). Latent, sensible and soil heat fluxes were sampled in all fields, whereas net radiation was only recorded in EC1 and EC2. Station EC3 was also equipped with an infrared thermometer for determining outgoing longwave radiation. All meteorological data re-

quired by the models (incoming solar radiation, air temperature, air humidity, wind speed) were acquired by the stations. Soil moisture and soil temperature observations, which are needed also for post-processing the soil heat fluxes (van der Tol 2012), were obtained at the camelina site (EC1) as well.

Raw data from the EC towers have been corrected following the procedures well assessed in literature (Foken 2008). The EC1 and EC2 data have been analyzed with the Alteddy software (Alterra, WUR, Netherlands, http://www.climatexchange.nl/projects/alteddy/) whereas the EC3 data with the PEC software (Corbari *et al.* 2012) due to the availability of only thirty minutes average data. Corbari *et al.* (2014) compared corrected fluxes from high frequency and from 30 min average data in a maize field showing that low errors can be obtained with mean absolute daily difference equal to 6.1 $W\,m^{-2}$ for *H* and 13.2 $W\,m^{-2}$ for *LE*. The obtained fluxes observed by the four stations at the airborne overpass times are reported in Table 2. As well-known from the literature, there is a general lack of energy balance closure in EC measurements (Foken 2008, Twine *et al.* 2000, Wilson *et al.* 2002) although a reasonable small closure gap is obtained for EC1 and EC3. A poor behavior is obtained for EC2 in the vineyard field. This seems to be linked to the net radiation which, especially during daytime, becomes consistently higher than the sum of the other components of the energy balance equation. This is due to the fact that the field of view of the net radiometer is dominated by canopy, resulting in a lower albedo and thus higher net radiation then when seen from the altitude of the airborne sensors. The ratio G_0/Rn is quite high over these fields, in the range of 46 to 60% in respect to literature values (Su 2002, Choudhury *et al.* 1987). This might have been caused by very low winds, which indeed are occurring near the surface, especially over these fields. This is also noted in Su *et al.* (2008), who report

Table 2

Observed fluxes by the four stations and energy balance closure
at 25 July at 9:28 UTC

Land use	Rn [$W\,m^{-2}$]	G_0 [$W\,m^{-2}$]	H [$W\,m^{-2}$]	LE [$W\,m^{-2}$]	$R_n - G_0$ [$W\,m^{-2}$]	$H + LE$ [$W\,m^{-2}$]	Energy budget closure [$W\,m^{-2}$]
Vineyard (EC2)	460	77	145	53	383	198	185
Camelina (EC1)	348	159	232	19	189	250	−62
Reforestation (EC3)	351	212	145	26	139	172	−33
Wheat stubble (LAS)	361	216	125				

similar rates for soil heat fluxes in the corridors between the vine stands in the same area in the same season, which were even not yet corrected for storage in the upper soil layer. Soil heat flux has also been shown to be a significant component in sparse vegetation (Kustas *et al.* 2000), and in semi-arid or arid regions G was found to account for up to 40% of Rn, which could be equal to or higher than LE (Verhoef *et al.* 1996).

The soil heat flux measurements at the individual sites were taken at depths of a few centimeters and needed to be corrected for storage in the soil layer above the sensors. Over the vineyard, one measurement was taken below the vine stand and another one in between the stands, so as to obtain representative observations for this particular site. Soil moisture and soil temperature observations were taken at different depths for the post-processing of the soil heat fluxes following the methodology described in van der Tol (2012). Unfortunately, these additional measurements were not taken at all four sites. However, following de Vries (1963) the soil heat flux may be described by:

$$G(z,t) = A(0)\,e^{-z/D}\,\sqrt{\omega\rho c\lambda}\,\sin\left[\omega t - \frac{z}{D} + \frac{\pi}{4}\right], \tag{19}$$

where z [m] is the depth from the surface, t is time (unit the same as ω), $A(0)$ is the amplitude of the temperature wave at the surface [K], ω is the period of the soil heat flux (here taken as one day, unit taken in hours), ρ is the soil density [kg m^{-3}], c the soil specific heat [kJ kg^{-1} K^{-1}], λ the soil thermal conductivity [W m^{-1} K^{-1}], and D the so-called damping depth [m]. The corrections made at the camelina site were used in combination with Eq. 13 to derive D and the time delay of the temperature wave between 2 different depths. Assuming that soil properties in the area were homogeneous, these were then used to correct soil heat flux measurements taken at the other sites. A detailed discussion of the turbulent flux observations is provided in van der Tol *et al.* (2015), which includes a discussion of the well-known closure problem.

Large aperture scintillometers provide a measurement of the structure parameter for the refractive index, C_N^2 [m$^{-2/3}$], derived from the intensity fluctuations of an optical beam between a transmitter and a receiver. The structure parameter for the refractive index can be linked to the structure parameter for temperature, C_T^2 [K^2 m$^{-2/3}$], which, in turn, through the use of MOST and the temperature scale, T [K], can be used to derive the sensible heat flux, H. The physical background of measurements of this type is provided in Chehbouni *et al.* (2000), Lagouarde *et al.* (2002), Wang *et al.* (1978), whereas the method described in Timmermans *et al.* (2009) is used to extract the proper footprint area of the LAS observation.

The so-called source, or footprint, area of the LAS and EC towers are then computed to compare simulated and observed turbulent fluxes. The footprint of the eddy covariance towers and LAS originated from a south eastern wind. Details of all the micro-meteorological observations are provided in (van der Tol *et al.* 2015).

However, in most of the cases the intensity of the wind was not enough to cause contribution of other land use covers to the energy fluxes measurements. In the vineyard, however, the observation was influenced by the dry wheat-stubble during the time of plane overpass. For the validation of the modelled energy fluxes, a weighted integration of the pixels inside the footprint is computed in order to compare these values with the ground measurements (Timmermans *et al.* 2009). In Fig. 1 the spatial extent of the footprint areas for the analyzed moment of airplane overpass is shown.

3.2 Airborne data

During the campaign, 2 daytime and 1 nighttime flights of the CASA 212-200 N/S 270 "Paternina" airplane of INTA have been performed with the Airborne Hyperspectral Scanner (AHS) and Compact Airborne Imaging Spectrometer (CASI) sensors on board. The AHS sensor covers the thermal infrared part of the electromagnetic spectrum which is fundamental for estimating energy fluxes. A total of 13 daytime and 5 nighttime images are available at a spatial resolution of 4 m (Table 3). More details on these observations are provided in (de Miguel *et al.* 2015).

Table 3

FEST-EWB calibration against LST images from AHS

UTC time	Not calibrated				Calibrated			
	MAE [%]	MD (AHS-FEST-EWB) [°C]	MAD [°C]	RMSD [°C]	MAE [%]	MD (AHS-FEST-EWB) [°C]	MAD [°C]	RMSD [°C]
25 at 8:43	8.5	-0.6	3.0	4.1	4.8	−2.2	1.7	1.4
25 at 8:51	9.5	0.2	3.3	4.7	4.1	−1.9	1.7	1.8
25 at 9:02	8.9	1.3	3.4	5.1	3.7	0.7	1.9	2.9
25 at 9:11	9.5	2.5	3.1	4.4	3.5	0.9	1.9	2.7
25 at 9:19	8.6	1.7	2.9	4.3	3.9	−0.03	1.8	2.7
25 at 9:28	8.5	1.2	2.9	4.3	4.2	−0.7	1.0	1.8
25 at 9:38	8.3	0.9	3.1	4.4	3.1	−1.4	0.5	1.5
25 at 9:46	8.4	1.3	3.2	4.4	3.7	−1.1	1.4	2.2
26 at 8:42	11.1	−2.9	4.1	4.7	3.5	−2.9	1.2	1.8
26 at 8:51	12.1	2.7	3.8	4.8	2.4	1.8	1.5	2.2
26 at 9:07	10.3	2.8	3.3	4.3	3.0	0.15	1.8	2.5
26 at 9:25	7.8	1.3	2.7	3.9	3.2	0.21	0.9	1.7
26 at 9:38	11.9	−3.2	5.1	6.2	1.2	−5.4	2.4	2.3
All images	9.5	0.7	3.4	4.6	3.4	−0.9	1.5	2.1

Land surface temperature values are obtained with the Temperature and Emissivity Separation method (TES) described in Gillespie *et al.* (1998) and applied to AHS data following Sobrino *et al.* (2008). The entire dataset was used for FEST-EWB model calibration, whereas the TSEB and FEST-EWB validation is performed for the image acquired on 25 July at 9:28 UTC.

Additional remote sensing based input, required, such as albedo, NDVI, LAI, and f_v was computed following Timmermans *et al.* (2011) and Richter and Timmermans (2009).

4.   RESULTS

The results focus on the comparison between model output of FEST-EWB and TSEB for 25 July at 9:28 UTC. Simulated energy fluxes for both models are validated *versus* ground observations of these fluxes over different land-cover types. Use is made of the data collected in the 4 aforementioned observation sites. Furthermore, a spatial intercomparison of the two models is made, in order to investigate also model output not covered by any one of the four validation sites.

For the evaluation of the models, different statistics are utilized: the mean difference (MD), the mean absolute difference (MAD), the mean absolute error (MAE), the root mean square difference (RMSD), the mean value (MA), and its standard deviation (SD):

$$\text{MA} = \frac{\sum_{i=1}^{n}\left(X_i\right)}{n} \ , \tag{20}$$

$$\text{SD} = \left[\frac{\sum_{i=1}^{n}\left(X_i - \text{MA}\right)^2}{n-1}\right]^{0.5} \ , \tag{21}$$

$$\text{MD} = \frac{\sum_{i=1}^{n}\left(X_i - Y_i\right)}{n} \ , \tag{22}$$

$$\text{MAD} = \frac{\sum_{i=1}^{n}\left|X_i - Y_i\right|}{n} \ , \tag{23}$$

$$\text{MAE} = \frac{100}{\text{MA}}\left(\frac{\sum_{i=1}^{n}\left|X_i - Y_i\right|}{n}\right) \ , \tag{24}$$

$$\text{RMSD} = \left[\frac{\sum_{i=1}^{n} \left(X_i - Y_i \right)^2}{n} \right]^{0.5} , \tag{25}$$

where X_i and Y_i are the ith observed or measured variable, and n is the sample size.

4.1 Models calibration

4.1.1 FEST-EWB calibration

FEST-EWB is run in a continuous mode at a temporal resolution of 10 min and at the spatial resolution of 4 m. The configuration is simplified without computing surface and subsurface discharges and without snow dynamics which are considered not relevant for the area of interest.

The initial conditions of the model are derived from distributed soil moisture measurements made during the field campaign in the different fields. The simulation time is from 24 to 26 July, as such using the entire dataset of AHS images.

The calibration procedure is based on a pixel-to-pixel modification of the soil and vegetation parameters (Table 1) used as input in the model through the minimization of the differences between the model internal state variable RET and the remotely observed LST. This innovative methodology is based on remote sensing images of land surface temperature and provides the opportunity to calibrate and validate the distributed hydrological model in each pixel of the domain when ground data of evapotranspiration or discharge are not available. Moreover, with this methodology there is a possibility to calibrate model's internal state variables (*e.g.*, land surface temperature) in addition to the traditional external fluxes (*e.g.*, discharge) to obtain better understanding of hydrologic process and model analysis at pixel scale (Dooge 1986). In fact, a traditional calibration (as typically done in classical hydrological models) is based only on ground discharge data in few rivers sections. Such an approach lumps all the hydrological processes together so that the correct spatial determination of mass and energy fluxes is more difficult. Instead, when a pixel by pixel calibration is performed, a better spatial distribution should be achieved. Corbari and Mancini (2013) and Corbari *et al.* (2015) demonstrated the reliability of this procedure for two different case studies in Italy and China.

Soil parameters have been defined starting from the soil type of the area taken from the Harmonized World Soil Database (FAO/IIASA/ISRIC/ ISSCAS/JRC 2009). The parameter values are modified paying attention that their values remain within their physical ranges (Rawls and Brakensiek 1985).

In Table 3 the difference statistics between LST from AHS and RET for the different available flights are shown. FEST-EWB before calibration generally overestimates observed values, while after the calibration a reasonable agreement is reached with RMSD that goes from 4.6 to 2.1 °C.

4.1.2 TSEB calibration

The TSEB model does not require any calibration, since it is entirely physically based. A minor exception is made in the current contribution, however. The constant used in Eq. 14 that describes the ratio between soil heat flux and net radiation reaching the soil is calibrated using local observations. For the time of overpass, the adjusted coefficient, c_g, equals 0.48 (-) instead of the original value of 0.35 (-) (Andreu *et al.* 2015). This higher value reflects the arid conditions in the area under study, where typically a large part of the radiation is used for heating up the soil surface. The effect of the calibration of this c_g factor has an average increasing effect of 33 $\mathrm{Wm^{-2}}$ on G_0 (28 $\mathrm{Wm^{-2}}$ for forest nursery, 36 $\mathrm{Wm^{-2}}$ for wheat, 30 $\mathrm{Wm^{-2}}$ for camelina, and 38 $\mathrm{Wm^{-2}}$ for vineyard) and a similar decreasing effect, mainly on H (due to the fact that LE is generally low in the area).

4.2 Models intercomparison

4.2.1 Point validation

The comparison between modelled energy fluxes by both models with measured values yields a general good agreement, as shown in Fig. 2. Statistical comparison between modelled and measured fluxes is then shown in Table 4 in terms of MAD and MAE.

T a b l e 4

Statistics between energy fluxes modelled by the FEST-EWB and TSEB models with measured values for 25 July at 9:28 UTC

		EC1		EC2		EC3		LAS	
		MAD $[\mathrm{Wm^{-2}}]$	MAE [%]	MAD $[\mathrm{Wm^{-2}}]$	MAE [%]	MAD $[\mathrm{Wm^{-2}}]$	MAE [%]	MAD $[\mathrm{Wm^{-2}}]$	MAE [%]
Rn	FEST-EWB	22	6	140	30	10	3	56	15
Rn	TSEB	29	8	140	30	26	7	67	19
G	FEST-EWB	51	32	10	13	98	46	146	68
G	TSEB	49	31	62	81	110	52	82	38
H	FEST-EWB	40	17	60	41	33	23	11	9
H	TSEB	41	18	4	3	38	26	8	6
LE	FEST-EWB	7	38	7	12	12	47		
LE	TSEB	1	5	13	25	13	49		
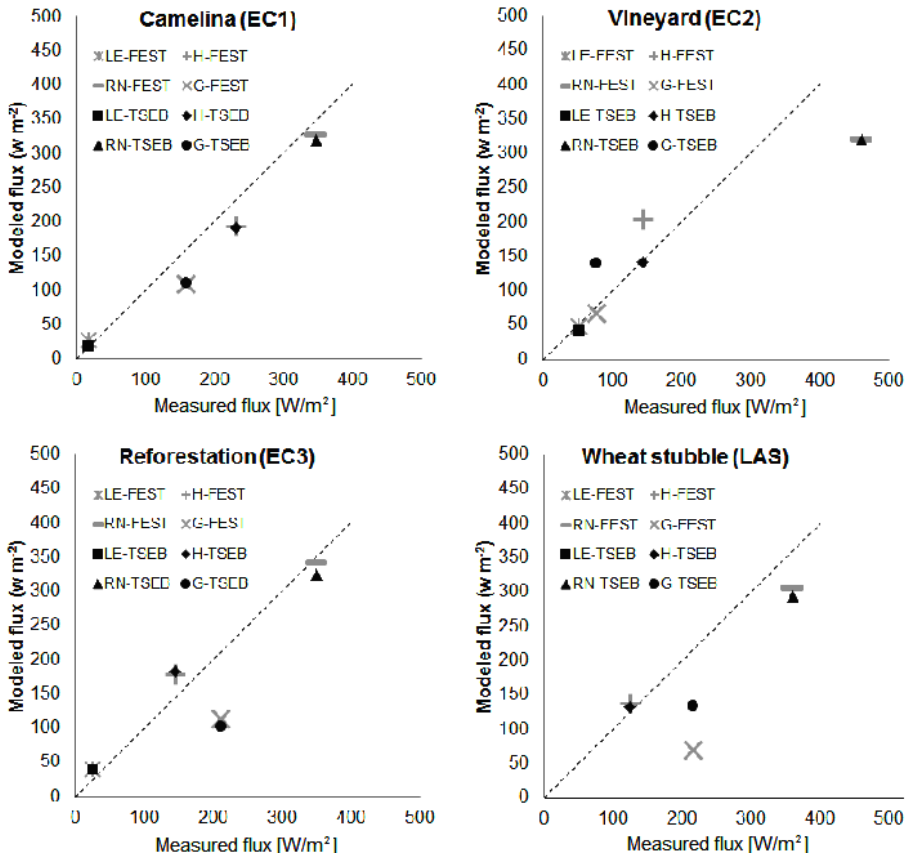
Fig. 2. Comparison between energy fluxes modelled by the FEST-EWB and TSEB models with measured values for 25 July at 9:28 UTC.

In general, according to Fig. 2 a good agreement is found between all observed and modelled energy fluxes in EC1. The EC3 results are still in a reasonable agreement with observations, except for *G*. Instead, a larger residual is found in Vineyard EC2 site (~185 Wm^{-2}), probably related to net radiometer positioning, but also due to turbulent source area which some-times is bigger than the vineyard field.

The observed and modelled net radiation estimates are in a similar agreement for both models with MAD between 10 and 67 Wm^{-2}, except for the vineyard stations where MAD reaches 140 Wm^{-2}. This is attributed to the net radiometer positioning, as mentioned above.

Soil heat fluxes present large discrepancies between observed and mod-elled values by both models, in particular in the reforestation and in the wheat stubble fields with MAD reaching values of 146 Wm^{-2}. However,

observations of G are very local and can vary a lot over just few meters, especially over sparsely and heterogeneously vegetated areas (Kustas *et al.* 2000). In the light of this high spatial variation of soil heat flux, the number of soil heat flux observations was rather limited. Most probably, they were insufficient to cover the full range of spatial variation at several observation sites. This holds especially true for the soil heat flux observations made at the wheat stubble field and the reforestation area. Typically at these sites the soil heat flux plates had to be buried at locations characterized by a low canopy cover. As such, the observations made at these sites are most probably higher than the representative site average.

Turbulent fluxes are generally well reproduced by both models. The modelled values are weighted according to the stations footprint estimates in order to be comparable to measured fluxes (as described in Section 3.1).

The MAD for sensible heat flux in the four stations from FEST-EWB is between some 10 and 60 $\mathrm{Wm^{-2}}$, while for TSEB it is between 5 and 40 $\mathrm{Wm^{-2}}$. Good agreements are obtained for the latent heat flux showing even lower MAD values, under 15 $\mathrm{Wm^{-2}}$, for both models in the three eddy covariance sites, comparable with the measurement uncertainties. Anyhow, it should be noted that the measured LE values are generally very low, between some 20 and 50 $\mathrm{Wm^{-2}}$, meaning that only small range of model applicability is tested.

It is interesting to note the large differences in the H performances between the two models over the vineyard, where TSEB reaches MAD values of 4 $\mathrm{Wm^{-2}}$ and MAE of 3%, while FEST-EWB shows values of 60 $\mathrm{Wm^{-2}}$ and 41%, respectively. This discrepancy is attributed to the different nature of the models. TSEB is a two-source model which works better for high and partially vegetated area, such as is the case in the vineyard field. FEST-EWB is based on an equilibrium temperature and, despite FEST-EWB differentiates between soil and vegetation resistances, a single representative equilibrium temperature is computed.

This result over the vineyard confirms previous findings by Kustas and Norman (1999), Timmermans *et al.* (2007), Crow *et al.* (2005), although the sparsely vegetated forest nursery shows similar results for both models. However, the vegetation cover is so low over this site that the vegetation contribution to the fluxes is almost negligible.

Nevertheless, with the notable exception of part of the deviating Rn and G observations, the overall model performances are rather good. RMSD values are comparable or better than those obtained in previous validation studies (French *et al.* 2005, Kustas *et al.* 2012, Timmermans *et al.* 2007, Cammalleri *et al.* 2012).

4.2.2 *Distributed validation*

To understand the reliability and variability of the two models estimates, spatially distributed analyses are performed, which are even more important in extremely heterogeneous area such as Barrax site where high differences in magnitude of latent and sensible heat fluxes are present. Despite the good agreement at the flux towers, which are typically positioned at larger fields comprising of a uniform cover, spatial intercomparison of the FEST-EWB and TSEB models (Fig. 3) reveals significant discrepancies. An exception is made for the net radiation estimates, which show a rather similar behavior for both models (see Fig. 3 and Table 5).
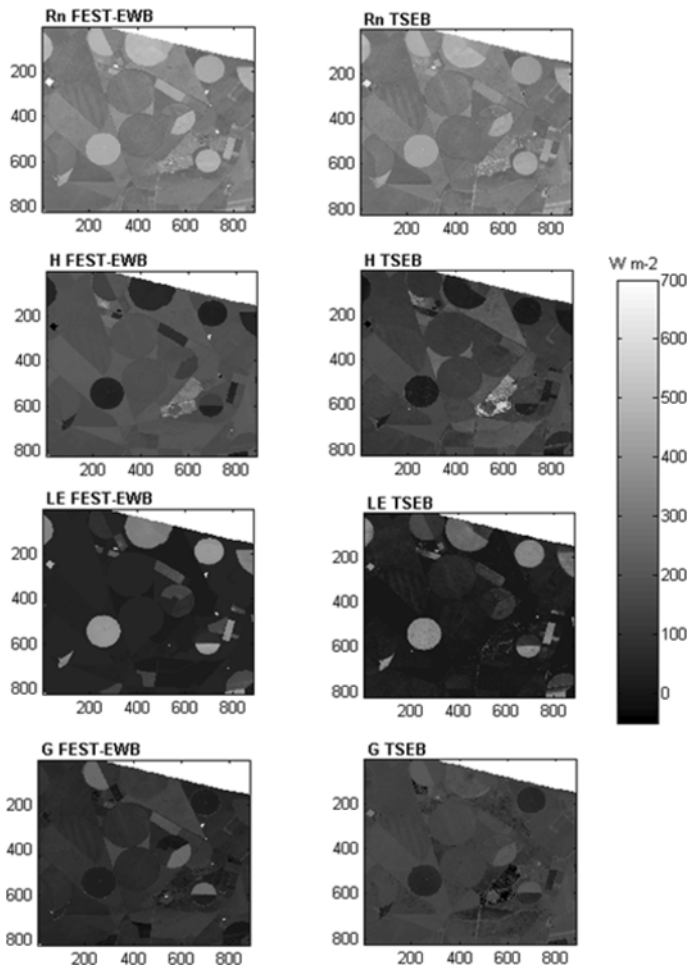
Fig. 3. Spatial MD values of the energy fluxes between TSEB minus FEST-EWB for 25 July at 9:28 UTC.

Spatial statistics between energy fluxes modelled by the FEST-EWB
and TSEB models for 25 July at 9:28 UTC

	MA (TSEB) [W m^{-2}]	SD (TSEB) [W m^{-2}]	MA (FEST-EWB) [W m^{-2}]	SD (FEST-EWB) [W m^{-2}]	AE [%]	MD (TSEB-FEST-EWB) [W m^{-2}]	MAD [W m^{-2}]	RMSD [W m^{-2}]
Rn	330	58.1	339	64	5.2	−8.7	18.4	23
G	136	47	82	44	145.9	54.2	68.1	60
H	135	67	177	54	31.7	−36.3	51.5	40
LE	59	95	80	100	60.9	−15.9	32.1	38

Relative to FEST-EWB model, TSEB yields smaller (larger) average estimates of *LE* and *H* (*G*) while predicting a similar spatial variation in all fluxes (Table 5). These results are also supported by the frequency diagrams of each flux from the two models (Fig. 4) which highlight a significant heterogeneity in the fluxes due to the high thermodynamic heterogeneity of the Barrax area.

These plots show that *Rn* from FEST-EWB and TSEB have the same shape as well as the same mean and standard deviation values, while for *G* the mean for TSEB is some 50 Wm^{-2} lower than for FEST-EWB despite having a similar standard deviation. The turbulent fluxes histograms have a quasi-bimodal distribution for both models due to the distinction between irrigated crops and bare soil or harvest crops. Moreover, the latent heat flux histogram shows a higher tail-end, ranging from 300 to 700 W m^{-2}. These are due to the presence of small fields with crops at different growth stages and with different soil moisture conditions.

Spatial variability in flux predictions is driven largely by differences in landcover types with different vegetation fraction and different irrigation practice. To demonstrate how these two fundamentally different models treat these different landcover types and different spatial variation, different statistics are computed for each landcover (Fig. 5).

These analyses confirm the agreement between the two models for net radiation with absolute mean difference less than 30 Wm^{-2}, but also the generally high discrepancies in soil heat flux estimates. As also commented in Section 4.2.1, *G* is a difficult variable to assess its reliability; moreover, the models have a very different algorithm for its computation. TSEB computed and calibrated *G* using the ratio with *Rn* reaching the soil (Eq. 14), while the *G* estimation in FEST-EWB is based on the heat conduction equation (Eq. 7).

For almost all landcover types, with the main exception of the well-irrigated grassland, TSEB shows larger values for *G*. This may be attributed
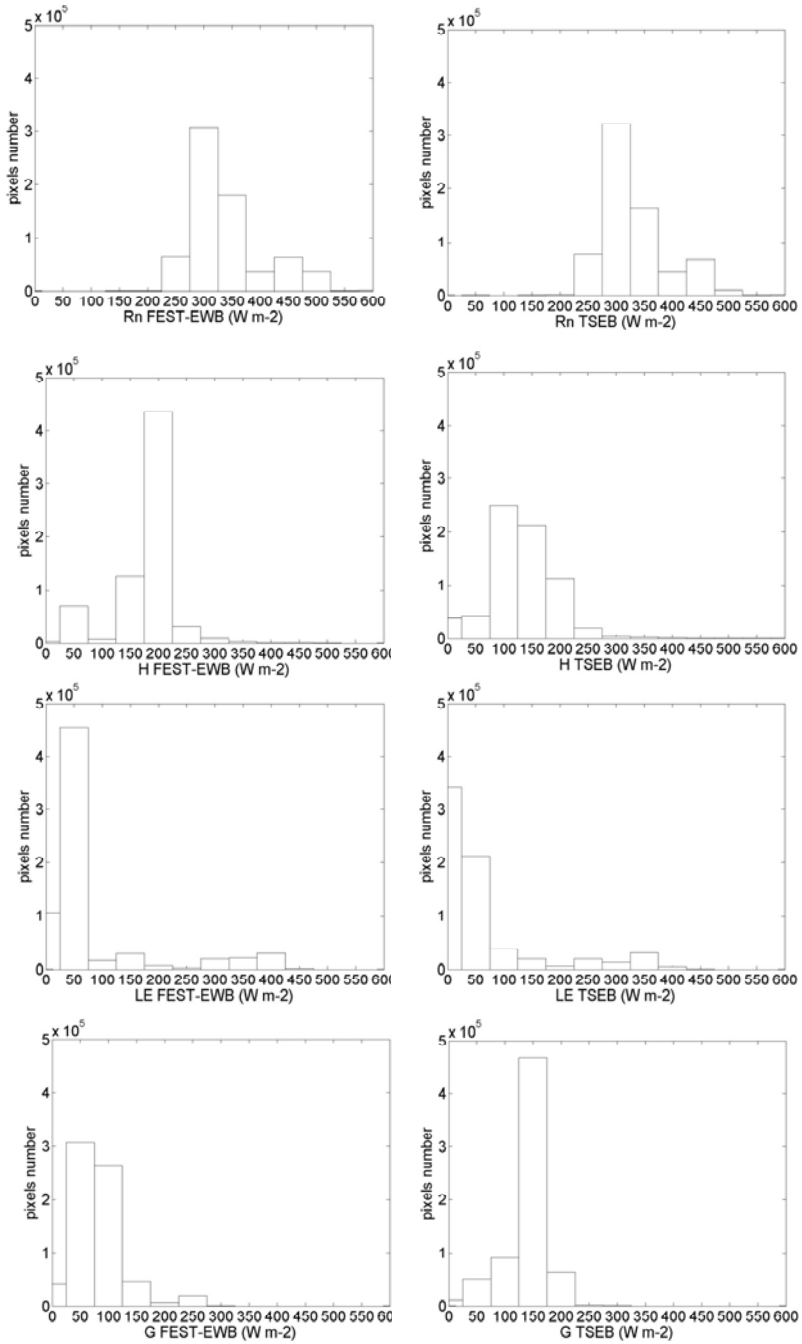
Fig. 4. Histograms of the energy fluxes of TSEB and FEST-EWB for 25 July at 9:28 UTC.
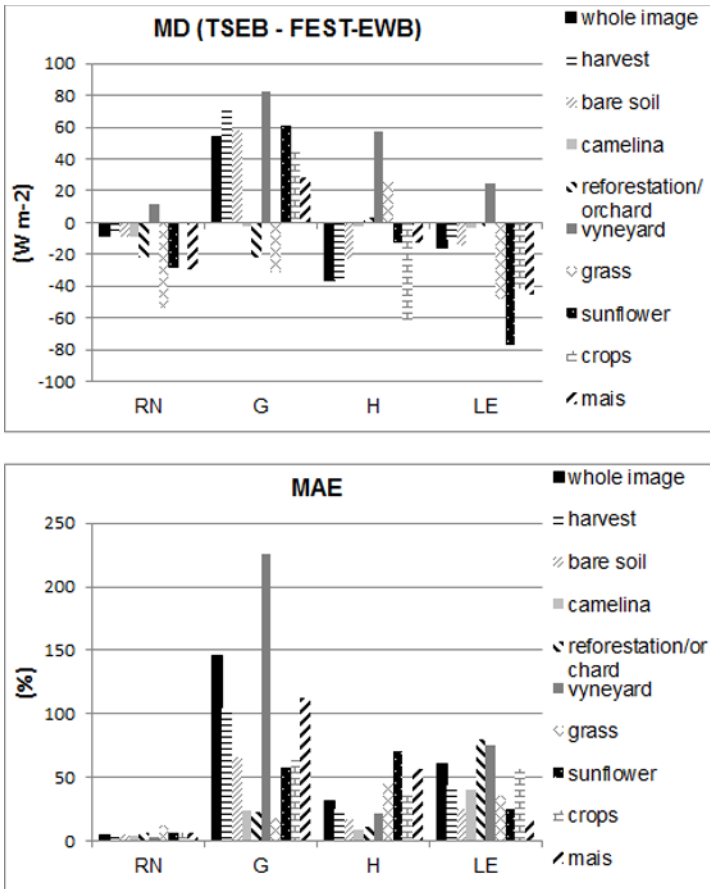
Fig. 5. Spatial statistics between energy fluxes modelled by the FEST-EWB and TSEB models for 25 July at 9:28 UTC divided by landcover classes.

to the local calibration performed in TSEB with respect to G estimates. The value of c_g in Eq. 14 was increased by some 40% with respect to the original formulation of TSEB due to this calibration. At average values of G between 130 and 140 Wm^{-2} this explains a large part of the observed difference with FEST-EWB.

The turbulent fluxes behavior is discordant between the different land-covers. The bare soil, camelina, stubble, and harvest fields are characterized by a uniform coverage and extremely high land surface temperature, and a reasonable agreement between the two models in terms of H and also of LE is reached. In the reforestation field a general agreement on all fluxes is noted.

Relatively high differences in latent and sensible heat fluxes between the models are noted in the vineyard field, as can be explained from the dual source character of TSEB. FEST-EWB provides lower estimates of G and LE and especially of H with respect to TSEB (Fig. 5) in this landcover type. This is also the reason why TSEB shows higher values for H over the orchard, which is a landcover type that is typically represented better by a two-source approach.

The grass, sunflower, crops and maize fields are irrigated crops with low land surface temperature values which cause high evapotranspiration fluxes. Relatively high MAD values, between 38 and 80 Wm^{-2}, are obtained for G, LE and H, where FEST-EWB shows higher estimates of latent and sensible heat fluxes than TSEB which in turn shows higher values for the ground heat flux.

A rather striking difference is seen in recently irrigated fields that are irrigated by rotating pivot systems. Recently irrigated land, for example noted in the large sunflower field in the north of the area, shows a drastically lower LST resulting in a lower H for TSEB as compared to that part of the field that is not yet irrigated. Since LST is not an input to FEST, this within-field difference does not appear in the FEST-EWB results. This indicates that the thermo-dynamic variation is reflected better in the TSEB approach.

Therefore, within-field variation of the evaporative fraction is noted more clearly in the TSEB output. The FEST-EWB model computes, in addition to the energy budget, also the water balance, for which the irrigation amount is an important input. As mentioned above, some fields are irrigated with a rotating pivot. For FEST-EWB this means that knowing its exact position during the airborne overpasses is almost a must.

5. DISCUSSION AND CONCLUSIONS

An intercomparison between the Energy Water Balance model (FEST-EWB) and Two-Source Energy Balance model (TSEB) has been performed over an extremely heterogeneous agricultural area with respect crop fraction and soil moisture conditions.

Both models performed well against energy fluxes measured at the eddy covariance stations and at the large aperture scintillometer. However, when a spatial analysis is performed, significant differences between the two approaches are highlighted, showing an agreement between the two for net radiation with absolute mean difference less than 30 Wm^{-2}, but also high discrepancies in soil heat flux estimates. Latent and sensible heat fluxes have discordant behavior for the different landcovers with reasonable agreement over uniform coverage area while high differences over sparse landcover and irrigated fields. In general, model outputs were comparable over large and

homogeneous fields whereas discrepancies were mainly noted over relatively small and sparsely vegetated heterogeneous areas.

Models, like TSEB, that use LST from remote sensing as an input parameter may provide generally accurate instantaneous estimates in particular of H, although a certain sensitivity related to LST accuracy should be considered. Instead, hydrological models, like FEST-EWB, provide continuous estimates of soil moisture dynamic and energy fluxes overcoming the limitations related to temporal integration, typical of flux estimates based solely on remote sensing input, and cloud coverage, typical of satellite images. Therefore, they are usually more complex and over-parameterized so that a precise calibration is always needed in contrast to a model using remote sensing input only. Another disadvantage is the need of the timing and volume of irrigation that are not always easy to obtain.

Despite the completely different approaches of the two models, a rather well spatial agreement is noted for most of the landcover types, especially over larger fields with a uniform vegetation cover. Small-scale variations in turbulent flux exchange are better reflected in the remote sensing-based TSEB model. This highlights the idea that instantaneous sensible heat flux estimates of TSEB could be assimilated to update the state of a continuous distributed hydrological model in order to obtain a robust tool for water resources management.

References

Anderson, M.C., J.M. Norman, W.P. Kustas, F. Li, J.H. Prueger, and J.R. Mecikalski (2005), Effects of vegetation clumping on two-source model estimates of surface energy fluxes from an agricultural landscape during SMACEX, *J. Hydrometeorol.* **6**, 6, 892-909, DOI: 10.1175/JHM465.1.

Andreu, A., W.J. Timmermans, D. Skokovic, and M.P. Gonzalez-Dugo (2015), Influence of component temperature derivation from dual angle thermal infrared observations on TSEB flux estimates over an irrigated vineyard, *Acta Geophys.* **63**, 6, 1540-1570, DOI: 10.1515/acgeo-2015-0037 (this issue).

Bastiaanssen, W.G.M., M. Menenti, R.A. Feddes, and A.A.M. Holtslag (1998), A remote sensing surface energy balance algorithm for land (SEBAL). 1. Formulation, *J. Hydrol.* **212-213**, 198-212, DOI: 10.1016/S0022-1694(98)00253-4.

Brath, A., A. Montanari, and E. Toth (2004), Analysis of the effects of different scenarios of historical data availability on the calibration of a spatially-distributed hydrological model, *J. Hydrol.* **291**, 3-4, 232-253, DOI: 10.1016/j.jhydrol.2003.12.044.

Brutsaert, W. (1982), *Evaporation into the Atmosphere*, Reidel, Dordrecht.

Brutsaert, W. (2005), *Hydrology: An Introduction*, Cambridge University Press, Cambridge.

Cammalleri, C., M.C. Anderson, G. Ciraolo, G. D'Urso, W.P. Kustas, G. La Loggia, and M. Minacapilli (2012), Applications of a remote sensing-based two-source energy balance algorithm for mapping surface fluxes without in situ air temperature observations, *Remote Sens. Environ.* **124**, 502-515, DOI: 10.1016/j.rse.2012.06.009.

Chehbouni, A., C. Watts, J.-P. Lagouarde, Y.H. Kerr, J.-C. Rodriguez, J.-M. Bonnefond, F. Santiago, G. Dedieu, D.C. Goodrich, and C. Unkrich (2000), Estimation of heat and momentum fluxes over complex terrain using a large aperture scintillometer, *Agr. Forest Meteorol.* **105**, 1-3, 215-226, DOI: 10.1016/S0168-1923(00)00187-8.

Chehbouni, A., J.C.B. Hoedjes, J.-C. Rodriguez, C.J. Watts, J. Garatuza, F. Jacob, and Y.H. Kerr (2008), Using remotely sensed data to estimate area-averaged daily surface fluxes over a semi-arid mixed agricultural land, *Agr. Forest Meteorol.* **148**, 330-342, DOI: 10.1016/j.agrformet.2007.09.014.

Choudhury, B.J., S.B. Idso, and R.J. Reginato (1987), Analysis of an empirical model for soil heat flux under a growing wheat crop for estimating evaporation by an infrared-temperature based energy balance equation, *Agr. Forest Meteorol.* **39**, 4, 283-297, DOI: 10.1016/0168-1923(87)90021-9.

Corbari, C., and M. Mancini (2013), Calibration and validation of a distributed energy – water balance model using satellite data of land surface temperature and ground discharge measurements, *J. Hydrometeorol.* **15**, 1, 376-392, DOI: 10.1175/JHM-D-12-0173.1.

Corbari, C., G. Ravazzani, J. Martinelli, and M. Mancini (2009), Elevation based correction of snow coverage retrieved from satellite images to improve model calibration, *Hydrol. Earth Syst. Sci.* **13**, 639-649, DOI: 10.5194/hess-13-639-2009.

Corbari, C., J.A. Sobrino, M. Mancini, and V. Hidalgo (2010), Land surface temperature representativeness in a heterogeneous area through a distributed energy-water balance model and remote sensing data, *Hydrol. Earth Syst. Sci.* **14**, 2141-2151, DOI: 10.5194/hessd-7-5335-2010.

Corbari, C., G. Ravazzani, and M. Mancini (2011), A distributed thermodynamic model for energy and mass balance computation: FEST-EWB, *Hydrol. Process.* **25**, 9, 1443-1452, DOI: 10.1002/hyp.7910.

Corbari, C., D. Masseroni, and M. Mancini (2012), Effetto delle correzioni dei dati misurati da stazioni eddy covariance sulla stima dei flussi evapotraspirativi, *Ital. J. Agrometeorol.* **1**, 35-51 (in Italian).

Corbari, C., J.A. Sobrino, M. Mancini, and V. Hidalgo (2013), Mass and energy flux estimates at different spatial resolutions in a heterogeneous area through a distributed energy-water balance model and remote-sensing data, *Int. J. Remote Sens.* **34**, 9-10, 3208-3230, DOI: 10.1080/ 01431161. 2012.716924.

Corbari C., D. Masseroni, A. Ceppi, A. Facchi, C. Gandolfi, and M. Mancini (2014), Comparison between high frequency and thirty minutes averaged data from eddy covariance measurements for operative water management, *J. Irrig. Drainage Eng.* (in review).

Corbari, C., M. Mancini, J. Li, and Z. Su (2015), Can satellite land surface temperature data be used similarly to river discharge measurements for distributed hydrological model calibration?, *Hydrol. Sci. J.* **60**, 2, 202-217, DOI: 10.1080/02626667.2013.866709.

Crow, W.T., E.F. Wood, and M. Pan (2003), Multiobjective calibration of land surface model evapotranspiration predictions using streamflow observations and spaceborne surface radiometric temperature retrievals, *J. Geophys. Res.* **108**, D23, 4725, DOI: 10.1029/2002JD003292.

Crow, W.T., F. Li, and W.P. Kustas (2005), Intercomparison of spatially distributed models for predicting surface energy flux patterns during SMACEX, *J. Hydrometeorol.* **6**, 6, 941-953, DOI: 10.1175/JHM468.1.

Crow, W.T., W.P. Kustas, and J.H. Prueger (2008), Monitoring root zone soil moisture though the assimilation of a thermal remote sensing-based soil moisture proxy into a water balance model, *Remote Sens. Environ.* **112**, 4, 1268-1281, DOI: 10.1016/j.rse.2006.11.033.

Dai, Y., X. Zeng, R.E. Dickinson, I. Baker, G.B. Bonan, M.G. Bosilovich, A. Scott Denning, P.A. Dirmeyer, P.R. Houser, G. Niu, K.W. Oleson, C. Adam Schlosser, and Z.-L. Yang (2003), The Common Land Model, *Bull. Amer. Meteor. Soc.* **84**, 8, 1013-1023, DOI: 10.1175/BAMS-84-8-1013.

de Miguel, E., M. Jiménez, I. Pérez, Ó.G. de la Cámara, F. Muñoz, and J.A. Gómez-Sánchez (2015), AHS and CASI processing for the REFLEX remote sensing campaign: methods and results, *Acta Geophys.* **63**, 6, 1485-1498, DOI: 10.1515/ acgeo-2015-0031 (this issue).

de Vries, D.A. (1963), Thermal properties of soils. **In:** W.R. van Wijk (ed.), *Physics of Plant Environment*, North Holland, Amsterdam, 210-233.

Dooge, J.C.I. (1986), Looking for hydrologic laws, *Water Resour. Res.* **22**, 9S, 46-58, DOI: 10.1029/WR022i09Sp0046S.

Famiglietti, J.S., and E.F. Wood (1994), Multiscale modeling of spatially variable water and energy balance processes, *Water Resour. Res.* **30**, 11, 3061-3078, DOI: 10.1029/94WR01498.

FAO/IIASA/ISRIC/ISSCAS/JRC (2009), Harmonized world soil database (version 1.1), FAO, Rome, Italy and IIASA, Laxenburg, Austria.

Foken, T. (2008), *Micrometeorology*, Springer, Berlin.

Franks, S.W., and K.J. Beven (1999), Conditioning a multiple-patch SVAT Model using uncertain time-space estimates of latent heat fluxes as inferred from remotely sensed data, *Water Resour. Res.* **35**, 9, 2751-2761, DOI: 10.1029/1999WR900108.

French, A.N., F. Jacob, M.C. Anderson, W.P. Kustas, W. Timmermans, A. Gieske, Z. Su, H. Su, M.F. McCabe, F. Li, J. Prueger, and N. Brunsell (2005), Surface energy fluxes with the Advanced Spaceborne Thermal Emission and Reflection radiometer (ASTER) at the Iowa 2002 SMACEX site (USA), *Remote Sens. Environ.* **99**, 1-2, 55-65, DOI: 10.1016/j.rse.2005.05.015.

Gillespie, A., S. Rokugawa, T. Matsunaga, J.S. Cothern, S. Hook, and A.B. Kahle (1998), A temperature and emissivity separation algorithm for Advanced Spaceborne Thermal Emission and Reflection Radiometer (ASTER) images, *IEEE Geosci. Remote S.* **36**, 4, 1113-1126, DOI: 10.1109/36.700995.

Gonzalez-Dugo, M.P., C.M.U. Neale, L. Mateos, W.P. Kustas, J.H. Prueger, M.C. Anderson, and F. Li (2009), A comparison of operational remote sensing-based models for estimating crop evapotranspiration, *Agr. Forest Meteorol.* **149**, 11, 1843-1853, DOI: 10.1016/j.agrformet.2009.06.012.

Gutmann, E.D., and E.E. Small (2010), A method for the determination of the hydraulic properties of soil from MODIS surface temperature for use in land-surface models, *Water Resour. Res.* **46**, 6, W06520, DOI: 10.1029/ 2009WR008203.

Huntingford, C., S.J. Allen, and R.J. Harding (1995), An intercomparison of single and dual-source vegetation-atmosphere transfer models applied to transpiration from sahelian savannah, *Bound.-Lay. Meteorol.* **74**, 4, 397-418, DOI: 10.1007/BF00712380.

Jarvis, P.G. (1976), The interpretation of the variations in leaf water potential and stomatal conductance found in canopies in the field, *Phil. Trans. R. Soc. Lond. B* **273**, 593-610, DOI: 10.1098/rstb.1976.0035.

Kustas,W.P., and J.M. Norman (1999), Evaluation of soil and vegetation heat flux predictions using a simple two-sourcemodel with radiometric temperatures for partial canopy cover, *Agr. Forest Meteorol.* **94**, 1, 13-29, DOI: 10.1016/S0168-1923(99)00005-2

Kustas, W.P., K.S. Humes, J.M. Norman, and M.S. Moran (1996), Single- and dual-source modeling of surface energy fluxes with radiometric surface temperature, *J. Appl. Meteor.* **35**, 1, 110-121, DOI: 10.1175/1520-0450(1996) 035<0110:SADSMO>2.0.CO;2.

Kustas, W.P., X. Zhan, and T.J. Schmugge (1998), Combining optical and micro-wave remote sensing for mapping energy fluxes in a semiarid watershed, *Remote Sens. Environ.* **64**, 2, 116-131, DOI: 10.1016/S0034-4257(97)00176-4.

Kustas, W.P., J.H. Prueger, J.L. Hatfield, K. Ramalingam, and L. Hipps (2000), Variability in soil heat flux from a mesquite dune site, *Agr. Forest Meteorol.* **103**, 3, 249-264, DOI: 10.1016/S0168-1923(00)00131-3.

Kustas, W.P., M.C. Anderson, A.N. French, and D. Vickers (2006), Using a remote sensing field experiment to investigate flux-footprint relations and flux sampling distributions for tower and aircraft-based observations, *Adv. Water Resour.* **29**, 2, 355-368, DOI: 10.1016/j.advwatres.2005.05.003.

Kustas, W.P., J.G. Alfieri, M.C. Anderson, P.D. Colaizzi, J.H. Prueger, S.R. Evett, C.M.U. Neale, A.N. French, L.E. Hipps, J.L. Chávez, K.S. Copeland, and T.A. Howell (2012), Evaluating the two-source energy balance model using local thermal and surface flux observations in a strongly advective irrigated agricultural area, *Adv. Water Resour.* **50**, 120-133, DOI: 10.1016/j.advwatres.2012.07.005.

Lagouarde, J.-P., F. Jacob, X.F. Gu, A. Olioso, J.-M. Bonnefond, Y. Kerr, K.J. McAneney, and M. Irvine (2002), Spatialization of sensible heat flux over a heterogeneous landscape, *Agronomie* **22**, 6, 627-633, DOI: 10.1051/agro:2002032.

Lhomme, J.-P., and A. Chehbouni (1999), Comments on dual-source vegetation-atmosphere transfer models, *Agr. Forest Meteorol.* **94**, 3-4, 269-273, DOI: 10.1016/S0168-1923(98)00109-9.

Liang, X., D.P. Lettenmaier, E.F. Wood, and S.J. Burges (1994), A simple hy-drologically based model of land surface water and energy fluxes for GCMs, *J. Geophys. Res.* **99**, D7, 14415-14428, DOI: 10.1029/94JD00483.

Mancini, M. (1990), La modellazione distribuita della risposta idrologica: effetti della variabilità spaziale e della scala di rappresentazione del fenomeno dell'assorbimento, Ph.D. Thesis, Politecnico di Milano, Milan (in Italian).

McCumber, M.C., and R.A. Pielke (1981) Simulation of the effects of surface fluxes of heat and moisture in a mesoscale numerical model: 1. Soil layer, *J. Geophys. Res.* **86**, C10, 9929-9938, DOI: 10.1029/JC086iC10p09929.

Norman, J.M., W.P. Kustas, and K.S. Humes (1995), Source approach for estimating soil and vegetation energy fluxes in observations of directional radiometric surface temperature, *Agr. Forest Meteorol.* **77**, 3-4, 263-293, DOI: 10.1016/0168-1923(95)02265-Y.

Rabuffetti, D., G. Ravazzani, C. Corbari, and M. Mancini (2008), Verification of operational Quantitative Discharge Forecast (QDF) for a regional warning system – the AMPHORE case studies in the upper Po River, *Nat. Hazards Earth Syst. Sci.* **8**, 161-173, DOI: 10.5194/nhess-8-161-2008.

Ravazzani, G., D. Rametta, and M. Mancini (2011), Macroscopic Cellular Automata for groundwater modelling: A first approach, *Environ. Modell. Softw.* **26**, 5, 634-643, DOI: 10.1016/j.envsoft.2010.11.011.

Rawls, W.J., and D.L. Brakensiek (1985), Prediction of soil water properties for hydrologic modeling. **In:** E.B. Jones and T.J. Ward (eds.), *Watershed Management in the Eighties*, *A Symposium of ASCE Convention; April 30-May 1, 1985, Denver, Colorado, United States,* ASCE, New York, NY, 293-299.

Richter, K., and W.J. Timmermans (2009), Physically based retrieval of crop characteristics for improved water use estimates, *Hydrol. Earth Syst. Sci.* **13**, 5, 663-674, DOI: 10.5194/hess-13-663-2009.

Roerink, G.J., Z. Su, and M. Menenti (2000), S-SEBI: A simple remote sensing algorithm to estimate the surface energy balance, *Phys. Chem. Earth B* **25**, 2, 147-157, DOI: 10.1016/S1464-1909(99)00128-8.

Sobrino, J.A., J.C. Jiménez-Muñoz, G. Sòria, M. Gómez, A. Barella Ortiz, M. Romaguera, M. Zaragoza, Y. Julien, J. Cuenca, M. Atitar, V. Hidalgo, B. Franch, C. Mattar, A. Ruescas, L. Morales, A. Gillespie, L. Balick, Z. Su, F. Nerry, L. Peres, and R. Libonati (2008), Thermal remote sensing in the framework of the SEN2FLEX project: field measurements, airborne data and applications, *Int. J. Remote Sens.* **29**, 17-18, 4961-4991, DOI: 10.1080/01431160802036516.

Su, Z. (2002), The Surface Energy Balance System (SEBS) for estimation of turbulent heat fluxes, *Hydrol. Earth Syst. Sci.* **6**, 1, 85-100, DOI: 10.5194/hess-6-85-2002.

Su, Z., T. Schmugge, W.P. Kustas, and W.J. Massman (2001), An evaluation of two models for estimation of the roughness height for heat transfer between the land surface and the atmosphere, *J. Appl. Meteor.* **40**, 1933-1951, DOI: 10.1175/1520-0450(2001)040<1933:AEOTMF>2.0.CO;2.

Su, Z., W. Timmermans, A. Gieske, L. Jia, J.A. Elbers, A. Olioso, J. Timmermans, R. van der Velde, X. Jin, H. van der Kwast, D. Sabol, J.A. Sobrino, J. Moreno, and R. Bianchi (2008), Quantification of land-atmosphere exchanges of water, energy and carbon dioxide in space and time over the heterogeneous Barrax site, *Int. J. Remote Sens.* **29**, 17-18, 5215-5235, DOI: 10.1080/01431160802326099.

Sun, S.F. (1982), Moisture and heat transport in a soil layer forced by atmospheric conditions, M.Sc. Thesis, University of Connecticut, Storrs.

Thom, A.S. (1975), Momentum, mass and heat exchange of plant communities. **In:** J.L. Monteith (ed.), *Vegetation and Atmosphere*, Academic Press, London, 57-110.

Timmermans, W.J., W.P. Kustas, M.C. Anderson, and A.N. French (2007), An intercomparison of the Surface Energy Balance Algorithm for land (SEBAL) and the Two-Source Energy Balance (TSEB) modeling schemes, *Remote Sens. Environ.* **108**, 4, 369-384, DOI: 10.1016/j.rse.2006.11.028.

Timmermans, W.J., Z. Su, and A. Olioso (2009), Footprint issues in scintillometry over heterogeneous landscapes, *Hydrol. Earth Syst. Sci.* **13**, 11, 2179-2190, DOI: 10.5194/hess-13-2179-2009.

Timmermans, W.J., J.C. Jiménez-Muñoz, V. Hidalgo, K. Richter, J.A. Sobrino, G. D'Urso, F. Mattia, G. Satalino, E. De Lathauwer, and V.R.N. Pauwels (2011), Estimation of the spatially distributed surface energy budget for AgriSAR 2006, Part I: Remote sensing model intercomparison, *JSTARS-IEEE* **4**, 2, 465-481, DOI: 10.1109/JSTARS.2010.2098019.

Timmermans, W., C. van der Tol, J. Timmermans, M. Ucer, X. Chen, L. Alonso, J. Moreno, A. Carrara, R. Lopez, F. de la Cruz Tercero, H.L. Corcoles, E. de Miguel, J.A.G. Sanchez, I. Pérez, B. Franch, J.-C.J. Munoz, D. Skokovic, J. Sobrino, G. Soria, A. MacArthur, L. Vescovo, I. Reusen, A. Andreu, A. Burkart, C. Cilia, S. Contreras, C. Corbari, J.F. Calleja, R. Guzinski, C. Hellmann, I. Herrmann, G. Kerr, A.-L. Lazar, B. Leutner, G. Mendiguren, S. Nasilowska, H. Nieto, J. Pachego-Labrador, S. Pulanekar, R. Raj, A. Schikling, B. Siegmann, S. von Bueren, and Z.B. Su (2015), An overview of the Regional Experiments For Land-atmosphere Exchanges 2012 (REFLEX 2012) campaign, *Acta Geophys.* **63**, 6, 1465-1484, DOI: 10.2478/s11600-014-0254-1 (this issue).

Twine, T.E., W.P. Kustas, J.M. Norman, D.R. Cook, P.R. Houser, T.P. Meyers, J.H. Prueger, P.J. Starks, and M.L. Wesely (2000), Correcting eddy-covariance flux underestimates over a grassland, *Agr. Forest Meteorol.* **103**, 3, 279-300, DOI: 10.1016/S0168-1923(00)00123-4.

van der Tol, C. (2012), Validation of remote sensing of bare soil ground heat flux, *Remot. Sens. Environ.* **121**, 275-286, DOI: 10.1016/j.rse.2012.02.009.

van der Tol, C., W.J. Timmermans, C. Corbari, A. Carrara, J. Timmermans, and Z. Su (2015), An analysis of turbulent heat fluxes and the energy balance during the REFLEX campaign, *Acta Geophys.* **63**, 6, 1516-1539, DOI: 10.1515/acgeo-2015-0061 (this issue).

Verhoef, A., B.J.J.M. van den Hurk, A.F.G. Jacobs, and B.G. Heusinkveld (1996), Thermal soil properties for vineyard (EFEDA-I) and savanna (HAPEX-Sahel) sites, *Agr. Forest Meteorol.* **78**, 1-2, 1-18, DOI: 10.1016/0168-1923(95)02254-6.

Wang, T., G.R. Ochs, and S.F. Clifford (1978), A saturation-resistant optical scintillometer to measure C^2_n, *J. Opt. Soc. Am.* **68**, 3, 334-338, DOI: 10.1364/JOSA.68.000334.

Wilson, K., A. Goldstein, E. Falge, M. Aubinet, D. Baldocchi, P. Berbigier, C. Bernhofer, R. Ceulemans, H. Dolman, C. Field, A. Grelle, A. Ibrom, B.E. Law, A. Kowalski, T. Meyers, J. Moncrieff, R. Monson, W. Oechel, J. Tenhunen, S. Verma, and R. Valentini (2002), Energy balance closure at FLUXNET sites, *Agr. Forest Meteorol.* **113**, 1-4, 223-243, DOI: 10.1016/S0168-1923(02)00109-0.

Wood, E.F., D.P. Lettenmaier, X. Liang, D. Lohmann, A. Boone, S. Chang, F. Chen, Y. Dai, R.E. Dickinson, Q. Duan, M. Ek, Y.M. Gusev, F. Habets, P. Irannejad, R. Koster, K.E. Mitchel, O.N. Nasonova, J. Noilhan, J. Schaake, A. Schlosser, Y. Shao, A.B. Shmakin, D. Verseghy, K.Warrach, P. Wetzel, Y. Xue, Z.-L. Yang, and Q. Zeng (1998), The Project for Inter-comparison of Land-surface Parameterization Schemes (PILPS) Phase 2(c) Red-Arkansas river basin experiment: 1. Experiment description and sum-mary intercomparisons, *Global Planet. Change* **19**, 1-4, 115-135, DOI: 10.1016/S0921-8181(98)00044-7.

Estimating Flood Quantiles on the Basis of Multi-Event Rainfall Simulation – Case Study

Elżbieta JAROSIŃSKA[1] and Katarzyna PIERZGA[2]

[1]Institute of Water Engineering and Water Management,
Cracow University of Technology, Cracow, Poland;
e-mail: ejarosin3@gmail.com (corresponding author)

[2]Hydromodel Center of Hydrologic and Environmental Engineering,
Brzezna, Poland; e-mail: katarzyna.pierzga@hydromodel.pl

A b s t r a c t

This paper presents an approach to estimating the probability distribution of annual discharges Q based on rainfall-runoff modelling using multiple rainfall events. The approach is based on the prior knowledge about the probability distribution of annual maximum daily totals of rainfall P in a natural catchment, random disaggregation of the totals into hourly values, and rainfall-runoff modelling. The presented Multi-Event Simulation of Extreme Flood method (MESEF) combines design event method based on single-rainfall event modelling, and continuous simulation method used for estimating the maximum discharges of a given exceedance probability using rainfall-runoff models. In the paper, the flood quantiles were estimated using the MESEF method, and then compared to the flood quantiles estimated using classical statistical method based on observed data.

Key words: rainfall event, precipitation generating, rainfall-runoff modelling, probability distribution of annual maximum discharges, antecedent runoff conditions, flood quantiles.

1. INTRODUCTION

It is projected that climate changes (SPA 2020 (2013)) and inconsistent system of urban planning (including accelerated catchment sealing process) (KPZK 2030 (2013)) will have a significant impact on causing negative changes in water regime in Poland until 2030. According to Kowalczak (2011), it is changes in land use (land sealing) that should be seen as the major cause of floods, while the changing climate will contribute to changing the precipitation character. Forecasts estimate that despite almost unchanged annual precipitation total, the character of this phenomenon will become more random and heavy rainfalls (above 20 mm/day) will likely become noticeable, especially in the southern part of Poland.

Seeing how these reasons pose challenges that demand appropriate methods of engineering hydrology, the authors undertook to analyse a new approach to estimating probability distribution of maximum annual discharges. This approach makes it possible to consider future changes in urban planning of a catchment as well as consider the changeable character of precipitation. Both of these phenomena have a significant impact on the increase in maximum discharge and the change in their probability distribution.

The presented method is based on the information about probability distribution of maximum daily rainfall totals in catchment, their random distribution into hourly values (disaggregation), and multi-event rainfall-runoff modelling. It also involves considering different moisture conditions of the soil in the catchment, because catchment moisture condition before the rainfall event resulting in a flood wave is essential for the discharge values (Pathiraja et al 2012).

The method combines the design event method based on single event modelling (Pilgrim and Cordery 1993) and the continuous simulation method (Boughton and Droop 2003, Calver and Lamb 1995), both used for estimating probable maximum discharges with the application of rainfall-runoff models. For brevity, the new method is called Multi-Event Simulation of Extreme Flood (MESEF).

The design event method assumes that the estimation of a flood of selected exceedance probability results from a design rainfall of the same exceedance probability. A hyetograph is used as the input data for the rainfall-runoff model, with the precipitation duration equal to (or greater than) the time of concentration in the catchment (DVWK 1984) and usually with a method of disaggregation into smaller time steps.

The major advantage of the design event method lies in its simplicity of use and easiness in interpreting results. On the other hand, many of its elements raise questions. It is debatable, for instance, what rainfall duration

should be considered – whether it should be equal to or greater than concentration time (DVWK 1984), whether over 8.5 hours (Nowicka *et al*. 1997) or 24 hours (USDA 1986). Also, the issue of establishing the antecedent runoff conditions in the catchment has not been definitely resolved; at present, average conditions are assumed or maximum catchment saturation prior the rainfall event is implied. A similar simplification is used in relation to temporal distribution of rainfall; it is common to apply fixed temporal distributions (4 types) (USDA 1986), or a distribution with a peak in the middle of a rainfall event (DVWK 1984), or to simply search for a distribution that will generate the maximum runoff (Banasik 2009).

The second method – the continuous simulation method – requires a stochastic rainfall generator. The generated continuous rainfall sequences provide input for the continuous rainfall-runoff model (Cameron *et al*. 1999). Continuous sequences of modelled runoff are then obtained, and their maximum values (as in the case of the observed data) are subjected to statistical analysis to identify the probability distribution and calculate quantile values.

Considering the application of rainfall-runoff models for estimating quantile values of probable maximum discharges, the design event method is a classical approach. At the same time, the continuous simulation method is recognized as its practical alternative.

So far, the continuous simulation method has not been used in Poland in practical application, although there have been first attempts to use it for designing a storm drain system (Licznar 2009). It is worth noting that this method eliminates most of the disadvantages of the design event method. What is more, Pathiraja *et al.* (2012) observed its superiority in considering catchment moisture condition in modelling, which is important on account that underestimating its correct simulation could result in underestimating discharge peak values. Boughton and Droop (2003) pointed out the possibility to eliminate the necessity to match the duration and rainfall time distribution in modelling, which raises many questions and concerns in the design event method. However, the rainfall-runoff models used in this method are more complex, *i.e.*, they have more parameters, and hence the calibration of these models is more difficult. It is also essential that a stochastic rainfall generator with parameters adjusted to the local conditions be used in the method, because it allows for generation of long synthetic rainfall series.

Alongside the application of both methods separately, there have also been approaches combining them both, *e.g.*, SCHADEX (Paquet *et al*. 2013), or other described by Francés *et al.* (2008), as well as applications related to the use of the Monte Carlo method for multidimensional probability distributions (Rahman *et al*. 2002). The SCHADEX method uses an approach described as semi-continuous. A continuous rainfall-runoff model (MORDOR) is used along with rainfall data from multiannual period whose

fragments are substituted with synthetic rainfall events. This approach makes it possible to obtain the probability distribution of maximum discharges without making assumptions about the condition of the catchment prior to the rainfall – the condition results from a real historical period. SCHADEX method was applied in Poland for the first time by Osuch *et al.* (2013), using the Nysa Kłodzka catchment as a case study. Somewhat different solutions are proposed in the approach presented by Francés *et al*. (2008). Their methodology implies identifying annual discharges Q on the basis of modelling of nonrandomized synthetic rainfall events for different known moisture conditions.

The present study evaluates whether the MESEF method could be used to receive the probability distribution of maximum discharges on the basis of multi-event rainfall simulation. In order to prove the validity of the proposed method, the quantiles received from the MESEF were compared with the quantiles received from the classical statistical method.

2. STUDY AREA

The MESEF method was applied in the Czarny River catchment, situated in south-eastern Poland with the area of 95.2 km^2 to the Polana gauge (Fig. 1). The elevation differences in the catchment reach 600 m. The drainage system is very well developed, and its density reaches almost 3 km/km^2. Over 80% of this catchment is forestland.
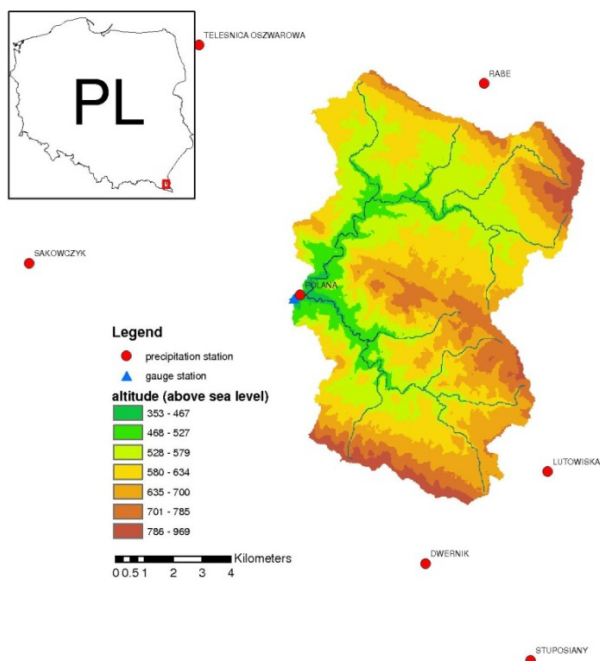
Fig. 1. The Czarny River catchment with the network of precipitation stations.

Sequence of annual maximum daily rainfall totals P_o and annual discharges Q_o from a 36-year period (1977-2012) from the Polana precipitation and Polana gauge stations, respectively, were chosen for analyses. A simplifying assumption was made that the data from the Polana station are equivalent to the areal precipitation of the entire catchment.

The Czarny catchment planning did not change in a significant way throughout the period from which the data in the article was sourced. In other words, the catchment retained its natural character thanks to which the land use changes did not affect the discharge values, and, in consequence, could be chosen as representative for the purposes of the article. This particular catchment is therefore a solid starting point for analyzing the influence of catchment planning changes on changes in discharge maximum values.

3.   MESEF – ASSUMPTIONS AND STAGES

The MESEF method is based on the assumption that rainfall-runoff modelling replicated for multiple rainfall events, originating from the probability distribution of annual maximum daily rainfall totals P_o, will make it possible to obtain the probability distribution of annual maximum discharges Q_o. This distribution is developed on the basis of peak discharge values obtained from modelling. An assumption was also made about rainfall disaggregation: in order to break down the maximum daily precipitation into hourly values, beta probability distribution function, with parameters α and β, was used. The values of these parameters were generated from a known two-dimensional distribution of α and β based on measurement data. The MESEF method assumes conducting rainfall-runoff modelling for three types of antecedent runoff conditions (ARC) in the catchment: dry, normal, and wet (Hawkins *et al.* 2009).

The MESEF method is conducted in three stages.

❑ Rainfall generation:
  – identification of the probability distribution of observed P_o,
  – generating synthetic values of P_s from the identified probability distribution,
  – generating pairs of parameters α and β from their two-dimensional frequency distribution,
  – creating hyetographs with an hourly time step by disaggregation of synthetic P_s;

❑ Rainfall-runoff modelling:
  – identification of parameters of the selected model on the basis of physiographic characteristics of the catchment,
  – calibration of the model for the assumed ARC in the catchment,
  – creating synthetic runoff hydrographs on the basis of rainfall hyetographs for three kinds of ARC by modelling;

❑ Estimating probability distributions of synthetic Q_s for the best proportion ARC, description of the procedure of finding the best proportion ARC in Section 6:

– estimating the flood quantiles.

The following chapters contain detailed description of the work carried out during the specific stages of the MESEF.

4. RAINFALL GENERATION

In general, synthetic hyetographs are generated by a rainfall generator. In order to generate a hyetograph, it is necessary to provide annual maximum daily rainfall totals and the α and β parameters of the beta distribution. The proposed MESEF method requires an analysis of many rainfall events (many hyetographs). This is why synthetic daily totals generation from the probability distribution of observed P_o was used, as well as generation of the beta distribution parameters α and β from their two-dimensional frequency distribution.

It was assumed that the observed annual maximum daily rainfall totals P_o have the three-parameter Weibull distribution $W(\lambda, \kappa, \gamma)$ (Fig. 2), where λ, $\kappa > 0$ and the density function was expressed by the following formula 1:

$$f_w\left(p_0, \lambda, \kappa, \gamma\right) = \begin{cases} \dfrac{\kappa}{\lambda}\left(\dfrac{p_0 - \gamma}{\lambda}\right)^{\kappa-1} \exp\left(-\left(\dfrac{p_0 - \gamma}{\lambda}\right)^{\kappa}\right) & \text{for } p_0 \geq \gamma \\ 0 & \text{for } p_0 < \gamma \end{cases} \tag{1}$$
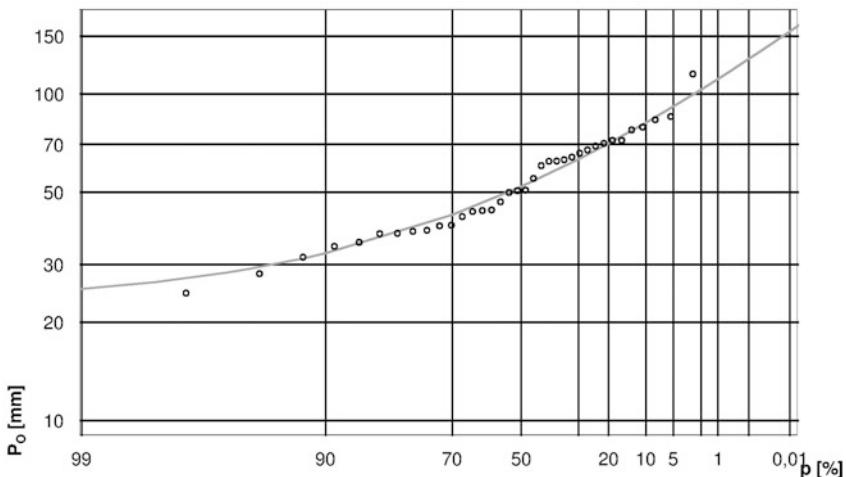
Fig. 2. Empirical (circles) and theoretical (solid line) probability exceedance function of P_o from the 36-year period (1977-2012) from the Polana precipitation station (Weibull distribution $\lambda = 1.7107$, $\kappa = 36.137$, $\gamma = 22.827$).

The parameters of this distribution were estimated using the maximum likelihood method.

The description of the generator's operation was based on the example of generating 100-element rainfall sample. From the Weibull distribution, 100 synthetic P_s values were generated. In order to estimate the uncertainty related to generating precipitation, there were ten 100-element samples generated from Weibull distribution. All of the generated samples underwent Pearson goodness-of-fit test χ^2 (χ^2 P) with Weibull theoretical distribution. None of the samples was rejected by that test at the level of significance alpha = 0.05, even though the test statistics differed. Finally, in order to limit the uncertainty of the MESEF method, it was assumed that the best input for the rainfall-runoff model will be the sample whose test statistics had the lowest value, in other words – the one that performed best in χ^2 test. It can be expected that greater number of generated precipitation samples will allow choosing the best of them, *i.e.* closest to the theoretical distribution.

Each of 100 synthetic P_s values was broken down into hourly values using density function $f_B(y; \alpha, \beta)$ and the method of generating α and β parameters of the beta distribution $Be(\alpha, \beta)$, where $\alpha, \beta > 0$, and the density function was expressed using the following formula 2:

$$f_B(y, \alpha, \beta) = \begin{cases} \dfrac{1}{B(\alpha, \beta)} y^{\alpha-1} (1-y)^{\beta-1} & \text{for } y \in (0,1) \\ 0 & \text{for } y \notin (0,1) \end{cases}, \qquad (2)$$

where $B(\alpha, \beta)$ is the beta function.

The properties of this distribution, *i.e.*, the arbitrary asymmetry (dependent on the values of the parameters α and β) and its double-sided limitation make it applicable in the distribution of the daily precipitation into the values for smaller time steps (Więzik 2010).

Because α and β parameters have an influence on how the rainfall totals are broken down into hourly values (Fig. 3), information was searched for concerning the possible values of these parameters.

In the end, the range and the frequency of occurrence of the values of α and β parameters of the beta distribution $Be(\alpha, \beta)$ were used. These were obtained by fitting beta distribution to daily precipitation broken down into hourly values, based on the multiannual period of 1961-1985 for Cracow, with an assumption that the data used are representative of catchments in the Carpathian region. Making such an assumption, the authors are aware that it may cause a kind of bias in generating α and β parameters of the beta distribution $Be(\alpha, \beta)$; however, only these data with a one-hour step were available for their calculations.
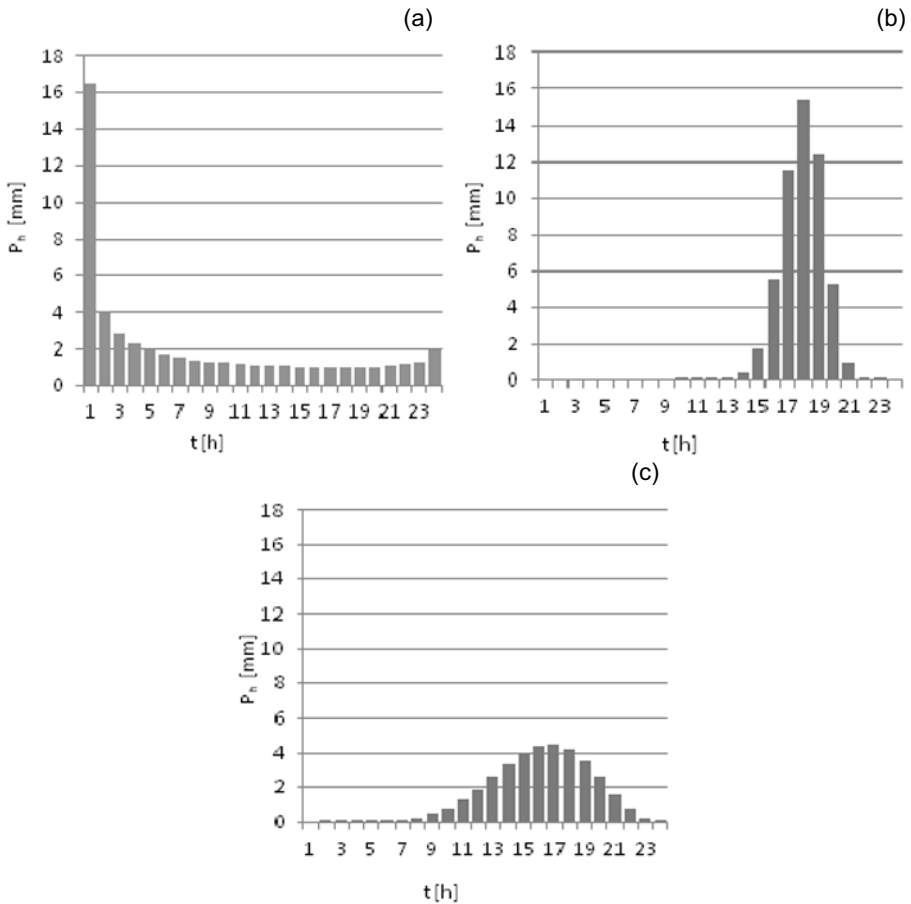
Fig. 3. Exemplary hyetographs of annual maximum daily rainfall totals: (a) $P = 51.2$ mm, (b) $P = 53.4$ mm, (c) $P = 36.7$ mm, broken down into 24 hourly values, for which the values of the beta parameters (α, β) are: (a) $\alpha = 0.313$, $\beta = 0.725$, (b) $\alpha = 45.391$, $\beta = 17.131$, and (c) $\alpha = 8.251$, $\beta = 4.418$.

Only rainfalls with at least 10 mm daily total were used for the calculations. As a result, 274 pairs of parameters (α, β) were obtained with values ranging from 0 to 60 (Table 1).

In order to generate values of the parameter pairs (α, β), a two-dimensional distribution of the frequency of occurrence was used in accordance with Table 1. Generating of pairs (α, β) should be performed in three stages: i.e., firstly an interval $\Delta\alpha_i$ from the marginal distribution of α is generated, then $\Delta\beta_j$ from the conditional probability distribution $P(\beta \in \Delta\beta_j | \alpha \in \Delta\alpha_i)$, and then, independently of each other, α and β from the uniform distribution

Table 1

Frequency of parameters (α, β) occurrence of the beta distribution
in the $(0,60) \times (0,60)$ domain*)

| | | β | | | | | | | | | | | | | Total | |
| | | (0, 1) | | [1, 2) | | [2, 5) | | [5, 10) | | [10, 20) | | [20, 30) | | [30, 60) | | | |
		a.f.	r.f. [%]	a.f.	r.f. [%]	a.f.	r.f. [%]	a.f.	r.f. [%]	a.f.	r.f. [%]	a.f.	r.f. [%]	a.f.	r.f. [%]	a.f.	r.f. [%]
	(0,1)	18	6.6	7	2.6	6	2.2	0	0	0	0	0	0	0	0	31	11.3
	[1,2)	2	0.7	14	5.1	13	4.7	5	1.8	0	0	1	0.4	0	0	35	12.8
	[2,5)	3	1.1	7	2.6	17	6.2	12	4.4	6	2.2	2	0.7	2	0.7	49	17.9
α	[5,10)	1	0.4	11	4.0	9	3.3	7	2.6	5	1.8	1	0.4	4	1.5	38	13.9
	[10,20)	0	0	2	0.7	7	2.6	6	2.2	9	3.3	7	2.6	3	1.1	34	12.4
	[20,30)	0	0	0	0	2	0.7	7	2.6	19	6.9	19	6.9	3	1.1	50	18.2
	[30,60)	0	0	0	0	1	0.4	3	1.1	27	9.9	6	2.2	0	0	37	13.5
	Total	24	8.8	41	15.0	55	20.1	40	14.6	66	24.1	36	13.1	12	4.4	274	100

*)The calculations were performed in 2013 by Stanisław Węglarczyk, Cracow University of Technology, Institute of Water Engineering and Water Management.
Explanations: a.f. – absolute frequency, r.f. – relative frequency.

(a)   (b)
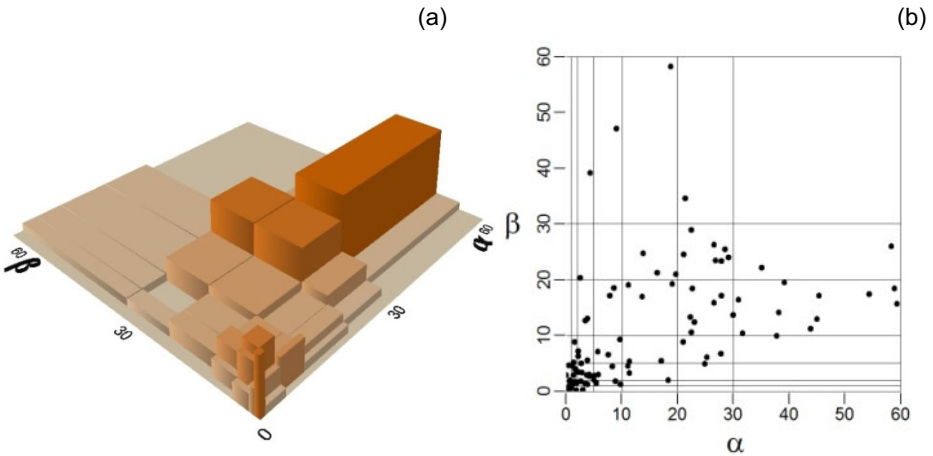
Fig. 4. Two-dimentional distribution of parameters α and β: (a) 2D histogram of (α, β) values in the $(0,60) \times (0,60)$ domain based on calculations by Stanisław Węglarczyk, and (b) generated 100 pairs of (α, β) parameters used in that work.

of the appropriate intervals $\Delta\alpha_i$ and $\Delta\beta_j$. This, in practice, comes down to generating 100 pairs of parameters (α, β) from the areas marked out by the occurrence interval boundaries of parameters α and β (Fig. 4).
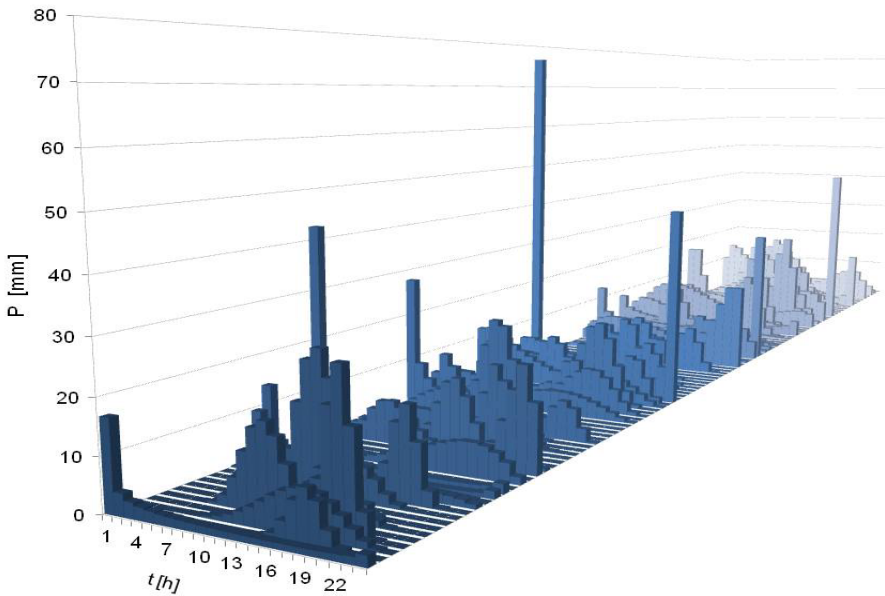
Fig. 5. Exemplary generated hyetographs.

Parameters α and β are independent of the daily rainfall totals. This means that since there was no correlation found either between parameter α and daily totals of rainfall P, or parameter β and daily totals of rainfall P, parameters α and β can be generated independently of synthetic P_s generation.

Using the beta density function $f_B(y; \alpha, \beta)$ for disaggregation of synthetic P_s for hourly values P_h allowed for 100 rainfall hyetographs to be obtained (Fig. 5), and they constitute the input data for the rainfall-runoff model. It means that only one pair (α, β) was applied to every generated rainfall total.

5. RAINFALL-RUNOFF MODEL

Version 3.5 of the Hydrologic Engineering Center Hydrologic Modeling System (HEC-HMS) (Scharffenberg and Fleming 2010) was used for modelling the runoff from the investigated catchment.

The Soil Conservation Service (now the Natural Resources Conservation Service) Curve Number loss method (SCS CN), based on the knowledge of total precipitation, soil type, land cover type, and soil moisture at the beginning of the rainfall, was used to determine the value of effective rainfall. All of these factors are taken into account in the CN parameter (Mishra and Singh 2003). The Unit Hydrograph method (SCS UH), used to determine the value of the peak discharge, total runoff volume, hydrograph shape, and time history, was chosen for the rainfall-runoff transformation. To determine the

baseflow, the Recession Method was used. It allows the approximation of a typical streamflow behaviour also after the rainfall event. This situation – the descending part of the hydrograph – is depicted in the form of an exponential recession curve (Scharffenberg and Fleming 2010).

The choice of these simple methods was driven by their widespread use, small number of parameters, as well as their applicability in ungauged catchments due to the possibility of parameter estimation on the basis of catchment characteristics. Moreover, the loss and transformation models allow to diversify the parameter values of the HEC-HMS model according to the catchment antecedent runoff conditions which have an influence on the values of peak discharges. This is significant for the MESEF method proposed in this paper.

Data from three flood hydrographs from 1997, 2007, and 2008 were used for calibration and verification of the model parameters. The data included precipitation from the Polana station and discharges from the Polana gauge on the Czarny River. The calibration procedure was conducted using HEC-HMS software. Five parameters from the model underwent calibration: the initial abstraction, CN parameter, T_{Lag} parameter, baseflow threshold coefficient, and recession constant. Different ARC which had impact on the value of the CN parameter and the value of the dependent T_{Lag} parameter were allowed for in the calibration procedure. During this procedure, it has been observed that sensitivity of SCS CN loss model for changes of an initial abstraction is not as significant as in the case of other models (Lee and Huang 2013).

In order to assess the quality of the chosen rainfall-runoff model, a direct comparison between the observed and simulated peak discharges was carried out (Table 2). The values of relative errors show at least good quality of the model and this is why it could be used for generating synthetic discharge hydrographs.

Table 2

Comparison between the observed and simulated peak discharges

Year	Observed peak discharges [m^3/s]	Simulated peak discharges [m^3/s]	Relative error [%]
1997	111.0	107.61	3.1
2007	63.4	54.89	13.4
2008	111.0	115.12	3.7

Rainfall-runoff modelling was conducted for a set of generated rainfall events, for three kinds of antecedent runoff conditions (ARC) in the catchment: dry (ARC I), normal (ARC II), and wet (ARC III) (Fig. 6).

(a)   (b)

(c)
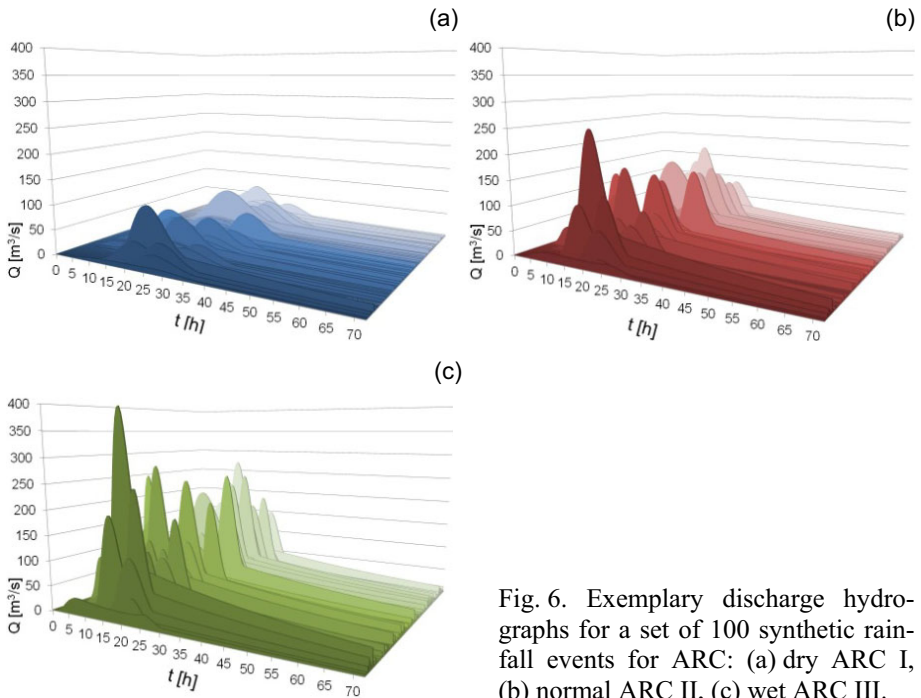
Fig. 6. Exemplary discharge hydro-
graphs for a set of 100 synthetic rain-
fall events for ARC: (a) dry ARC I,
(b) normal ARC II, (c) wet ARC III.

6. FINDING THE BEST PROPORTION OF ARC FOR SYNTHETIC PEAK DISCHARGE VALUES Q_S

According to Hawkins *et al.* (2009), the absolute average conditions ARC
may be variable depending on factors such as local climate, soil, vegetation,
and land use. This is the purpose behind finding the most frequently occur-
ring runoff conditions. In the case of the Czarny catchment, these conditions
were searched for by means of estimating the best proportion of antecedent
runoff conditions ARC for 100 synthetic rainfall events.

The analyses performed in this part of the work were supposed to answer
the question about the conditions required to be fulfilled by the synthetic da-
ta Q_s to identify the probability distribution of observed Q_o. It was assumed
that the probability distribution of observed Q_o was the actual distribution,
and attempts were made to make the synthetic data yield the best possible fit
to that distribution, including events with a very small exceedance probabil-
ity.

6.1 Estimation of the probability distribution of Q_o

From among several analysed probability distributions (Węglarczyk 2010,
Stedinger *et al.* 1993), *i.e.*, the two-parameter gamma, Gumbel (Fisher-

Tippett type I), Weibull (Fisher-Tippett type III), GEV, and log-normal, the two-parameter log-normal distribution demonstrated the best fit to the observations Q_o (Table 3, Fig. 7). The density function of the log-normal distribution $LN(\mu, \sigma)$, where $\mu, \sigma > 0$, was expressed by the following formula 3:

$$f(q_0, \mu, \sigma) \begin{cases} \dfrac{1}{q_0 \sigma \sqrt{2\pi}} \exp\left[-\dfrac{\left(\ln(q_0) - \mu\right)^2}{2\sigma^2} \right] & \text{for } q_0 > 0 \\ 0 & \text{for } q_0 \leq 0 \end{cases} \tag{3}$$

The parameters of this distribution were estimated using the maximum likelihood method.

Table 3

Statistic values of the Kolmogorov–Smirnov goodness-of-fit test
for examined probability distributions for observed Q_o
from the 36-year period (1977-2012) from the Polana gauge*

Probability distribution	Kolmogorov–Smirnov		Sample size	Critical value at the alpha level of significance	
	Statistic value	Rank		alpha = 0.2	alpha = 0.1
log-normal (two-parameter)	0.0756	1	36	0.1742	0.1991
GEV	0.0795	2			
gamma	0.0868	3			
Weibull	0.0937	4			
Gumbel max	0.1152	5			

*⁾Source of data: Institute of Meteorology and Water Management, Polish National Research Institute.
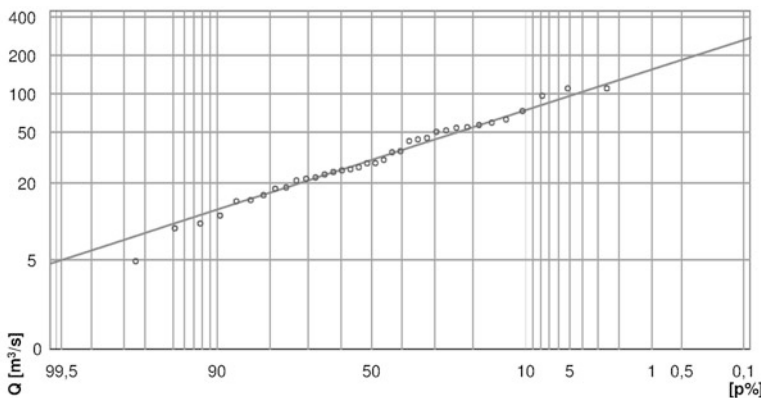
Fig. 7. Empirical (circles) and theoretical (solid line) probability exceedance function of Q_o from the 36-year period (1977-2012) from the Polana gauge (log-normal distribution: $\mu = 3.4149$, $\sigma = 0.71172$).

6.2 Creating combinations Q_{sci} of synthetic peak discharge values Q_s for different ARC

In order to create combinations Q_{sci} sequences of synthetic peak discharge values Q_s for three kinds of ARC were used. 300 synthetic peak discharge values Q_s were read off from the 300 synthetic hydrographs (Fig. 5), *i.e.*, 100 values for each of the three kinds of ARC (Fig. 8), namely Q_{s_I}, Q_{s_II}, and Q_{s_III}.

In the next stage, the combinations Q_{sci} ($i = 1, …, 38$) of the values of Q_{s_I}, Q_{s_II}, and Q_{s_III} were created to find the best fit between the probability distribution of the combination Q_{sci} and the theoretical probability distribution of the observed Q_o data.

For this purpose, an appropriate number of values was generated from each of the Q_{s_I}, Q_{s_II}, and Q_{s_III} sets, creating – as a result – new 100-element series of randomly intermixed discharge values for different ARC. Generating was performed for 38 possible combinations, creating thirty-eight 100-element discharge series. Thus, the combination **2-0-1** indicates, for example, that from Q_{s_I} 67 values were generated, which accounts for 2/3 of the elements of the entire series, while from Q_{s_III} 33 values were generated, which accounts for the remaining 1/3 of the elements of the entire series. In this case no discharge value was generated from Q_{s_II}. It means that this combination was affected by dry (2/3 of all values) and wet (1/3 of all values) runoff conditions in the catchment.
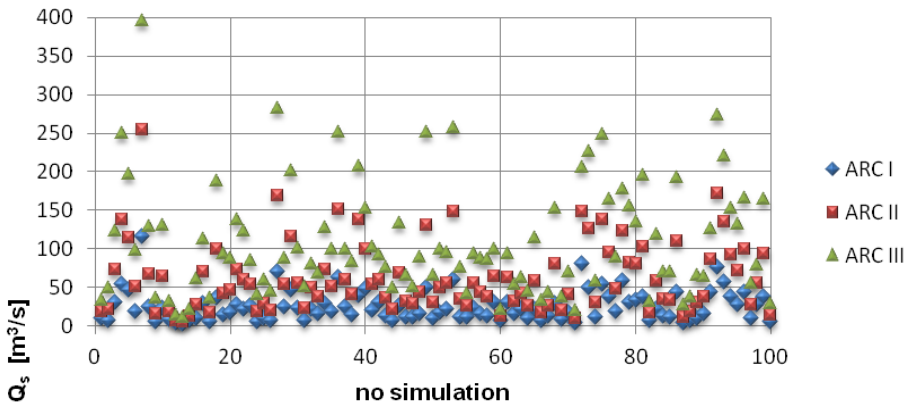
Fig. 8. Synthetic peak discharge values Q_s for three types of ARC.

6.3 An analysis of compatibility of the synthetic probability distributions of Q_{sci} and the probability distribution of observed Q_o

The created combinations Q_{sci} were tested for goodness-of-fit to the theoretical probability distribution for the observed data Q_o. The goodness-of-fit of

Table 4

Test statistic values for the Kolmogorov–Smirnov (K-S), Anderson–Darling (A-D),
and Pearson (χ^2 P) goodness-of-fit tests
calculated for thirty-eight 100-element combinations of synthetic Q_{sci}

i	Q_{sci} combinations where $i=1, …, 38$	K-S	K-S$_{crit.}$	A-D	A-D$_{crit.}$	χ^2 P	χ^2 $_{crit.}$
1	**1-0-0**	2.49		26.17		61.60	
2	**0-1-0**	2.85		16.74		46.80	
3	**0-0-1**	5.66		101.25		312.40	
4	**1-1-0**	**1.06**		4.16		17.80	
5	**1-0-1**	4.35		15.11		74.60	
6	**0-1-1**	2.36		46.86		131.40	
7	**0-1-2**	4.55		53.81		173.20	
8	**0-2-1**	3.35		25.82		63.80	
9	**1-0-2**	3.35		29.03		133.00	
10	**1-1-1**	2.11		11.68		45.00	
11	**1-2-0**	**1.25**		3.00		**14.60**	
12	**2-0-1**	1.49		9.05		38.80	
13	**2-1-0**	1.97		12.27		31.80	
14	**0-1-3**	4.68		60.85		190.40	
15	**0-3-1**	3.05		21.75		53.60	
16	**1-0-3**	3.76		40.20		160.60	
17	**1-1-2**	3.15		24.28		92.00	
18	**1-2-1**	2.15		10.61		34.40	
19	**1-3-0**	1.55	1.36	4.15	2.50	**15.60**	16.92
20	**2-1-1**	**1.25**		6.96		25.60	
21	**3-0-1**	1.79		11.66		40.60	
22	**3-1-0**	2.17		16.72		42.40	
23	**0-1-4**	4.96		71.79		234.60	
24	**0-2-3**	4.75		57.37		182.20	
25	**0-3-2**	3.85		37.32		98.80	
26	**0-4-1**	3.05		21.85		57.80	
27	**1-0-4**	4.26		53.72		204.00	
28	**1-1-3**	3.78		35.23		144.20	
29	**1-2-2**	3.15		25.44		85.60	
30	**1-3-1**	2.25		10.13		30.60	
31	**1-4-0**	1.95		6.65		23.40	
32	**2-0-3**	3.15		24.61		117.00	
33	**2-1-2**	2.35		14.66		59.80	
34	**2-2-1**	1.61		7.11		25.00	
35	**2-3-0**	**1.21**		2.99		**15.60**	
36	**3-0-2**	1.86		10.53		53.60	
37	**3-1-1**	1.44		9.32		28.80	
38	**3-2-0**	1.37		7.38		24.40	

Note: grey colour means that test did not reject the combination.
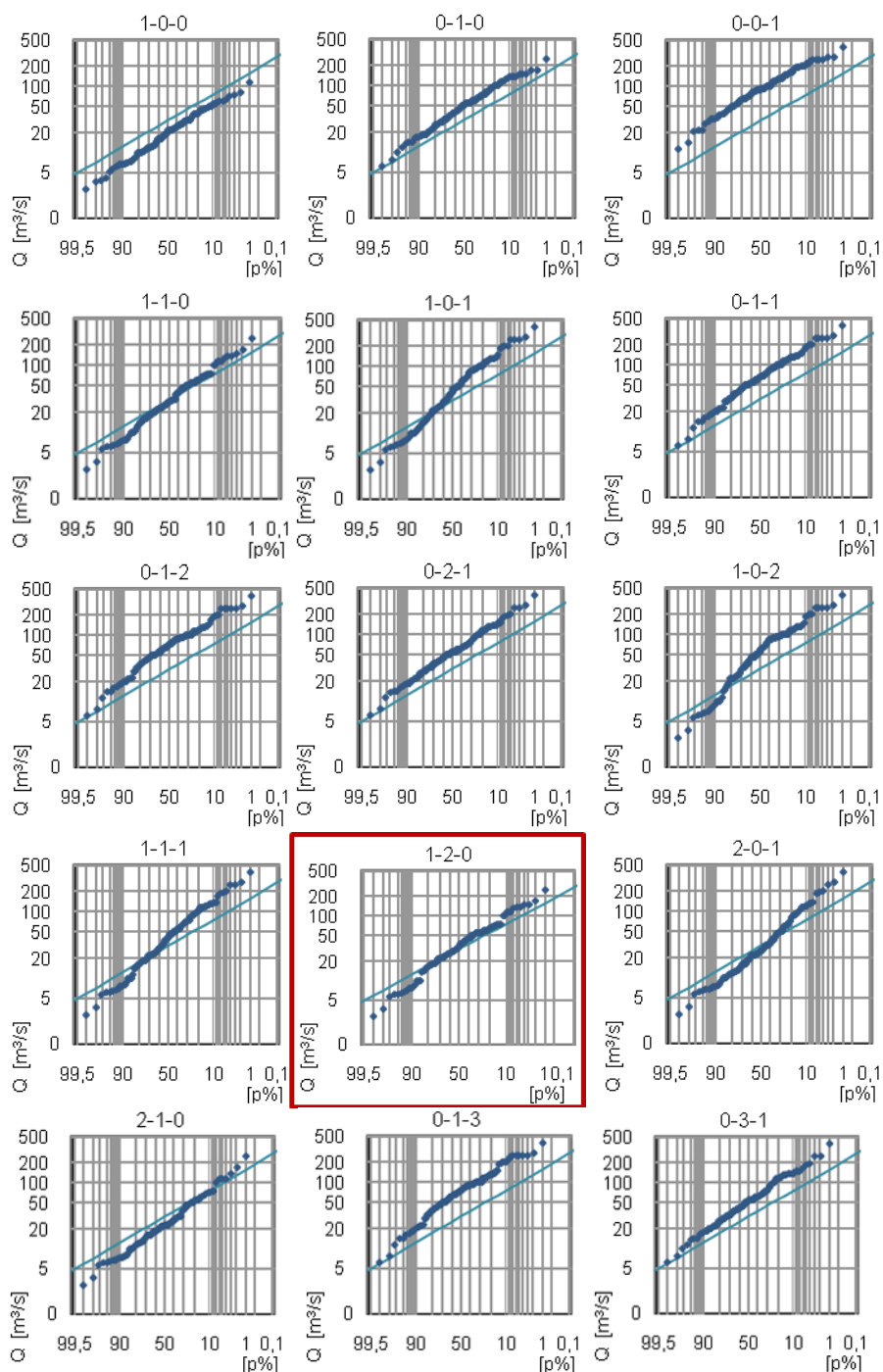
Fig. 9. Continued on next page.
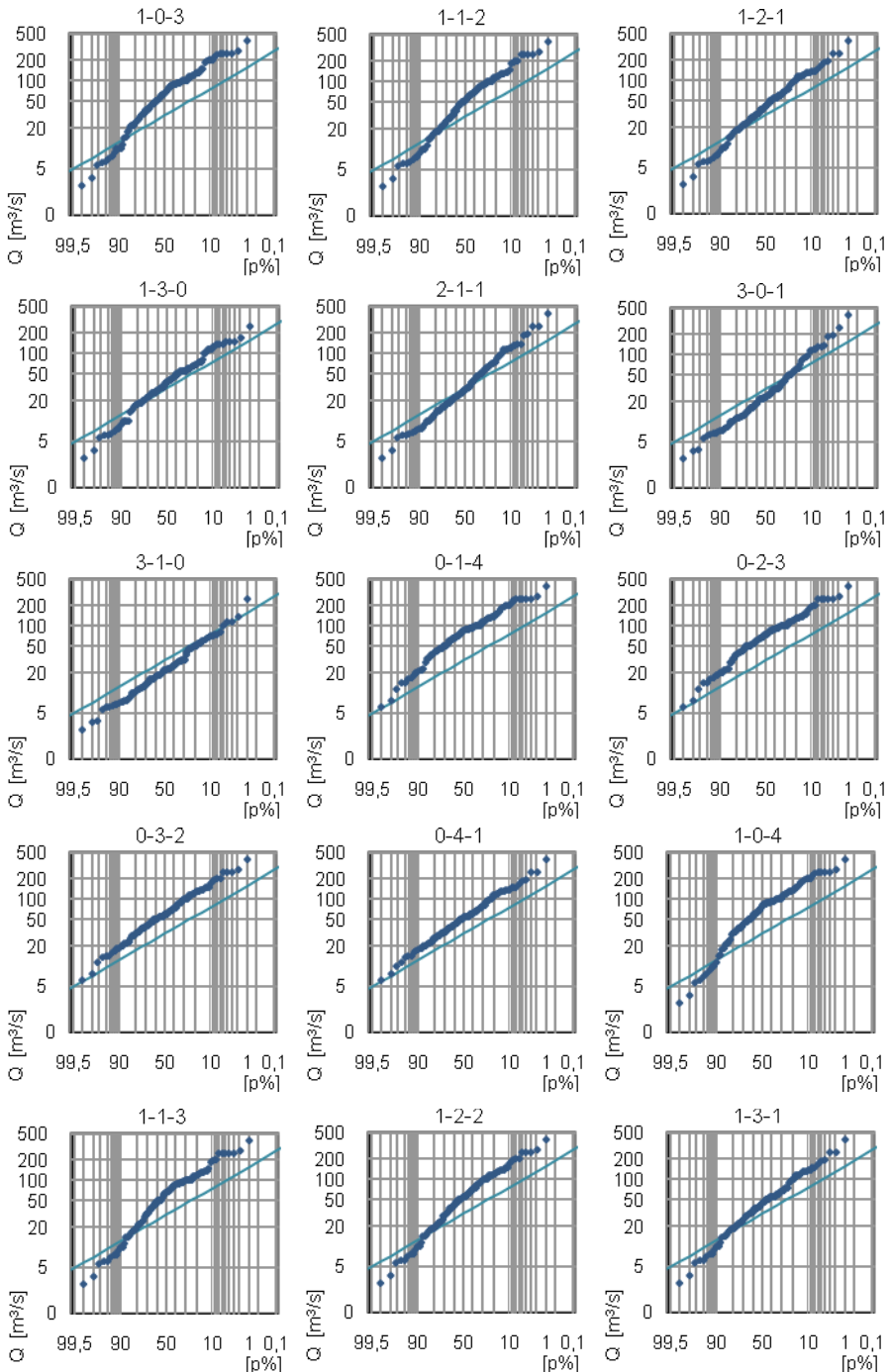
Fig. 9. Continued on next page.
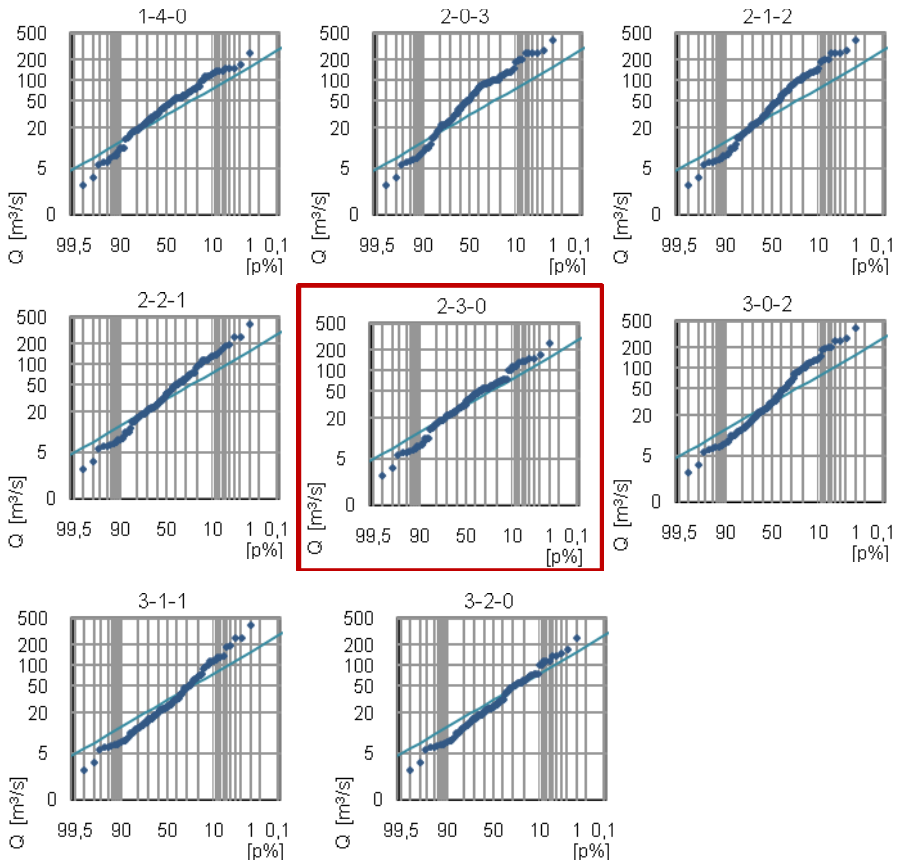
Fig. 9. Combinations of probability exceedance function of synthetic Q_{sci} (full circles) and observed discharges Q_o (solid line) at Polana cross-section in the Czarny catchment for different ARC. Combinations not rejected by the two tests are marked by framing.

both distributions was assessed using three tests: Kolmogorov–Smirnov (K-S), Anderson–Darling (A-D), and Pearson χ^2 (χ^2 P) (Table 4), under an assumption that the compatibility of distributions for a given combination must be not rejected by at least two tests.

The results of the K-S test did not reject the compatibility of both distributions in four cases, for the combinations: **1-1-0**, **1-2-0**, **2-1-1**, **2-3-0**, the χ^2 P − in three cases for the combinations: **1-2-0**, **1-3-0**, **2-3-0**, while the A-D test rejected the compatibility for all the combinations. In consequence, there were two tests (K-S and χ^2 P) that did not reject the compatibility of both distributions in only two cases, for the combinations: **1-2-0** and **2-3-0** (Fig. 9).

An analysis of the basic combination types **1-0-0**, **0-1-0**, and **0-0-1** which represent discharge series from dry, normal, and wet conditions, respectively, did not reveal that it was only one of those conditions that would bear the greatest similarity to the observed data (Fig. 9). This finding was also confirmed by the K-S, A-D, and χ^2 P tests, whose statistic values for **1-0-0** are 2.49, 26.74, 61.60, for **0-1-0** are 2.85, 16.74, 46.80, and for **0-0-1** are 5.66, 101.25, 312.40, respectively, and which significantly exceed the critical test values: 1.36, 2.50, and 16.92, respectively. In the case of combinations **1-2-0** and **2-3-0**, for which the goodness-of-fit of both distributions was not reject by at least two tests, the statistic values are much lower than the critical values, and they are: 1.25 (K-S), and 14.6 (χ^2 P) for **1-2-0**, and 1.21 (K-S), and15.6 (χ^2 P) for **2-3-0**, respectively. However, compatibility of distributions of these combinations were rejected by the A-D test, but their statistic values are not much greater than the critical test values at the significance level alpha = 0.05.

Based on the test of statistic values it can be concluded that the synthetic discharge values in proportions **1-2-0** and **2-3-0** of the ARC conditions in the river Czarny catchment demonstrate the best compatibility with the observed data.

In these optimal combinations, the synthetic discharge values come from only dry (from 33 to 40%) and normal (from 60 to 67%) antecedent conditions in the catchment. Wet antecedent runoff conditions (ARC III) do not affect the synthetic discharge values.

7. ESTIMATING PROBABILITY DISTRIBUTION OF SYNTHETIC Q_S FOR THE BEST ARC

For two specific best proportions of antecedent runoff conditions ARC (**1-2-0** and **2-3-0**), estimated for the Czarny catchment in the Polana cross-section, discharge exceedance probability curves of Q_s were created. At the same time, in order to increase the credibility of the flood quantiles from the probability distribution for very small exceedance probability, the modelling was performed on a 10 000-element rainfall sample. Then, 10 000 synthetic values of P_s from the identified probability distribution and 10 000 pairs of parameters α and β from their two-dimensional frequency distribution were generated, so that for every one rainfall value there is one pair of (α, β) parameters. This way, there were 10 000 hyetographs with an hourly time step created by disaggregation of synthetic P_s, which were the input data for the rainfall-runoff model. In the process of modelling, there were three 10 000-element series of peak discharges for three kinds of ARC obtained, which were further mixed in proportions **1-2-0** and **2-3-0**, thus creating two 10 000-element combinations Q_{sci}. In consequence, for both combinations, probability distributions were estimated (Fig. 10). The values of synthetic flood
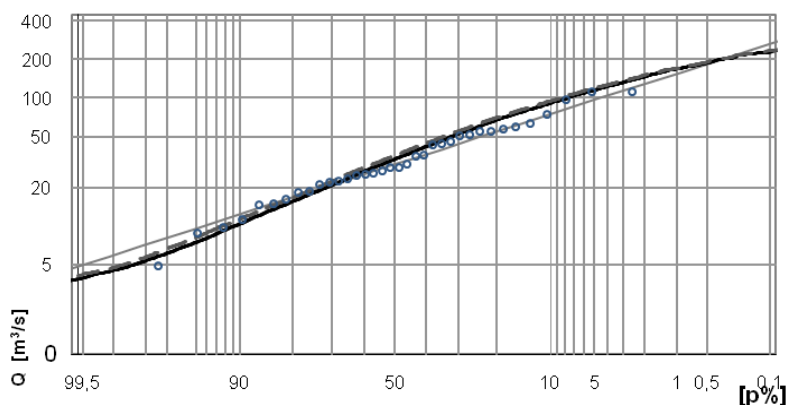
Fig. 10. Empirical (circles), theoretical (solid grey line), MESEF 1-2-0 (dotted line), and MESEF 2-3-0 (solid black line) flood quantiles for the Czarny catchment in the gauge station Polana.

quantiles for the asked probabilities p were compared to the quantiles from the observed data.

8. COMPARING FLOOD QUANTILES ESTIMATED USING THE MESEF AND THE CLASSICAL STATISTICAL METHOD

In order to verify the efficiency of the proposed method, it was necessary to compare the flood quantiles Q_p estimated using the MESEF and the classical statistical method (SM). SM is a direct method, common in Poland, used in controlled catchments and based on the observed values of maximum discharges Q_o. A comparison was carried out for two combinations: **1-2-0** and **2-3-0** (Table 5).

As it can be observed, in case of both combinations, the flood quantiles estimated using the MESEF method reveal slightly higher values than those estimated using the statistical method (for $p \geq 0.5\%$). Only for $p = 0.1\%$ the flood quantile estimated using the MESEF method is slightly lower than the quantile estimated using the statistical method (SM).

What is more, relative errors of flood quantiles for the **1-2-0** and **2-3-0** combinations were calculated in order to find out which of the established proportions of antecedent moisture conditions ARC would bear the greatest similarity to the observed discharges. It can be observed here that for the **2-3-0** proportion, the relative error – in almost all of the cases, except for the $p = 0.1\%$ – reveals lower values than for the **1-2-0** proportion. It can be inferred from this information that the peak discharge probability distribution was most similar to the discharges for the **2-3-0** proportion of antecedent runoff conditions ARC.

Table 5

Comparison of flood quantiles estimated using the statistical method (SM)
and the MESEF method for two combinations: 1-2-0 and 2-3-0

p [%]	Q_p (SM) [m³/s]	$Q_{p(1\text{-}2\text{-}0)}$ (MESEF) [m³/s]	$Q_{p(2\text{-}3\text{-}0)}$ (MESEF) [m³/s]	Difference Δ_1[a] (1-2-0) [m³/s]	Difference Δ_2[b] (2-3-0) [m³/s]	Relative error δ_1[c] (1-2-0) [%]	Relative error δ_2[d] (2-3-0) [%]
0.1	242.0	**236.7**	**236.0**	5.4	6.0	2.2	2.5
0.5	190.2	**196.7**	**191.8**	−6.4	−1.5	3.4	0.8
1	147.2	**173.7**	**170.4**	−26.5	−23.2	18.0	15.7
2	123.2	**153.1**	**148.8**	−29.9	−25.7	24.3	20.9
5	94.1	**120.5**	**117.0**	−26.4	−22.9	28.0	24.3
10	74.0	**95.4**	**92.2**	−21.4	−18.2	28.9	24.6
20	55.2	**70.7**	**67.9**	−15.5	−12.7	28.1	23.0
30	44.5	**55.2**	**52.7**	−10.7	−8.2	24.0	18.4
50	31.1	**35.4**	**33.3**	−4.4	−2.2	14.0	7.1

[a] $\Delta_1 = Q_p(\text{SM}) - Q_{p(1\text{-}2\text{-}0)}(\text{MESEF})$, [b] $\Delta_2 = Q_p(\text{SM}) - Q_{p(2\text{-}3\text{-}0)}(\text{MESEF})$,
[c] $\delta_1 = \Delta_1 / Q_p(\text{SM}) \times 100\%$, [d] $\delta_2 = \Delta_2 / Q_p(\text{SM}) \times 100\%$.

Table 6

Comparison of flood quantiles estimated using classical methods:
statistical (SM) and area regression equation (RE)

p [%]	$Q_p(\text{SM})$ [m³/s]	$Q_p(\text{RE})$ [m³/s]	Difference Δ_3[a] [m³/s]	Relative error δ_3[b] [%]
0.1	242.0	149.4	92.7	38.3
0.5	190.2	117.0	73.2	38.5
1	147.2	102.3	44.9	30.5
2	123.2	88.0	35.2	28.6
5	94.1	69.0	25.1	26.7
10	74.0	54.8	19.2	25.9
20	55.2	40.0	15.2	27.5
30	44.5	32.0	12.5	28.1
50	31.1	16.5	14.6	47.0

[a] $\Delta_3 = Q_p(\text{SM}) - Q_p(\text{RE})$, [b] $\delta_3 = \Delta_3 / Q_p(\text{SM}) \times 100\%$.

Additionally, another method was verified that is widespread in use in
Poland for estimating flood quantiles using the area regression equation
(RE). RE is a method used in uncontrolled catchments with an area from 50

to 2000 km^2 (RZGW 2014). The true values used, similarly to the assessment of the MESEF method, were quantiles based on observed data obtained from the SM method (Table 6).

The flood quantiles obtained using the regression equation (RE) reveal significantly lower values than the quantiles obtained using the statistical method (SM) for all cases. This is confirmed by the calculated values of the relative error. The highest significant relative error applies to flood quantiles with a $p = 50\%$ exceedance probability and it is 47%. The obtained results show limitations of the RE method; therefore, the proposed MESEF method could prove to be a good alternative.

9. CONCLUSION AND PERSPECTIVES

The article presents a new approach to estimating flood quantiles based on rainfall-runoff modelling using multiple rainfall events. This approach is a new idea in a practical application in Poland, including: applying rainfall generator, disaggregation of rainfall by generating parameters α and β of the beta distribution $Be(\alpha, \beta)$, as well as discharge modelling that considers different catchment antecedent runoff conditions ARC. The proposed MESEF method was applied in a natural catchment of the Czarny River, in a cross-section Polana. The values of flood quantiles obtained from the MESEF method are similar to the quantiles obtained using the statistical method (SM), and are burdened with smaller error than the quantiles estimated using the regression equation (RE). This means that they are of good similarity to the discharges from observed data.

It can be concluded that the new approach, which is based on generated precipitation and considers catchment antecedent runoff conditions ARC, marks a good direction to estimating flood quantiles in small catchments to 100 km^2. It is interesting whether the same proportion of ARC would be confirmed in other catchments. Further research in this area might produce valuable information.

Finding new methods for estimating flood quantiles is important, especially in the context of considering changes in both climate and catchment planning – the new factors influencing floods. What is more, the obtained flood quantiles are based on many rainfall events rather than a single one, as opposed to the currently used classical design event method. In result, flood distributions obtained by rainfall modelling make it possible to analyse the efficiency of technical and non-technical flood control methods in both gauged and ungauged catchments.

It should be noted here that the applicability of the MESEF method needs to be additionally tested in different catchments, and the authors would like to elaborate on the problem in their future publications as part of the on-going research.

References

Banasik, K. (2009), *Determining of Flood-swelling in Small Urban Catchments*, Warsaw University of Life Sciences Press, Warsaw, 42 pp. (in Polish).

Boughton, W., and O. Droop (2003), Continuous simulation for design flood estimation − a review, *Environ. Modell. Softw.* **18**, 4, 309-318, DOI: 10.1016/S1364-8152(03)00004-5.

Calver, A., and R. Lamb (1995), Flood frequency estimation using continuous rainfall-runoff modelling, *Phys. Chem. Earth* **20**, 5-6, 479-483, DOI: 10.1016/S0079-1946(96)00010-9.

Cameron, D.S., K.J. Beven, J. Tawn, S. Blazkova, and P. Naden (1999), Flood frequency estimation by continuous simulation for a gauged upland catchment (with uncertainty), *J. Hydrol.* **219**, 3-4, 169-187, DOI: 10.1016/S0022-1694(99)00057-8.

DVWK (1984), *Arbeitsanleitung zur Anwedung von Niederschlag-Abfluss Modellen in kleinen Einzugsgebieten, Teil II: Synthese*, Deutscher Verband für Wasserwirtschaft und Kulturbau, Vol. 113, Paul Parey Verlag, Hamburg (in German).

Francés, F., R. García-Bartual, E. Ortiz, S. Salazar, J. Miralles, G. Blöschl, J. Komma, C. Habereder, A. Bronstert, and T. Blume (2008), CRUE Research Report No. I-6: Efficiency of non-structural flood mitigation measures: "room for the river" and "retaining water in the landscape", CRUE Funding Initiative on Flood Risk Management Research, London, 172-213.

Hawkins, R.H., T.J. Ward, D.E. Woodward, and J.A. van Mullem (eds.) (2009), *Curve Number Hydrology: State of the Practice*, ASCE/EWRI Curve Number Hydrology Task Committee, American Society of Civil Engineers. Reston, DOI: 10.1061/9780784410042.

Kowalczak, P. (2011), Climate variability and the causes of the floods in Poland, Institute for Agricultural and Forest Environment, Polish Academy of Sciences, Poznań, Poland, http://www.umweltaktion.de/pics/medien/1_1324305988/Vortrag_Kowalczak.pdf (in Polish).

KPZK 2030 (2012), National Spatial Development Concept 2030, Monitor Polski, Warszawa, 27.04.2012, Poz. 252 (in Polish).

Lee, K.T., and J.K. Huang (2013), Runoff simulation considering time-varying partial contributing area based on current precipitation index, *J. Hydrol.* **486**, 443-454, DOI: 10.1016/j.jhydrol.2013.02.016.

Licznar, P. (2009), *Generators of Synthetic Rain Rows for Modelling of the Storm-water Drainage and Combined Sewage Systems*, Wrocław University of Environmental and Life Sciences Publ., Wrocław, 180 pp. (in Polish).

Mishra, S.K., and V.P. Singh (2003), *Soil Conservation Service Curve Number (SCS-CN) Methodology*, Water Science and Technology Library, Vol. 42, Kluwer Academic Publishers, Dordrecht, 519 pp.

Nowicka, B., U. Soczyńska, and U. Somorowska (1997), Prediction of the design floods frequency. **In:** U. Soczyńska (ed.), *Prediction of the Design Storms and Floods*, University of Warsaw Publisher, Warsaw, 143-177 (in Polish).

Osuch, M., R.J. Romanowicz, E. Paquet, and F. Garavaglia (2013), Application of the SCHADEX method to estimate annual maximum flow of given exceedance probability of the Nysa Kłodzka river. **In:** S. Węglarczyk (ed.), *The Problems of Calculating Extreme Discharge in Controlled and Uncontrolled Catchments*, Monographs of Committee of Environmental Engineering PAS, Vol. 35, 73-86 (in Polish).

Paquet, E., F. Garavaglia, R. Garçon, and J. Gailhard (2013), The SCHADEX method: A semi-continuous rainfall-runoff simulation for extreme flood estimation, *J. Hydrol.* **495**, 23-37, DOI: 10.1016/j.jhydrol.2013.04.045.

Pathiraja, S., S. Westra, and A. Sharma (2012), Why continuous simulation? The role of antecedent moisture in design flood estimation, *Water Resour. Res.* **48**, 6, W0653, DOI: 10.1029/2011WR010997.

Pilgrim, D.H., and I. Cordery (1993), Flood runoff. **In:** D.R. Maidment (ed.), *Handbook of Hydrology*, McGraw-Hill Inc., New York, 9.1-9.42.

Rahman, A., P.E. Weinmann, T.M.T. Hoang, and E.M. Laurenson (2002), Monte Carlo simulation of flood frequency curves from rainfall, *J. Hydrol.* **256**, 3-4, 196-210, DOI: 10.1016/S0022-1694(01)00533-9.

RZGW (2014), Regulation no. 4/2014 of Director of Regional Water Management Board in Kraków (the RZGW in Kraków) of 16 January 2014 on conditions to use water of Górna Wisła water region, Regionalny Zarząd Gospodarki Wodnej, Kraków, Poland, http://bip.malopolska.pl/rzgwkrakow/Article/get/id,848610.html (in Polish).

Scharffenberg, W., and M. Fleming (2010), Hydrologic modeling system HEC-HMS v.3.5 user's manual, U.S. Army Corps of Engineers, Davis, USA.

SPA 2020 (2013), Polish National Strategy for Adaptation to Climate Change (SPA 2020), Ministry of Environment, Warszawa, Poland, http://klimada.mos.gov.pl/wp-content/uploads/2013/10/SPA2020.pdf (in Polish).

Stedinger, J.R., R.M. Vogel, and E. Foufoula-Georgiou (1993), Frequency analysis of extreme events. **In:** D.R. Maidment (ed.), *Handbook of Hydrology*, McGraw-Hill Inc., New York, 18.1-18.66.

USDA (1986), Urban hydrology for small watersheds, Technical Release No. 55, United States Department of Agriculture, U.S. Government Printing Office, Washington DC.

Węglarczyk, S. (2010), *Statistics in Environmental Engineering*, Cracow University of Technology Publisher, Cracow (in Polish).

Więzik, B. (2010), Annual maximum discharges of given exceedance probability in small ungauged catchments. **In:** B. Więzik (ed.), *Hydrology in Engineering and the Water Management*, Monographs of Committee of Environmental Engineering PAS, Vol. 68, 153-165 (in Polish).

Effect of the North Atlantic Oscillation on the Pattern of Lake Ice Phenology in Poland

Dariusz WRZESIŃSKI[1], Adam CHOIŃSKI[1], Mariusz PTAK[1], and Rajmund SKOWRON[2]

[1]Institute of Physical Geography and Environmental Planning, Adam Mickiewicz University, Poznań, Poland; e-mails: darwrze@amu.edu.pl, choinski@amu.edu.pl, marp114@wp.pl (corresponding author)

[2]Department of Hydrology and Water Management, Nicolaus Copernicus University, Toruń, Poland; e-mail: rskowron@umk.pl

A b s t r a c t

This paper presents an analysis of the influence of the North Atlantic Oscillation on the pattern of lake ice phenology in Poland. The research embraced 22 lakes in Poland over the period 1961-2010. Strong relations were found to hold between NAO and individual characteristics of ice phenology. In a negative NAO phase, one can observe a later appearance of ice phenomena and ice cover compared with the average values, ice cover persisting even 30 days longer and being thicker even by more than 10 cm. In turn, in a positive NAO phase the duration of ice phenomena and ice cover is shorter, the cover being less thick and solid. The observed spatial differences in the effect of NAO on the pattern of ice phenomena in Poland show this matter to be fairly complex. The most significant factor changes in climatic conditions, which manifest themselves in the continentality of the climate growing eastwards.

Key words: climate change, ice cover, teleconnections.

1. INTRODUCTION

Of key significance for the operation of lakes in the middle and high geographical latitudes is thermal seasonality connected with ice phenology. The process of ice formation itself is well known and follows from an exchange of heat between a water mass and the surroundings. Its rate and scale are determined by many factors, among which Majewski (2007) lists air temperature, water temperature, water depth, *etc.* As a result of the appearance of ice, considerable changes take place in the operation of lake ecosystems that follow from the isolation of water from external factors (no waving, reduced light, *etc.*). Those issues are discussed in many works, a survey of which has been made by Gerten and Adrian (2000). An effect of the observed changes in climatic conditions is a shift in thermal seasons of the year (Thomson 2009) leading, among other things, to disturbances in the ice regime of lakes. Long-term observations show that the ice season tends to shorten and the thickness of ice cover to diminish (Futter 2003, Korhonen 2006, Jensen *et al.* 2007, Leppäranta 2014). The interpretation of the observed trends should accommodate the cyclicity of macro-scale factors embracing atmospheric and oceanic circulation (Brown and Duguay 2010). What exerts a strong influence on the climatic conditions in Europe is the North Atlantic Oscillation (NAO). Its effect is visible in the pattern of climatic and hydrological characteristics, and has been documented in several works on precipitation (Bednorz 2011, Castro *et al.* 2011), air temperature (Scaife *et al.* 2008, Heape *et al.* 2013), and river runoff (Pociask-Karteczka 2006, Wrzesiński and Paluszkiewicz 2011). The effect of the NAO has also been proved with reference to lake ice phenology (Maher *et al.* 2005, George 2007, Weyhenmeyer 2009, Soja *et al.* 2014, Sharov *et al.* 2014).

This paper seeks to establish spatial differences in the parameters of lake ice phenology in Poland in average conditions and under the influence of the variable intensity of atmospheric circulation in the North Atlantic sector. The research conducted was designed to show that the level of intensity of the North Atlantic Oscillation caused significant differences in the ice phenology of lakes in Poland. The study was carried out on the lakes of northern Poland, *i.e.*, a lakeland area embraced by the last Scandinavian glaciation. No detailed analysis of this issue has so far been made for such a large set of lakes in this part of Europe and for a 50-year-long observation period. Earlier studies of the effect of the North Atlantic Oscillation on the parameters of lake ice phenology in Poland only focused on small groups of lakes (Girjatowicz 2003, Wrzesiński *et al.* 2013), four and three, respectively. The results obtained in those works reveal a strong link between this circulation and lake ice phenology, and encourage making such an analysis for a larger set of lakes.

2. MATERIAL AND METHODS

Observations of ice phenomena on lakes in Poland started as early as the 19th century. They mostly focused on the thickness of ice cover, more rarely on the start and end of its occurrence. Such measurements were performed for the purposes of fishing trade, but this material was scattered and non-systematic, hence of little scientific worth (Skowron 2011). Constant observations of ice phenomena are conducted by the Institute of Meteorology and Water Management (IMGW). Records are made of the dates of appearance of ice phenomena (the presence of ice in water in any form: shore ice, frazil ice), the appearance of ice cover, its breakup, the disappearance of ice phenomena, and the thickness of ice cover. At present, observations of the characteristics of ice phenology are conducted on 22 out of the country's 7000 lakes (of 1 ha and more in area) (Fig. 1), the morphometric parameters of which are presented in Table 1. This paper offers an analysis of the pattern of ice phenomena on those lakes in the period 1961-2010.

An analysis was made of ten parameters of lake ice phenology: the start and the end of ice phenomena (the first and the last day when any form of ice in water, identified with shore ice, was recorded) the start and the end of ice cover (the first and the last day when the lake surface in the observer's arc of visibility was completely covered with ice), the duration of ice phenomena and ice cover (the dates when shore ice and ice cover were observed for the first and the last time), ice cover thickness measured every five days, and the date of its maximum thickness (in the case of five lakes, no informa-
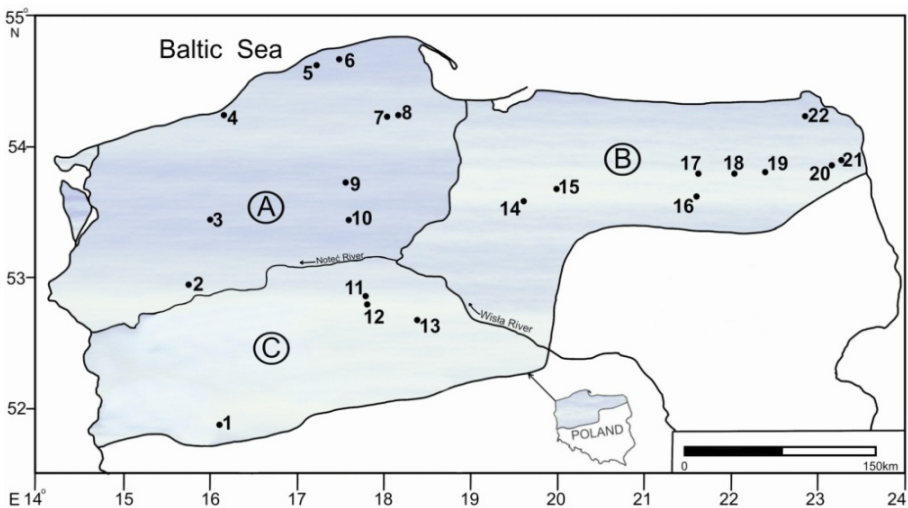
Fig. 1. Location of the studied lakes (numbering in accordance with Table 1), marked area is that of Last Glaciation; A – Pomeranian Lakeland, B – Mazurian Lakeland, C – Wielkopolska–Kujavia Lakeland.

Table 1

Morphometric data of the studied lakes

No.	Lake	Area [ha]	Volume [thous.m^3]	Depth average [m]	Altitude [m a.s.l.]
1	Sławskie	822.5	42664.8	5.2	56.9
2	Osiek	514.0	50065.0	9.3	51.4
3	Lubie	1487.5	169880.5	11.6	95.4
4	Jamno	2231.5	31528	1.4	0.1
5	Gardno	2337.5	30950.5	1.3	0.3
6	Łebsko	7080.0	117521	1.6	0.2
7	Raduńskie Górne	362.5	60158.7	15.5	161.6
8	Ostrzyckie	296.0	20785.2	6.7	160.1
9	Charzykowskie	1336.0	134533.2	9.8	120
10	Sępoleńskie	157.5	7501.6	4.8	112.8
11	Żninskie Duże	420.5	29492.6	6.8	77.7
12	Biskupińskie	107.0	6397.2	5.5	78.6
13	Gopło	2121.5	78497.0	3.6	77.0
14	Jeziorak	3152.5	141594.2	4.1	99.2
15	Drwęckie	780.0	50140.1	5.7	94.8
16	Nidzkie	1750.0	113872.3	6.2	117.9
17	Mikołajskie	424.0	55739.7	11.2	115.7
18	Orzysz	1012.5	75326.2	6.6	120.0
19	Ełckie	385.0	57420.3	15.0	119.9
20	Studzieniczne	244.0	22073.6	8.7	123.4
21	Serwy	438.5	67181.5	14.1	126.8
22	Hańcza	291.5	120364.1	38.7	227.3

tion was obtained about appearance of maximum ice thickness). On the basis of those observations it was possible to determine ice cover durability, understood as the proportion of the number of days with ice cover to the number of days between the first and the last day with ice cover [%], and its duration, which means the proportion of the number of days with ice cover in the entire period of ice phenomena, *i.e.*, from the first to the last day when those phenomena could be observed (*e.g.*, shore ice, ice floe, *etc.*) [%].

In order to determine the dependence of changes in the ice phenology parameters on the intensity of the North Atlantic Oscillation, Pearson's coefficient of linear correlation was calculated (*r*), the correlation holding between the ice phenology parameters under study and Hurrell's winter NAO$_{DJFM}$ index. In the case of the start of ice phenomena and the formation of ice cover, also calculated were coefficients of correlation with seasonal NAO indices from the periods September-November (NAO$_{SON}$), October-December (NAO$_{OND}$), and November-January (NAO$_{NDJ}$).

Changes in the parameters of ice phenomena on the examined lakes in a positive and a negative NAO_{DJFM} phase were determined on the basis of how those parameters differed from the average values from the years 1961-2010. The average values of those parameters were calculated for years with high ($NAO_{DJFM} > 1.63$) and low ($NAO_{DJFM} < -1.09$) values of the winter NAO_{DJFM} index. Those figures correspond to the first and third quartiles from the entire set of NAO_{DJFM} indices in the years 1961-2010. The statistical significance of those differences was examined using the *T*-test for stratified samples. Each time the hypothesis tested was $H_0: \mu = \mu_0$ of the equality of the expected values against $H_1: \mu \neq \mu_0$. The rejection of the hypothesis allowed a conclusion about there being significant differences between the mean parameters of ice phenomena observed in the different NAO_{DJFM} phases and the average values. To verify the hypothesis, use was made of a test for a small sample based on Student's *t*-distribution, with $n - 1$ degrees of freedom:

$$ t = \left| \frac{\bar{x} - \mu_0}{\sigma} \sqrt{n} \right| , \tag{1} $$

where n is the sample size, σ the standard deviation, x the mean of the sample, and μ_0 the mean of the population.

In this paper use was made of the winter NAO index (NAO_{DJFM}) and seasonal NAO indices worked out by Hurrell (1995).

To present spatial differences in changes in the parameters of lake ice phenology, the Surfer 10 Program (GoldenSoftware) was employed, and isolines were drawn using the kriging procedure.

3.   RESULTS AND DISCUSSION

3.1 Average parameters of lake ice phenology in Poland in the years 1961-2010

On the lakes under study, ice phenomena begin in mid-December. The earliest ones start in the first half on the lakes in the Wielkopolska–Kujavia Lakeland, the western part of the Mazurian Lakeland, and the coastal lakes Łebsko and Gardno (Fig. 2a). On most lakes of the Pomeranian and Mazurian Lakelands, ice phenomena begin in the last decade of December, and in the case of Lake Lubie, in the first decade of January.

The spatial distribution of the dates of ice cover formation is similar, but about 10 days later (Fig. 2b). On the lakes of the central part of the lakeland zone and on the coast, ice cover appears on average in the last decade of December, and on most lakes of the Pomeranian and Mazurian Lakelands, in the first decade of January, appearing the latest on Lake Lubie (11 January).
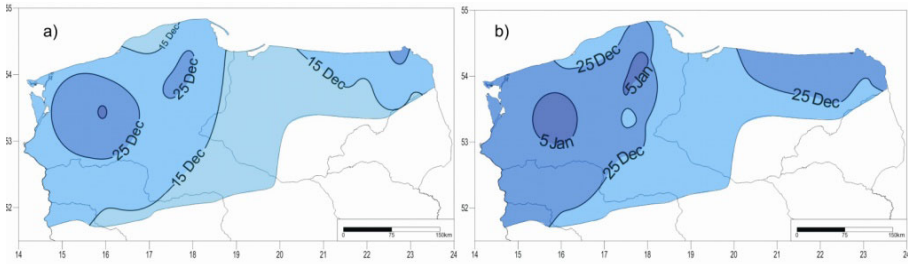
Fig. 2. Spatial differences in the dates of the start of: (a) ice phenomena, and (b) ice cover.
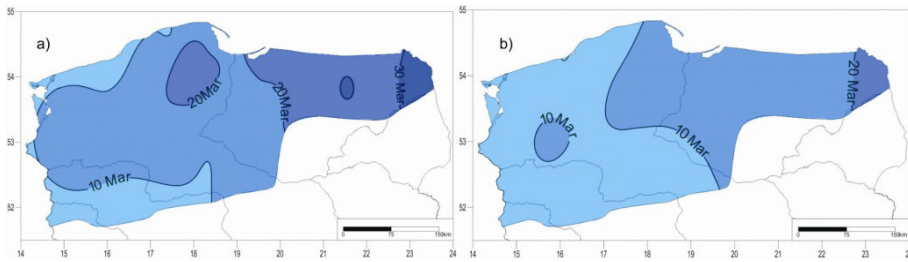
Fig. 3. Spatial differences in the dates of the end of: (a) ice phenomena, and (b) ice cover.

What is highly characteristic is the spatial distribution of the date of the end of ice phenomena and ice cover. Those ice phenomenology parameters are the earliest on lakes in the western part of the study area: in the case of ice cover, in late February and early March (Fig. 3b), and in case of ice phenomena, in the first decade of March (Fig. 3a). Those dates are ever later in the easterly direction. In the eastern part of the Mazurian Lakeland, ice cover usually disappears in the third decade of March, and ice phenomena in the first decade of April.

The spatial distributions of the duration of ice phenomena and ice cover are similar. Ice phenomena last the shortest (under 70 days) on lakes in the western part of the area and near the sea, and the longest (over 100 days) in the east; cf. Fig. 4a. As to the ice cover, it persists for less than 60 days on the lakes in the west, and over 80 days in the east; cf. Fig. 4b.

Also the mean maximum thickness of ice cover on lakes grows eastwards, from about 20 cm in the western part of the area to over 30 cm in the east; cf. Fig. 5a. Spatial differences are wider in the case of the date when it attains its maximum thickness. This occurs the earliest on the lakes of the Wielkopolska–Kujavia Lakeland and on coastal lakes (late January and early February); cf. Fig. 5b. For most lakes this date falls in mid-February, and for those in the eastern part of the area, in the third decade of February.
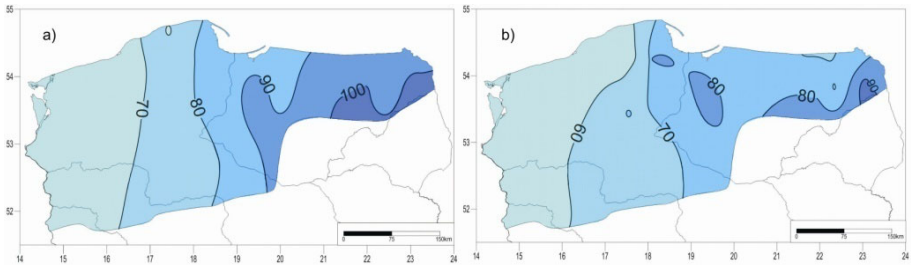
Fig. 4. Spatial differences in the duration of: (a) ice phenomena, and (b) ice cover.
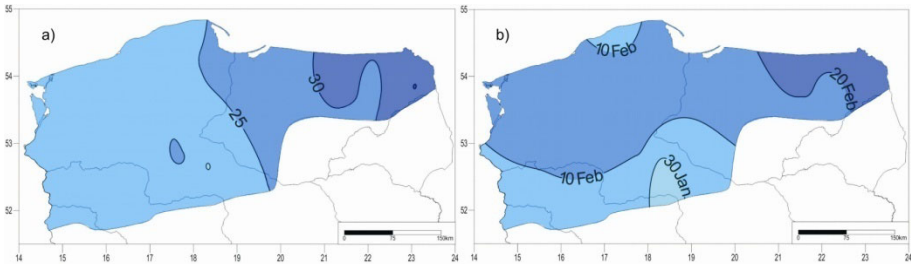
Fig. 5. Spatial differences in: (a) the thickness of ice cover, and (b) the date of occurrence of the maximum thickness of ice cover.
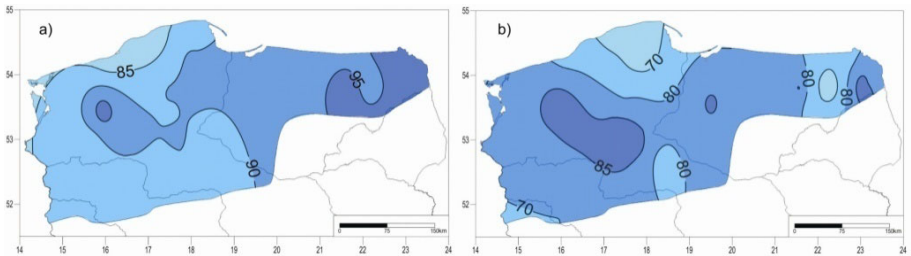
Fig. 6. Spatial differences in: (a) the degree of durability of ice cover, and (b) duration of ice cover divided by total period of phenomena.

The durability of ice cover is the shortest in the case of coastal lakes (about 80%) and grows markedly eastwards to over 90%; *cf.* Fig. 6a. There is no such regularity in the spatial variability of the share of ice cover in ice phenomena. In the case of the coastal lakes, it is under 80%, and over 85% for the lakes in the central part of the Pomeranian Lakeland and the western part of the Mazurian Lakeland (Fig. 6b).

3.2 Relations between lake ice phenology and the NAO

The results obtained show that the intensity of the North Atlantic Oscillation in the winter season strongly affects the pattern of ice phenomena on Polish

lakes. This is corroborated by both, the correlation of the NAO_{DJFM} index with the parameters of ice phenomena (Table 2), and the calculated differences between those parameters in the different NAO_{DJFM} phases and the average values (Figs. 7-14).

In a positive NAO_{DJFM} phase, the dates of the end of ice phenomena and ice cover on the lakes under study are usually about 15 days later than the average, and the calculated differences in the dates are statistically significant ($p < 0.05$); cf. Figs. 7 and 8. The date of the end of those phases of ice phenology is even over 20 days later on lakes in the direct neighbourhood of the Baltic (coastal lakes). In a negative NAO_{DJFM} phase, the ending dates come earlier than average, and statistically significant differences ($p < 0.05$) range from under 15 days in the west and east of the lakeland belt to over 20 days in the case of the coastal lakes.

The deviations of the ending dates of ice phenomena and ice cover in the different NAO_{DJFM} phases from the average values cause also their duration
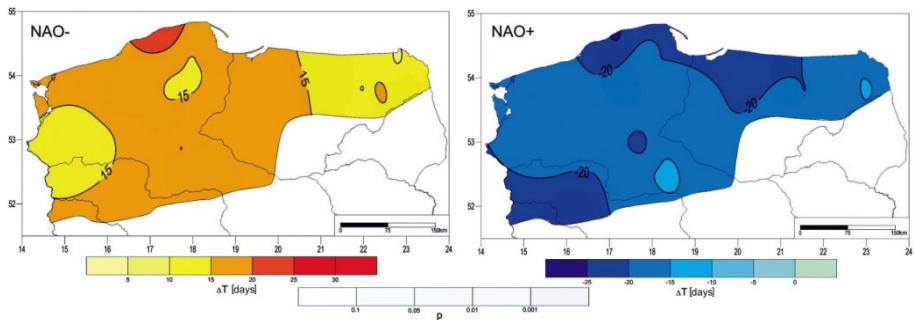
Fig. 7. Differences between the dates of the end of ice phenomena in a negative (NAO-) and a positive (NAO+) NAO phase, and the average values from the years 1961-2010; results of the test of the significance of the differences.
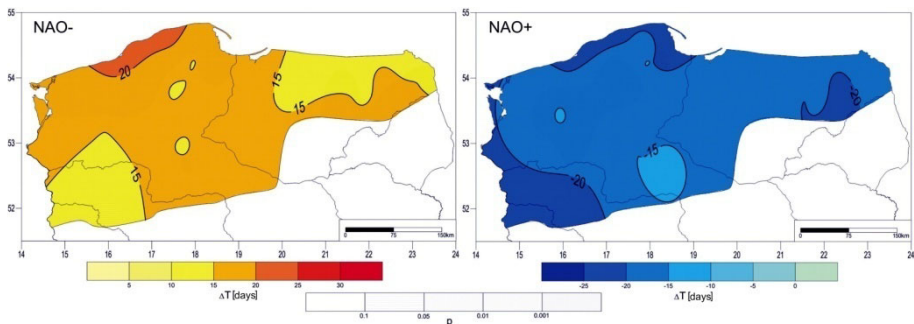
Fig. 8. Differences between the dates of the end of ice cover in a negative (NAO-) and a positive (NAO+) NAO phase, and the average values from the years 1961-2010; results of the test of the significance of the differences.

Table 2

Coefficients of correlation between the parameters of ice phenomena and NAO$_{DJFM}$

Lake	Beginning of		End of		Duration		Maximum thickness of ice cover	Date max. thickness of ice cover	Degree of durability of ice cover	Duration of ice cover divided by total period of ice phenomena
	ice phenomena	ice cover	ice phenomena	ice cover	ice phenomena	ice cover				
Sławskie	0.141	0.138	**-0.610**	**-0.555**	**-0.701**	**-0.679**	**-0.476**	-0.220	-0.260	-0.243
Osiek	0.218	0.244	**-0.603**	**-0.665**	**-0.694**	**-0.697**	**-0.623**	*-0.386*	-0.246	**-0.462**
Lubie	0.594	0.346	**-0.557**	**-0.550**	**-0.711**	**-0.631**	**-0.534**	*-0.370*	-0.103	0.118
Jamno	0.077	0.134	**-0.650**	**-0.608**	**-0.782**	**-0.719**	**-0.556**	no data	-0.238	*-0.329*
Gardno	0.139	0.202	**-0.719**	**-0.638**	**-0.743**	**-0.736**	**-0.646**	**-0.551**	*-0.330*	**-0.501**
Łebsko	0.205	0.114	**-0.630**	**-0.645**	**-0.758**	**-0.748**	**-0.677**	**-0.498**	-0.236	*-0.434*
Raduńskie Górne	0.199	0.387	**-0.626**	**-0.572**	**-0.727**	**-0.712**	**-0.681**	no data	-0.236	**-0.531**
Ostrzyckie	-0.064	-0.073	**-0.609**	**-0.663**	**-0.647**	**-0.656**	**-0.669**	**-0.500**	**-0.494**	*-0.303*
Charzykowskie	0.124	0.326	**-0.599**	**-0.566**	**-0.658**	**-0.708**	**-0.657**	**-0.513**	*-0.330*	**-0.489**
Sępoleńskie	0.023	-0.033	**-0.711**	**-0.647**	**-0.737**	**-0.711**	**-0.650**	no data	*-0.390*	*-0.363*
Żnińskie Duże	0.182	0.264	**-0.592**	**-0.582**	**-0.736**	**-0.757**	**-0.559**	*-0.302*	*-0.454*	-0.054
Biskupińskie	0.103	0.021	**-0.658**	**-0.643**	**-0.728**	**-0.716**	**-0.649**	*-0.420*	**-0.505**	*-0.323*
Gopło	0.116	0.263	**-0.592**	**-0.513**	**-0.706**	**-0.633**	**-0.656**	*-0.373*	-0.283	-0.232
Jeziorak	-0.091	-0.014	**-0.648**	**-0.625**	**-0.654**	**-0.665**	**-0.678**	**-0.474**	*-0.459*	*-0.417*
Drwęckie	0.039	0.124	**-0.672**	**-0.615**	**-0.664**	**-0.638**	**-0.676**	no data	*-0.314*	**-0.483**
Nidzkie	0.258	0.138	**-0.672**	**-0.676**	**-0.485**	**-0.651**	**-0.614**	*-0.424*	-0.152	**-0.620**
Mikołajskie	0.138	0.223	**-0.710**	**-0.606**	**-0.632**	**-0.667**	**-0.724**	**-0.521**	**-0.516**	*-0.323*
Orzysz	-0.010	0.216	**-0.581**	**-0.616**	**-0.585**	**-0.695**	**-0.657**	*-0.330*	-0.205	**-0.556**
Ełckie	0.145	0.171	**-0.639**	**-0.635**	**-0.618**	**-0.712**	**-0.651**	*-0.327*	*-0.318*	**-0.486**
Studzieniczne	0.068	0.070	**-0.628**	**-0.675**	**-0.555**	**-0.580**	**-0.700**	**-0.605**	-0.132	*-0.358*
Serwy	0.002	-0.025	**-0.643**	**-0.630**	**-0.536**	**-0.530**	**-0.687**	no data	*-0.299*	*-0.323*
Hańcza	0.164	0.086	**-0.521**	**-0.539**	**-0.539**	**-0.570**	**-0.613**	*-0.309*	-0.217	*-0.344*

Note: Significance of correlation coefficients at the levels: *p < 0.05*, *p < 0.01*, **p < 0.001**.

in those phases to differ markedly, and statistically significantly ($p < 0.05$), from the means. In a positive NAO$_{DJFM}$ phase, the duration of those characteristics is clearly shorter than the average, by more than 30 days in the case of the coastal lakes and those located in the western part of the country, dropping to under 20 days in the east. In a negative NAO$_{DJFM}$ phase, the duration of ice phenomena, as well as of ice cover, is markedly longer than the average, from under 20 to over 30 days. The observed differences are statistically significant ($p < 0.05$), but more diversified spatially, although still greater in the case of the lakes in the west (especially the coastal ones) and smaller in the east − under 20 days; *cf.* Figs. 9 and 10.

Changes in the intensity of the North Atlantic Oscillation also affect the maximum thickness of ice cover and the date of its appearance. In a positive NAO$_{DJFM}$ phase, the thickness is smaller, from under 10 cm on the lakes in the west of the country to over 10 cm in the eastern part of the lakeland zone; *cf.* Fig. 11. In a negative NAO$_{DJFM}$ phase, the maximum thickness fig-
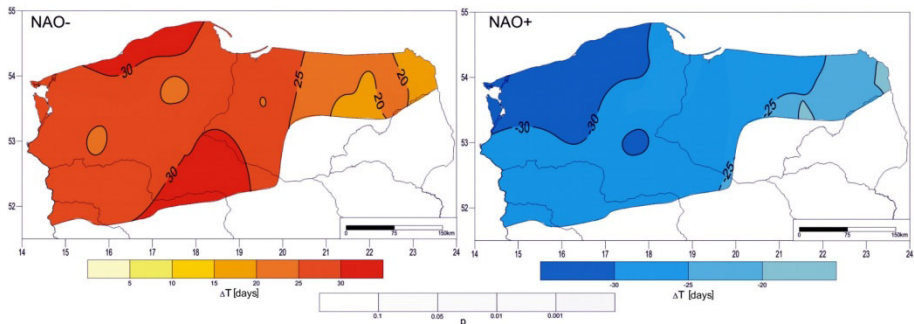
Fig. 9. Differences between the duration of ice phenomena in a negative (NAO–) and a positive (NAO+) NAO phase, and the average values from the years 1961-2010; results of the test of the significance of the differences.
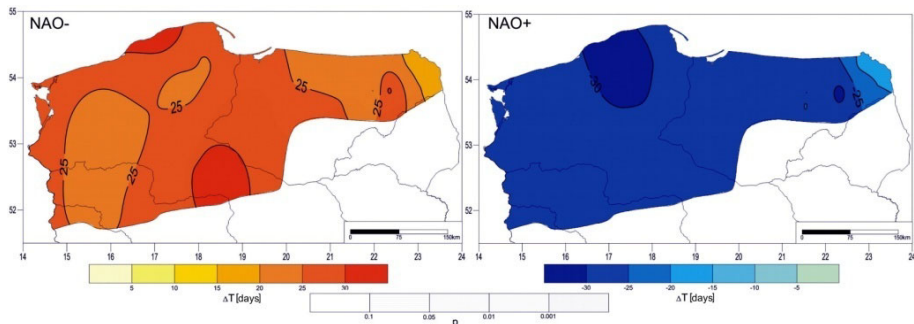
Fig. 10. Differences between the duration of ice cover in a negative (NAO-) and a positive (NAO+) NAO phase, and the average values from the years 1961-2010; results of the test of the significance of the differences.
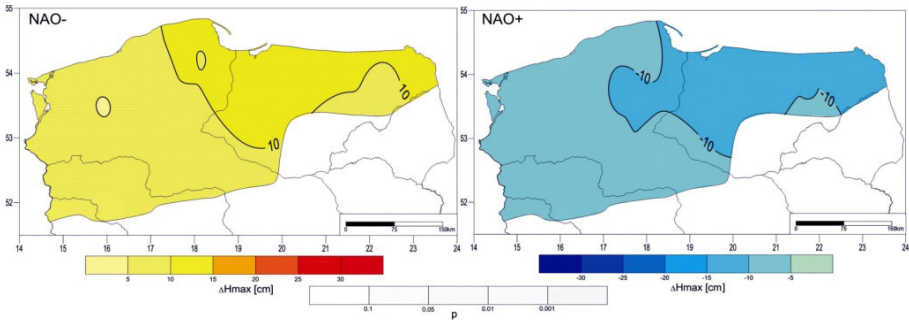
Fig. 11. Differences between the maximum thickness of ice cover in a negative (NAO-) and a positive (NAO+) NAO phase, and the average values from the years 1961-2010; results of the test of the significance of the differences.
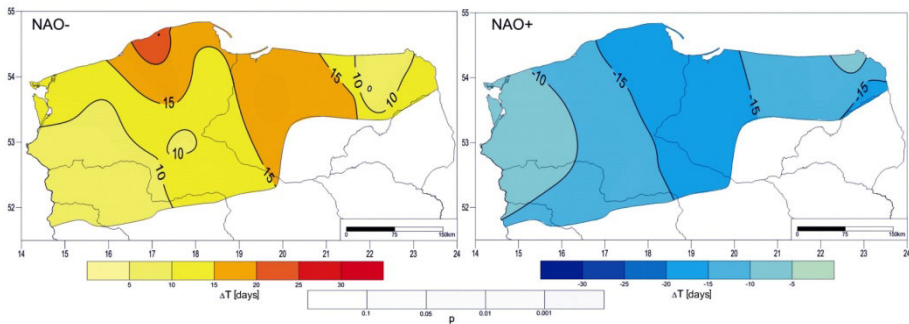
Fig. 12. Differences between the dates of occurrence of the maximum thickness of ice cover in a negative (NAO–) and a positive (NAO+) NAO phase, and the average values from the years 1961-2010; results of the test of the significance of the differences.

ures are greater, in the western part of the lakeland by about 5 cm, although the observed differences from the average values are not statistically signifcant ($p > 0.01$). By contrast, the maximum thickness of ice cover on the lakes in the eastern part of the study area differs then in a statistically significant way ($p < 0.05$), by more than 10 cm; *cf*. Fig. 11.

Also the date of the appearance of the maximum thickness of ice cover changes significantly depending on the NAO_{DJFM} phase. In a positive phase it comes from under 10 to over 15 days earlier than the average, and in a negative phase, later; *cf*. Fig. 12. The smallest deviations from average values, statistically not significant, can be observed on the lakes in the western and eastern parts of the lakeland belt, while the greatest, statistically significant ($p < 0.05$), differences occur on those in the central belt embracing the coastal lakes in the north and those of the Kujavia Lakeland in the south. In a negative NAO_{DJFM} phase, the date of the maximum thickness of ice cover on

the coastal lakes is later than the average even by more than 20 days, and the observed differences are statistically significant ($p < 0.01$).

The durability of ice cover in a positive NAO_{DJFM} phase is from less than 5% to over 10% smaller than the average, and the observed differences are usually not statistically significant; *cf.* Fig. 13. In a negative NAO_{DJFM} phase the durability is greater. On the lakes in Poland's western part, however, this increase is not statistically significant, while in the central and eastern parts it is significant at $p < 0.001$.

Also smaller in a positive NAO_{DJFM} phase is the share of the duration of ice cover in the entire period of occurrence of ice phenomena; *cf.* Fig. 14. The drop in this proportion observed then against average values varies from under 5 to over 15%, only the greatest differences being statistically significant ($p < 0.05$). In turn, in a negative NAO_{DJFM} phase this proportion grows and is 5-10% higher than the average.
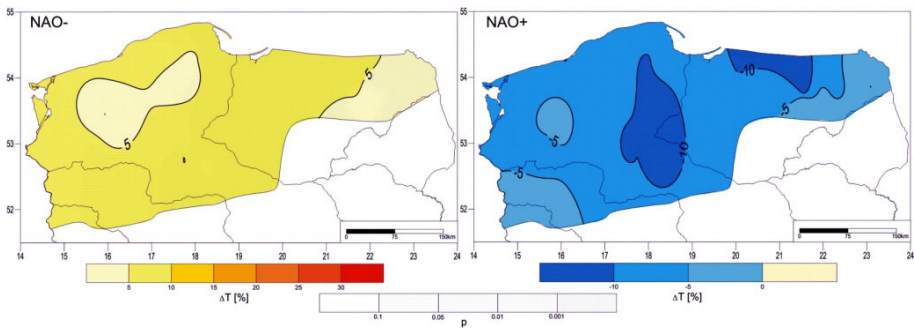
Fig. 13. Differences between the level of degree of durability of ice cover in a negative (NAO–) and a positive (NAO+) NAO phase, and the average values from the years 1961-2010; results of the test of the significance of the differences.
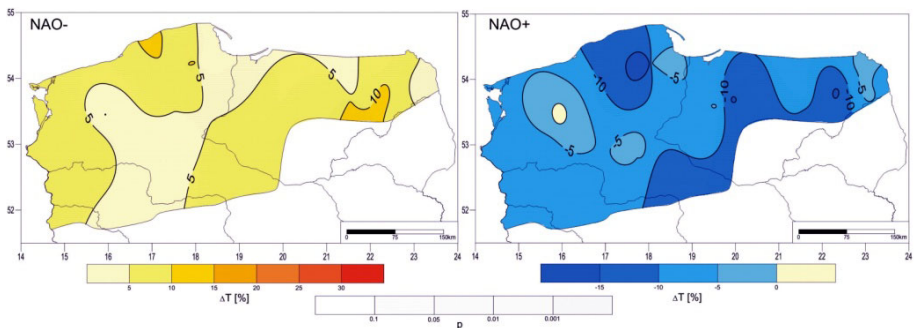
Fig. 14. Differences between the proportion of ice cover duration in the duration of ice phenomena in a negative (NAO–) and a positive (NAO+) NAO phase, and the average values from the years 1961-2010; results of the test of the significance of the differences.

Table 3

Coefficients of the correlation between the starting dates
of ice phenomena and ice cover and the seasonal NAO indices

Index NAO	NAO_{SON}		NAO_{OND}		NAO_{NDJ}		NAO_{DJF}	
	Beginning of		Beginning of		Beginning of		Beginning of	
Lake	ice phenomena	ice cover	ice phenomena	ice cover	ice phenomena	ice cover	ice phenomena	ice cover
Sławskie	*0.284*	*0.344*	*0.322*	***0.408***	0.355	***0.397***	0.132	0.145
Osiek	*0.335*	0.238	**0.452**	***0.369***	***0.447***	**0.481**	0.225	0.171
Lubie	0.106	0.085	***0.418***	0.342	**0.684**	**0.547**	**0.546**	*0.291*
Jamno	0.231	0.257	*0.313*	0.298	0.319	***0.367***	0.105	0.231
Gardno	0.256	0.167	0.275	*0.291*	0.334	***0.421***	0.109	0.205
Łebsko	0.264	0.179	*0.356*	0.239	***0.374***	*0.316*	0.176	0.133
Raduńskie Górne	0.181	0.176	0.231	0.270	***0.371***	**0.458**	0.176	*0.303*
Ostrzyckie	*0.290*	*0.316*	0.258	*0.294*	0.225	0.252	−0.008	0.022
Charzykowskie	*0.323*	*0.305*	***0.409***	**0.436**	***0.424***	**0.545**	0.122	0.247
Sępoleńskie	*0.279*	*0.279*	***0.376***	*0.343*	0.308	0.242	0.023	−0.024
Żnińskie Duże	0.152	0.214	0.235	*0.346*	0.229	***0.420***	0.152	0.215
Biskupińskie	0.253	*0.285*	***0.373***	*0.349*	0.353	0.295	0.112	0.073
Gopło	*0.290*	0.269	***0.385***	*0.356*	***0.370***	***0.409***	0.056	0.158
Jeziorak	0.160	*0.291*	0.166	***0.368***	0.074	0.247	−0.053	0.035
Drwęckie	0.016	0.242	0.120	0.262	0.154	0.275	0.066	0.046
Nidzkie	0.246	0.242	***0.377***	*0.349*	***0.429***	*0.358*	0.230	0.145
Mikołajskie	0.215	0.264	*0.294*	*0.345*	0.355	***0.373***	0.129	0.173
Orzysz	*0.318*	*0.346*	0.277	***0.430***	0.197	**0.478**	−0.012	0.241
Ełckie	*0.330*	*0.326*	*0.344*	***0.375***	*0.292*	*0.349*	0.112	0.128
Studzieniczne	*0.282*	*0.337*	0.270	*0.348*	0.255	*0.318*	0.106	0.111
Serwy	*0.304*	*0.355*	0.261	*0.304*	0.182	0.260	−0.007	−0.032
Hańcza	*0.291*	0.216	***0.362***	*0.283*	0.326	0.271	0.122	0.055

Note: Significance of correlation coefficients at the levels: $p < 0.05$, $p < \boldsymbol{0.01}$, $p < \textbf{0.001}$.

Out of the parameters under study, only the starting dates of ice phenomena and ice cover do not show any relation with the intensity of the North Atlantic Oscillation as expressed by the NAO_{DJFM} index. Those dates usually fall in December; hence, the lack of a relation with the index determined for a later period is understandable. However, an analysis showed there to be a connection between the starting dates of ice phenomena and ice cover and NAO indices calculated for earlier seasons, especially NAO_{OND} and NAO_{NDJ}.

It is statistically significant ($p < 0.05$) for all the lakes with the exception of Drwęckie (Table 3). Twelve of the examined lakes also show statistically significant relations between the dates of appearance of ice phenomena and ice cover and the NAO_{SON} index for the September-November period ($p = 0.05$).

In the study period, the lowest value of the NAO_{DJFM} index was recorded in 1969 (–4.89), and the highest in 1989 (5.08). In those years extremely different parameters of ice phenomena were observed on the lakes. In 1969 the average duration of ice cover was 113 days (the longest one, 136 days, persisting on Lake Sępoleńskie), as against a mere 16 days in 1989, while on Żnińskie Duże, Sławskie, and Gopło it was not recorded at all that year. The mean thickness of maximum ice cover in 1969 was 43.4 cm as against a mere 10.2 cm in 1989. It should be emphasized that in the entire multi-year period under analysis the year 1969 was the one when the maximum thickness of ice was recorded; in two cases (Lakes Studziennicze and Mikołajskie) it reached 65 cm.

4.   DISCUSSION

The duration of ice phenology in midland water bodies basically grows with the geographical latitude (Livingstone *et al.* 2009). However, this dependence can be modified by macro-scale circulation (which variously affects climatic conditions in different parts of the world, depending on its type), and by individual characteristics of lakes (Choiński and Ptak 2012), their surroundings (Choiński *et al.* 2013), and the local circulation (Blenckner *et al.* 2004).

Ice phenology is directly connected with the thermal balance of a lake. Over the last decades, there has been a more rapid increase in air temperature in the spring period (Benson *et al.* 2012). This translates into higher temperatures of lake water. In the case of Polish lakes, it is precisely in spring that it grows the fastest, 0.2-0.5°C decade^{-1} (Skowron 2011). A consequence has been a quicker disappearance of ice cover, and thus its shorter duration. As a result, the tendencies of change in the pattern of ice phenology recorded for Polish lakes in the second half of the 20th century are mostly downward ones (Pasławski 1982, Marszelewski and Skowron 2006, Choiński *et al.* 2014).

The relations between the temperatures of air and water are closely associated regionally with the macro-scale circulation of the atmosphere (Dąbrowski *et al.* 2004, Livingstone *et al.* 2010). The analysis of NAO-related changes in the thermal conditions of lakes in Poland conducted by Wrzesiński *et al.* (2015) showed considerable deviations from mean values (both 1°C lower and higher, depending on the circulation phase), and those deviations were readily visible in spring, *i.e.*, in the period of ice cover destruction.

In the case of European lakes, also their ice regime shows strong relations with the NAO circulation (Dokulil 2013). When analysing the pattern of ice phenomena on the largest lake in England (Windermere), George (2007) found that this circulation type had greatly influenced ice formation on it for over 30 years, and the link between this phenomenon and the NAO accounted for 50% of inter-year changes. In the case of Lake Erken located in the east of Sweden, an earlier decay of its ice cover was closely related with a high NAO index (Blenckner and Chen 2003). In turn, Maher *et al.* (2005) analysed two winter seasons in the different NAO phases on Lake Vendyurskoe in the northern part of Russia and noted that ice cover tended to be thicker in a negative phase, while its duration did not differ significantly in the two periods analysed. The relations between lake ice phenology and the NAO have also been documented for other regions of the Northern Hemisphere, *e.g.*, in Siberia (Livingstone 1999) or North America (Livingstone 2000). The ice cover of the North American Great Lakes has a linear connection with the NAO and is thicker or thinner depending on its phase (Bai *et al.* 2012).

In the case of Polish lakes, all the examined characteristics of ice phenology respond to variations in the pattern of macro-scale circulation by deviating from the mean values. This is especially significant for the duration of ice cover, which isolates a lake from the influence of external factors, and this, as has been mentioned in the Introduction, completely changes the operation of the given ecosystem. The inter-year variability of this characteristic in Poland is considerable and amounts to over a month, depending on the phase and intensity of the NAO.

The NAO is an essential but not the only element responsible for the pattern of lake ice phenology in this part of Europe. This is indicated by the spatial differences in conditions of lake ice phenology in Poland reported in this paper. Karetnikov and Naumenko (2008) came to similar conclusions in the case of Lake Ladoga; they found a connection between the NAO and ice phenology which was absent when ice cover exhibited extreme characteristics. In principle, the severity of ice phenomena on Polish lakes grows eastwards. This has been observed by, *e.g.*, Girjatowicz (2003) for four coastal lakes. Thus, what should be taken as the basic feature influencing the length of the ice season on the lakes under study is their location. Departures from this rule are connected with morphometric characteristics of individual lakes and local conditions. Of key significance for lakes located in the lowland zone are the former, and the effect of the surroundings on the pattern of lake ice phenology is especially readily visible in mountain lakes, as corroborated by the research conducted, among others, by Novikmec *et al.* (2013).

The most important morphometric feature of lakes in terms of ice phenology is their depth, because it decides about the amount of accumulated

warmth and hence about the time needed for cooling and freezing (Korhonen 2006). However, in the case of the lakes analysed here, this feature is not readily visible. A later start of the appearance of ice cover was recorded in both, one of the deepest lakes (*e.g.*, Raduńskie Górne) and one of the shallowest ones (*e.g.*, Gopło). This situation illustrates the complexity of overlapping processes and environmental features, the resultants of which are the formation and disappearance of ice in lakes.

The transformation occurring in the conditions of the ice phenology of lakes affects their operation throughout the year, not only in winter. There are many works that connect the physico-chemical conditions of lakes (Leppäranta *et al.* 2003, Witek and Jarosiewicz 2010, Mihu-Pintilie *et al.* 2014) and biological ones (Pettersson 1990, Hurst 2007, Vehmaa and Salonen 2009) with their ice phenology. The effect (or its absence) of ice phenology on living conditions is also observed with reference to lakes in Poland (Toporowska *et al.* 2010, Wojciechowska and Lenard 2014, Sienkiewicz and Gąsiorowski 2014, Messyasz *et al.* 2015, Pełechata *et al.* 2015). The considerable differences in the duration of ice cover may change the species composition of both flora and fauna, which in consequence can lead to the replacement of present species by other organisms. As has been observed by Ptak (2013), the disappearance of the most endangered species would be especially detrimental.

5. CONCLUSIONS

The results presented in this paper concerning the pattern of lake ice phenology in Poland against changes in the intensity of the North Atlantic Oscillation are similar to those established earlier for lakes of the Northern Hemisphere. In the different NAO phases, wide, statistically significant differences can be observed between the values of ice phenology parameters (*e.g.*, those concerning shore ice, ice cover, its thickness, *etc.*) and the mean figures. Of special importance are the considerable deviations from the duration of ice cover − an element which, by isolating water masses from external factors and processes, has the strongest influence on the operation of lakes. Also established were spatial differences in the scale of the effect of the NAO on the conditions of ice phenology of individual lakes. Like the studies by other authors cited here, it is a proof of the complexity of this issue. The effect of the NAO circulation can be stronger or weaker, depending on individual morphometric characteristics of lakes.

The results obtained can be a valuable starting point for further research on lake ice phenology. In the future it might be advisable to build models describing variations in the characteristics (both chemical-physical and biological) of lake ecosystems by accommodating changes in their ice regimes. With detailed multi-year information on the pattern of lake ice phenology for

a large set of objects, it will be possible to formulate general regularities concerning lakes in this part of Europe.

R e f e r e n c e s

Bai, X., J. Wang, C. Sellinger, A. Clites, and R. Assel (2012), Interannual variability of Great Lakes ice cover and its relationship to NAO and ENSO, *J. Geophys. Res.* **117**, C3, C03002, DOI: 10.1029/2010JC006932.

Bednorz, E. (2011), Synoptic conditions of the occurrence of snow cover in central European lowlands, *Int. J. Climatol.* **31**, 8, 1108-1118, DOI: 10.1002/joc.2130.

Benson, B.J., J.J. Magnuson, O.P. Jensen, V.M. Card, G. Hodgkins, J. Korhonen, D.M. Livingstone, K.M. Stewart, G.A. Weyhenmeyer, and N.G. Granin (2012), Extreme events, trends, and variability in Northern Hemisphere lake-ice phenology (1855-2005), *Climatic Change* **112**, 2, 299-323, DOI: 10.1007/s10584-011-0212-8.

Blenckner, T., and D. Chen (2003), Comparison of the impact of regional and North Atlantic atmospheric circulation on an aquatic ecosystem, *Climate Res.* **23**, 2, 131-136, DOI: 10.3354/cr023131.

Blenckner, T., M. Järvinen, and G.A. Weyhenmeyer (2004), Atmospheric circulation and its impact on ice phenology in Scandinavia, *Boreal Environ. Res.* **9**, 5, 371-380.

Brown, L.C., and C.R. Duguay (2010), The response and role of ice cover in lake-climate interactions, *Prog. Phys. Geog.* **34**, 5, 671-704, DOI: 10.1177/0309133310375653.

Castro, A., M.I. Vidal, A.I. Calvo, M. Fernández-Raga, and R. Fraile (2011), May the NAO index be used to forecast rain in Spain? *Atmósfera* **24**, 3,251-265.

Choiński, A., and M. Ptak (2012), Variation in the ice cover thickness on Lake Samołęskie as a result of underground water supply, *Limnol. Rev.* **12**, 3, 133-138, DOI: 10.2478/v10194-012-0053-5.

Choiński, A., M. Ptak, and A. Strzelczak (2013), Areal variation in ice cover thickness on lake Morskie Oko (Tatra Mountains), *Carpat. J. Earth Environ. Sci.* **8**, 3, 97-102.

Choiński, A., M. Ptak, and R. Skowron (2014), Trends to changes in ice phenomena in Polish lakes in the years 1951-2010, *Prz. Geogr.* **86**, 1, 23-40, DOI: 10.7163/PrzG.2014.1.2 (in Polish).

Dąbrowski, M., W. Marszelewski, and R. Skowron (2004), The trends and dependencies between air and water temperatures in lakes in northern Poland in 1961-2000, *Hydrol. Earth Syst. Sci.* **8**, 1, 79-87, DOI: 10.5194/hess-8-79-2004.

Dokulil, M.T. (2013), Impact of climate warming on European inland waters, *Inland Waters* **4**, 1, 27-40, DOI: 10.5268/IW-4.1.705.

Futter, M.N. (2003), Patterns and trends in Southern Ontario lake ice phenology, *Environ. Monit. Assess.* **88**, 1-3, 431-444, DOI: 10.1023/A:1025549913965.

George, D.G. (2007), The impact of the North Atlantic Oscillation on the development of ice on Lake Windermere, *Climatic Change* **81**, 3-4, 455-468, DOI: 10.1007/s10584-006-9115-5.

Gerten, D., and R. Adrian (2000), Climate-driven changes in spring plankton dynamics and the sensitivity of shallow polymictic lakes to the North Atlantic Oscillation, *Limnol. Oceanogr.* **45**, 5, 1058-1066, DOI: 10.4319/lo.2000.45.5.1058.

Girjatowicz, J.P. (2003), The influence of the North Atlantic Oscillation on ice conditions in coastal lakes of the Southern Baltic Sea, *Ann. Limnol. – Int. J. Limnol.* **39**, 1, 71-80, DOI: 10.1051/limn/2003007.

Heape, R., J. Hirschi, and B. Sinha (2013), Asymmetric response of European pressure and temperature anomalies to NAO positive and NAO negative winters, *Weather* **68**, 3, 73-80, DOI: 10.1002/wea.2068.

Hurrell, J. (1995), The Climate Data Guide: Hurrell North Atlantic Oscillation (NAO) Index, National Center for Atmospheric Research, Boulder, USA, https://climatedataguide.ucar.edu/climate-data/hurrell-north-atlantic-oscillation-nao-index-station-based, last modified 20 October 2015.

Hurst, T.P. (2007), Causes and consequences of winter mortality in fishes, *J. Fish Biol.* **71**, 2, 315-345, DOI: 10.1111/j.1095-8649.2007.01596.x.

Jensen, O.P., B.J. Benson, J.J. Magnuson, V.M. Card, M.N. Futter, P.A. Soranno, and K.M. Stewart (2007), Spatial analysis of ice phenology trends across the Laurentian Great Lakes region during a recent warming period, *Limnol. Oceanogr.* **52**, 5, 2013-2026, DOI: 10.4319/lo.2007.52.5.2013.

Karetnikov, S.G., and M.A. Naumenko (2008), Recent trends in Lake Ladoga ice cover, *Hydrobiologia* **599**, 1, 41-48, DOI: 10.1007/s10750-007-9211-1.

Korhonen, J. (2006), Long-term changes in lake ice cover in Finland, *Nord. Hydrol.* **37**, 4-5, 347-363, DOI: 10.2166/nh.2006.019.

Leppäranta, M. (2014), Interpretation of statistics of lake ice time series for climate variability, *Hydrol. Res.* **45**, 4-5, 673-683, DOI: 10.2166/nh.2013.246.

Leppäranta, M., A. Reinart, A. Erm, H. Arst, M. Hussainov, and L. Sipelgas (2003), Investigation of ice and water properties and under-ice light fields in fresh and brackish water bodies, *Nord. Hydrol.* **34**, 3, 245-266, DOI: 10.2166/nh.2003.015.

Livingstone, D.M. (1999), Ice break-up on southern Lake Baikal and its relationship to local and regional air temperatures in Siberia and to the North Atlantic Oscillation, *Limnol. Oceanogr.* **44**, 6, 1486-1497, DOI: 10.4319/lo.1999.44.6.1486.

Livingstone, D.M. (2000), Large-scale climatic forcing detected in historical observations of lake ice break-up, *Verh. Int. Verein. Theor. Angew. Limnol.* **27**, 5, 2775-2783.

Livingstone, D.M., R. Adrian, T. Blenckner, G. George, and G.A. Weyhenmeyer (2009), Lake ice phenology. **In:** G. George (ed.), *The Impact of Climate Change on European Lakes*, Aquatic Ecology Series, Vol. 4, Springer, Dordrecht, 51-61, DOI: 10.1007/978-90-481-2945-4_4.

Livingstone, D.M., R. Adrian, L. Arvola, T. Blenckner, M.T. Dokulil, R.E. Hari, G. George, T. Jankowski, M. Järvinen, E. Jennings, P. Nõges, T. Nõges, D. Straile, and G.A. Weyhenmeyer (2010), Regional and supra-regional coherence in limnological variables. **In:** G. George (ed.), *The Impact of Climate Change on European Lakes*, Aquatic Ecology Series, Vol. 4, Springer, Dordrecht, 311-337, DOI: 10.1007/978-90-481-2945-4_17.

Maher, O.A., C. Bertacchi Uvo, and L. Bengtsson (2005), Comparison between two extreme NAO winters and consequences on the thermal regime of Lake Vendyurskoe, Karelia, *J. Hydrometeorol.* **6**, 5, 775-783, DOI: 10.1175/JHM449.1.

Majewski, W. (2007), Flow in open channels under the influence of ice cover, *Acta Geophys.* **55**, 1, 11-22, DOI: 10.2478/s11600-006-0041-8.

Marszelewski, W., and R. Skowron (2006), Ice cover as an indicator of winter air temperature changes: case study of the Polish Lowland lakes, *Hydrol. Sci. J.* **51**, 2, 336-349, DOI: 10.1623/hysj.51.2.336.

Messyasz, B., M. Gąbka, J. Barylski, G. Nowicki, Ł. Lamentowicz, A. Goździcka-Józefiak, A. Rybak, R. Dondajewska, and L. Burchardt (2015), Phytoplankton, culturable bacteria and their relationships along environmental gradients in a stratified eutrophic lake, *Carpath. J. Earth Environ. Sci.* **10**, 1, 41-52.

Mihu-Pintilie, A., G. Romanescu, and C. Stoleriu (2014), The seasonal changes of the temperature, pH and dissolved oxygen in the Cuejdel Lake, Romania, *Carpathian J. Earth Environ. Sci.* **9**, 2, 113-123.

Novikmec, M., M. Svitok, D. Kočický, F. Šporka, and P. Bitušík (2013), Surface water temperature and ice cover of Tatra Mountains lakes depend on altitude, topographic shading, and bathymetry, *Arct. Antarct. Alp. Res*. **45**, 1, 77-87, DOI: 10.1657/1938-4246-45.1.77.

Pasławski, Z. (1982), Ice conditions of the lakes in Poland, *Prz. Geof.* **27**, 1-2, 79-92 (in Polish).

Pełechata, A., M. Pełechaty, and A. Pukacz (2015), Winter temperature and shifts in phytoplankton assemblages in a small Chara-lake, *Aquat. Bot.* **124**, 10-18, DOI: 10.1016/j.aquabot.2015.03.001.

Pettersson, K. (1990), The spring development of phytoplankton in Lake Erken: species composition, biomass, primary production and nutrient conditions – a review, *Hydrobiologia* **191**, 1, 9-14, DOI: 10.1007/BF00026033.

Pociask-Karteczka, J. (2006), River hydrology and the North Atlantic Oscillation: A general review, *Ambio* **35**, 6, 312-314, DOI: 10.1579/05-S-114.1.

Ptak, M. (2013), Variability of temperature and ice phenomena on Łebsko and Gardno lakes, *Parki Narodowe i Rezerwaty Przyrody* **32**, 2, 45-55 (in Polish).

Scaife, A.A., C.K. Folland, L.V. Alexander, A. Moberg, and J.R. Knight (2008), European climate extremes and the North Atlantic Oscillation, *J. Climate* **21**, 1, 72-83, DOI: 10.1175/2007JCLI1631.1.

Sharov, A.N., N.A. Berezina, L.E. Nazarova, T.N. Poliakova, and T.A. Chekryzheva (2014), Links between biota and climate-related variables in the Baltic region using Lake Onega as an example, *Oceanologia* **56**, 2, 291-306, DOI: 10.5697/oc.56-2.291.

Sienkiewicz, E., and M. Gąsiorowski (2014), Changes in the trophic status of three mountain lakes – natural or anthropogenic process? *Pol. J. Environ. Stud.* **23**, 3, 875-892.

Skowron, R. (2011), The Differentiation and the Changeability of Chosen Elements of the Thermal Regime of Water in Lakes on Polish Lowland, Wyd. Nauk. Uniwersytetu Mikołaja Kopernika, Toruń, 245 pp. (in Polish).

Soja, A.-M., K. Kutics, K. Maracek, G. Molnár, and G.Soja (2014), Changes in ice phenology characteristics of two Central European steppe lakes from 1926 to 2012 – influences of local weather and large scale oscillation patterns, *Climatic Change* **126**, 1, 119-133, DOI: 10.1007/s10584-014-1199-8.

Thomson, D.J. (2009), Climate change: Shifts in season, *Nature* **457**, 7228, 391-392, DOI: 10.1038/457391a.

Toporowska, M., B. Pawlik-Skowrońska, D. Krupa, and R. Kornijów (2010), Winter versus summer blooming of phytoplankton in a shallow lake: Effect of hypertrophic conditions, *Pol. J. Ecol.* **58**, 1, 3-12.

Vehmaa, A., and K. Salonen (2009), Development of phytoplankton in Lake Pääjärvi (Finland) during under-ice convective mixing period, *Aquat. Ecol.* **43**, 3, 693-705, DOI: 10.1007/s10452-009-9273-4.

Weyhenmeyer, G.A. (2009), Do warmer winters change variability patterns of physical and chemical lake conditions in Sweden? *Aquat. Ecol.* **43**, 3, 653-659, DOI: 10.1007/s10452-009-9284-1.

Witek, Z., and A. Jarosiewicz (2010), The oxygen budget of two closed, dimictic lakes in the vicinity of Bytów (West Pomeranian Lake District, northern Poland), *Oceanol. Hydrobiol. Stud.* **39**, 2, 135-145, DOI: 10.2478/v10009-010-0022-8.

Wojciechowska, W., and T. Lenard (2014), Effect of extremely severe winters on under-ice phytoplankton development in a mesotrophic lake (Eastern Poland), *Oceanol. Hydrobiol. Stud.* **43**, 2: 147-153, DOI: 10.2478/s13545-014-0127-x.

Wrzesiński, D., and R. Paluszkiewicz (2011), Spatial differences in the impact of the North Atlantic Oscillation on the flow of rivers in Europe, *Hydrol. Res.* **42**, 1, 30-39, DOI: 10.2166/nh.2010.077.

Wrzesiński, D., M. Ptak, and A. Baczyńska (2013), Effect of the North Atlantic Oscillation on ice phenomena on selected lakes in Poland over the years 1961-2010, *Quaest. Geogr.* **32**, 3, 119-128, DOI: 10.2478/quageo-2013-0020.

Wrzesiński, D., A. Choiński, and M. Ptak (2015) Effect of the North Atlantic Oscillation on the thermal characteristics of lakes in Poland, *Acta Geophys.* **63**, 3, 863-883, DOI: 10.1515/acgeo-2015-0001.

Experimental Study on Velocity Profiles with Different Roughness Elements in a Flume

Xie-Kang WANG[1], Chen YE[1], Bing-Jie WANG[1], and Xu-Feng YAN[2]

[1]State Key Laboratory of Hydraulics and Mountain River Engineering,
Sichuan University, Chengdu, China;
e-mail: wangxiekang@scu.edu.cn (corresponding author)

[2]Department of Civil and Environmental Engineering, Hong Kong Polytechnic
University, Hong Kong, China; e-mail: xufeng.yan@connect.polyu.hk

A b s t r a c t

The classical log law for velocity profile is applied to engineering practice. Field observations indicate that the composition of the bed materials obviously influences the shape of vertical velocity distribution. To clearly understand the roughness effect, six types of materials were laid separately at various depths for the investigation of the effects of roughness elements on the vertical velocity distribution. A down-looking 3D acoustic Doppler velocimeter was used to measure the velocity profiles. The experimental results showed that the curve characteristics of velocity profiles are strongly dependent on the roughness scale and related flow parameters. If d/R, Fr, and Re are larger than 0.15, 0.47, and 60 000, respectively, the velocity distribution may resemble an S-shape profile. The inflexion position Z_*/H for a given S-shape profile was empirically deduced as $Z_*/H = -0.4481 d/R + 0.3225$. Otherwise, the velocity profile agrees well with the logarithmic law. The findings of this study are useful in engineering practice (*i.e.*, depth-averaged velocity and flow rate estimate).

Key words: velocity profiles, acoustic Doppler velocimeter, roughness elements, logarithmic law, S-shape curve.

1.   INTRODUCTION

Most flow structure studies in open channel focus mainly on the velocity profile since it has been often used to examine the local effects due to roughness elements on the flow field and flow resistances (Nowell and Church 1979, Raupach 1981, Dong and Ding 1990, Dong *et al.* 1992, Robert *et al.* 1992, Wohl and Ikeda 1998, Tachie *et al.* 2000, Ferro 2003a, b). The classical logarithmic velocity profile is employed as the boundary condition linking the boundary node and the first calculated internal node, so that the large computational time consumption can be reduced in modeling the boundary layer (Lin and Li 2002, Knopp *et al.* 2006). The velocity profile indicates the mass transport distribution and the momentum transfer.

Back to the last century, Kuelegan (1938) proposed the velocity profile fitting the log-law along the entire depth. With the advanced experimental investigation and theoretical analysis, the velocity distribution often varied with the bed roughness scales. In the 1980s, the previous studies (Zippe and Graf 1983, Nezu and Rodi 1986) showed that the log law could only be established in the region of near-wall, and the logarithmic formula should be extended with a wake function for the whole depth (Coles 1956, Kirkgöz 1989, Kirkgöz and Ardiçlioğlu 1997, Liu *et al.* 2005). Cardoso *et al.* (1989), however, pointed out that wake function might be affected by secondary flows, upstream flows, and so forth. Wang *et al.* (1998), comparing the developing flows within the boundary layer, thought that the wake function was essentially an empirical processing of measured data, and thus no universal wake function exists to cover all situations. Papanicolaou *et al.* (2012) successfully introduced the velocity defect law to describe the velocity distribution around the boulder within the array. Many research studies also document the characteristics of velocity profile regarding the effects of different roughness scales. Bathurst *et al.* (1981) defined roughness as small a scale as $h/d_{50} > 7.5$ or $h/d_{84} > 4.0$, (d_{50}, the particles for which 50% are finer; d_{84}, the particles for which 84% are finer); however, Bray (1988) believed that the quantity of the relative depth for small scale roughness is $h/d_{50} > 20$. Dong and Ding (1990) and Dong *et al.* (1992) studied the influence of boundary roughness on flow characteristics by changing the value of h/k_s. He suggested that the velocity profile is able to be fitted just by the logarithmic formula if $h/k_s < 2.0$ (k_s is 10 mm, the maximum diameter of bed materials), while the wake function should be introduced if $h/k_s \geq 5.0$. He and Wang (2004) also pointed out that the velocity profile on rough beds cannot be described with a single logarithmic formula. Jiménez (2004) believed that for the logarithmic layer to occur the relative depth (flow depth to the roughness height ratio) should exceed at least 40. On the basis of the flume experiments using pingpong balls instead of sand grains, Yang and Yang (2005) showed

that the velocity profile only complies with the log law when $h/k_s > 1.9$ (k_s is 4.0 cm, the diameter of pingpong ball).

The log law for fitting the boundary flow velocity distribution is classical due to its simple description, the explanation of mechanism, and universality for the boundary conditions. The velocity profile, however, does not frequently satisfy the log law in realistic rivers, in particular steep mountain rivers with high flow condition and large-scale roughness (*i.e.*, gravel and cobble) (Biron *et al*. 1998, Wohl and Thompson 2000). Katul *et al*. (2002) believed that when the ratio of the water depth and roughness scale is small (< 10), the boundary layer theory becomes invalid to estimate the flow discharge and flow resistance. Byrd *et al*. (2000) presented that only a small proportion (10%) among all field measured velocity distributions could be described by the logarithmic profile, while the majority was attributed to other profiles, including S-shape profile, irregular profile, and linear profile. Schmeeckle and Nelson (2003) reported that the wake effect induced by roughness elements plays significant role in formation of S-shape velocity profile. Studies by Shvidchenko and Pender (2001) show that the drag force induced by the large-scale roughness elements significantly negatively contributes to the velocity distribution within the lower layer of the water depth. Byrd *et al*. (2000), employing the scaling analysis of the momentum and kinetic energy equations, showed that terms usually neglected in cases with small-scale roughness became significant in very rough mountain rivers. This change was the rooted reason for occurrence of the non-logarithmic velocity profiles such as S-shape profiles. Similar S-shape velocity profiles can be extensively identified regarding the flow through canopies, including terrain canopies and aquatic canopies (Raupach *et al*. 1996, Nepf and Ghisalberti 2008) and atmospheric flow over urban roughness (Kastner-Klein and Rotach 2004, Coceal *et al*. 2006). The S-shape velocity profile also frequently coincides with the bed-forms such as large-scale dunes due to bed-load transport. The above-mentioned studies all indicate that the velocity profile is highly correlated to the roughness scale. The logarithmic profile corresponds with small-scale roughness, while the S-shape profile with large-scale roughness (Franca 2005).

In order to explore the cause of occurrence of the irregular velocity profile (*i.e.*, S-shape profile), the turbulence structure near the bed with large-scale roughness (*i.e.*, gravels and cobbles) were examined recently. Roy *et al*. (2004) with the field investigation results showed that the large-scale turbulent flow structures over the gravel bed developed within the entire water depth, which led to the disappearance of the boundary layer. Hardy *et al*. (2009) demonstrated that the turbulent coherent structure was triggered by the flow wake flapping around the roughness (gravels), and more well-organized with the increase in the Reynolds number. Further, other more re-

lated studies can be found to understand the flow turbulent behavior near the rough bed (Buffin-Bélanger and Roy 2005, Legleiter *et al.* 2007, Singh *et al.* 2010). Because of the complicated flow structure characteristics induced by the rough boundary, researchers (Nikora *et al.* 2007, Aberle *et al.* 2008, Stoesser and Nikora 2008) have recently employed the time-averaging concept to spatially average the Reynolds averaged Navier–Stokes equations, obtaining a new term referred to as form-induced stress analogous to Reynolds stress. With the simplification, it is found that the form-induced stress and associated turbulent kinetic energy might be the source to result in the irregular velocity profile (Cooper and Tait 2008, Mignot *et al.* 2008, 2009).

The categories of velocity profiles are conventionally divided into log-law and log-wake-law types within the open channel. Based on the experimental studies (Marchand *et al.* 1984, Bathurst 1988, Ferro and Baiamonte 1994), the velocity profile, however, may be described as an S-shaped type with near-surface velocities significantly greater than near-bed velocities over large scale roughness with the depth/sediment ratio (h/d_{84}) ranging from 1.0 to 4.0. At the same time, two conditions for the development of an S-shaped profile were given by Bathurst (1988). These were (i) channel slopes above 1.0%, the depth sediment ratio h/d_{84} from 1.0 to 4.0, and (ii) particular bed materials with non-uniform condition to allow the development of the lower zone flow. Ferro (2003a) developed a mathematical equation with four parameters to reproduce the measured S-shaped velocity profile in a laboratory flume. Ferguson (2007) agreed that the log law becomes invalid as the ratio of the water depth and the roughness layer thickness decrease below 4.0, while the S-shape profile is applicable.

Bathurst (1985) pointed out the depth/sediment ratio (h/d_{84}) has to vary from 1.0 to 4.0 to form an S-shaped velocity profile, and the upper limit of h/d_{84} defines the point at which the projection of bed material into the flow becomes relatively insignificant. Ferro (2003a) agreed on Bathurst's statement, while further modified the depth sediment ratio h/d_{84} ranging from 1.17 to 12.12 according to experimental data. Afzalimehr *et al.* (2011) also achieved a similar result of S-shape velocity profile within the cobble-bed rivers but not for all cases. The range of the relative submergence is suggested as $2.0 < h/d_{84} < 4$. In this present study, a filed surveys firstly verified that the different roughness element affected changes of vertical velocity profile in mountain river with wide size distribution sediment, and then, the effects of relative roughness ratio $4.9 < h/k_s < +\infty$ and $1.0 < B/h < 4.0$ on velocity profiles are further explored in the flume experiment. Also discussed are the two other questions: (i) whether or not there exists an S-shaped profile on a artificial bed with a flat slope arrangement, and (ii) how to determine the logarithmic or S-shape curves according the flow and

boundary conditions; in other words, how to achieve the inflexion position for the given S-shape curve.

2. METHODOLOGY

2.1 Experimental setup

Most field surveys show that there is a non-uniform sediment on the bed materials in mountain river, the patterns of sediment sorting in this wide size distribution sediment commonly result from the segregation of particles with the interaction between flow and sediment, and then the uniform sediment region often occurs in some local small unit area. In order to choose the diameter of experimental sediment in the flume, we investigated the characteristics of bed materials at the intersection between the Baisha River and Mingjian River at Dujiangyan irrigation system in Chengdu, China. Physically, the typical vertical velocity distribution and the flow rate were measured using the FlowTracker Handheld acoustic Doppler velocimeter (ADV) manufactured by SonTek/YSI. Figure 1 presents the monitoring photos and the related sediment characteristics on the river bed. Figure 1a indicates that different uniform sediment groups were distributed on the river bed. Figure 2a shows the vertical water depth distribution at Baisha River. The mean flow velocity was estimated at the 0.6 local water depth (see Fig. 2b). The flow rate was calculated by the single-point method in hydrological analysis, as a consequence of 0.512 m^3/s of the flow discharge with respect to Baisha River. The detailed vertical velocity profile in Fig. 2c has been monitored at four typical positions (*i.e.*, a distance of 1.4, 1.8, 2.8, and 3.8 m, respectively), showing that in the shape of velocity profile there obviously exist some differences; this result may affect the precision of flow rate calculation assuming the logarithmic law of velocity profile. The velocity data at regions from the river bed to the 0.2 dimensionless water depth, however, cannot be obtained because of the limitation of the FlowTracker Handheld ADV system monitoring blindness zone. The flume experiment would be designed and completed to systematically explore the influence of bed roughness on the velocity distribution.

The experiments were carried out in a flume with size of 0.60 m (width) × 0.60 m (depth) × 13.5 m (length) and a flat slope, located in the State Key Laboratory of Hydraulics and Mountain River at Sichuan University (China). The test zone shown in Fig. 3 is 4.0 m long, where two typical cross-sections with intervals of 20 cm among sections were selected in the middle reach within the flume. The velocity profile was uniformly measured along five verticals distributed at each cross-section, *i.e.*, line 1#, line 2#, line 3#, line 4#, and line 5#, at positions of 0.10, 0.20, 0.30, 0.40, and 0.50 m, respectively. The measurement interval distance is 0.5 cm within regions of

(a)

(b)
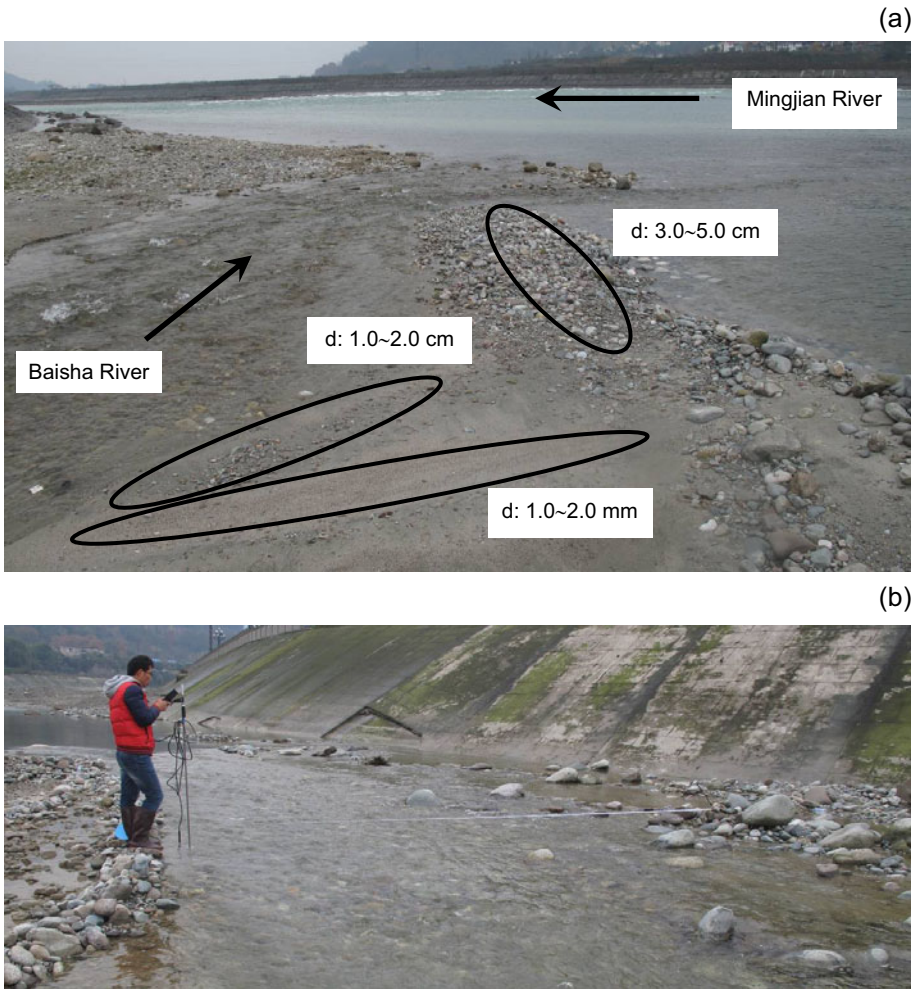
Fig. 1. Field observation photos showing the diameters of bed materials and flow velocity: (a) the diameter characteristics of bed materials at Baisha River in river confluence, and (b) observational section of vertical velocity profile and flow rate at Baisha River.

2.0 cm above the bottom, and 1.0 cm within outer regions in order to obtain detailed velocity field in each vertical monitoring line. Based on findings of previous studies which investigated velocity profiles, the uniform sands were used in this study to dispose of the effects of k_s on the conditions of roughness scales because of the uncertainty of roughness height k_s for the different selection criteria, *i.e.*, $k_s = d_{65}$, d_{75}, d_{84} or d_{90} (Einstein and El-Samni 1949, Lane and Carlson 1953, Bathurst *et al.* 1981, Meyer-Peter and Müller 1948).
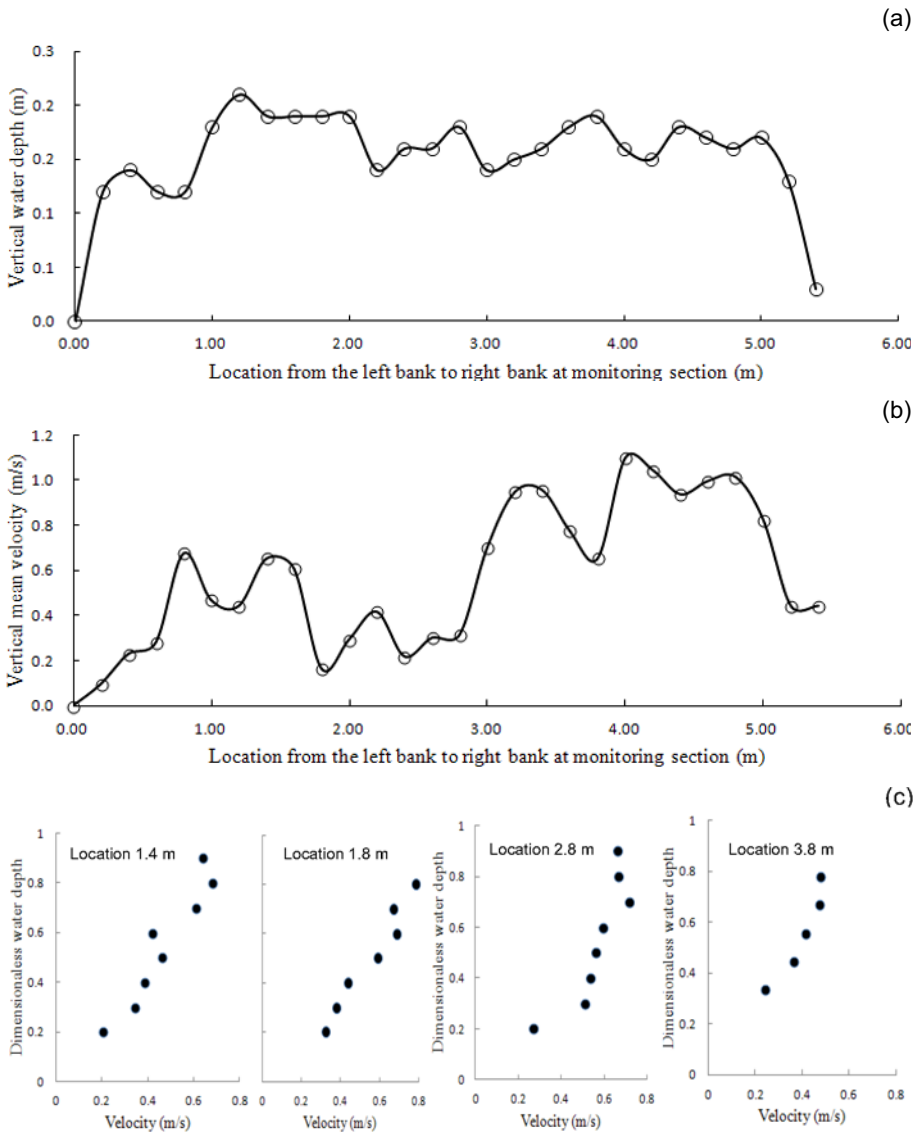
Fig. 2. The flow characteristics at flow rate monitoring section in Baisha River: (a) the vertical water depth distribution at flow rate monitoring section, (b) the vertical velocity distribution at 0.6 h position in flow rate monitoring section, and (c) the vertical velocity profile at typical locations in flow rate monitoring section.

Beds with five types of sediment roughness and a smooth bed were set up, the diameter of the uniform sands ranging from 2.0 to 40 mm, as shown in Figs. 4 and 5.
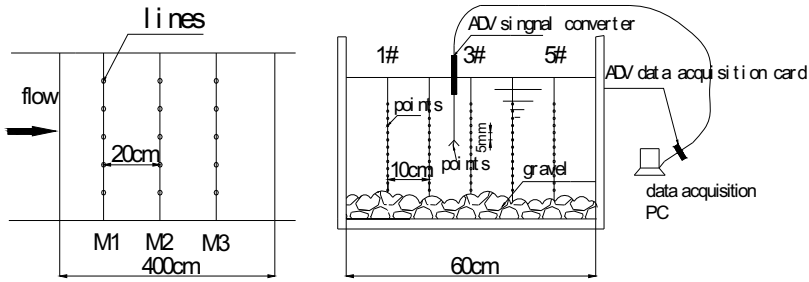
Fig. 3. Arrangement of measurements.
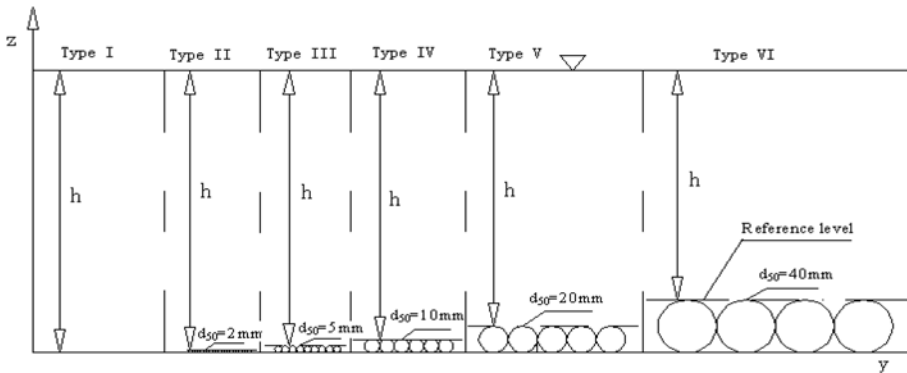
Fig. 4. Schemes of bed types in experiments.
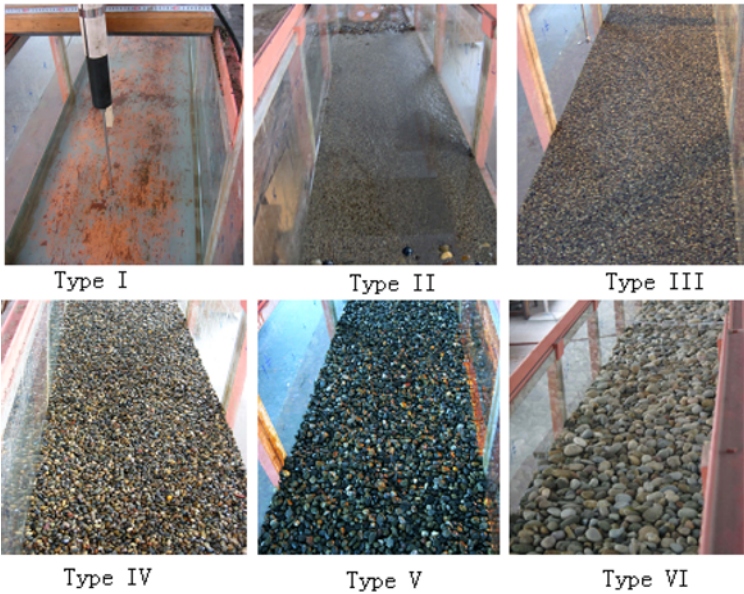
Fig. 5. Photos of bed types used in experiments.

Parameters of experimental runs

Bed shape	Run	Section	h [cm]	B/h	R [m]	Q [l s^{-1}]	h/k_s	V [ms^{-1}]	d/R	Fr	u^* [cms^{-1}]	Re	Mean velocity shape
Type I	1	1#	50.2	1.2	0.19	83.3	$+\infty$	0.28	0.00	0.12	1.30	41915	Log
		2#	50.1	1.2	0.19	83.3	$+\infty$	0.28	0.00	0.12	1.28	41967	Log
	2	2#	29.3	2.0	0.15	84.2	$+\infty$	0.48	0.00	0.28	2.11	57300	Log
		6#	29.3	2.0	0.15	84.2	$+\infty$	0.48	0.00	0.28	2.20	57300	Log
Type II	3	1#	42.0	1.4	0.18	74.9	210	0.30	0.01	0.15	1.60	41981	Log
		2#	42.0	1.4	0.18	74.9	210	0.30	0.01	0.15	1.48	41981	Log
Type III	4	1#	37.0	1.6	0.17	84.9	74.0	0.38	0.03	0.20	2.30	51137	Log
		2#	37.0	1.6	0.17	84.9	74.0	0.38	0.03	0.20	2.11	51137	Log
	5	2#	24.5	2.4	0.13	78.1	49.0	0.53	0.04	0.34	2.95	57830	Log
		4#	24.7	2.4	0.14	78.1	49.4	0.53	0.04	0.34	2.65	57619	Log
Type IV	6	1#	30.7	2.0	0.15	71.7	30.7	0.39	0.07	0.22	3.09	47668	Log
		2#	30.7	2.0	0.15	71.7	30.7	0.39	0.07	0.22	2.88	47668	Log
	7	2#	17.4	3.4	0.11	71.7	17.4	0.69	0.09	0.53	3.51	61044	S
		4#	18.1	3.3	0.11	71.7	18.1	0.66	0.09	0.50	3.42	60155	S
	8	2#	16.7	3.6	0.11	77.6	16.7	0.77	0.09	0.61	4.04	67057	S
		3#	17.1	3.5	0.11	77.6	17.1	0.76	0.09	0.58	4.26	66487	S
	9	2#	18.0	3.3	0.11	76.9	18.0	0.71	0.09	0.54	4.71	64652	S
		4#	18.0	3.3	0.11	76.9	18.0	0.71	0.09	0.54	4.72	64652	S
Type V	10	2#	31.0	1.9	0.15	61.2	15.5	0.33	0.13	0.19	2.79	40487	Log
		4#	31.0	1.9	0.15	61.2	15.5	0.33	0.13	0.19	2.96	40487	Log
	11	2#	28.6	2.1	0.15	72.3	14.3	0.42	0.14	0.25	4.12	49790	Log
		6#	29.0	2.1	0.15	72.3	14.5	0.42	0.14	0.25	4.12	49452	Log
	12	2#	18.4	3.3	0.11	76.8	9.2	0.70	0.18	0.52	5.51	64035	S
		4#	19.5	3.1	0.12	76.8	9.8	0.66	0.17	0.47	5.40	62612	S
	13	2#	17.9	3.4	0.11	77.2	9.0	0.72	0.18	0.54	6.41	65040	S
		3#	17.2	3.5	0.11	77.2	8.6	0.75	0.18	0.58	6.20	66005	S
Type VI	14	1#	22.8	2.6	0.13	98.3	5.7	0.72	0.31	0.48	9.24	75131	S
		2#	22.1	2.7	0.13	98.3	5.5	0.74	0.31	0.50	9.14	76140	S
	15	1#	20.2	3.0	0.12	101	5.1	0.83	0.33	0.59	9.75	81193	S
		2#	19.7	3.0	0.12	101	4.9	0.85	0.34	0.61	9.66	82009	S

Explanations: Type I – smooth bed; Type II – uniform sand with 2 mm diameter; Type III – uniform sand with 5 mm diameter; Type IV – uniform sand with 10 mm diameter; Type V – uniform sand with 20 mm diameter; and Type VI – uniform sand with 40 mm diameter.

In this experiment, the flow velocities were measured by a down-looking 3D acoustic Doppler velocimeter (ADV) probe with the standard 16-MHz, which is manufactured by SonTek Inc. The research was done under the fol-

lowing conditions: (i) the sampling volume by ADV was small (*i.e.*, 0.125 cm^3), (ii) the sampling location was situated 5.0 cm below the sensor head, and (iii) the instrument sensed the distance between the bottom of the measuring volume and the bed surface with a high degree of accuracy (±1 mm). The above enables precise determination of the position of each velocity measurement (Bergeron and Abrahams 1992), and acquisition of a high-resolution record of the vertical velocity variation with minimal profile disturbance due to the presence of the probe.

2.2 Analysis of velocity profiles

The flow velocity measurements were carried out under different discharges, and related hydraulic variations were calculated as shown in Table 1, *i.e.*, values of the width/depth ratio B/h and of depth/roughness height ratio h/k_s, (k_s is the median diameter of uniform sands), hydraulic radius R, relative roughness d/R, average velocity $V = Q/(B h)$, the Froude number Fr = $Q/(g^{1/2}B h^{3/2})$, Reynolds number (Re = VR/v; v is water kinematic viscosity with magnitude of 0.01239 cm^2/s with water temperature 12° in this experiment).

2.3 Vertical velocity profiles

Figure 6 shows that the longitudinal velocities at the same cross-section for an individual run nearly collapse onto the logarithmic profile despite different transverse distances against the wall. This indicates the limited side boundary effect on the velocity distribution so that the measurements are reliable. Figure 7 shows that an alternative S-shape velocity profile occurs for different bed roughness and flow conditions. Traveling along this profile, the velocity at lower layers is significantly resisted, with an inflexion point at the upper layer. This phenomenon is consistent with the descriptions based on previous studies (Marchand *et al.* 1984, Liu *et al.* 2005, Afzalimehr *et al.*
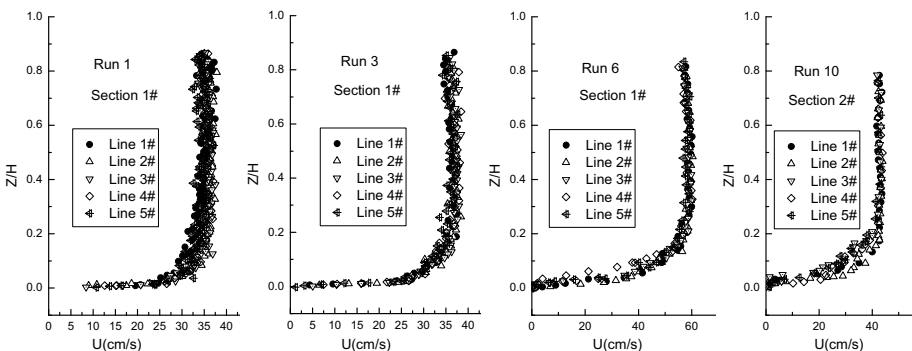
Fig. 6. Logarithmic curves of vertical velocity profiles.
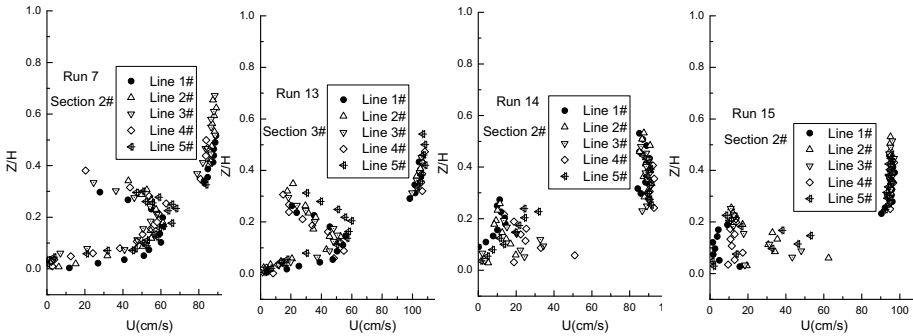
Fig. 7. The S-shape curves of vertical velocity profiles.

2011). However, the previous studies, besides the scale of roughness, did not adopt the flow condition characterized by the Froude number, Fr, as a factor to determine the pattern of velocity profiles. The influence of the Froude number, Fr, on the velocity profile will be analyzed and discussed in the subsequent part of the article.

2.4 Shear velocity estimation

The analysis of velocity profiles frequently employs the shear velocity to represent the dimension of velocity to obtain the formula of velocity description. However, the shear velocity is a somewhat artificially created variable, able to be calculated from the bed shear stress. Rowiński *et al.* (2005) discussed 10 methods including the gravity method, logarithmic profile method, near-bed Reynolds-stress method, turbulent kinetic energy method, Prandtl-based method, *etc*. Those authors pointed out the variability of different methods which can be applied to estimate bed shear stress. With the measurement of high-frequency velocity fluctuations, the measured turbulence may be used in the determination of the shear velocity. For example, Laser Doppler Anemometers (LDA) or ADV provides information on the instantaneous 3D velocities within a small sampling volume that makes it possible to obtain various turbulence parameters (*e.g.*, Nikora and Goring 1998). Conventionally, the most frequently used method to calculate the shear frictional velocity is fitting the log-law velocity profile. However, the velocity profile does not satisfy the log law any longer when large-scale roughness exists at the bottom, as mentioned above. Comparably, the kinetic energy method is very straightforward to calculate the shear velocity once the distribution of the turbulent kinetic energy is obtained by measurements. Wang *et al.* (2007) stated that the 3-D turbulence kinetic energy method (*i.e.*, Kim *et al.* 2000, Biron *et al.* 2004) is the correct method to determine the shear velocity on a rough river bed. This method, therefore, is also used in this study. The method is based on the formula $\tau_0 = \rho U_*^2 = 0.5 C \rho (\overline{u'^2} + \overline{v'^2} + \overline{w'^2})$, where C

is assumed to be equal to 0.19. This method has been proved to be applicable in gravel beds (Schindler and Robert 2005).The shear velocities for each run are listed in Table 1.

Figure 8 presents mean velocity profiles with normalization of the shear velocity at the selected cross-section for each run, in which the mean velocity has been calculated by averaging velocities with respect to five vertical lines and normalized with the shear velocity, as shown in Table 1. It is to be noted from Fig. 8 that the velocity increases and fits log law through the increasing water depth in Runs 1-6 and 10-11. Further, there occurred an inflexion located within the range of 0.15~0.30 Z/H (H is the averaged depth) away from the bed for the Runs 7-9 and 12-15. As a result, the mean velocity collapses into an S-shape curve. Comparing Run 6 with Run 7, the mean velocity profiles are respectively characterized by logarithmic and S-shape curves with the same discharge of $71.7\,1\,s^{-1}$ and bed materials with uniform sands of 10 mm diameter and but different flow depths. Generally speaking, the flow structures are strongly dependant on flow conditions (*i.e.*, Froude number, Fr; Reynolds number, Re) and boundary conditions (*i.e.*, hydraulic radius, relative roughness d/R, the value of width/depth ratio B/h).

To further reveal the relationships among the bottom roughness, d/R, flow conditions, Fr, and Reynolds number, Re, on the patterns of velocity profile, the relationship between the profile pattern and the influential factors is plotted in Fig. 9. The roughness scale d/R is set as the *x*-axis and the Froude number, Fr, and Reynolds number, Re, as the *y*-axis. As shown in the diagram, the S-shape velocity profile coincides with the relatively large-scale roughness, which has the roughness height of 10 mm above. With respect to these situations, the Froude number has larger value; when Fr > 0.47, the S-shape velocity profile could be formed in this study. In addition, the character of flow turbulence (Reynolds number) indicates that when Re > 60 000, the S-shape curve occurs in these runs.

As discussed above, the logarithmic velocity profile is not satisfactory for description of the velocity over the very rough bed with the high Froude number and Reynolds number. The S-shape velocity profile may be an alternative distribution. Generally speaking, the wall function method that employs the log law or power law for velocity connection between the boundary node and the first internal node is very powerful to in the numerical simulation of turbulent flows. However, within the situation that the S-shape velocity may occur, it is more appropriate to use an S-shape velocity profile to set the wall function. The hyperbolic tangent function as proposed by Katul *et al.* (2002) can be used to describe the S-shape velocity profile which inherently has an inflexion point on the profile. It is clearly noted that the inflexion position varies with the roughness scale and flow condition. Determination of the inflexion position regarding different boundary and flow
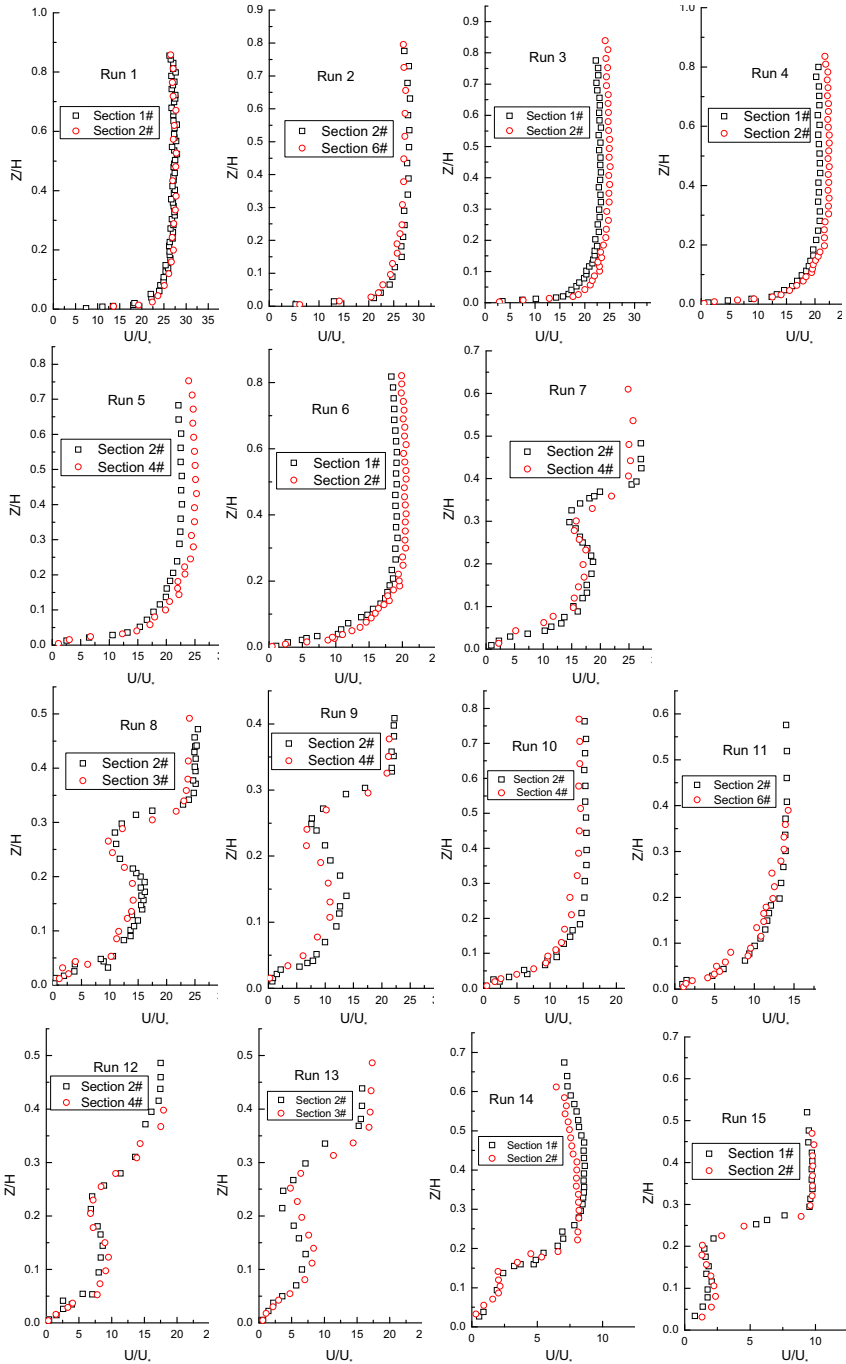
Fig. 8. Mean velocity profiles at selected cross-sections in each run.
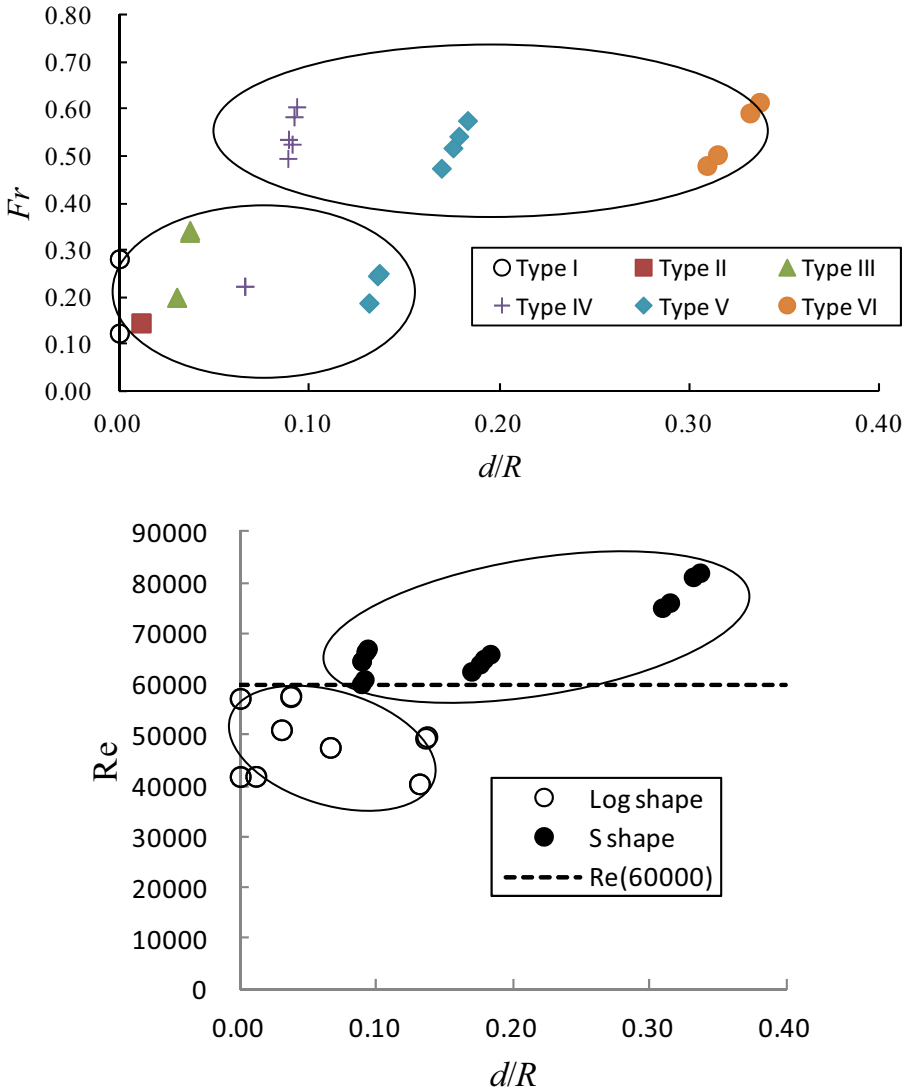
Fig. 9. The relationship between the patterns of velocity profile and related influential factors.

flow configurations is very important in engineering practice. Based on the present experiment, the inflexion position of the S-shape velocity profiles may be obtained. The linear regression equation $Z_*/H = -0.4481d/R + 0.3225$ with high correlation coefficient $r^2 = 0.8206$ can be easily obtained, as shown in Fig. 10. This equation indicates that the inflexion position decreases as the roughness scale increases.
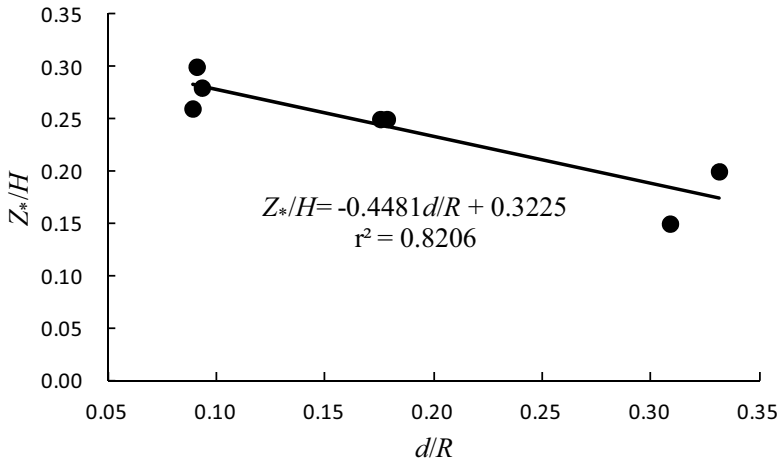
Fig. 10. The relationship between inflexion position Z_*/H and d/R.

3. CONCLUSIONS

The main aim of this study, based on previous studies, is to discuss the influence of the flow and boundary conditions (*i.e.*, $1.0 < B/h < 4.0$ and $4.9 < h/k_s < +\infty$) on the pattern of the velocity profile, namely logarithmic and S-shaped curves. Firstly, the field observations of sediment characteristics and vertical velocity profile in a mountain river with bed of different roughness have been carried out, and then the bed materials of uniform sands in flume experiment were used to observe the effects of roughness height k_s on the roughness scale, and to examine conditions of bed materials and bed slope in the development of such S-shaped velocity profiles as proposed by Bathurst (1988). The experimental results present the S-shaped velocity distribution that may occur when the uniform sands and flat slope are given. Secondly, the conditions of flow and boundary for different velocity profile types were also obtained. Based on the results of the present study it is shown that the patterns of the velocity profile are dependent on both the bottom roughness scale and the flow conditions, as compared with previous studies in which the former parameter was regarded as the only influential factor. The velocity profile may resemble an S-shape curve when the roughness height/hydraulic radius ratio $d/R > 0.15$, Froude number $Fr > 0.47$, and $Re > 60\,000$. Considering that the S-shape velocity profile occurs instead of the classical logarithmic profile for cases with large bottom roughness scale and fast velocity flows (relatively high Fr and Re), it is very important to localize the inflexion position on the S-shape profile for practical applications, such as the boundary specification in the numerical modeling. It is identified that the inflexion position Z_*/H for a given S-shape curve

could be empirically deduced as $Z_*/H = -0.4481 d/R + 0.3225$ with high correlation coefficient $r^2 = 0.8206$. The velocity profile, otherwise, agrees with the logarithmic law. Finally, the regression formula of velocity profiles is not further explored because it has been satisfactorily examined in most previous studies on logarithmic velocity distributions (Keulegan 1938, Coles 1956, Marchand *et al.* 1984, Bathurst 1988, Kirkgöz 1989, Dong and Ding 1990, Dong *et al.* 1992, Ferro and Baiamonte 1994, Kirkgöz and Ardiçlioğlu 1997, Ferro 2003a, Liu *et al.* 2005, Yang and Yang 2005).

Nomenclature

ADV	–	acoustic Doppler velocimeter
B	–	the main flume width
C	–	the empirical coefficient
d	–	the sediment diameter
d_{50}	–	the particles for which 50% are finer
d_{65}	–	the particles for which 65% are finer
d_{75}	–	the particles for which 75% are finer
d_{84}	–	the particles for which 84% are finer
d_{90}	–	the particles for which 90% are finer
Fr	–	Froude number
g	–	the gravity acceleration
h	–	the water depth
H	–	the average water depth
i#	–	the measurement vertical number
k_s	–	the bed roughness
LDA	–	laser Doppler anemometers
M_i	–	the *i*-th measurement cross-section in the flume experiment
Q	–	the discharge [m^3/s]
R	–	the hydraulic radius
Re	–	Reynolds number
$u*$	–	the bottom shear velocity
u', v', w'	–	the fluctuating velocity in *x*-, *y*-, and *z*-directions
v	–	the mean velocity
Z	–	the measuring position of vertical velocity above smooth bed

$Z*$	– the inflexion position of velocity profile above smooth bed
ρ	– the water density
τ_0	– the bottom shear friction

R e f e r e n c e s

Aberle, J., K. Koll, and A. Dittrich (2008), Form induced stresses over rough gravel-beds, *Acta Geophys.* **56**, 3, 584-600, DOI: 10.2478/s11600-008-0018-x.

Afzalimehr, H., J. Gallichand, J. Sui, and E. Bagheri (2011), Field investigation on friction factor in mountainous cobble-bed and boulder-bed rivers, *Int. J. Sediment Res.* **26**, 2, 210-221, DOI: 10.1016/S1001-6279(11)60087-5.

Bathurst, J.C. (1985), Flow resistance estimation in mountain rivers, *J. Hydraul. Eng. ASCE* **111**, 4, 625-643, DOI: 10.1061/(ASCE)0733-9429(1985)111:4 (625).

Bathurst, J.C. (1988), Velocity profile in high-gradient, boulder-bed channels. **In:** *Proc. Int. Conference on Fluvial Hydraulics, IAHR, 30 May – 3 June 1988, Budapest, Hungary*, 29-34.

Bathurst, J.C., D.B. Simons, and R.M. Li (1981), Resistance equation for large-scale roughness, *J. Hydraul. Div. ASCE* **107**, 12, 1593-1613.

Bergeron, N.E., and A.D. Abrahams (1992), Estimating shear velocity and roughness length from velocity profiles, *Water Resour. Res.* **28**, 8, 2155-2158, DOI: 10.1029/92WR00897.

Biron, P.M., S.N. Lane, A.G. Roy, K.F. Bradbrook, and K.S. Richards (1998), Sensitivity of bed shear stress estimated from vertical velocity profiles: The problem of sampling resolution, *Earth Surf. Process. Land.* **23**, 2, 133-139, DOI: 10.1002/(SICI)1096-9837(199802)23:2<133::AID-ESP824>3.0.CO; 2-N.

Biron, P.M., C. Robson, M.F. Lapointe, and S.J. Gaskin (2004), Comparing different methods of bed shear stress estimates in simple and complex flow fields, *Earth Surf. Process. Land.* **29**, 11, 1403-1415, DOI: 10.1002/esp. 1111.

Bray, D.I. (1988), A review of flow resistance in gravel bed rivers. **In:** C. Colosimo and M. Veltri (eds.), *Leggi morfologiche e loro verifica di campo*, BIOS, 23-57.

Buffin-Bélanger, T., and A.G. Roy (2005), 1 min in the life of a river: Selecting the optimal record length for the measurement of turbulence in fluvial boundary layers, *Geomorphology* **68**, 1-2, 77-94, DOI: 10.1016/j.geomorph.2004. 09.032.

Byrd, T.C., D.J. Furbish, and J. Warburton (2000), Estimating depth-averaged velocities in rough channels, *Earth Surf. Process. Land.* **25**, 2, 167-173, DOI: 10.1002/(SICI)1096-9837(200002)25:2 <167::AID-ESP66> 3.0.CO;2-G.

Cardoso, A.H., W.H. Graf, and G. Gust (1989), Uniform flow in a smooth open channel, *J. Hydraul. Res.* **27**, 5, 603-616, DOI: 10.1080/ 00221688909499113.

Coceal, O., T.G. Thomas, I.P. Castro, and S.E. Belcher (2006), Mean flow and turbulence statistics over groups of urban-like cubical obstacles, *Bound.-Lay. Meteorol.* **121**, 3, 491-519, DOI: 10.1007/s10546-006-9076-2.

Coles, D. (1956), The law of the wake in the turbulent boundary layer, *J. Fluid Mech.* **1**, 2, 191-226, DOI: 10.1017/S0022112056000135.

Cooper, J.R., and S.J. Tait (2008), The spatial organisation of time-averaged streamwise velocity and its correlation with the surface topography of water-worked gravel beds, *Acta Geophys.* **56**, 3, 614-642, DOI: 10.2478/ s11600-008-0023-0.

da Franca, M.J.R.P. (2005), A field study of turbulent flows in shallow gravel-bed rivers, Ph.D. Thesis, École Polytechnique Fédérale De Lausanne, Lausanne, Switzerland.

Dong, Z.N., and Y. Ding (1990), Turbulence characteristics in smooth open-channel flow, *Sci. Chi. A* **33**, 2, 244-256.

Dong, Z.N., J.J. Wang, C.Z. Chen, and Z.H. Xia (1992), Hydraulic characteristics of open channel flows over rough beds, *Sci. Chi. A* **35**, 8, 1007-1016.

Einstein, H.A., and E.A. El-Samni (1949), Hydrodynamic forces on a rough wall, *Rev. Modern Phys.* **21**, 3, 520-524, DOI: 10.1103/RevModPhys.21.520.

Ferguson, R. (2007), Flow resistance equations for gravel- and boulder-bed streams, *Water Resour. Res.* **43**, 5, W05427, DOI: 10.1029/2006WR005422.

Ferro, V. (2003a), ADV measurements of velocity distributions in a gravel-bed flume, *Earth Surf. Process. Land.* **28**, 7, 707-722, DOI: 10.1002/esp.467.

Ferro, V. (2003b), Flow resistance in gravel-bed channels with large-scale roughness, *Earth Surf. Process. Land.* **28**, 12, 1325-1339, DOI: 10.1002/ esp.589.

Ferro, V., and G. Baiamonte (1994), Flow velocity profiles in gravel-bed rivers, *J. Hydraul. Eng. ASCE* **120**, 1, 60-80, DOI: 10.1061/(ASCE)0733-9429 (1994)120:1(60).

Hardy, R.J., J.L. Best, S.N. Lane, and P.E. Carbonneau (2009), Coherent flow structures in a depth-limited flow over a gravel surface: The role of near-bed turbulence and influence of Reynolds number, *J. Geophys. Res.* **114**, F01003, DOI: 10.1029/2007JF000970.

He, J.J., and H.M. Wang (2004), Hydraulic characteristics of open channel flow over a rough bed, *Hydro-Sci. Eng.* **3**, 3, 19-23 (in Chinese).

Jiménez, J. (2004), Turbulent flows over rough walls, *Ann. Rev. Fluid Mech.* **36**, 173-196, DOI: 10.1146/annurev.fluid.36.050802.122103.

Kastner-Klein, P., and M.W. Rotach (2004), Mean flow and turbulence characteristics in an urban roughness sublayer, *Bound.-Lay. Meteorol.* **111**, 1, 55-84, DOI: 10.1023/B:BOUN.0000010994.32240.b1.

Katul, G., P. Wiberg, J. Albertson, and G. Hornberger (2002), A mixing layer theory for flow resistance in shallow streams, *Water Resour. Res.* **38**, 11, DOI: 10.1029/2001WR000817.

Kim, S.C., C.T. Fredrichs, J.P.Y. Maa, and L.D. Wright (2000), Estimating bottom stress in tidal boundary layer from Acoustic Doppler Velocimeter data, *J. Hydraul. Eng. ASCE* **126**, 6, 399-406, DOI: 10.1061/(ASCE)0733-9429(2000)126:6(399).

Kirkgöz, M.S. (1989), Turbulent velocity profiles for smooth and rough open channel flow, *J. Hydraul. Eng. ASCE* **115**, 11, 1543-1561, DOI: 10.1061/(ASCE)0733-9429(1989)115:11 (1543).

Kirkgöz, M.S., and M. Ardiçlioğlu (1997), Velocity profiles of developing and developed open channel flow, *J. Hydraul. Eng. ASCE* **123**, 12, 1099-1105, DOI: 10.1061/(ASCE)0733-9429(1997)123:12(1099).

Knopp, T., T. Alrutz, and D. Schwamborn (2006), A grid and flow adaptive wall-function method for RANS turbulence modelling, *J. Comput. Phys.* **220**, 1, 19-40, DOI: 10.1016/j.jcp.2006.05.003.

Kuelegan, G.H. (1938), Laws of turbulent flow in open channels, Paper RP1181, *J. Res. Natl. Bur. Stand.* **21**, 701-741.

Lane, E.W., and E.J. Carlson (1953), Some factors affecting the stability of canals constructed in coarse granular materials. **In:** *Proc. Minnesota International Hydraulics Convention, 1-4 September 1953, Minneapolis, USA*, 37-48.

Legleiter, C.J., T.L. Phelps, and E.E. Wohl (2007), Geostatistical analysis of the effects of stage and roughness on reach-scale spatial patterns of velocity and turbulence intensity, *Geomorphology* **83**, 3-4, 322-345, DOI: 10.1016/j.geomorph.2006.02.022.

Lin, P., and C.W. Li (2002), A σ-coordinate three-dimensional numerical model for surface wave propagation, *Int. J. Numer. Meth. Fluids* **38**, 11, 1045-1068, DOI: 10.1002/fld.258.

Liu, C.J., D.X. Li, and X.K. Wang (2005), Experimental study on friction velocity and velocity profile of open channel flow, *J. Hydraul. Eng.* **36**, 8, 950-955 (in Chinese).

Marchand, J.P., R.D. Jarrett, and L.L. Jones (1984), Velocity profile, water-surface slope and bed-material size for selected streams in Colorado, Open-file Report 84-773, U.S. Geological Survey, Washington, USA.

Meyer-Peter, E., and R. Müller (1948), Formulas for bed-load transport. **In:** *Proc. 2nd Congress of the International Association for Hydraulic Research, Stockholm, Sweden*, 39-64.

Mignot, E., E. Barthélemy, and D. Hurther (2008), Turbulent kinetic energy budget in a gravel-bed channel flow, *Acta Geophys.* **56**, 3, 601-613, DOI: 10.2478/s11600-008-0020-3.

Mignot, E., D. Hurther, and E. Barthelemy (2009), On the structure of shear stress and turbulent kinetic energy flux across the roughness layer of a gravel-bed channel flow, *J. Fluid Mech.* **638**, 423-452, DOI: 10.1017/S0022112009990772.

Nepf, H., and M. Ghisalberti (2008), Flow and transport in channels with submerged vegetation, *Acta Geophys.* **56**, 3, 753-777, DOI: 10.2478/s11600-008-0017-y.

Nezu, I., and W. Rodi (1986), Open-channel flow measurements with a Laser Doppler Anemometer, *J. Hydraul. Eng. ASCE* **112**, 5, 335-355, DOI: 10.1061/(ASCE)0733-9429(1986)112:5(335).

Nikora, V.I., and D.G. Goring (1998), ADV measurements of turbulence: Can we improve their interpretation? *J. Hydraul. Eng. ASCE* **124**, 6, 630-634, DOI: 10.1061/(ASCE)0733-9429(1998)124:6(630).

Nikora, V.I., I. McEwan, S. McLean, S. Coleman, D. Pokrajac, and R. Walters (2007), Double-averaging concept for rough-bed open-channel and overland flows: Theoretical background, *J. Hydraul. Eng.* **133**, 8, 873-883, DOI: 10.1061/(ASCE)0733-9429(2007)133:8(873).

Nowell, A.R.M., and M. Church (1979), Turbulent flow in a depth-limited boundary layer, *J. Geophys. Res:* **84**, C8, 4816-4824, DOI: 10.1029/JC084iC08p04816.

Papanicolaou, A.N., C.M. Kramer, A.G. Tsakiris, T. Stoesser, S. Bomminayuni, and Z. Chen (2012), Effects of a fully submerged boulder within a boulder array on the mean and turbulent flow fields: Implications to bedload transport, *Acta Geophys.* **60**, 6, 1502-1546, DOI: 10.2478/s11600-012-0044-6.

Raupach, M.R. (1981), Conditional statistics of Reynolds stress in rough-wall and smooth-wall turbulent boundary layers, *J. Fluid Mech.* **108**, 363-382, DOI: 10.1017/S0022112081002164.

Raupach, M.R., J.J. Finnigan, and Y. Brunet (1996), Coherent eddies and turbulence in vegetation canopies: the mixing-layer analogy, *Bound.-Lay. Meteorol.* **78**, 3-4, 351-382, DOI: 10.1007/BF00120941.

Robert, A., A.G. Roy, and B. de Serres (1992), Changes in velocity profiles at roughness transitions in coarse grained channels, *Sedimentology* **39**, 5, 725-735, DOI: 10.1111/j.1365-3091.1992.tb02149.x.

Rowiński, P.M., J. Aberle, and A. Mazurczyk (2005), Shear velocity estimation in hydraulic research, *Acta Geophys. Pol.* **53**, 4, 567-583.

Roy, A.G., T. Buffin-Bélanger, H. Lamarre, and A.D. Kirkbride (2004), Size, shape and dynamics of large-scale turbulent flow structures in a gravel-bed river, *J. Fluid Mech.* **500**, 1-27, DOI: 10.1017/S0022112003006396.

Schindler, R.J., and A. Robert (2005), Flow and turbulence structure across the rip-ple-dune transition: an experiment under mobile bed conditions, *Sedimen-tology* **52**, 3, 627-649, DOI: 10.1111/j.1365-3091.2005.00706.x.

Schmeeckle, M.W., and J.M. Nelson (2003), Direct numerical simulation of bedload transport using a local, dynamic boundary condition, *Sedimentology* **50**, 2, 279-301, DOI: 10.1046/j.1365-3091.2003.00555.x.

Shvidchenko, A.B., and G. Pender (2001), Macroturbulent structure of open-channel flow over gravel beds, *Water Resour. Res.* **37**, 3, 709-719, DOI: 10.1029/2000WR900280.

Singh, A., F. Porté-Agel, and E. Foufoula-Georgiou (2010), On the influence of gravel bed dynamics on velocity power spectra, *Water Resour. Res.* **46**, 4, W04509, DOI: 10.1029/2009WR008190.

Stoesser, T., and V.I. Nikora (2008), Flow structure over square bars at intermediate submergence: Large Eddy Simulation study of bar spacing effect, *Acta Geophys.* **56**, 3, 876-893, DOI: 10.2478/s11600-008-0030-1.

Tachie, M.F., D.J. Bergstrom, and R. Balachandar (2000), Rough wall turbulent boundary layers in shallow open channel flow, *J. Fluids Eng.* **122**, 3, 533-541, DOI: 10.1115/1.1287267.

Wang, D.C., X.K. Wang, and D.X. Li (1998), Mean velocity distributions and im-pact factor analysis of open channel flows, *J. Sediment. Res.* **3**, 86-90 (in Chinese).

Wang, X.Y., X.K. Wang, X.N. Liu, W.Z. Lu, and Q.Y. Yang (2007), Calculation methods of shear velocity in open gravel channel, *Adv. Sci. Technol. Water Res.* **27**, 5, 14-18 (in Chinese).

Wohl, E.E., and H. Ikeda (1998), The effect of roughness configuration on velocity profiles in an artificial channel, *Earth Surf. Process. Land.* **23**, 2, 159-169, DOI: 10.1002/(SICI)1096-9837(199802)23:2<159::AID-ESP829>3.0.CO; 2-P.

Wohl, E.E., and D.M. Thompson (2000), Velocity characteristics along a small step-pool channel, *Earth Surf. Process. Land.* **25**, 4, 353-367, DOI: 10.1002/(SICI)1096-9837(200004)25:4 <353::AID-ESP59>3.0.CO;2-5.

Yang, B., and S.F. Yang (2005), The experimental study on the velocity distribution over the high gradient gravel bed, *J. Hydrodyn.* **20**, 2, 207-213 (in Chinese).

Zippe, H.J., and W.H. Graf (1983), Turbulent boundary-layer flow over permeable and non-permeable rough surfaces, *J. Hydrol. Res.* **21**, 1, 51-65, DOI: 10.1080/00221688309499450.